A Two-Phase Flow Theory for Thermal-Moisture-Hydro-Mechanical Multi-Physical Coupling in Fractured Shale

By

Huimin Wang

B. Eng. (Hons) (Engineering mechanics)

China Agricultural University

M. Eng. (Geotechnical engineering)

China University of Mining & Technology

School of Engineering, University of Tasmania

Submitted in fulfilment of the requirements for the degree of

Doctor of Philosophy

January 2021

UNIVERSITY*of* TASMANIA

SUMMARY

Gas-liquid two-phase flow widely exists in nature and industrial processes. Due to the characteristics of non-linear flow, the complexity of the coupling process and the non-uniformity, the two-phase flow is a basic theoretical problem that needs further study. In energy engineering, the flow process in shale gas production and CO_2 geological storage has an opposite target but shares the same scientific problem: two-phase flow coupling with multi-physical processes in the fractured shale. Therefore, a two-phase flow theory coupling with a multi-physical model in porous media with structural complexity should be developed for the fractured shale. This theory can reveal the flow mechanism of shale gas flowback and CO_2 storage and thus this research is of important scientific background and engineering significance. In this thesis, experimental study, theoretical modelling and numerical simulations are integrated to investigate the thermal-moisture-hydro-mechanical coupling mechanisms. The model is verified using field data and compared with other conventional models. It is expected that the research outcomes can provide better theoretical guidance for engineering applications.

The shale immersion tests were conducted to reveal the variations of shale composition, surface morphology, internal pore structure and tensile strength under acid-base deterioration. First, the tests of dissolution effect on shale with three solutions were conducted. X-ray diffraction (XRD) was used to semi-quantitatively analyze the change of mineral composition. Results showed that the dissolution effect of three solutions on shale ranked: alkaline solution>acid solution>distilled water. Then the field emission electron microscopy (FE-SEM) was used to observe the change of shale surface morphology. It was found that the water-rock reaction had a significant impact on the shale surface morphology and mainly

concentrated on micron-scale cracks and inter-particle pores. The adsorption experiments with nitrogen and CO_2 were conducted to qualitatively analyze the internal microscopic pore structure of shale, and to quantitatively describe the fractal characteristics of pore size distributions. Finally, the Brazilian splitting experiment further revealed the change in the mechanical properties of shale under acid-base degradation. The average tensile strength of shale dropped significantly after being soaked in distilled water, reaching 27.4%.

A novel gas-water relative permeability fractal model was then derived by considering pore-structure parameters (pore-size distribution fractal dimension and tortuosity fractal dimension), water film, geometric correction factor, and real gas effect. This model was verified by comparing with two classic relative permeability models and several sets of experimental data. The effects of pore structure parameters, water film, geometric correction factors and real gas effects on the gas-water relative permeability were explored in detail. Results showed that the pore size distribution determined the flow pattern and the fractal dimension of the pore size distribution had more significant impacts on the change of gas-water effective permeability. The pore geometry directly affected the gas flow mechanism. When the irregularity of pore geometry increased, the Knudsen number decreased, the collision between gas molecules was strengthened, and the gas flow was gradually transitioned into a continuous medium flow.

A three-zone model with multi-scale flow-diffusion was further proposed to investigate the effect of water-based fracturing fluid on shale gas production. The effects of fracture parameters (such as fracture spacing, fracture width, fracture uniformity, and fracture geometry) on shale gas production were investigated. The contribution of multi-scale flow-diffusion and the gas exchange rate in different zones to shale gas production were carefully studied. It was found that the cumulative shale gas production of this two-phase

flowback model decreased by 58.2% after the initial stage of flowback (230 days in our example). The permeability of the micro-fractures in the matrix gradually increased and approached the permeability of the fractured zone.

A moisture-hydro-mechanical multi-physical coupling model was established in shale gas flowback and the migration mechanism of water-based fracturing fluid after the two-phase flow stage was revealed. With the moisture transport, the effects of threshold pressure gradient under the residual water saturation, the water film evaporation on the fracture surface and the gas-liquid-solid mixed adsorption mechanism in the matrix were further investigated. It was found that the structure of the water film in the fracture was the main reason for the non-Darcy flow. The relationship of the gas adsorption decay coefficient, the water coverage factor and the amount of gas adsorption in the matrix was clarified.

A thermal-hydro-mechanical multi-physical coupling model was developed to investigate the coexistence of CO_2 three phases in the CO_2 critical-depth caprock. The effects of temperature and pressure on the sealing efficiency of a shallow caprock at the burial depth of 800 m were numerically studied. The physical properties of CO_2 in the phase transition zone varying with gas partial pressure and formation temperature were discussed. By defining the CO_2 penetration depth in the caprock, the sealing efficiency of the caprock was effectively evaluated. This study found that the CO_2 penetration depth increased by 5.9% after considering the real gas effect in 400 years of storage.

The thermal effects (thermal stress and Joule-Thomson cooling) on the CO_2 migration in deep saline aquifers were studied using the thermal-hydro-mechanical multi-physical and migration mechanisms. The variation of CO_2 physical properties, the accumulation of pore pressure, adsorption expansion and thermal contraction were included in this porosity model. The evolution of temperature near the injection well was analyzed through the coupling of

two-phase flow, porous medium deformation, heat transfer, and Joule-Thomson effect. Finally, the effect of capillary entry pressure on the distribution of CO_2 plume was numerically investigated. The effect of injection boundary conditions on the CO_2 accumulation pressure was explored. These results indicated that an appropriate injection rate was critical to the sealing efficiency of CO_2 storage.

DECLARATION OF ORIGINALITY

This thesis contains no material which has been accepted for a degree or diploma by the University or any other institution, except by way of background information and duly acknowledged in the thesis, and to the best of my knowledge and belief no material previously published or written by another person except where due acknowledgement is made in the text of the thesis, nor does the thesis contain any material that infringes copyright.

AUTHORITY OF ACCESS

This thesis may be made available for loan and limited copying and communication in accordance with the Copyright Act 1968.

Huimin Wang

09/12/2020

ACKNOWLEDGEMENTS

First, I sincerely appreciate Prof. Jianguo Wang, my primary supervisor at China University of Mining and Technology, whose constant guidance, insights and encouragement have been invaluable throughout the period of my Ph.D. study. He has walked me through all published papers which contribute to this thesis. Without his consistent and illuminating instruction, I would never complete the thesis in present form.

Second, I wish to give my deepest gratitude to Prof. Xiaolin Wang, my primary supervisor at University of Tasmania. Without his support and encouragement, I would never have the opportunity to start my double Ph.D. degree in Australia. His knowledge is my precious wealth, which guided me from a comprehensive perspective. Thanks for his thoughtful comments during the completion of this thesis. I would also like to express my special thanks to Prof. Andrew Chan, my co-supervisor at University of Tasmania, who helped me improve my thesis.

Last but least, I would like to sincerely thank my colleagues at the workshop of School of Engineering for their technical support and kind help throughout the completion of my thesis. They are Dr. Gang Shen, Dr. Chengjiang Li, Mr. Haoyu Han, Dr. Kai Tao, Ms. Yingyao Chen, Mr. Fansheng Huang, and Mr. Gang Zhao.

This thesis is dedicated to my supervisors, parents and friends, for their accompanying, encouragement and support in the pursuit of my dream.

STATEMENT REGARDING PUBLISHED WORK CONTAINED IN THESIS

The publishers of the papers comprising Chapter 3, 4, 5, 6 and 7 hold the copyright for that content and access to the material should be sought from the respective journals. The remaining non published content of the thesis may be made available for loan and limited copying and communication in accordance with the Copyright Act 1968.

STATEMENT OF CO-AUTHORSHIP

The following people and institutions contributed to the publication of work undertaken as part of this thesis:

Candidate: Huimin Wang, School of Engineering, University of Tasmania, Hobart, Tasmania, Australia.

Author 1: Professor Jianguo Wang, Primary Supervisor, School of Mechanics and Civil Engineering, China University of Mining and Technology, Xuzhou, Jiangsu, China.

Author 2: Professor Xiaolin Wang, Primary Supervisor, School of Engineering, University of Tasmania, Hobart, Tasmania, Australia.

Author 3: Professor Andrew Chan, Co-Supervisor, School of Engineering, University of Tasmania, Hobart, Tasmania, Australia.

Author 4: Professor Feng Gao, State Key Laboratory for Geomechanics and Deep Underground Engineering, China University of Mining and Technology, Xuzhou, Jiangsu, China.

Author 5: Dr Bowen Hu, State Key Laboratory for Geomechanics and Deep Underground Engineering, China University of Mining and Technology, Xuzhou, Jiangsu, China.

Author 6: Dr Fakai Dou, State Key Laboratory for Geomechanics and Deep Underground Engineering, China University of Mining and Technology, Xuzhou, Jiangsu, China.

PAPER 1: Located in Chapter 3

Huimin Wang, J. G. Wang, Xiaolin Wang, Bowen Hu. 'An improved relative permeability model for gaswater displacement in fractal porous media'. Water, 2020, 12(1): 27.

PAPER 2: Located in Chapter 4

Huimin Wang, J. G. Wang, Feng Gao, Xiaolin Wang. 'A two-phase flowback model for multiscale diffusion and flow in fractured shale gas reservoirs'. Geofluids, 2018, 2018: 1-15.

PAPER 3: Located in Chapter 5

Huimin Wang, J. G. Wang, Xiaolin Wang, Fakai Dou. 'Interaction of shale gas recovery and moisture transport in post two-phase flowback stage'. Journal of Natural Gas Science and Engineering, 2019, 68: 102897.

PAPER 4: Located in Chapters 6

J. G. Wang, Huimin Wang. 'Sealing efficiency analysis for shallow-layer caprocks in CO_2 geological storage'. Environmental Earth Sciences, 2018, 77(21): 738-752.

PAPER 5: Located in Chapter 7

Huimin Wang, J. G. Wang, Xiaolin Wang, Fakai Dou, Bowen Hu. 'Coupled hydro-thermal-mechanical analysis for cold CO_2 injection into a deep saline aquifer'. Thermal Science, 2019, 23(S3): 917-925.

PAPER 6: Located in Chapter 3 and Chapter 5

Huimin Wang, J. G. Wang, Xiaolin Wang, Andrew Chan. 'Multi-scale insights on the threshold pressure gradient in low-permeability porous media'. Symmetry, 2020, 12(3): 364.

Author contributions for papers 1, 3, 4 and 6:

The Candidate developed the multi-physical fully coupled model, analysed the results, and drafted the manuscript. Author 1 was the corresponding author who evaluated the fully coupled model, analysed the results and finalized the manuscript. Author 2 provided valuable comments on the manuscript, edited and enhanced the writings. Author 3 modified and improved the manuscript. Author 4 gave the thoughtful comments for the quality of this manuscript. Authors 5 and 6 assisted with the numerical modelling.

Author contributions for paper 2 and 5:

The Candidate collected the relevant literature, proposed the novel fractal model and drafted the manuscript. Author 1 was the corresponding author who analysed the results and finalized the manuscript. Author 2 contributed to improving the content. Author 5 assisted with validation work.

We, the undersigned, endorse the above stated contribution of work undertaken for each of the published (or submitted) peer-reviewed manuscripts contributing to this thesis:

Signed:

	Huimin Wang Candidate School of Engineering University of Tasmania	Xiaolin Wang Professor Primary Supervisor School of Engineering University of Tasmania	Damien Holloway Associate Professor On behalf of Head of School School of Engineering University of Tasmania
Date:	09/12/2020	09/12/2020	09/12/2020

NOMENCLATURE

V_a	Nitrogen adsorption volume at pressure equilibrium（m^3）
p_0	Saturated vapor pressure of nitrogen at -196.15℃(MPa）
p_b	Nitrogen balance pressure（MPa）
σ_t	Tensile strength of shale sample（MPa）
$P_{\max}$	Peak loading（kN）
D	Diameter of shale sample（cm）
h	Thickness of shale sample（cm）
k_{rw}	Relative permeability of liquid phase
k_{rg}	Relative permeability of gas phase
s_w^*	Effective saturation of water
p_c	Capillary pressure（MPa）
s_w	Water saturation
s_g	Gas saturation
μ_r	The ratio of the viscosity of water to gas
λ	Pore size distribution factor
μ_g	Gas viscosity（$Pa \cdot s$）
μ_w	Liquid viscosity（$Pa \cdot s$）
ϕ	Rock porosity
ρ_g	Gas density（kg/m^3）
ρ_{ga}	Gas density at atmospheric pressure（kg/m^3）
ρ_c	Rock density（kg/m^3）
T	Temperature（K）
P_L	Langmuir adsorption pressure（MPa）
V_L	Langmuir volume constant（m^3）
p_g	Gas pressure（MPa）
p_e	Capillary entry pressure（MPa）
$k_{rw}^{\max}$	Maximum relative permeability of the wetting phase at the endpoint
$k_{rg}^{\max}$	Maximum relative permeability of the non-wetting phase at the endpoint
N_w	Correction factor of wetting phase
N_g	Correction factor of non-wetting phase
S_{rw}	Residual water saturation
S_{rg}	Residual gas saturation
$m_e(p)$	The equilibrium gas content when the fracture gas pressure is p（kg）
τ_d	Diffusion time（s）

D_g	Diffusion coefficient between fracture and matrix（m^2/s）
a	Shape factor of matrix block
L_x	Fracture opening in x direction（m）
L_y	Fracture opening in y direction（m）
k	Permeability（m^2）
μ	Fluid viscosity（$Pa\cdot s$）
τ_0	Yield stress（MPa）
p_p	Pore pressure（MPa）
δ	Representative capillary length（m）
$r_{\max}$	Maximum pore radius（m）
$r_{\min}$	Minimum pore radius（m）
r_{wg}	The distance from the center of the hole to the air-water contact surface（m）
r	Pore radius（m）
D_f	Fractal dimension of pore size distribution
D_t	Tortuosity fractal dimension
d	Euclidean dimension
σ	Surface Tension（N/m）
κ	Contact angle of water-gas-rock interface（ °）
r_c	Critical capillary size（m）
L	Actual capillary length（m）
L_0	Representative capillary length（m）
γ	Geometric correction factor
η	Mean free path of gas molecules（m）
K_n^*	Modified Knudsen number
R	Ideal gas constant（$J/(mol\cdot K)$）
M	Gas molecular mass（g/mol）
Z	Gas compressibility factor
p_{gc}	Gas critical pressure（MPa）
T_{gc}	Gas critical temperature（K）
μ_a	Gas viscosity under standard conditions（$Pa\cdot s$）
β	Dimensionless sparsity coefficient
α	Slip coefficient
μ_{wf}	High viscosity of water film（$Pa\cdot s$）
ζ	Correction factor for vapor flow rate
v_v	Flow rate of vapor （m/s）
M_v	Vapor molecular mass （g/mol）
D_{va}	Vapor diffusion coefficient （m^2/s）
r_{mean}	Average radius of rock particles（m）
c_K	Dimensionless Kozeny constant

τ_h	Tortuosity of the rock
e	Volume ratio of pore to matrix
e_{100}	The volume ratio of pores to matrix when the effective stress is 0.1 MPa
χ	Clay mineral content
o	The angle between the average pore arrangement and the bedding direction（ °）
ρ_{gf}	Gas density in micro-fractures（kg/m^3）
ϕ_f	Porosity of micro-fractures
p_f	Gas pressure in micro-fractures（MPa）
k_{mapp}	Apparent permeability of micro-fractures in the matrix（m^2）
d_f	Diameter of micro-fractures（m）
b	Klinberg constant
p_m	Gas pressure in the matrix（MPa）
k_k	Apparent permeability of the matrix（m^2）
ρ_{gm}	Gas density in the matrix（kg/m^3）
D	Effective diffusion coefficient of gas in the matrix（m^2/s）
D_c	Diffusion coefficient caused by viscous flow（m^2/s）
D_e	Effective molecular-Knudsen diffusion coefficient（m^2/s）
D_{es}	Effective surface diffusion coefficient（m^2/s）
d_{hf}	Average width of hydraulic fracture（m）
ϕ_{hf}	Porosity of hydraulic fracture
k_{hf}	Permeability of hydraulic fracture（m^2）
ρ_v	Density of water vapor（kg/m^3）
$\vec{u}$	Moisture Convection Velocity（m/s）
c_w	The concentration of discontinuous water in the fracture（mol/m^3）
D_w	Diffusion coefficient driven by water concentration gradient（m^2/s）
θ	Volume content of water film on the surface of fracture
K	Evaporation rate（$kg/(m^2 \cdot s)$）
c_{sat}	Saturated vapor concentration（mol/m^3）
c_v	Current vapor concentration （mol/m^3）
a_w	Water activity
V^*	Maximum adsorption capacity per unit volume（m^3）
A	Specific surface area of pores（m^2）
χ	Water molecule coverage factor
λ_d	Gas adsorption decay factor in wet shale matrix
m_{wet}	Adsorbed gas content of wet shale（kg）

G	Shear modulus（MPa）
ν	Poisson's ratio
α_T	Thermal expansion coefficient（1/K）
ε_v	Volume strain
K_s	Bulk modulus of porous media（MPa）
K_{nw}	Bulk modulus of gas（MPa）
α_{nw}	Thermal expansion coefficient of gas（1/K）
C_{nw}	Specific heat constant of gas（$J/(kg\cdot K)$）
λ_M	Thermal conductivity of the caprock（$W\cdot m^{-1}\cdot K^{-1}$）
λ_s	Thermal conductivity of the matrix（$W\cdot m^{-1}\cdot K^{-1}$）
λ_{nw}	Thermal conductivity of gas（$W\cdot m^{-1}\cdot K^{-1}$）
μ_{JT}	Joule-Thomson coefficient
K_{eq}	Thermal conductivity（$W\cdot m^{-1}\cdot K^{-1}$）

LIST OF FIGURES

LIST OF TABLES

CONTENTS

Chapter 1: Introduction

1.1. Background

Gas-liquid two-phase flow is one of the most common and complex forms of multi-phase flow. Due to structural inhomogeneity, flow nonlinearity and coupling complexity during the displacement process, the two-phase flow has become a challenging theoretical topic [1-3]. The gas-liquid interface changes in the displacement process and is affected by various factors (pore size distribution, capillary pressure, wetting angle, and relative permeability) [4-8]. Two-phase flow is widely observed in nature and used in industrial production, such as vapor and water in chemical engineering, biological blood circulation, pipeline transportation, shale gas flowback, and CO_2 geological storage [9-11]. Especially, shale gas flowback and CO_2 geological storage are two-phase flow problems in porous media [8]. On the other hand, the multi-physical influences of the gas diffusion in the matrix, the thermal effect, the deformation of fractured rock, and the moisture transport are vital to the two-phase flow in porous media.

Fig. 1.1 describes the applications of two-phase flow in shale gas flowback and CO_2 geological storage. In shale gas production, the concern is how to effectively extract the shale gas. But, the remaining fracturing fluid in the reservoir will form a two-phase flow with the shale gas and then affect the shale gas production [12-15]. In CO_2 geological storage, a large amount of supercritical CO_2 is injected into the target formation or storage reservoir. CO_2 drives the brine to form the front of two-phase flow. It is not only related to the CO_2 sealing efficiency in the reservoir but also affects the safety of caprock [16]. Either shale gas production or long-term storage of CO_2 has the same scientific problem - the theory of two-phase flow. These two applications are different in time and space scale, but the

two-phase flow for multi-physical coupling in fractured shale is their common theoretical basis. An accurate theoretical model could guide engineering applications in fractured shale.

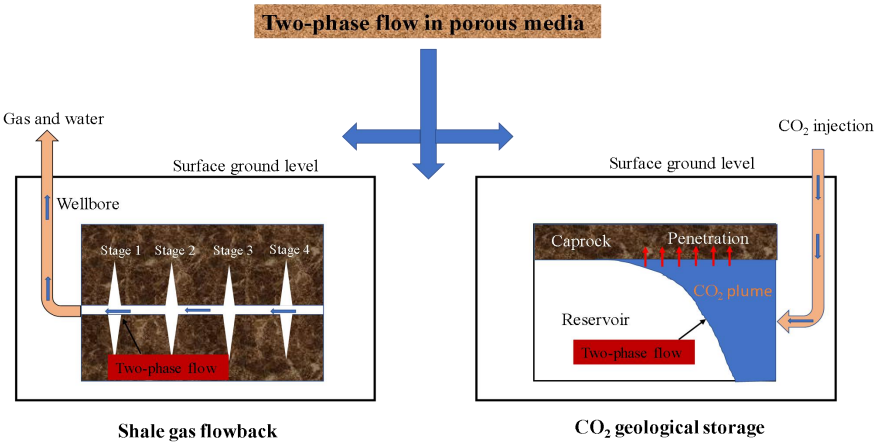

Fig. 1.1. Applications of two-phase flow in porous media

The two-phase flow theory for multi-physical coupling in fractured shale for both shale gas production and CO_2 geological storage has attracted researchers' attention, but there is still a lack of relevant research [17-23]. For example, the macroscopic relative permeability model could not well describe the influence of complex pore-structure on the flow mechanism; The numerical simulation did not take into account the effect of multi-physical coupling on the two-phase flow. The existence of residual water at different time scales was not distinguished in the physical concept model. Therefore, establishing a two-phase flow theory for multi-physical coupling in fractured shale can further explore the flowback mechanism at different stages of shale gas production and the CO_2 migration in geological storage, thus being of great scientific significance. This thesis combines experimental testing, theoretical derivation and numerical simulation to investigate the two-phase flow theory for the engineering problems in the shale gas flowback and the CO_2 geological storage. This research aims to provide theoretical guidance for shale gas flowback and CO_2 storage engineering applications.

1.1.1. Background of two-phase flow in shale gas production

The "Energy Development Strategic Action Plan of China (2014-2020)" designed the energy strategy, focusing on the implementation of three elements of "saving, clean, and safe" in Chinese energy plan [24]. According to EIA (United States Energy Information Agency) 2016 statistics [25]: Global natural gas production will gradually increase from 97×10^8 m^3 in 2015 to 157×10^8 m^3 in 2040. Shale gas, as an emerging unconventional natural gas energy source, is characterized by high efficiency, clean, abundant reserves and requirement. The large-scale development of shale gas is quietly changing the future energy structure and territory of the world. Shale gas production is expected to grow three times from 2015 to 2040 and will account for 30% of global gas production in 2040. The distribution of global technically recoverable shale gas is shown in Fig. 1.2, which shows that Chinese shale gas reserves are extremely abundant compared with other countries in the world. The total amount of shale gas reserves reached 144 trillion cubic meters, accounting for 20% of the world's total reserves. The recoverable reserves of shale gas in China are 36.1 trillion cubic meters, accounting for about 22% of the global technologically recoverable reserves [26].

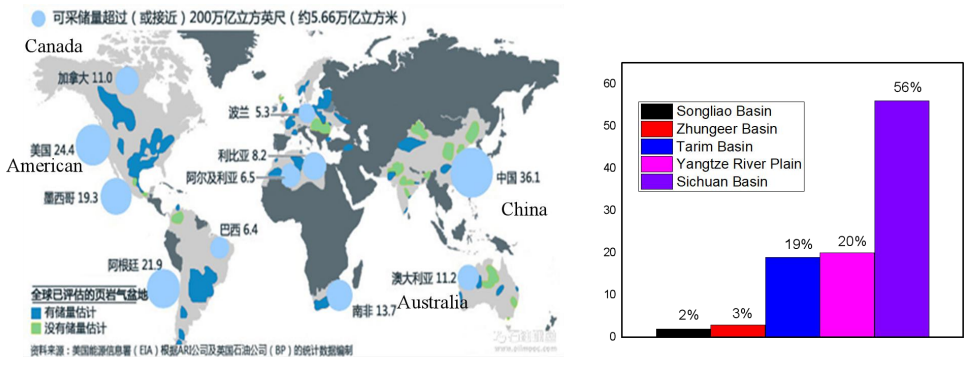

（a） （b）

Fig. 1.2. Distribution of technically recoverable shale gas resources [26, 27] (a) Distribution in the world (b) Distribution in China

China's shale gas reserves are abundant. But, compared with the United States and Canada, China still faces some difficulties in the extraction of shale gas reservoirs (late start-up and underdeveloped technology) [28-31]. In 1921, the first shale well in the United States was drilled successfully in New York [32, 33]. However, the commercialization process was slow due to high costs at that time. Until the late of the 1990s, U.S. shale gas development entered a period of rapid development as the breakthrough of key technologies such as horizontal well drilling and hydro-fracturing was achieved. Large-scale commercial exploitation has turned the United States into an energy export country and changed the world energy landscape [34, 35]. From 2006 to 2010, US shale gas production achieved nearly 20 times growth in five years. In 2013, US shale gas production reached 336.9 billion square meters, accounting for 40% of total natural gas production [36].

With the establishment of three national-level demonstration zones of marine shale gas in Fuling, Weiyuan-Changning and Zhaotong, the shale gas production in China has entered a new growth stage [37, 38]. At the end of the "Twelfth Five-Year Plan", total geological reserves of marine shale gas in China have reached 544.1 billion cubic meters. The production of marine shale gas reached 4.5 billion cubic meters. It indicated that China’s large-scale development of marine shale gas has initially realised and China has become one of the four countries in the world to commercialize shale gas exploitation.

Compared with conventional natural gas reservoirs, shale gas reservoirs are generally characterized by high formation stress, low porosity and ultra-low permeability [39]. 20%-85% of shale gas exists with the adsorption state in high carbon shale [40]. In order to achieve large-scale industrial exploitation of shale gas, hydraulic fracturing is usually

required to form an effective fracture network, increasing the contact area between the hydraulic fracture and the shale matrix [41, 42]. However, this behavior will inevitably lead to a large amount of water-based fracturing fluids remaining in the reservoir. This remaining water in the reservoir has a significant impact on the migration of shale gas in the fracture and matrix system. According to field measurements, the flowback rate of water-based fracturing fluids is usually low, ranging from 10% to 30%. Due to different geological conditions, different wells have different variability, and the well with the lowest flowback rate can reach 5%. Therefore, reasonable analysis of the two-phase flow mechanism during shale gas flowback can accurately predict shale gas production.

1.1.2. Background of two-phase flow in CO_2 geological storage

According to the 2007 Intergovernmental Panel on Climate Change report, the average global temperature has increased by 0.74 ℃ in the past 100 years [43]. If the emission of CO_2 is not controlled, temperature changes more dramatically, which will cause many natural disasters, such as melting of glaciers, increased pests and diseases, ocean storms, and rise of sea level. Therefore, many countries have signed the famous "Kyoto Agreement" and “Paris Agreement” to control the concentration of greenhouse gases in the atmosphere. In December 2009, the United Nations Climate Change Conference was held to limit CO_2 emissions and control the rise of global temperature within 2 ℃ [44]. In the global environment of emission reduction, China's emission reduction targets in Paris agreement are: by 2030, domestic CO_2 emissions per unit of GDP decreased by 60% to 65% compared with 2005, and the proportion of non-fossil energy increased up to 20% [45].

As one of the forward-looking technologies that can effectively reduce the CO_2 emissions of traditional energy industries and mitigate climate change, CCUS (Carbon

Dioxide Capture and Utilization) has been rapidly developed and widely used in the world in recent years. Fig. 1.3 shows the process of CO_2 geological storage. It can be seen that the CO_2 produced in industry or life cannot be directly discharged into the atmosphere but is captured by physical-chemical methods, and then transported to a well-sealed geological site for long-term storage, such as abandoned oil/gas reservoirs, deep saline aquifers, abandoned coal mines. The saline aquifer is currently regarded as the best geological storage site, accounting for 90% of all CO_2 storage projects.

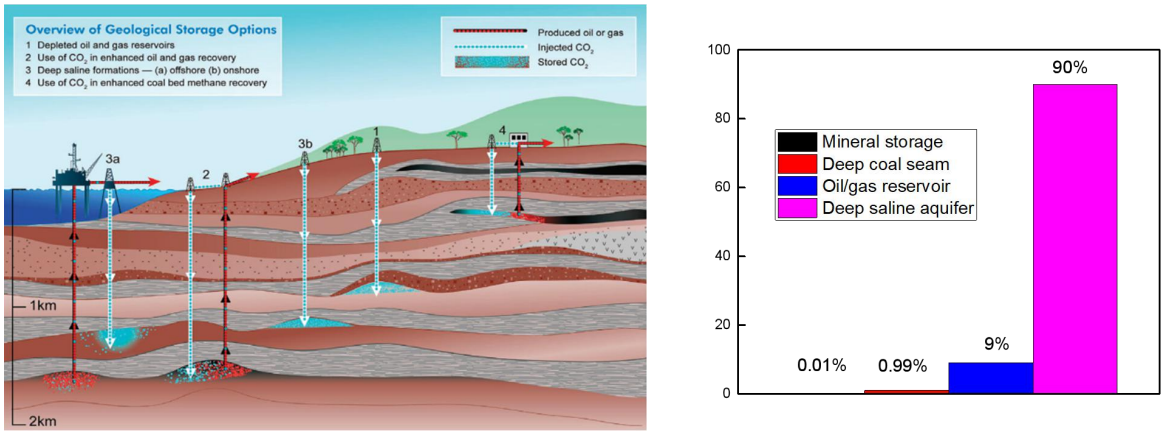

（a） （b）

Fig. 1.3. Schematic diagram of the CO_2 geological storage (IPCC report) (a) Process of CO_2 storage (b) CO_2 storage space

The study on CO_2 migration in saline aquifers is the supercritical CO_2 displacing brine water in complex porous media. The theory of two-phase flow is its flow mechanism. When supercritical CO_2 is injected into the saline aquifer below 800 m, there are four main storage mechanisms under the complex geophysical-chemical action: (1) Structural storage: The density of supercritical CO_2 is less than the brine water in the reservoir, and will migrate to the bottom of the shale caprock under the action of buoyancy. Due to the tightness and low permeability of shale caprocks, the accumulated CO_2 pressure (non-wetting phase) is not enough to displace the brine water (wetting phase) in the caprock. Thus, CO_2 is enclosed by

capillary pressure. (2) Residual gas storage: supercritical CO_2 displaces brine water, forming a front of two-phase flow. However, when the CO_2 injection is stopped, the brine water in the reservoir re-occupies the pore space, and part of the CO_2 loses fluidity under the action of capillary pressure. (3) The supercritical CO_2 injected into the reservoir will be partially dissolved in the brine water. (4) When CO_2 exists with a dissolved state, it will further geochemically react with the mineral components in the reservoir to generate new carbonate minerals. Among the above four main storage mechanisms, the first two are physical storage, and the latter two are chemical storage. Although the storage mechanism and time scale are different, the four storage mechanisms jointly guarantee the safety of CO_2 geological storage.

The China Geological Survey has successively researched the capture and resource utilization of carbon dioxide. For example, since 2010, the "National Carbon Dioxide Geological Storage Potential Evaluation and Demonstration" project has assessed the CO_2 geological storage potential and suitability of 417 land areas and shallow sea sedimentary basins [46]. Li et al. [47] assessed the CO_2 storage potential of China's saline aquifers, which could reach 143.5 Gt. The geological storage sites in China's main sedimentary basins were evaluated. After considering the geological conditions of sedimentary basins in China, Zhang et al. [48] concluded that the Songliao Plain, Sichuan Basin, Bohai Sea Plain, Yangtze River Delta are suitable CO_2 storage sites. Also, CCS (Carbon Dioxide Capture and Storage) is also widely used in the world. The representative projects in operation are shown in Table 1.1 [49].

Table 1.1. Representative projects of CO_2 geological storage [49]

Representative projects	Storage capacity （Mt/a）	Description
In Salah (Algeria)	1.2	The first commercial-scale land-based CCS project
Sleipner (Norway)	1	The first commercial CCS project
Frio (United States)	/	The first feasibility demonstration project
Gorgon (Australia)	3.3	Commercial scale

Snohvit (Norway)	0.75	Commercial scale

The Sleipner project in Norway is the world's first commercial CCS project. 1 million tons of CO_2 is injected into the saline aquifer every year, and it is planned to last for 20 years; The In Salah project in Algeria is the world's first commercial land-based saline aquifer CCS project, which separates the CO_2 from natural gas and stores it in the saline aquifer. It plans to inject 1.2 million tons of CO_2 annually. Furthermore, there are some CCS projects for the purpose of scientific experiments, such as the Nagaoka project in Japan, the Frio project in the United States, the Ketzin project in Germany, and the Otway project in Australia. Rutqvist et al. [50] found that long-term underground storage of CO_2 not only pollutes the upper water source through the CO_2 leakage but also causes the earthquake or even structural damage to the ground building. In China, the Shenhua CO_2 deep saline aquifer storage project in the Ordos plans to inject 100,000 tons of CO_2 each year. It is China's first deep saline aquifer CO_2 geological storage demonstration project [51].

Overall, China is taking the way of green development. Both energy conservation and emission reduction have got more attention [52]. In the long-term underground storage of CO_2, the sealing efficiency of the caprock directly determines the safety of CO_2 geological storage. The penetration of CO_2 in the caprock would cause geological deformation, two-phase flow and the chemical reaction of dissolution or sedimentation. How to evaluate the sealing efficiency of caprock is important.

1.2. Literature review

1.2.1. Research of water-based fracturing fluid flowback

1.2.1.1. Research on the flowback model of gas-water two-phase flow

Compared with conventional natural gas reservoirs, shale gas reservoirs have the characteristics of deep burial depth, low porosity and ultra-low permeability [53, 54]. In order to increase shale gas production , hydraulic fracturing is usually required to form an effective fracture network [55]. When the bottom hole pressure drops or the injection of the water-based fracturing fluid is stopped, the water-based fracturing fluid in the reservoir will flow back along with the production of shale gas. This gas-water two-phase flow after hydraulic fracturing is called "flowback" in shale gas production [56, 57]. In many previous studies, single-phase flow models were used to predict shale gas production, and flowback data of water-based fracturing fluids were often ignored [58-60]. This single-phase flow model that simplifies the water-gas interaction makes numerical calculations faster, but the prediction of shale gas production is not very consistent with the measured data on-site, especially in the early stages of production [61]. Crafton and Gunderson [62] used high-frequency single-phase flowback data to characterize the properties of hydraulic fractures. Williams-Kovacs [63] proposed a single-phase flow equation based on the conservation of flow mass. However, these single-phase flow models ignore the flowback data of the water-based fracturing fluid, and cannot guarantee the accuracy of model predictions in the two-phase flow stage.

In order to overcome the limitations of the single-phase flow model, more attentions have been paid to the water-rock interaction in shale gas production. Yuan and Huang [64] proposed a three-porosity fracture-matrix model for shale reservoirs to investigate the

phenomenon that water diffuses into the micro-fractures due to capillary pressure. Li et al. [65] immersed the core of well YY1HF in resistance-reducing water for pretreatment and conducted core displacement experiments to investigate the impact of resistance-reducing water on the physical properties of shale. Shale pulse overlay physical property test found that porosity and permeability of shale samples were improved after immersion in low-resistance water. Nitrogen adsorption and desorption test showed that the nitrogen adsorption capacity and the specific surface area was reduced by 33%. These results indicated that closing well could improve the petrophysical parameters and change the channel of gas flow. Ni et al. [66] conducted immersion experiments on shale cores of the Longmaxi Formation in the Sichuan Basin and explored the flow mechanism of the liquid infiltrated into the reservoir during drilling and stimulation. The results showed that the water phase trap was automatically released by shutting down the well. Zhao et al. [67] experimentally investigated the influence of water content on permeability evolution and gas adsorption.

On the basis of laboratory tests, more two-phase flow numerical models are proposed to further explore the gas-water flowback mechanism in fractured shale. Jiang et al. [68] established a numerical model for gas reservoir combined with wellbore flow. The effects of parameters such as viscosity, pressure coefficient, bottom hole pressure, half-length of fracture, fracture conductivity, and irreducible water saturation on the flowback rate were discussed. Yin et al. [69] established a two-phase flow model in a shale gas reservoir based on Langmuir isotherm adsorption and Fick's pseudo-steady-state diffusion law, and explored the influence of adsorbed gas on bottom hole pressure. A transient flowing model considering the effect of two-phase flow after the hydraulic fracturing was also developed for gas production [70]. This model further analyzes the response of transient pressure. Yang et al. [71] developed a semi-analytical model to simulate the two-phase flow during the flowback

period with complex fracture networks. They found that increasing the fracture network complexity was favorable to gas production enhancement. Ezulike and Dehghanpour [72] applied a dynamic relative permeability on the two-phase flow in the hydraulic fractures. Their results showed that the relative permeability varied with reservoir parameters in the early flowback period. Xu et al. [73] analyzed the mechanisms for flowback behaviors and put forward a material balance approach to estimate the effective fracture volume in the Horn River Basin. Ezulike et al. [74] developed a two-phase flowback tank model for estimating fracture pore volume independent of fracture geometry. Their results indicated that the effective fracture pore volume was the most sensitive to fracture pore volume compressibility. Alkouh et al. [75] provided an effective method to estimate fracture volume through the water flowback and gas production data. Therefore, different methods have been used to characterize the fracture properties but the interaction between fracture flow and shale gas diffusion has not been considered in the two-phase flowback stage.

1.2.1.2. Research on the mechanism of moisture transport

Engelder et al. [76] estimated that more than 50% of fracturing fluid was retained in shale formation after flowback. Wattenbarger and Alkouh [77] indicated that only 10-40% of water-based fracturing fluid could be recovered. However, Zhang and Ehlig-Ecnomides [78] observed much higher water recovery (up to 60%) during the long-term period of shale gas production. This indicated that the two-phase flowback might be only one stage of water flowback. With continuous gas production, the fracturing fluid might flow out not only in two-phase flow but also in moisture transport.

The flowback process of shale gas can be divided into the following three stages, as shown in Fig. 1.4. Stage 1: the reflux of fracturing fluid contains a small amount of free gas, which is called bubble flow; Stage 2: in the initial stage of gas production, shale gas displaces

fracturing fluid, forming a gas-liquid two-phase flow in the fracture; Stage 3: in the late stage of gas production, the water film on the surface of the fracture is extracted by evaporation.

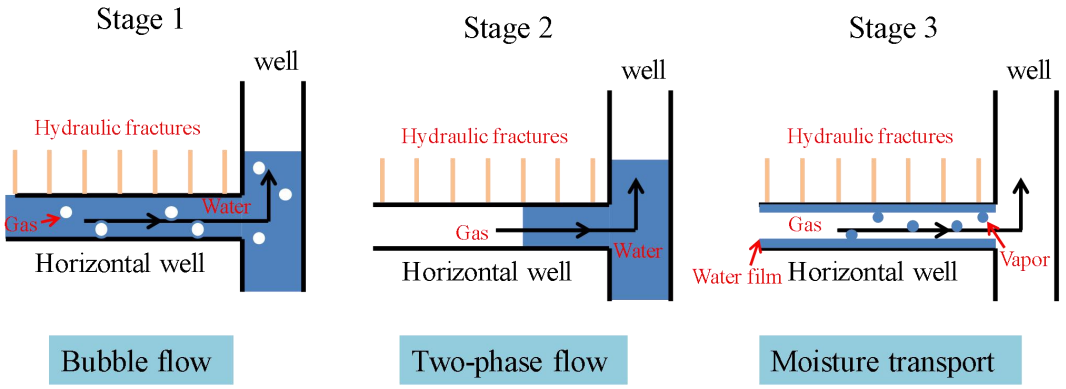

Fig. 1.4. Schematic diagram of flowback in three stages

Therefore, the flowback rate of fracturing fluid should be higher during the long-term exploitation of shale gas. Meanwhile, the evaporation of the water film increases the flow channels in the fractures and improves the permeability. This phenomenon will also lead to an increase in shale gas production. Zuluaga et al. [79] observed the displacement process of residual water in water-saturated cores. With continuous gas replacement, the water saturation further decreased to 12.4-14.7%. This residual water was extracted with the gas in the form of humidity. The water saturation directly changed the relative permeability and further affected the shale gas production. Therefore, moisture transport after the two-phase flow stage was critical for shale gas production. Wang et al. [80] studied the two-phase flow of fracturing fluid and shale gas in the flowback stage, but the transport mechanism of the residual fracturing fluid was still unclear.

1.2.2. Research of carbon dioxide geological storage

A large amount of CO_2 is directly emitted into the atmosphere without treatment, and this emission has become one of the important causes of global warming [81]. Therefore, the geological storage of CO_2 has received more attention in recent years. It is regarded as the

most effective measure to reduce the concentration of CO_2 in the atmosphere [82, 83]. After CO_2 is injected into the deep reservoir, it will undergo two stages of migration: the first stage is the lateral migration of CO_2 in the storage reservoir; the second stage is the CO_2 penetration into the caprock [84]. In addition, some studies show that a part of CO_2 leaks to shallow reservoirs through faults, polluting freshwater resources [85, 86]. Therefore, a comprehensive assessment of the sealing efficiency of the caprock is essential to the CO_2 geological storage.

1.2.2.1. Geochemical reactions in the caprock

The transport mechanism of CO_2 in the caprock is relatively complicated. Due to the physical-chemical multi-physical coupling in the caprock, the fractures will self-heal or self-elevate [7, 87, 88]. Experiments observed that CO_2 reduced the pH of the brine water, leading to the dissolution of calcite [89], while precipitation reactions were observed in the caprock containing anhydrite [90]. Andreas et al. [91] experimentally found when CO_2 was injected into a shale formation, mineralization would occur on its surface, and permeability and porosity decreased. It was seen that the shale was regarded as a caprock for sequestration of carbon dioxide, the risk of leakage can be reduced. Chasset et al. [92] found that after CO_2 injection for a period of time, salt precipitation occurred around the injection well, and the permeability of the caprock reduced by 24%-33%. Anthony et al. [93] studied the chemical reaction of CO_2 with different mineral components through experiments. It was found that carbonate rock and CO_2 reacted most easily, and the reaction was more intense and shorter than other minerals. Carbonate minerals would dissolve in a large amount in a short period of time, and then other types of carbonates would be formed in a long period of time. Clay minerals were relatively stable and kaolinite was relatively unstable. Therefore, geochemical reactions needed to be considered in the safety assessment of CO_2 geological storage. Gaus et

al. [94] conducted a numerical simulation study on the sealing efficiency of the caprock. The model assumed that the caprock was homogeneous. After CO_2 injection, it dissolved and migrated, and a series of geochemical reactions occurred with the brine water and caprock. In the initial stage of injection, carbonate minerals were mainly dissolved, which lasted for more than 1000 years. However, with the continuous injection of CO_2, the dissolution of anorthite and albite was also increasing, and some minerals were also produced. Finally, the porosity of the caprock was slightly reduced, which was mostly in the bottom region of the caprock. Gao et al. [95] studied the velocity distribution and relative permeability curve of two-phase flow during CO_2 storage based on the LBM method of Shan-Chen multiphase model. The results showed that although a higher CO_2 injection rate increased the residual CO_2 capture volume, it also reduced the chemical capture volume. Therefore, geochemical reaction was a problem that must be considered in the safety evaluation of CO_2 geological storage caprock. In the second chapter of this thesis, we used shale immersion experiments to further explore the changes in shale microstructure and mechanical characteristics under acid-base degradation.

1.2.2.2. Real gas effects in the critical depth caprock

The CO_2 is usually injected into a saline-formation in a supercritical state. This CO_2 is immiscible with water and has a liquid-like density but a gas-like viscosity. When CO_2 migrates towards shallow layers (through faults, fractures, or improperly abandoned wells), it experiences a large decrease in both pressure and temperature as well as a great volume expansion above the depth of 800 m [96]. At the shallow layers, subcritical CO_2 can form a two-phase mixture of gas and liquid, with significant latent heat effects. This state change would be favorable to CO_2 leakage. Pruess et al. [97] conducted analyses of phase transition and Joule-Tomson cooling phenomenon during CO_2 leakage from a deep storage reservoir to

a shallow aquifer. The change of three phases was considered by extended fluid property module "ECO2N" and the effects of dissolved NaCl and precipitated halite were explored. Fang et al. [98] proposed a viscosity model based on the Peng-Robinson equation. In addition, experimental observations showed that temperature had a significant effect on the physical properties of CO_2, especially when the viscosity of CO_2 was close to the supercritical range [99]. Therefore, it is necessary to consider the phase change effect of CO_2 in the shallow critical depth caprock and establish a thermal-hydro-mechanical multi-physical coupling model based on two-phase flow to effectively evaluate the sealing safety of the shallow caprock.

1.2.2.3. CO_2 heating effect in the reservoir

Injected CO_2 is usually colder than the reservoir. This causes thermal contraction and thermal stress. When high-pressure CO_2 is injected into the low-pressure reservoir, the CO_2 expands, causing further temperature drop due to Joule-Thomson cooling. In this case, the physical properties of CO_2 do not only change with pressure but also varies with these temperature drops. Vilarrasa et al. [99] compared the flow behaviors of liquid CO_2 and supercritical CO_2 in the reservoir. They found that the injection efficiency of liquid CO_2 was higher due to the higher density of liquid CO_2 and smaller resultant overpressure. This indicated that the change of CO_2 physical properties during injection was indeed worth of multi-physical modeling. Mathias et al. [101] developed a simple analytical solution and found that Joule-Thomson cooling was a negative factor for CO_2 storage. In their solutions, the permeability of the reservoir was constant and the accumulation of pore pressure and thermal stress were not considered. Gao et al. [102] proposed the travelling-wave solutions for both linear and non-linear heat transfers. They only considered the temperature variation without the thermal-mechanical coupling. This was not enough to understand the CO_2 flow

behaviors in the geological storage. Gor et al. [103] established a multi-phase model to investigate the effect of thermal stress on caprock integrity. Their simulations showed that the stress above the horizontal injection well led to tensile or shear failure of the caprock. Kim and Hosseini [104] conducted a numerical simulation to include fluid flow, thermal stress and thermal diffusion. However, their simulations were based on single-phase flow. The effects of relative permeability parameters on CO_2 migration in the reservoir were not included. The above studies demonstrated the importance of non-isothermal flow of CO_2 migration in deep saline aquifer, but a coupled hydro-thermal-mechanical model was still missing.

1.3. Research objectives

This research aims to study the two-phase flow coupling with multi-physical in fractured shales. It comprises the key objectives detailed as follows:

(1) The shale immersion tests are conducted to reveal the variations of shale composition, surface morphology, internal pore structure and tensile strength under acid-base deterioration.

(2) A novel gas-water relative permeability fractal model is derived by considering pore-structure parameters (pore-size distribution fractal dimension and tortuosity fractal dimension), water film, geometric correction factor, and real gas effect.

(3) A three-zone model with multi-scale flow-diffusion is further proposed to investigate the effect of water-based fracturing fluid on shale gas production. The effects of fracture parameters on shale gas production are investigated. The contribution of multi-scale flow-diffusion and the gas exchange rate in different zones to shale gas production are carefully studied.

(4) A moisture-hydro-mechanical multi-physical coupling model is established in shale gas flowback and the migration mechanism of water-based fracturing fluid after the two-phase flow stage is revealed.

(5) A thermal-hydro-mechanical multi-physical coupling model is developed to investigate the coexistence of CO_2 three phases in the CO_2 critical-depth caprock.

(6) The thermal effects (thermal stress and Joule-Thomson cooling) on the CO_2 migration in deep saline aquifers are studied by the thermal-hydro-mechanical multi-physical model.

1.4. Thesis outline

Based on the above main research content, this thesis uses related theories such as seepage mechanics, rock mechanics, elastic mechanics to establish a two-phase flow coupling with the multi-physical model in the fractured shale. This fully coupled model is applied to the shale gas production and carbon dioxide geological storage. The main research contents include shale microstructure and mechanical characteristics analysis, gas-water relative permeability fractal model, multi-scale flow-diffusion mechanism, moisture-hydro-mechanical multi-physical coupling model considering the water film, and sealing efficiency of critical depth caprock and the thermal-hydro-mechanical multi-physical coupling mechanism in the saline aquifers. Combining multi-physical coupling analysis software COMSOL with MATLAB realizes the finite element solution of the coupled equations. Then, the simulation results are compared with the engineering example data and related theories in the literature. This thesis adopts a research method that combines experimental testing, theoretical derivation and numerical simulation. The research technical route is shown in Fig. 1.5.

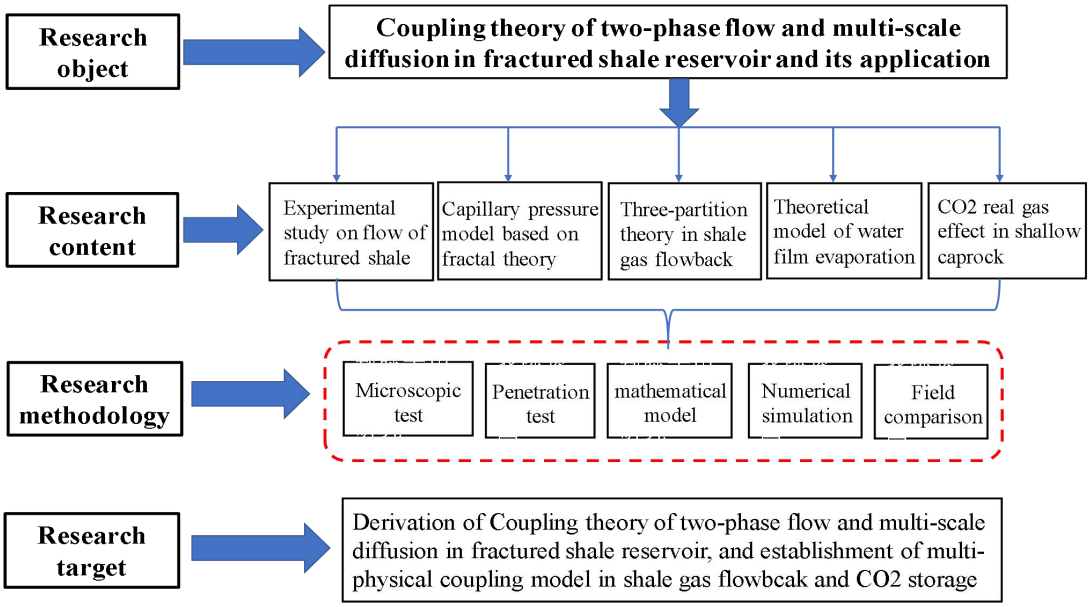

Fig. 1.5. The route of research technology

Chapter 1 emphasizes the important research significance of two-phase flow coupling with multi-physics theory in fractured shale for shale gas production and carbon dioxide geological storage. The literature on shale gas flowback and carbon dioxide storage in saline aquifers was reviewed, which showed that the two-phase flow coupling with multi-physical model was still missing.

Chapter 2 experimentally studied the pore-structure and mechanical characteristics of shale under acid-base degradation. First, the changes of mineral composition were semi-quantitatively analyzed by X-ray diffraction (XRD); Then, the changes of shale surface morphology were observed by field emission electron microscope (FE-SEM); Nitrogen adsorption and carbon dioxide adsorption experiments were conducted to qualitatively analyze the internal microscopic pore-structure of shale, and quantitatively describe the fractal characteristics of the pore size distribution; Finally, the Brazilian splitting experiment further revealed the changes in the mechanical properties of shale under acid-base degradation.

A novel gas-water relative permeability fractal model was derived in **Chapter 3**. This model considered pore-structure parameters (pore-size distribution fractal dimension and tortuosity fractal dimension), water film, geometric correction factor, and real gas effect. This model was then verified by comparing with two classic relative permeability models and several sets of experimental data. Finally, the effects of pore structure parameters, water film, geometric correction factors and real gas effects on the gas-water relative permeability were explored in details. *The findings of Chapter 3 were published in Water 12, PP. 27, MDPI, 2020.*

Chapter 4 proposed a three-zone model with multi-scale flow-diffusion to investigate the effect of water-based fracturing fluid on shale gas production. The effects of fracture parameters (such as fracture spacing, fracture width, fracture uniformity, and fracture geometry) on shale gas production were discussed. The contribution of multi-scale flow-diffusion and the gas exchange rate in different zones to shale gas production were carefully studied. *The findings of Chapter 4 were published in Geofluids 2018, PP. 1-15, Wiley, 2018.*

A moisture-hydro-mechanical multi-physical coupling model was established after considering the water film in shale gas flowback. The migration mechanism of water-based fracturing fluid after the two-phase flow stage was studied in **Chapter 5**. With the moisture transport, the effects of threshold pressure gradient under the residual water saturation, the water film evaporation on the fracture surface and the gas-liquid-solid mixed adsorption mechanism in the matrix were further investigated. The relationship of the gas adsorption decay coefficient, the water coverage factor and the amount of gas adsorption in the matrix was clarified. *The work of Chapter 5 was published in Journal of Natural Gas Science and Engineering, 68, PP.102897, Elsevier, 2019*.

In **Chapter 6**, a thermal-hydro-mechanical multi-physical coupling model was developed to consider the coexistence of CO_2 three phases in the CO_2 critical-depth caprock. The effects of temperature and pressure on the sealing efficiency of a shallow caprock at the burial depth of 800 m were numerically studied. The physical properties of CO_2 in the phase transition zone varying with gas partial pressure and formation temperature were discussed. By defining the CO_2 penetration depth in the caprock, the sealing efficiency of the caprock was effectively evaluated. *The findings of Chapter 6 were published in Environmental Earth Sciences, 77, PP. 738-752, Springer, 2018.*

Chapter 7 focused on the thermal-hydro-mechanical multi-physical coupling and migration mechanism of CO_2 in deep saline aquifers. The thermal effects (thermal stress and Joule-Thomson cooling) on CO_2 migration in deep saline aquifers were studied. The variation of CO_2 physical properties, the accumulation of pore pressure, adsorption expansion and thermal contraction were included in the revised porosity model. The evolutions of temperature and pressure of injected were analyzed through the coupling of two-phase flow, porous media deformation, heat transfer, and Joule-Thomson effect. Finally, the effect of capillary entry pressure on the distribution of CO_2 plume was numerically compared. *The part work of Chapter 7 was published in Thermal Science, 23, PP. 917-925, Vinca Inst Nuclear Sci, 2019.*

1.5. References

[1] Cao P, Liu J, Leong Y. A multiscale-multiphase simulation model for the evaluation of shale gas recovery coupled the effect of water flowback. Fuel, 2017, 199: 191-205.

[2] Zhang F, Zhou H, Lv T, Hu D, Sheng Q, Hu Q. Analysis of reservoir deformation and fluid transportation induced by injection of CO_2 into saline aquifer:(I) Two-phase flow-reservoir coupling model. Rock and Soil Mechanics, 2014, 9: 2549-2554 [in Chinese].

[3] Wang J. Research on the dynamic behavior of gas-liquid two-pase flow. Shanghai Jiao Tong University Press, 2012 [in Chinese].

[4] Iglauer S, Al-Yaseri A Z, Rezaee R, Lebedev M. CO_2 wettability of caprocks: implications for structural storage capacity and containment security. Geophysical Research Letters, 2015, 42(21): 9279-9284.
[5] Lee S, Fischer T B, Stokes M R, Klingler R J, Ilavsky J, Mccarty D K, Wigand M O, Derkowski A, Winans R E. Dehydration effect on the pore size, porosity, and fractal parameters of shale rocks: ultrasmall-angle x-ray scattering study. Energy & Fuels, 2014, 28(11): 6772-6779.
[6] Tonnet N, Mouronval G, Chiquet P, Broseta D. Petrophysical assessment of a carbonate-rich caprock for CO_2 geological storage purposes. 10th International Conference on Greenhouse Gas Control Technologies, 2011: 5422-5429.
[7] Wang J G, Peng Y. Numerical modeling for the combined effects of two-phase flow, deformation, gas diffusion and CO_2 sorption on caprock sealing efficiency. Journal of Geochemical Exploration, 2014, 144: 154-167.
[8] Zhao Z. Air-water two-phase flow pattern and identification in pebble-bed porous channel. Harbin Engineering University, 2010 [in Chinese].
[9] Alkouh A. New advances in shale gas reservoir analysis using water flowback data. Texas A&M University, 2014.
[10] Bandilla K W, Michael C A, Birkholzer J T, Cihan A. Multiphase modeling of geologic carbon sequestration in saline aquifers. Ground Water, 2015, 3(53): 362-377.
[11] Zhai W. Trans-scale numerical study of two-phase flow characteristics in shale gas reservoir. China University of Petroleum (East China), 2017 [in Chinese].
[12] Wang J G, Kabir A, Liu J, Chen Z. Effects of non-darcy flow on the performance of coal seam gas wells. International Journal of Coal Geology, 2012, 93: 62-74.
[13] Zhang T, Li X, Yang L, Li J, Wang Y, Feng D, Yang J, Li P. Effects of shut-in timing on flowback rate and productivity of shale gas wells. Natural Gas Industry, 2017, 37(8): 48-60 [in Chinese].
[14] Zhang J, Lie H, Xu B, Jiang S, Zhang P. Geological conditions of shale gas accumulation in the Sichuan Basin. Natural Gas Industry, 2008, 28(2): 151-156 [in Chinese].
[15] Zhou C, Dong D, Yang Y, Wang Y, Huang J, Wang S, Fu C. Conditions of shale gas accumulation and exploration practices in China. Natural Gas Industry, 2011, 31(12): 26-39 [in Chinese].
[16] Heath J E, Dewers T A, McPherson B J, Nemer M B, Kotula P G. Pore-lining phases and capillary breakthrough pressure of mudstone caprocks: sealing efficiency of geologic CO_2 storage sites. International Journal of Greenhouse Gas Control, 2012, 11: 204-220.
[17] Yang H, Li J, Shi X, Zhu J, Deng C, Wang D. Characteristics and significance of flow-back processes after fracturing in shale-gas reservoirs. Journal of China University of Petroleum(Edition of Natural Science), 2019, 43(4): 99-107 [in Chinese].
[18] Lee H, Seo J, Youngsoo J, Sung W. Regional CO_2 solubility trapping potential of a deep saline aquifer in pohang basin, korea. Geosciences Journal, 2016, 20(4): 561-568.
[19] Wang S, Song Z, Cao T, Song X. The methane sorption capacity of paleozoic shales from the sichuan basin, China. Marine and Petroleum Geology, 2013, 44(3): 112-119.
[20] Hu Y, Wang Y, Ren J. Analysis of factors affecting the leakage of CO_2 along the fault zone in deep saline aquifers. China Sciencepaper, 2016, 11(13): 1437-1444 [in Chinese].
[21] Yang F, Ning Z, Liu H. Fractal characteristics of shales from a shale gas reservoir in the Sichuan basin, China. Fuel, 2014, 115: 378-384.
[22] Fu C, Zhu Y, Chen S. Pore structure and fractal features of Hetang formation shale in western Zhejiang. Journal of China University of Mining and Technology, 2016, 45(1): 77-86 [in Chinese].

[23] Zhu W, Yuan Q. Study on the multi-scale nonlinear flow mechanism and model of shale gas. Scientia Sinica Technologica, 2016, 46(2): 111-119 [in Chinese].
[24] Office of the State Council. Notice of the general office of the state council on issuing the energy development strategic action plan (2014-2020). 2014: 8 [in Chinese].
[25] U.S. Energy information administration (EIA). Shale gas production drives world natural gas production growth. https://www.eia.gov/todayinenergy/detail.php?id=27512.
[26] EIA. Technically recoverable shale oil and shale gas resources: an assessment of 137 shale formations in 41 countries sutside the United States. 2013.
[27] Zhao X, Yang Y. The current situation of shale gas in Sichuan, China. Renewable and Sustainable Energy Reviews, 2015, 50: 653-664.
[28] Bilgen S, Sarikaya I. New horizon in energy: shale gas. Journal of Natural Gas Science and Engineering, 2016, 35: 637-645.
[29] Dong D, Wang Y, Li X, Zou C, Guan Q, Zhang C, Huang J, Wang S, Wang H. Breakthrough and prospect of shale gas exploration and development in China. Natural Gas Industry, 2016, 36(1): 19-32 [in Chinese].
[30] Wang S. Shale gas exploitation: Status, issues and prospects. Natural Gas Industry, 2017, 37(6): 115-130 [in Chinese].
[31] Xie H, Gao F, Ju Y, Xie L, Wang J. Novel idea of the theory and application of 3D volume fracturing for stimulation of shale gas reservoirs. Chinese Science Bulletin, 2016, 61(1): 36-46 [in Chinese].
[32] Qian B, Zhu J. Shale gas development: today and tomorrow. Natural gas technology, 2010, 4(2): 11-13 [in Chinese].
[33] Pan J, Lou Y, Wang L. Target post-evaluation of China's "12th Five-Year" oil and gas exploration and development planning and its "13th Five-Year" target prediction. Natural Gas Industry, 2016, 36(1): 11-18 [in Chinese].
[34] National energy administration: notice on printing and distributing shale gas development plan (2016-2020). Energy Conservation and Environment Protection, 2016, 10: 9-9 [in Chinese].
[35] EIA. World Shale Gas Resources: An Initial Assessment of 14 Regions outside the United States. 2011.
[36] Deng J. Nonlinear seepage theory of multistage fractured horizontal wells for shale gas reservoirs. University of Science and Technology Beijing, 2015 [in Chinese].
[37] Fang C. Evaluation of the reservoir-forming conditions of shale gas potential of the upper paleozoie in eastern Ordos Basi. Xi'an Shiou University, 2013 [in Chinese].
[38] Zeng S, Yang L, Zeng K. Status, problems and solutions to China' s shale gas development. China Population Resources and Environment, 2013, 23(3):33-38 [in Chinese].
[39] Zhang D, Yang T, Wu T, Li X, Zhao J. Recovery mechanisms and key issues in shale gas development. Chinese Science Bulletin, 2016, 61(1): 62-71 [in Chinese].
[40] Pan Z, Connell L D. Reservoir simulation of free and adsorbed gas production from shale. Journal of Natural Gas Science and Engineering, 2015, 22: 359-370.
[41] Chen Z, Liao X, Yu W, Zhao X. Transient flow analysis in flowback period for shale reservoirs with complex fracture networks. Journal of Petroleum Science and Engineering, 2018, 170: 721-737.
[42] Xu Y, Adefidipe O A, Dehghanpour H. Estimating fracture volume using flowback data from the horn river basin: a material balance approach. Journal of Natural Gas Science and Engineering, 2015, 25: 253-270.

[43] Liu Y. A fundamental study on the underground sequestration and enhanced oil recovery utilization of carbon dioxide. Dalian University of Techonology, 2011 [in Chinese].
[44] Zhang W, Zhang D, Tian K. Carbon capture and sequestration technology. Sino-global Energy, 2009, 14(11): 7-14 [in Chinese].
[45] Sun Y. Paris Climate Conference: A new starting point for transforming green development. Environmental Impact Assessment, 2016, 38(1): 17-19 [in Chinese].
[46] Wen H, Fan G, Zhai X, Ma R, Weng L. Atmospheric monitoring system and analysis of Shenhua CCS project. Safety and Environmental Engineering, 2015, 22(5): 73-78 [in Chinese].
[47] Li X, Liu Y, Bai B, Fang Z. Ranking and screening of CO_2 saline aquifer storage zones in china [J]. Chinese Journal of Rock Mechanics and Engineering, 2006, 25(5): 963-968 [in Chinese].
[48] Zhang H, Wen D, Li Y, Zhang J, Lu J. Conditions for CO_2 geological sequestration in China and some suggestions. Geological Bulletin of China, 2005, 24(12): 1107-1110 [in Chinese].
[49] Meng Q. Anumerical study of supercritical carbon dioxide migration in porous media under conditions of saline aquifers. University of Science and Technology of China, 2014 [in Chinese].
[50] Rutqvist J, Cappa F, Rinaldi A P, Godano M. Modeling of induced seismicity and ground vibrations associated with geologic CO_2 storage, and assessing their effects on surface structures and human perception. International Journal of Greenhouse Gas Control, 2014, 24: 64-77.
[51] Zhong P, Peng S, Jia L, Zhang J. Development of carbon capture, utilization and storage (CCUS) technology in China. China Population Resources and Environment, 2011, 21(12): 41-45 [in Chinese].
[52] Wen D, Guo J, Zhang S, Xu T, Jia X, Li X, Fan J, Zhang W, Diao Y. The progress in the research on carbon dioxide geological storage in China. Geology in China, 2014, 41(5): 1716-1723 [in Chinese].
[53] Yang B, Luo D, Zhang X, Wu D, Shang S. A study of stress sensitivity of abnormal high pressure shale gas reservoir and reasonable productivity allocation. Journal of Southwest Petroleum Institute, 2016, 38(2): 115-121 [in Chinese].
[54] Owolabi O O, Volz R. Can shale-like stimulations unlock the potential of extremely low permeability tight gas reservoirs? Society of Petroleum Engineers, 2013, DOI: 164001-MS.
[55] Abbasi M A, Ezulike D O, Dehganpour H, Hawkes R V. A comparative study of flowback rate and pressure transient behavior in multifractured horizontal wells completed in tight gas and oil reservoirs. Journal of Natural Gas Science and Engineering, 2014, 17: 82-93.
[56] Jia P, Cheng L, Clarkson C R,Williams-Kovacs J D. Flow behavior analysis of two-phase (gas/water) flowback and early-time production from hydraulically-fractured shale gas wells using a hybrid numerical/analytical model. International Journal of Coal Geology, 2017, 182: 14-31.
[57] Fu Y, Dehganpour H, Ezulike D O, Jones R S. Estimating effective fracture pore volume from flowback data and evaluating its relationship to design parameters of multistage-fracture completion. SPE Production & Operations, 2017, 32(4): 423-439.
[58] Jiang R, Wang Y, Liu H, He W, Zhang J. Analysis of shale gas production mechanism and influencing factors. Special Oil and Gas Reservoirs, 2014, 21(1): 84-87 [in Chinese].
[59] Deng J, Zhu W, Ma Q. A new seepage model for shale gas reservoir and productivity analysis of fractured well. Fuel, 2014, 124: 232-240.

[60] Zhou W, Banerjee R, Poe B, Spath J, Thambynayagam M. Semianalytical production simulation of complex hydraulic-fracture networks. SPE Journal, 2013, 19(1): 6-18.
[61] Xie W, Li X, Zhang L, Tan X, Wang J, Wang H. Production decline analysis for two-phase flow in multifractured horizontal well in shale gas reservoirs. Journal of Chemistry, 2015, DOI: 10.1155/2015/212103.
[62] Crafton J W, Gunderson D. Use of extremely high time-resolution production data to characterize hydraulic fracture properties. SPE Annual Technical Conference and Exhibition, 2006, DOI: 103591-MS.
[63] Williams-Kovacs J D, Clarkson C R. A modified approach for modeling two-phase flowback from multi-fractured horizontal shale gas wells. Journal of Natural Gas Science and Engineering, 2016, 30: 127-147.
[64] Yuan X, Huang C. Research on back row characteristics of fuling shale gas field.Unconventional oil and Gas, 2017, 4(5): 66-70 [in Chinese].
[65] Li L, Du Y, Zhao Z, Ni J. Preliminary research on flowback patterns of fractured shale gas wells. Sino-global Energy, 2016, 21(6): 31-34 [in Chinese].
[66] Ni J, Li L, Zhao Z, Du Y. Research status and understanding of post-compression flowback mode for shale gas wells. Well Testing, 2017, 26(1): 33-35 [in Chinese].
[67] Zhao Z, Li S, Zhao H, Ni J, Zhu J. Research on the mechanism of water blocking damage in the production process of gas well. Natural Gas Technology and economy, 2015, 9(3): 33-36 [in Chinese].
[68] Jiang T, Bian X, Wang H, Liu Z. Flow back mechanism study of multi-stage fracturing of shale gas horizontal wells. Petroleum Drilling Techniques, 2013, 41(5): 21-25 [in Chinese].
[69] Yin H, Wang X, Zhang F, Sun Y, Wang S, Chen G, Luan S. Influence of adsorbed gas on bottomhole pressure of shale gas wells with gas-water two-phase flow. Fault-Block Oil and Gas Field, 2013, 20(1): 74-76 [in Chinese].
[70] Xie W, Li X, Zhang H. Production decline analysis for two-phase flow in multi fractured horizontal well in shale gas reservoirs. Journal of Chemistry, 2015, 2: 1-10.
[71] Yang R, Huang Z, Li G. An innovative approach to model two-phase flowback of shale gas wells with complex fracture networks. SPE Technical Conference and Exhibition, 2016, SPE 181766-MS.
[72] Ezulike O D, Dehghanpour H. Modelling flowback as a transient two-phase depletion process. Journal of Natural Gas Science & Engineering, 2014, 19: 258-278.
[73] Xu Y, Adefidipe O A, Dehghanpour H. Estimating fracture volume using flowback data from the horn river basin: a material balance approach. 2015, 25: 253-270.
[74] Ezulike O, Dehghanpour H, Virues C, Hawkes R V, Jones R S. Flowback fracture closure: a key factor for estimating effective pore volume. SPE Reservoir Evaluation & Engineering, 2016, 19(4): 567-582.
[75] Alkouh A, Mcketta S Wattenbarger R. Estimation of effective-fracture volume using water-flowback and production data for shale-gas wells. Journal of Canadian Petroleum Technology, 2014, 53: 290-303.
[76] Engelder T, Cathles L, Bryndzia L. The fate of residual treatment water in gas shale. Journal of Unconventional Oil & Gas Resources, 2014, 7: 33-48.
[77] Wattenbarger R, Alkouh A. New advances in shale reservoir analysis using flowback data. Society of Petroleum Engineers, 2013, DOI: 10.2118/165721-MS.
[78] Zhang Y, Ehlig-Economides C. Accounting for remaining injected fracturing fluid in shale gas wells. Unconventional resources technology conference. 2014, DOI: SPE165721.

[79] Zuluaga E, Munoz N, Obando, I. An experimental study to evaluate water vaporisation and formation damage caused by dry gas flow through porous media. International Symposium on Oilfield Scale, 2001, DOI: 10.2118/68335-MS.
[80] Wang H, Wang J G, Gao F, Wang X. A two-phase flowback model for multiscale diffusion and flow in fractured shale gas reservoirs. Geofluids, 2018, 2018: 1-15.
[81] Salimi H, Wolf K, Bruining J. The influence of capillary pressure on the phase equilibrium of the CO_2-water system: application to carbon sequestration combined with geothermal energy. International Journal of Greenhouse Gas Control, 2012, 111: S47-S66.
[82] Li Q, Liu G, Leamon G, Liu L, Cai B, Chen Z. A national survey of public awareness of the environmental impact and management of CCUS technology in China. 13th International Conference on Greenhouse Gas Control Technologies. 2017, 114: 7237-7244.
[83] Li Y, Fang Q, Ke Y, Dong J, Yang G, Ma X. Effect of high salinity on CO_2 geological storage: a case study of Qianjiang depression in Jianghan basin. Earth Science-Journal of China University of Geosciences, 2012, 37(2): 283-288 [in Chinese].
[84] Heath J E, Dewers T A, McPherson B, Nemer M B, Kotula P G. Pore-lining phases and capillary breakthrough pressure of mudstone caprocks: sealing efficiency of geologic CO_2 storage sites. International Journal of Greenhouse Gas Control, 2012, 11: 204-220.
[85] Li Q, Song R, Shi H, Ma J, Liu X, Li X. U-tube based near-surface environmental monitoring in the shenhua carbon dioxide capture and storage (CCS) project. Environmental Science and Pollution Research, 2018, 25(12SI): 12034-12052.
[86] Smith M M, Sholokhova Y, Hao Y, Carroll S A. CO_2-induced dissolution of low permeability carbonates. Part i: characterization and experiments. Advances in Water Resources, 2013, 62: 370-387.
[87] Wang J G, Ju Y, Gao F, Peng Y, Gao Y. Effect of CO_2 sorption-induced anisotropic swelling on caprock sealing efficiency. Journal of Cleaner Production, 2015, 103: 685-695.
[88] Gherardi F, Xu T, Pruess K. Numerical modeling of self-limiting and self-enhancing caprock alteration induced by CO_2 storage in a depleted gas reservoir. Chemical Geology, 2007, 244(1-2): 103-129.
[89] Huerta N J, Hesse M A, Bryant S L, Strazisar B R, Lopano C. Reactive transport of CO_2-saturated water in a cement fracture: application to wellbore leakage during geologic CO_2 storage. International Journal of Greenhouse Gas Control, 2016, 44: 276-289.
[90] Bolourinejad P, Herber R. Experimental investigation of porosity and permeability variations in reservoirs and caprock following co-injection of sulfur dioxide and hydrogen sulfide with carbon dioxide. Journal of Petroleum Science and Engineering, 2015, 129: 137-144.
[91] Andreas B, Sascha A, Kroos B. Effects of physical sorption and chemical reactions of CO_2 in shale caprocks. Energy Procedia, 2009, 1: 3229-3235.
[92] Chasset C Jarsjo J, Erlstrom M. Scenario simulations of CO_2 injection feasibility, plume migration and storage in a saline aquifer, scania, Sweden. International Journal of Greenhouse Gas Control, 2011, 5(5): 1303-1318.
[93] Anthony C, Bildstein O, Michel J. Experimental and modeling study of geochemical reactivity between clayey caprocks and CO_2 in geological storage conditions. Energy Procedia, 2009, 1(1): 3445-3452.
[94] Gaus I, Azaroual M, Czernichowski I. Reactive transport modeling of the impact of CO_2 injection on the clayey cap rock at sleipner (North Sea). Chemical Geology, 2005, 217(3): 319-337.

[95] Gao C, Kang Q, Xu R Chen L, Jiang P. The numerical investigation of supercritical two phase fluid flow in support of carbon dioxide storage. Journal of Engineering Thermophysics, 2014, 35(5): 944-947 [in Chinese].
[96] Keating E H, Newell D L, Viswanathan H, Carey J W, Zyvoloskki G, Pawar R. CO_2/brine transport into shallow aquifers along fault zones. Environmental Science & Technology, 2013, 47(1): 290-297.
[97] Pruess K. Modeling CO_2 leakage scenarios, including transitions between super- and sub-critical conditions, and phase change between liquid and gaseous CO_2. Energy Procedia. 2011, 4(3): 3754-3761.
[98] Fan T, Wang L. A viscosity model based on peng-robinson equation of state for light hydrocarbon liquids and gases. Fluid Phase Equilibria, 2006, 247(1-2): 59-69.
[99] Heidaryan E, Moghadasi J, Rahimi M. New correlations to predict natural gas viscosity and compressibility factor. Journal of Petroleum Science and Engineering, 2010, 73(1-2): 67-72.
[100] Vilarrasa V, Rutqvist J. Thermal and capillary effects on the caprock mechanical stability at in salah, Algeria. Greenhouse Gases: Science and Technology, 2015, 5(4): 449-461.
[101] Mathias S A, Gluyas J G, Oldenburg, C M, et al. Analytical solution for joule-thomson cooling during CO_2 geo-sequestration in depleted oil and gas reservoirs. International Journal of Greenhouse Gas Control, 2010, 4(5): 806-810.
[102] Gao F, Yang X J, Zhang, Y. Exact traveling wave solutions for a new nonlinear heat transfer equation. Thermal Science, 2017, DOI: 10.2298/TSCI160512076G.
[103] Gor G Y, Elliot T R, Prevost. Effects of thermal stresses on caprock integrity during CO_2 storage. International Journal of Greenhouse Gas Control, 2013, 12: 300-309.
[104] Kim S, Hosseini S A. Hydro-thermo-mechanical analysis during injection of cold fluid into a geologic formation. International Journal of Greenhouse Gas Control, 2013, 12: 300-309.

Chapter 2: Experimental study on microstructure and mechanical characteristics of shale under acid-base deterioration

2.1. Introduction

The permeability of shale plays an important role in evaluating shale gas production and the sealing efficiency of CO_2 storage. The complex microscopic pore-structure of shale is the intrinsic reason for the evolution of permeability. Pore pressure, adsorption strain and thermal expansion strain change the microscopic pore structure of shale. Many studies have confirmed that these factors have an effect on enhancing or weakening the porosity of fractures [1]. However, in the shale gas production or CO_2 storage, the long-term geological condition is not a neutral environment due to the composition of fracturing fluid or the dissolution of CO_2. The water-rock interaction is enhanced under the acid-base degradation. Thus, the microscopic pore structure of shale is changed due to the variation of mineral composition. The permeability and mechanical properties of shale have also been affected. Thus, the experimental study on the microstructure and mechanical characteristics of shale under acid-base degradation has important research significance for the effects of the water-rock interaction on the evolution of shale permeability.

This chapter conducted shale immersion experiments in different pH solutions to discuss the variation of shale composition, surface morphology, internal pore-structure and tensile strength under acid-base degradation. First, X-ray diffraction (XRD) was used to semi-quantitatively analyze the changes of mineral composition, and then combined with field emission electron microscopy (FE-SEM) to observe the changes of shale surface

morphology. Nitrogen adsorption and carbon dioxide adsorption experiments were used to qualitatively analyze the microscopic pore-structure of shale, and quantitatively describe the distribution of pore size. Finally, the Brazilian split experiment further revealed the changes in the mechanical properties of shale under acid-base degradation.

2.2. Shale sample preparation

Due to the difficulty in obtaining shale drilling cores, the shale samples used in this chapter are taken from the outcrop shale from the Marine Silurian Longmaxi Formation in Chongqing, China, as shown in Fig. 2.1. The shale in this area is continuously distributed and is a deep-water basin deposit formed under the combined action of large-scale transgression, local subsidence and geological structure [2]. The Longmaxi Formation shale is a black carbonaceous shale rich in organic matter, with thin-medium-thick layers parallel and alternating. A small number of pyrite bands, graptolite fossils, shellfish fossils can be found on the bedding surface [3, 4]. After the surface weathering layer is removed, shale samples are prepared in the laboratory as required.

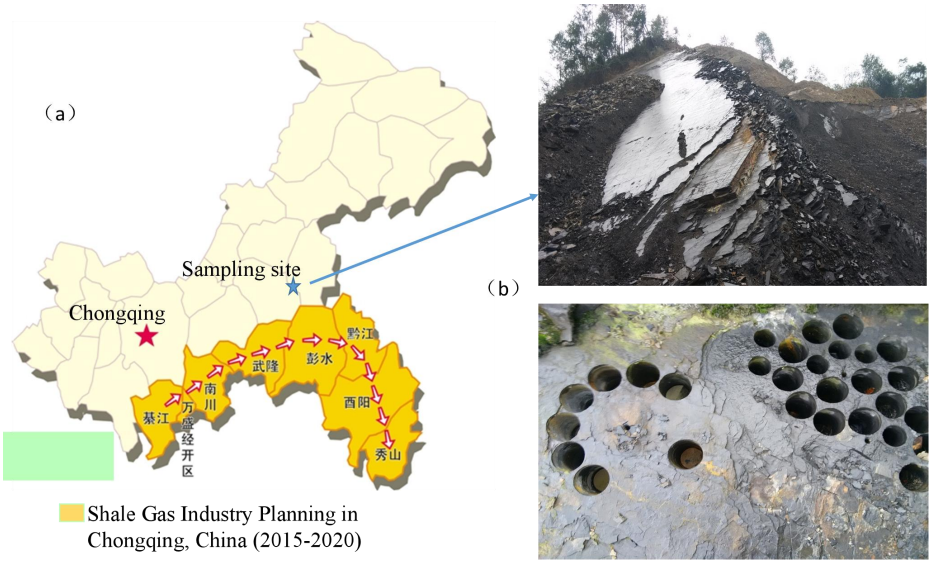

Fig. 2.1. Shale sample preparation (a) Source of shale sample (b) Shale sampling site

The test of mechanical characteristic in this chapter adopts standard cylindrical shale samples. In order to avoid the effect of micro-structure defects on the mechanical properties, shale with intact surface and no obvious fractures is selected for standard samples. The drilling holes are perpendicular to the shale bedding plane and cold water is continuously injected to reduce temperature and damage to the shale samples. The final prepared shale samples for the Brazilian splitting experiment has a diameter of 25 mm, a height of 50 mm, and an error of less than 0.05 mm on the upper and lower faces. A total of 43 shale samples are prepared, which are divided into 6 groups. Each group has 5 shale samples, and the remaining samples are reserved for future use. The fragments and powders in the preparation process of shale standard samples are collected, which are prepared and numbered according to the requirements of X-ray diffraction (XRD), field emission electron microscopy (FE-SEM), nitrogen adsorption and carbon dioxide adsorption testing. The specifications of the shale samples used in the above tests are shown in Table 2.1.

Table 2.1. Processing specifications of shale samples

Experiments	Sample specifications
X-ray diffraction	Broken shale particles(325 mesh sieve)
Field emission electron microscopy	10mm×10mm×2mm shale slices
Nitrogen adsorption method	Broken shale particles(40-60 mesh sieve)
Carbon dioxide adsorption method	Broken shale particles(40-60 mesh sieve)
Brazil Split	25mm×50mm standard cylindrical shale sample

2.3. XRD analysis of shale component

In order to investigate the mineral composition changes of shale under acid-base degradation, X-ray diffraction (XRD) was used to analyze the composition of shale powder after soaking in solutions with different pH. The above-mentioned test analysis was completed in the Modern and Analytical Computing Center of China University of Mining and Technology. The XRD analysis adopted the D8 Advance X-ray diffractometer produced

by the German Bruker Company, which consists of a closed ceramic tube X-ray source, X-ray high-voltage generator, high-precision wide-angle goniometer, high-sensitivity Links array detector, and cooling water system. The test conditions are: Cu target, K radiation, tube voltage 20-60 kV, tube current 10-60 mA, minimum step length 0.0001°, angle range 110-168°. According to the standard powder diffraction data provided by the International Data Center of the Powder Diffraction Federation, the comparison and analysis were performed based on the diffraction criterion and finally, the mineral composition in the shale sample can be obtained.

The reactions between shale powder and solutions have been taken in a flange-type pressure-resistant reactor, which is equipped with a polytetrafluoroethylene liner to prevent the inner wall of the reactor from participating in the reaction. The device is shown in Fig. 2.2. The shale immersion experiment is conducted with three pH solutions: (b) distilled water; (c) pH 4.5 acid solution; (d) pH 11.5 alkaline solution. An acidic solution with a pH of 4.5 is prepared from distilled water and 0.5 hydrochloric acid solution. The pH value of the acidic solution refers to the fracturing fluid prepared in the laboratory [5]. The alkaline solution with a pH of 11.5 is made up of distilled water and 1% sodium hydroxide solution. The pH value of the alkaline solution refers to the oil-based drilling fluid on-site [6].

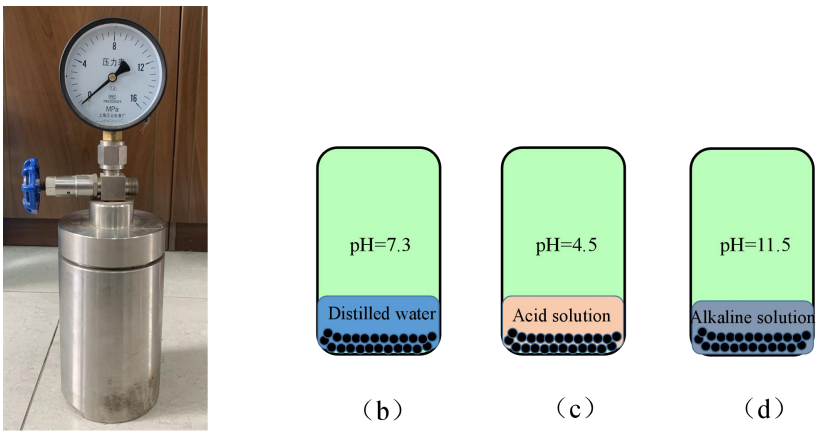

Fig. 2.2. Schematic diagram of soaking device for shale

By X-ray diffraction analysis on three different immersion cases (b, c, d) and unsoaked shale powder (a), the semi-quantitative mineral composition is shown in Fig. 2.3. It can be seen that the mineral composition of shale is relatively complex, mainly including quartz, albite, dolomite and layered structure of silicate muscovite, clay mineral plagioclase and a small amount of Pyrite. The characteristic peaks corresponding to minerals indicates that the content of quartz is the highest, and it remains basically unchanged after soaking in solutions of different pH, which also proves the chemical stability of quartz. The second highest content of shale sample is dolomite. In the three immersion cases, the content of dolomite decreased significantly. Especially in acidic and alkaline solutions, dolomite will have the obvious dissolution, and the peak strength is also lower than that of shale soaked in distilled water.

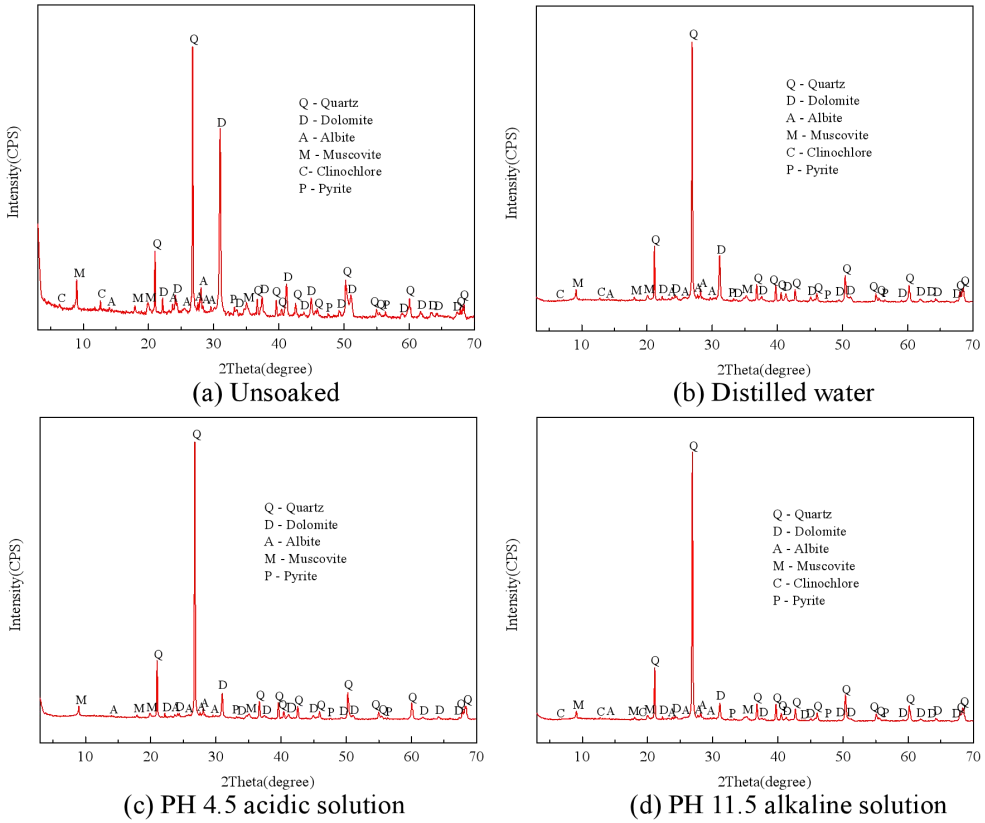

Fig. 2.3 X-ray diffraction patterns of shale under different pH

According to the peak curve in Fig. 2.3, the variation of shale mineral composition is semi-quantitatively analyzed, as shown in Table 2.2. Before soaking, the content of quartz in the shale sample was 32.59%, the content of dolomite was 23.12%, the content of albite was 14.44%, the content of muscovite was 24.75%, the content of clinochlore was 3.77%, and the content of pyrite was 1.33%. After immersing in distilled water for 120 hours, the content of quartz was 58.21%, the content of dolomite was 10.85%, the content of albite was 11.57%, the content of muscovite was 16.66%, the content of clinochlore was 1.86%, and the content of pyrite was 0.85%. It showed that after the shale sample reacted with water, the content of dolomite, albite, muscovite, plagiochlorite, and pyrite all decreased, and only the content of quartz had an increase. After immersed in a pH 4.5 acid solution for 120 h, the content of quartz was 65.16%, the content of dolomite was 6.03%, the content of albite was 9.91%, the content of muscovite was 18.05%, and the content of pyrite was 0.85%. Compared with the case of distilled water, the contents of dolomite, albite, muscovite, and pyrite all had a more obvious decrease, and plagioclase even disappeared. After being soaked in a pH 11.5 alkaline solution with for 120 h, the content of quartz was 70.09%, the content of dolomite was 4.67%, the content of albite was 9.46%, the content of muscovite was 13.34%, and the content of plagioclase was 1.68%, the pyrite content was 0.76%. Compared with the acid solution, the content of dolomite and muscovite had further decreased due to the higher pH value of the alkaline solution, the content of albite and pyrite remains almost unchanged, and the content of plagioclase was still 1.69%.

Table 2.2. Mineral contents of shale samples under different pH

Sample number	Quartz	Dolomite	Albite	Muscovite	Clinoclore	Pyrite
a	32.59	23.12	14.44	24.75	3.77	1.33
b	58.21	10.85	11.57	16.66	1.86	0.85
c	65.16	6.03	9.91	18.05		0.85
d	70.09	4.67	9.46	13.34	1.68	0.76

During the soaking process of shale samples, the pH of the solution in different periods has been kept recorded, as shown in Fig. 2.4. When the soaking solution is distilled water, the pH of the solution has a rapid rise within 6 hours, from the initial neutral to weakly alkaline. Finally, it maintains the weakly alkaline environment for a long-term time. When the soaking solution is a pH 4.5 acidic solution, the pH rises to neutral within 40 hours, and is finally maintained in a neutral environment. When the soaking solution is a pH 11.5 alkaline solution, the pH experiences a decrease. But compared with distilled water and acidic solution, the variation is slower. Finally, it maintains in a weakly alkaline environment. These results indicate that shale has a strong ability to release acid and alkali in the water-rock reaction. Compared with the reaction in alkaline solution, the dissolution reaction of shale in acid solution is faster.

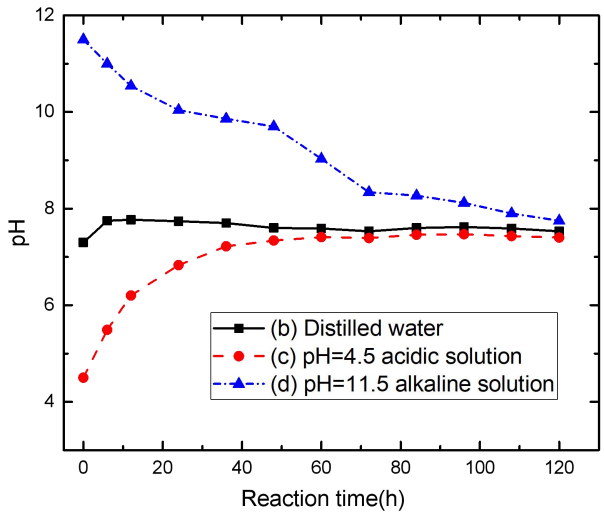

Fig. 2.4. Evolution of solution pH during reaction

2.4. Analysis of shale surface morphology characteristics under acid-base deterioration

In order to further verify the above-mentioned XRD component analysis, four groups of shale samples after treatment with different pH solutions were subjected to scanning electron microscope tests to investigate the morphological characteristics of the shale surface. Using high-resolution field emission electron microscope scanning combined with EDS energy spectrum analysis, the complex pore-structure and mineral composition of the shale surface were identified. The magnification of the high-resolution field emission scanning electron microscope (MAIA3 FSEM) could reach 1,000,000 times and the resolution could reach 0.7 nm. Shale flakes with a smooth surface were selected to prepare shale slices of about 10 mm×10 mm×2 mm. In addition, a gold film of about 10-20 nm was plated on the surface to maintain the most realistic surface pore characteristics.

From micron-scale natural fractures to nano-scale pores in the matrix, they together constitute gas migration channels in unconventional shale gas reservoirs. The complex multi-scale pore-structure is also the main storage space for shale gas. How to distinguish these pore-structures qualitatively or quantitatively has important research significance. With the development of field emission electron microscopy and transmission electron microscopy technologies, the type of pore-structure is distinguished by the relationship between pore occurrence and rock particles. Then, the representative Loucks classification has been developed. Loucks et al. [7] classified the complex pore-structure in shale into fracture pores and matrix pores. The matrix pores also included three basic types: intergranular pores between particles and crystals, intragranular pores contained in particles, and organic pores.

(1) Fracture pores: micron-scale natural fractures are the main gas migration channels in shale gas reservoirs, as shown in Fig. 2.5(a). The opening and closing of these fractures are affected by pore pressure, adsorption strain, thermal expansion and chemical reaction, and finally determined the production capacity of shale gas.

(2) Intergranular pores: intergranular pores are abundant in reservoirs with short accumulation time. They generally have good connectivity, which makes it easy to form an effective pore network. According to the different properties of particles, they are divided into plastic particles and brittle particles with intergranular pores. The plastic particles in shale include clay flakes, organic matter and mud debris. The brittle particles are mainly quartz, pyrite and feldspar. However, as the accumulation time increases, the inter-particle pores will be compacted under high ground stress and diagenesis.

(3) Intragranular pores: pores are developed in the grain boundary and mainly include: dissolution pores formed by dissolution of particles, honeycomb pores between pyrite crystals, and cleavage surfaces in clay and mica mineral particles, as shown in the Fig. 2.5(c, d) shown.

(4) Organic pores: the development of organic pores is closely related to the thermal maturity of hydrocarbons. The size of organic pores is usually between 5 and 750 nm. The shape of these pores shows an obvious irregularity.

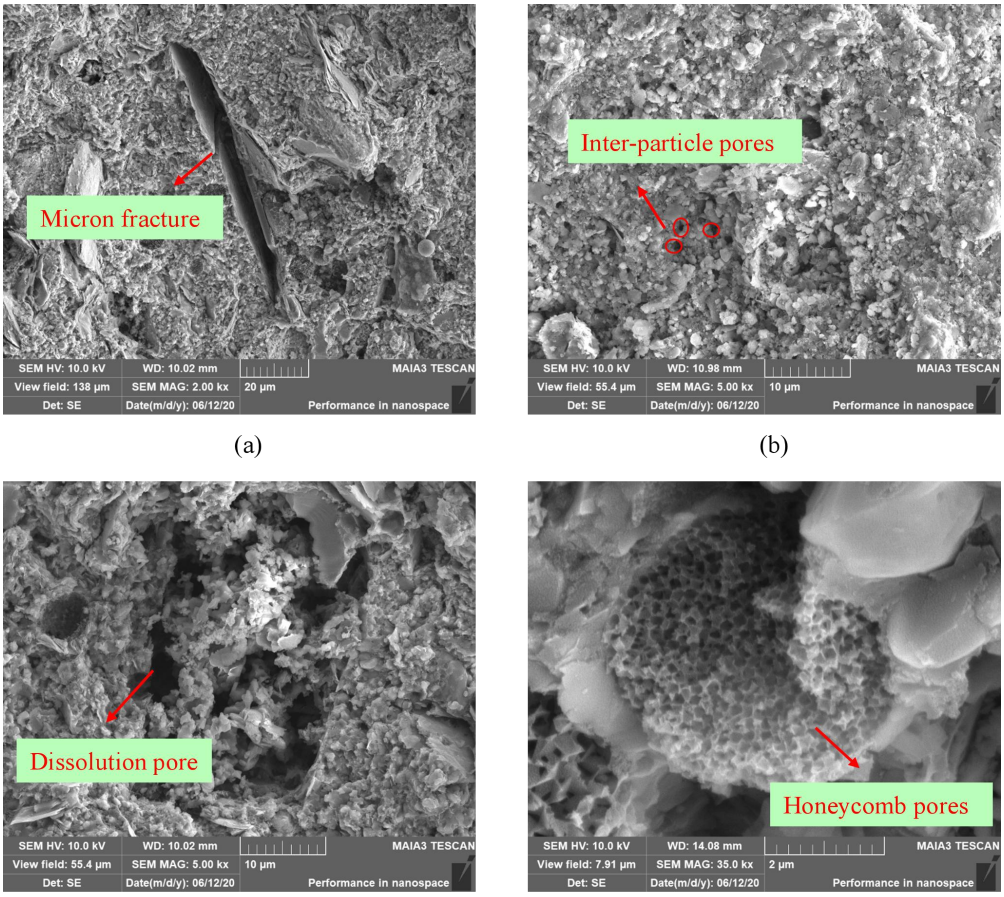

Fig. 2.5. Scanning electron microscope analysis of shale pore characteristics (a) Micron fracture (b) Interparticle pores (c) Dissolution pores (d) Honeycomb pores

After briefly describing the classification of pore-structures in shale, this chapter will further compare the changes of shale surface morphology characteristics after soaking in different pH solutions, based on the EDS energy spectrum. The scanning position of the electron microscope of the shale sample is marked to ensure the similarity of the before and after soaking. Fig. 2.6 shows the comparison results of shale soaking in different pH solutions. It can be seen that: (1) After soaking in distilled water, the surface morphology of the micron-scale fractures did not change significantly. The fracture showed a tendency to close due to the water absorption and expansion of clay minerals. The pores between the particles were slightly dissolved on the surface under the action of water immersion. Compared with

the unsoaked shale sample, the surface becomes flatter and smoother. In addition, the clay debris between the particles fills the pore space under the action of hydration, and the whole surface was in a compacted state. The intragranular pores had no obvious dissolution phenomenon in distilled water, but anisotropic expansion appeared on the cleavage surface in the clay and mineral particles, which led to an increase of the spacing between the crystal layers; (2) After soaking in acidic solution, the surface particles of shale were dissolved. The dissolution of carbonate minerals led to an increase of fracture opening. Compared with the unsoaked sample, the pores between the particles were significantly corroded under the action of the acid solution, and a corroded pore-structure with better connectivity was observed. However, the intragranular pores did not change significantly under the action of acidification; (3) After soaking in alkaline solution, the degree of dissolution of shale surface particles is not as good as acid solution. However, the opening of micron fractures also increased rather than closed. This was mainly because the alkaline solution had a strong dissolution effect on clay minerals, which offset the hydration expansion effect. The dissolution of the inter-particle pores was obviously enhanced compared with the sample with distilled water, but it was still not as good as the dissolution effect caused by the acid solution. There was no connection between the dissolution pores.

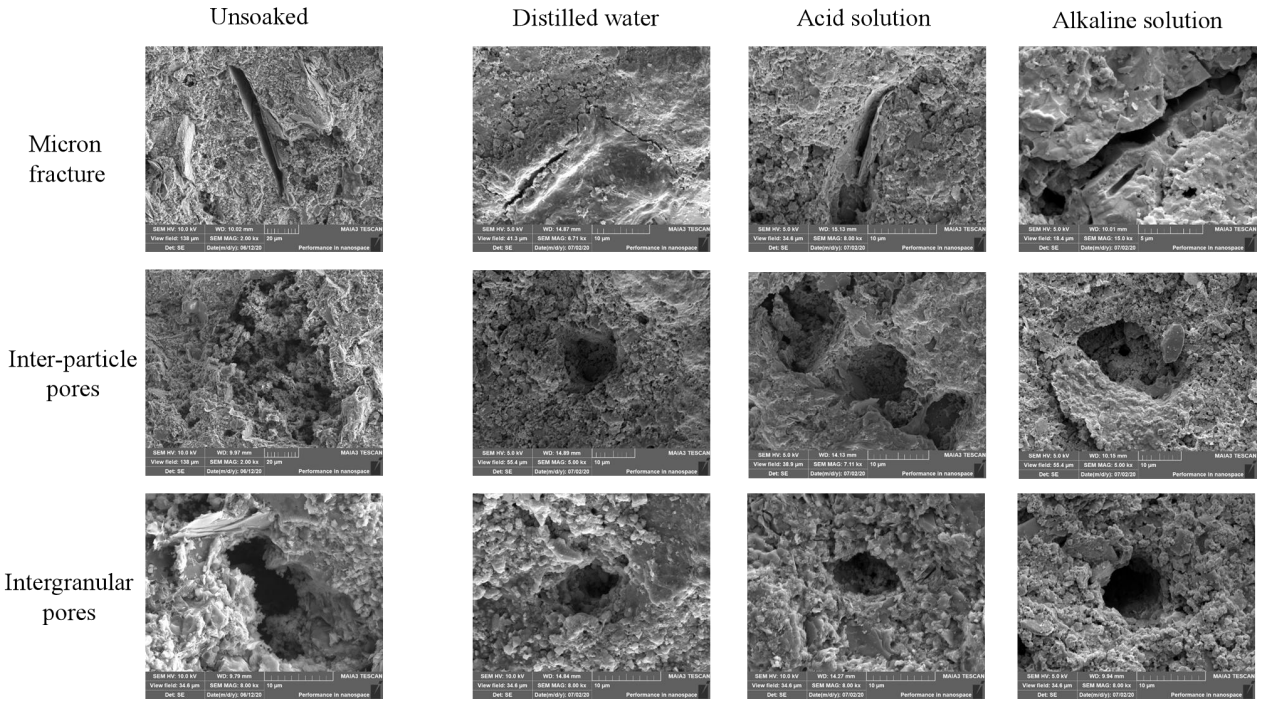

Fig. 2.6. Variation of surface pore characteristics before and after shale soaking

The EDS spectrum analysis of shale samples after soaking in acidic solution is presented in Fig. 2.7. Fig. 2.7(a) shows the results of unsoaked samples, and Fig. 2.7(b) shows the results of shale after immersing in the acidic solution for 120 hours. It can be found that the magnesium, aluminium, silicon, potassium, and iron elements in the shale sample have decreased after the reaction. This is most likely caused by the reaction of aluminosilicates (chlorite and feldspar) in an acidic environment. The increase of carbon and oxygen indicates that new carbonate minerals may be formed on the surface of the quartz. Furthermore, chlorite minerals generate amorphous substances similar to hydrated silica after being dissolved by acid. This is the reason that there are no obvious dissolution pores after the reaction, and the pore surface morphology is similar to that before the reaction.

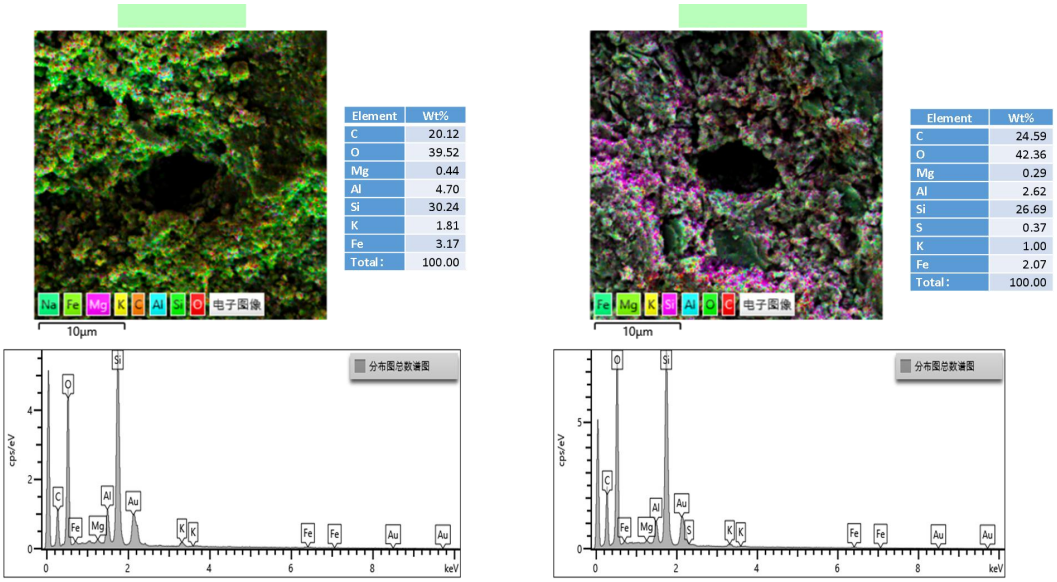

(a) (b)

Fig. 2.7. EDS spectrum analysis of shale immersed in acid solution (a) Unsoaked (b) Acid solution

2.5. Analysis of characteristics of internal pore-structure of shale under acid-base deterioration

The complex internal pore-structure of shale is the main medium for shale gas adsorption, which plays an important role in the storage of shale gas. According to the standards of the International Association for Theoretical and Applied Chemistry (IUPAC) [8], the pore-structure can be divided into micropores (pore size<2 nm), mesopores (pore size=2~50 nm), and macropores (pore size> 50 nm). The pore volume and pore size distribution of mesopores and macropores can be obtained by Nitrogen adsorption test, while the micro-pore structure only can be detected by the carbon dioxide adsorption test. Therefore, a method combined with nitrogen and carbon dioxide gas adsorption is used to characterize the pore-structure of Marine Silurian Longmaxi Formation Shale. The changes of pore geometry, pore volume, specific surface area and pore distribution under acid-base solution immersion are analysed.

Nitrogen and carbon dioxide adsorption tests were completed in the Key Laboratory of Coal Bed Methane Resources and Accumulation Process of Ministry of Education, China University of Mining and Technology. The automatic specific surface area and pore size distribution tester (Autosorb 1) of Kantar Corporation of the United States was used. About 10 g of shale samples under different immersion schemes were crushed into particles and passed through a 60-mesh sieve. According to the adsorption mechanism of the solid surface, the gas pressure corresponded to the adsorption amount on the solid surface when the gas reached the adsorption equilibrium at a constant temperature. Then, the specific surface area was obtained using the BET multipoint analysis, and the pore volume and pore size distribution was obtained using DFT density functional theory.

The shale of the Marine Silurian Longmaxi Formation has been immersed in distilled water, acidic solution and alkaline solution for 30 days. The adsorption curves show significant differences (Fig. 2.8(a)). In order to identify this difference more clearly, the adsorption capacity of the unsoaked shale sample and the samples of the three soaking schemes are compared in Fig. 2.8(b, c, d), respectively. It can be found that the shale samples after soaking have an obvious increase in gas adsorption capacity, which indicates that solution soaking will cause the dissolution pores and increase the specific surface area of the pores. Comparing the gas adsorption capacity, the soaking effect of the alkaline solution is greater than that of acidic solution, and that of the acidic solution is greater than distilled water. This result is also consistent with the XRD composition analysis in this chapter. Although the adsorption curves under different soaking schemes differ in the magnitude of the gas adsorption capacity, the overall trend is still similar, showing S-shaped (Fig. 2.8). According to the definition of IUPAC, this N_2 isotherm is similar to the type II adsorption isotherm and the type H3 hysteresis loop. When the relative pressure is in the low-pressure

range ($0 < p / p_0 < 0.05$), the adsorption curve rises slowly and slightly convex; when the relative pressure is in the high-pressure range ($p / p_0 > 0.5$), the adsorption curve rises rapidly and slightly concave. When the relative pressure is close to 1, the adsorption capacity still does not reach saturation. It shows that during the N_2 adsorption process, monolayer adsorption occurs on the shale surface when the relative pressure is low, and capillary condensation on the shale surface occurs when the relative pressure is high. As the relative pressure begins to decrease, the curve of desorption decreases significantly at the relative pressure ($0.4 < p / p_0 < 0.5$), forming a hysteresis loop with the adsorption curve. The shape of this hysteresis loop can indirectly link to the characteristics of the microscopic pore-structure in the shale. With reference to the classification of hysteresis loops based on adsorption-desorption curves in IUPAC [9], the pore-structures of shale in Fig. 2.8 have the following two types: (1) Parallel-plate fractured pores. These pores are similar to shale bedding, with wide pore-distribution and good connectivity, which is conducive to the gas migration; (2) Ink bottle pores. These pores have tiny pore-throats and connectivity between pores is weak. Although these pores are conducive to the storage of shale gas, they are not conducive to gas migration.

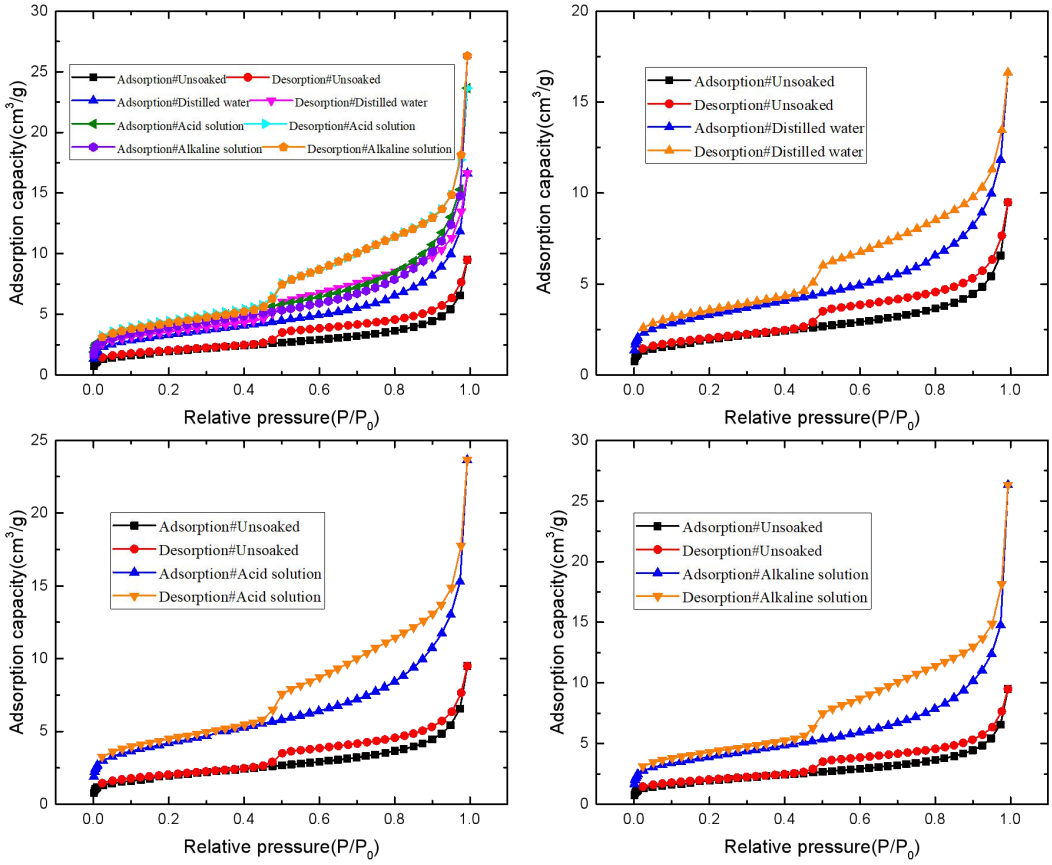

Fig. 2.8. Nitrogen adsorption-desorption isotherms of shale samples before and after reaction (a) Four cases (b) Distilled water (c) Acid solution (d) Alkaline solution

CO_2 isotherm adsorption tests under different soaking schemes were conducted to further investigate the characteristics of micro-pore adsorption in the Marine Silurian Longmaxi Formation Shale, as shown in Fig. 2.9. It was seen that the amount of CO_2 adsorbed by the micro-pores has reduced significantly compared with the amount of N_2 adsorbed. When the relative pressure is close to 1, the adsorption capacity is almost saturated and is similar to the type I adsorption isotherm curve specified by IUPAC. It indicates that the pore volume of the micro-pores is filled with adsorbed CO_2, and the saturated adsorption capacity is equal to the volume of the micro-pores. In addition, the adsorption capacity of the shale sample soaked in distilled water has been significantly improved, which links to the change of micro-pore

structure after soaking. The swelling of clay minerals may cause the disintegration of shale along the weak cleavage surface, which does not only increase the proportion of meso-pores and macro-pores, but also increases the proportion of micro-pores. Further, the dissolution effect of acidic and alkaline solutions will continue to increase the proportion of micro-pores. This result is also similar to the case of N_2 isotherm adsorption.

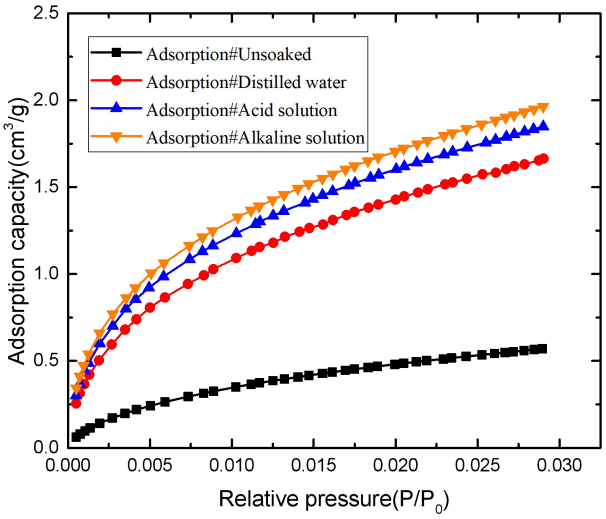

Fig. 2.9. Carbon dioxide adsorption isotherms of shale samples before and after the reaction

Specific surface area, pore volume and average pore diameter are critical parameters to characterize the pore-structure of porous media. Specific surface area refers to the total area per unit mass of solids. Pore volume is the total volume of pores per unit mass of solid. Based on the results of N_2 and CO_2 adsorption tests, the changes of pore structure parameters after soaking in different pH solutions can be further analysed. The specific results are shown in Table 2.3. For the unsoaked shale sample, the micro-pore volume of the CO_2 adsorption test is 0.002, which is much smaller than the meso-pore volume of the N_2 adsorption test. But in terms of specific surface area, since micro-pores are the main space for gas storage in shale gas reservoirs, the specific surface areas of N_2 and CO_2 adsorption tests are similar. After

soaking in distilled water, the specific surface area and pore volume of the shale sample increased significantly. It was considered that the immersion of distilled water created more dissolution pore in the shale sample. However, the average pore radius had no significant increase. After soaking in the acid-base solution, the specific surface area further increased. There was no significant increase in the pore volume of the micro-pores. This increase mainly focused on the pore volume of the meso-pores. It showed that the dissolution effect of the acid-base solution on the pore structure of shale was stronger than that of distilled water. But it was difficult to penetrate the micro-pores in a short time. Analysing the variation of average pore size, it was found that the different solutions all had the enhancement effect on the shale pore size, where alkaline solution>acid solution>distilled water.

Table 2.3. Comparison of pore-structure parameters after soaking in different pH solutions

Groups	BET surface area of N_2 （m^2/g）	BET surface area of CO_2 （m^2/g）	BJH Pore volume （m^3/g）	DFT Pore volume （m^3/g）	Aperture （nm）
Unsoaked	6.926	5.276	0.013	0.002	8.5
Distilled water	11.476	14.366	0.022	0.005	8.99
Acid solution	14.507	15.448	0.032	0.006	10.11
Alkaline solution	13.53	16.226	0.037	0.006	12.06

The DFT model was used to calculate the pore size distribution of micro-pores and meso-pores in shale samples under different acid-base immersion schemes, as shown in Fig. 2.10. Fig. 2.10(a) showed that the pore size distribution curve of unsoaked shale presented a single peak. After immersing in distilled water, acidic solution and alkaline solution, the pore size distribution curve showed the multi-peak distribution. The immersion of the acidic solution caused an obvious increase in the 3 nm pore size distribution. Fig. 2.10(b) showed that the pore size distribution curves after soaking in distilled water, acidic solution and

alkaline solution were similar. The three peaks in pore size distribution appeared at 0.35 nm, 0.5 nm and 0.6 nm.

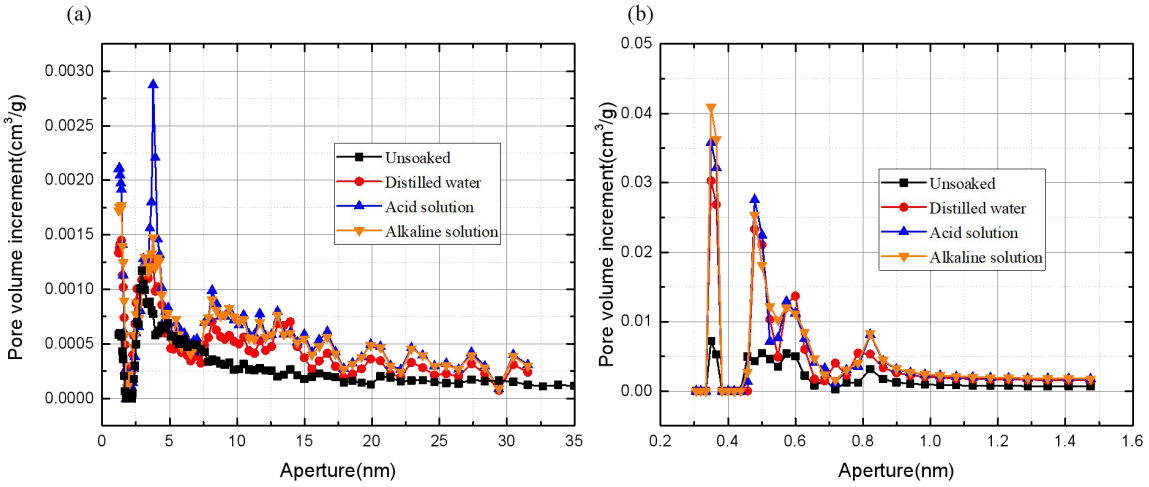

Fig. 2.10 (a) Distribution curve of mesopore (b) Distribution curve of micropore

The pore structure obtained by different tests needs to be characterized by different fractal models. The Frenkel-Halsey-Hill (FHH) model is often used to calculate the fractal dimension for the multi-layer molecular adsorption in the nitrogen adsorption test:

$$\ln V_a = Const + S\ln\left[\ln\left(P_0 / P_b\right)\right] \quad \text{* MERGEFORMAT (2.1)}$$

V_a is the nitrogen adsorption volume at pressure equilibrium. P_0 is the saturated vapor pressure of nitrogen at -196.15℃. P_b is the balance pressure. The above equation shows that there is a linear relationship between $\ln V$ and $\ln\left(P_0 / P\right)$. The fractal dimension can be calculated by the slope S, D=S+3. Therefore, the curve relationship between $\ln V$ and $\ln\left(P_0 / P\right)$ can be drawn by the N_2 adsorption test data, as shown in Fig. 2.11. On the whole, the curves of the four cases are very similar, showing a bilinear relationship. The curve is fitted piecewise linearly, and two fractal dimensions are obtained.

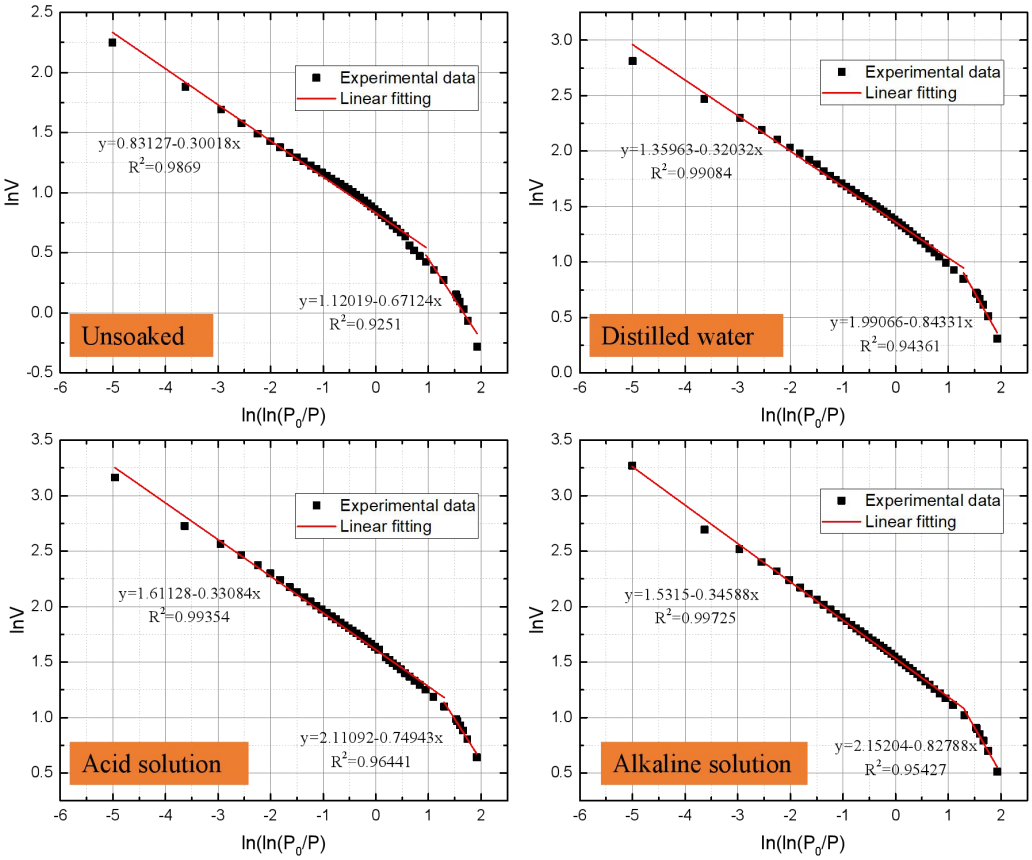

Fig. 2.11. Logarithmic curve of nitrogen adsorption volume and capillary pressure (a) Unsoaked (b) Distilled water (c) Acid solution (d) Alkaline solution

Table 2.4 lists the linear fitting slopes, correlation coefficients and fractal dimensions corresponding to shale samples in the 4 cases. All fitting correlation coefficients are greater than 0.925, indicating the reliability of the results. The fractal dimension of the unsoaked shale sample is the largest in the A and B sections, which shows that the pore size distribution in the original shale sample is relatively dispersed and the pore structure is heterogeneous. After immersion, the fractal dimension of the shale samples decreases, which indicates that the uniformity of the pore size distribution is increasing. Combined with the results in Fig. 2.10, the pore size distribution before soaking is a single-peak curve, while the pore size distribution after soaking is a multi-peak curve. It shows that the proportion of pores in each

scale becomes balanced. In general, soaking in alkaline solution makes the fractal dimension of shale smaller and the distribution of pore size more uniform.

Table 2.4. The fractal dimension of shale samples determined by nitrogen adsorption

Groups	Slope of linear fitting		Correlation coefficient		Fractal dimension	
	Section A	Section B	Section A	Section B	Section A	Section B
Unsoaked	-0.30018	-0.67124	0.9869	0.9251	2.69982	2.32876
Distilled water	-0.32032	-0.84331	0.99084	0.94361	2.67968	2.15669
Acid solution	-0.33084	-0.74943	0.99354	0.96441	2.66916	2.25057
Alkaline solution	-0.34588	-0.82788	0.99725	0.95427	2.65412	2.17212

2.6. Analysis of mechanical characteristics of shale under acid-base deterioration

In the interaction of water-rock, different pH solutions penetrate along the weak cleavage planes with the effect of imbibition. Due to the hydrophilicity of clay minerals, water molecules in infiltrating shale first combine with clay minerals, causing the expansion of the shale matrix. The expansion perpendicular to the bedding plane causes the shale layers to disintegrate more easily, that is, tensile failure. In addition, minerals in shale also undergoes dissolution reactions under different acid-base conditions. Thus, the shale bedding is in a compact state, and the mechanical characteristics do not change significantly. When shale is tensioned perpendicular to the bedding, the dissolution pores between the bedding significantly reduces the tensile strength of the shale. In the interaction of water-rock, the Brazilian split test effectively investigates the mechanical characteristics of shale under acid-base degradation.

The sample preparation for the Brazilian split test can be seen in Chapter 2.2. The main mineral components of the shale samples are quartz, albite, dolomite, muscovite, pyrite. The content of clay mineral (chlorite) is low. The bedding structure of shale in this area is well developed, with abundant bedding surfaces and weak cleavage surfaces. Because the bonding

force between shale bedding surfaces is weak, it is easy to disintegrate under anisotropic deformation. The part of unsoaked samples is shown in Fig. 2.12.

Fig. 2.12. Shale samples prepared for Brazilian split test

The Brazilian split test was completed using the CSS44100 electronic universal testing machine of China University of Mining and Technology, as shown in Fig. 2.13. The maximum loading of the testing machine is 20 kN, the range of force measurement accuracy is plus or minus 0.5%, and the range of deformation measurement accuracy is also plus or minus 0.5%. Initial loading force is given as 0.1 kN. The loading process is controlled by displacement, and the loading rate is 0.01 mm/min.

Fig. 2.13. CSS44100 electronic universal testing machine

2.6.1. Characteristic analysis of the load-displacement curve

According to the pH of the solution, the shale samples are divided into 6 groups: unsoaked, distilled water, acidic solution with pH=3, acidic solution with pH=5, alkaline solution with pH=9, and alkaline with pH=11 Solution. Five samples per group are soaked in a sealed glass container for 30 days, as shown in Fig. 2.14.

Fig. 2.14. Soaking container for shale samples

The variation of solution pH in Chapter 2.3 shows that shale has a slow-release effect on acid-base solutions, and the pH changes dramatically within 24 hours. Therefore, during the 30-day soaking process of the shale samples, the solution pH is re-measured every 24 hours. Then, the solution pH needs to be adjusted to the target value.

It is found that the quality of the shale samples also changed after 30 days of soaking in the solution. It was caused by the combined effect of the water-absorbing expansion of dry shale and the chemical reaction of minerals between weak cleavage surfaces. The quality data of shale before and after immersion and the peak load of Brazilian splitting are summarized in Table 2.5.

Table 2.5. Experimental data of Brazilian tests on shales

Groups	Sample number	Quality before soaking	Quality after soaking	Change of quality	Peak loading
Unsoaked	B-1	130.48			11.98
	B-2	126.65			10.76
	B-3	124.1			8.59
Distilled water	W-1	124.21	125.1	0.76	7.07
	W-2	126.03	126.79	0.71	7.61
	W-3	130.2	130.9	0.7	8.04
pH=5 solution	SL-1	125.41	125.92	0.56	7.72
	SL-2	124.82	125.37	0.55	6.07
	SL-3	129.78	130.26	0.61	7.41
pH=3 solution	SH-1	122.91	123.37	0.44	7.27
	SH-2	123.49	123.99	0.42	6.04
	SH-3	128.97	129.99	0.51	8.15
pH=9 solution	JL-1	123.72	124.52	0.65	5.56
	JL-2	124.78	125.44	0.65	7.27
	JL-3	125.22	125.87	0.71	5.97
pH=11 solution	JH-1	125.2	125.81	0.72	4.35
	JH-2	124.99	125.67	0.62	4.97
	JH-3	126.04	126.75	0.7	6.13

Table 2.5 presents that the shale samples immersed in distilled water for 30 days have the largest change in quality, followed by the shale samples immersed in alkaline solution. However, the strength of alkalinity has no obvious effect on the quality of shale samples. The shale immersed in the acidic solution has the least increase in quality. The acidity is stronger, the increase of quality less. There are two reasons: 1, the erosion of the acidic solution led to the decrease of clay minerals, aluminosilicate and carbonate minerals. 2, it was found that a lubricating viscous film was formed on the surface of the shale sample during the soaking process of the acid solution, which may hinder the shale imbibition process.

It can also be seen from Table 2.5 that the peak loading of the shale samples has an obvious difference after soaking in different pH solutions. A typical load-displacement curve in each group is selected to analyze this degradation law, as shown in Fig. 2.15. It shows that shale samples under different immersion cases generally exhibit similar mechanical

characteristics and are divided into three stages: compaction, elasticity and failure. Due to the large brittleness index of shale samples, there is no obvious yield stage in the Brazilian split test. When the indenter reaches the surface of shale samples, compaction deformation will only occur on the surface in contact with the indenter due to the internal weak cleavage surface or micro-crack structure. As the loading continues to increase, the shale sample is in the compaction stage and the load-displacement curve presents a concave upward trend. In the subsequent elastic stage, the load-displacement curve shows a linear growth relationship, which has obvious elastic characteristics. In the failure stage, the stress falls vertically after the peak loading, which is also consistent with the brittle mechanical characteristics of shale samples. However, the difference in the load-displacement curve is still significant due to the different pH of the soaking solution. The unsoaked shale samples have the largest peak loading, followed by the shale samples soaked in distilled water. When the shale samples are soaked in distilled water for 30 days, the swelling of the clay mineral causes anisotropic deformation, leading to the disintegration of the bedding. Compared with the unsoaked shale samples, the compaction stage of the shale samples soaked in distilled water is extended, especially its peak loading is dropped by 32.9%. The load-displacement curve of shale samples immersed in the acid solution (pH=3 and 5) is similar to that of shale samples immersed in distilled water. The extension of the compaction stage reflects the dissolution effect of the acid solution on the internal pores of the shale. The brittleness index of shale samples immersed in acid solution decreases. The shale samples immersed in alkaline solution (pH=9 and 11) have the most obvious compaction stage, which also shows the dissolution effect of alkaline solution on the internal pore structure of shale. According to the analysis of the shale components under acid-base degradation in Chapter 2.3, except for the acidic solution which has the most prominent dissolving effect on clay minerals, the changes

of other mineral components are also the most obvious in alkaline solutions. Therefore, the analysis of the component is consistent with the results of the mechanical characteristics of shale in this section.

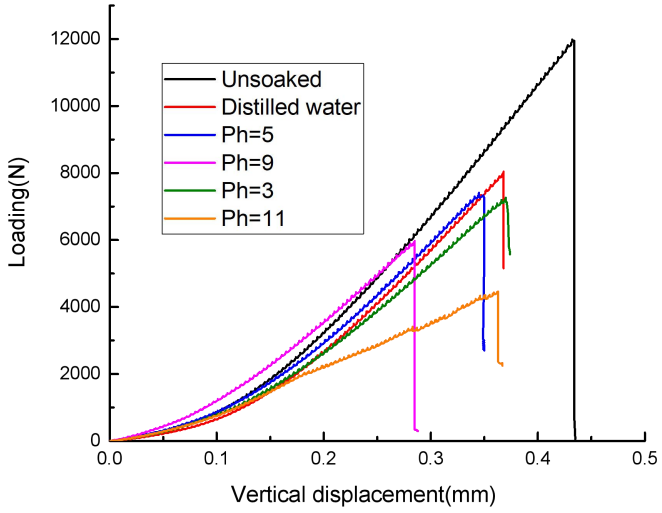

Fig. 2.15. Displacement-load curves of shale samples under different pH

2.6.2. Effects of acid-base deterioration on tensile strength and splitting modulus

The tensile strength of shale is much lower than the compressive strength, which is a vital parameter for fracturing optimization design in shale gas production. The impact of acid-base degradation on the tensile strength of shale samples is explored here. According to the split test of the Brazilian disc, the tensile strength of shale can be expressed by [10]

$$\sigma_t = \frac{2P_{\max}}{\pi D h} \qquad \text{* MERGEFORMAT (2.2)}$$

where σ_t is the tensile strength of shale. $P_{\max}$ represents the peak loading. D is the diameter of the shale sample. h is the thickness of the shale sample.

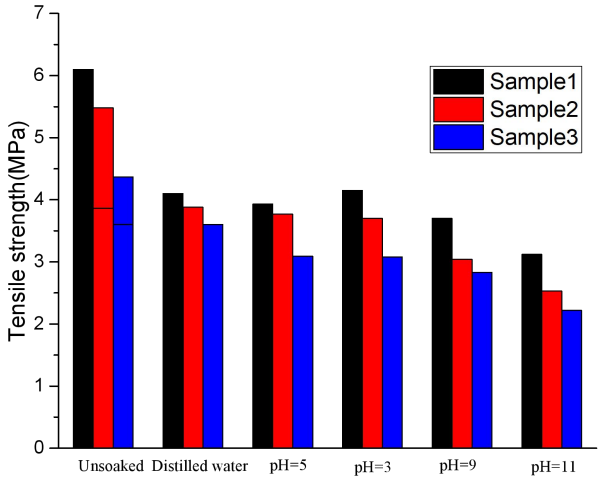

Fig. 2.16. Tensile strength of shale samples after soaking different pH solutions

The tensile strength obtained by the above equation is summarized in Table 2.6 and Fig. 2.16. The data of tensile strength under different immersion cases are discrete. In order to effectively analyze the regularity of the data, the maximum and minimum deviations from each group of data are deleted. It can be seen from Table 2.6 that the average tensile strength of shale is dropped significantly after being soaked in distilled water, reaching 27.4%. It proves that the shale swelling has the most significant impact on the mechanical characteristics of the shale. Compared with distilled water, the tensile strength of shale samples immersed in acid solution has a small decrease. But it is noted that the further decrease in the pH of the acidic solution no longer affects the tensile strength of the sample. This result is related to the content of carbonate and aluminosilicate in the shale sample. Alkaline solution degrades the tensile strength of the sample most obviously. Compared with the unsoaked shale sample, the average tensile strength is dropped by 50.8%.

Table 2.6. Summary of tensile strength for shale samples

Groups	Sample number	Tensile strength /MPa	Average value /MPa
Unsoaked	B-1	6.1	5.32
	B-2	5.48	
	B-3	4.37	
Distilled water	W-1	3.6	3.86
	W-2	3.88	
	W-3	4.1	
pH=5 solution	SL-1	3.93	3.6
	SL-2	3.09	
	SL-3	3.77	
pH=3 solution	SH-1	3.7	3.64
	SH-2	3.08	
	SH-3	4.15	
pH=9 solution	JL-1	2.83	3.19
	JL-2	3.7	
	JL-3	3.04	
pH=11 solution	JH-1	2.22	2.62
	JH-2	2.53	
	JH-3	3.12	

The splitting modulus is a critical parameter describing the strength of shale resistance to elastic deformation. According to the definition of Yu Yong et al. [11], the vertical displacement in the load-displacement curve is divided by the diameter of the shale sample, the loading is divided by the area of the meridian surface of the shale sample, and the slope of the straight line in the new curve is the split modulus of the shale. Fig. 2.17 shows that the splitting modulus of the shale sample is greatly decreased after immersion. The splitting modulus of the shale sample after soaking in acid solution varies from 0.38 to 0.47 GPa; while the splitting modulus of shale sample after soaking in alkaline solution varies from 0.23 to 0.44 GPa. It indicates that the shale sample soaked in an alkaline solution becomes more "soft" and has a weaker ability to resist elastic deformation.

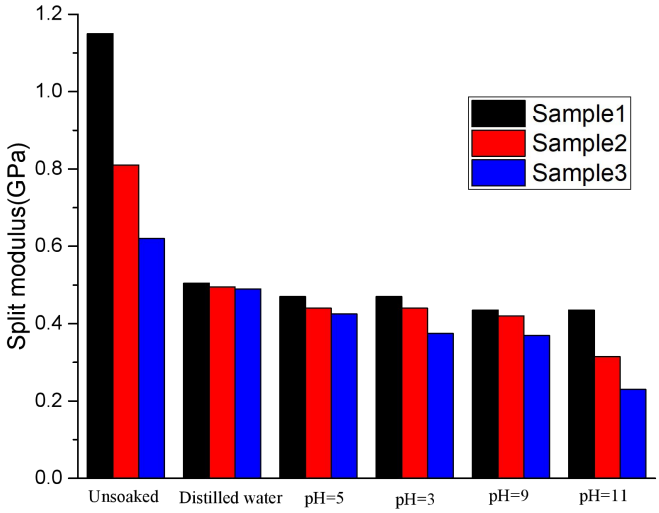

Fig. 2.17. Split modulus of shale samples after soaking different pH solutions

2.7. Conclusions

The water-rock geochemical reaction of shale in different geological environments irreversibly affects the mineral composition, micro-pore structure and mechanical properties of shale, which further affects the shale gas production or the CO_2 storage efficiency. In this chapter, immersion experiments under different pH were conducted. Through X-ray diffraction (XRD), field emission electron microscopy (FE-SEM), nitrogen adsorption method, carbon dioxide adsorption method and Brazil splitting test, the mineral composition, surface morphology, internal pore structure and mechanical properties of shale soaking in different acid-base solutions were investigated. The mechanisms of water-rock reaction under different pH were explored. Based on the above experimental results, the following conclusions were drawn:

When shale samples were immersed in distilled water, acidic solutions and alkaline solutions, clay minerals, carbonate minerals, muscovite and pyrite were dissolved. The

increase of quartz content after immersion was due to the decrease of other minerals by geochemical reactions. From the comparison of mineral components before and after immersion, the dissolution effect of the three solutions on shale was: alkaline solution>acid solution>distilled water. It was noted that the reaction of clay minerals in acidic solutions was the most obvious.

The water-rock reaction had an impact on the shale surface morphology, which was mainly concentrated on micron-scale fractures and inter-particle pores. There was no obvious change in intergranular pore-structure after 30 days of immersion. The combination of distilled water and clay minerals caused the matrix swelling, leading to the closure of micro-fractures. The dissolution effect of the acidic solution and alkaline solution on inter-particle pores was prominent.

The specific surface area, pore volume, and average pore diameter of the shale samples soaked in the solution increased. The increase of specific surface area and pore volume were caused by the dissolution of micro-pores in organic matter, while the increase of average pore diameter was the conversion of micro-pores into meso-pores or macro-pores under the action of dissolution. Therefore, the average pore diameter soaking in acidic solution and alkaline solution was much larger than that of the shale sample soaking in distilled water. The pore size distribution curve of the unsoaked shale had a single peak, but the pore size distribution curves of the shale after soaking in distilled water, acidic solution and alkaline solution all presented the characteristics of multi-peak. Soaking in alkaline solution made the fractal dimension smaller and pore size distribution more uniform.

The average tensile strength of shale dropped significantly after being soaked in distilled water, reaching 27.4%. It proved that the physical process of the swelling had the most significant impact on the mechanical characteristics of shale. Compared with distilled water,

the tensile strength of shale samples immersed in acid solution had a small decrease. The alkaline solution degraded the tensile strength of shale most obviously and the average tensile strength dropped by 50.8%. The splitting modulus of the shale sample also dropped significantly after immersion. The splitting modulus of the shale sample after soaking in acid solution varied from 0.38 to 0.47 GPa; while the splitting modulus of shale sample after soaking in alkaline solution varied from 0.23 to 0.44 GPa. It indicated that the shale sample soaked in alkaline solution becomes more "soft" and has a weaker ability to resist elastic deformation.

2.8. References

[1] Wang J G, Peng Y. Numerical modelling for the combined effects of two-phase flow, deformation, gas diffusion and CO_2 sorption on caprock sealing efficiency. Journal of Geochemical Exploration, 2014, 144: 154-167.

[2] Chen W.L, Zhou W, Luo P, Deng H, Li Q, Shan R, Qi M. Analysis of the shale gas reservoir in the lower Silurian longmaxi formation, Changxin 1 well, southeast sichuan basin, China. Acta Petrologica Sinica, 2013, 29(3): 1073-1086 [in Chinese].

[3] Guo T, Liu R. Implications from marine shale gas exploration breakthrough in complicated structural area at high thermal stage: taking Longmaxi formation in well jy1 as an example. Natural Gas Geoscience, 2013, 24(4): 643-651 [in Chinese].

[4] Zeng X, Liu S, Huang W, Zhang C. Comparison of Silurian Longmaxi Formation shale of Sichuan Basin in China and Carboniferous Barnett Formation shale of Fort Worth Basin in United States. Geological Bulletin of China, 2011, 30(Z1): 372-384 [in Chinese].

[5] Sun Z, Wang Y, Wu B, Zhuo S, Wei Z, Wang G, Xu L. Chemical reactions and effects of slick water fracturing fluid on the pore structures of shale reservoirs in different deposition environments. Journal of University of Chinese Academy of Sciences, 2018, 35(5): 712-719 [in Chinese].

[6] Fang C, Huang Z, Ge Z, Wang Y, Zheng D. The influence of working fluid on fracture propagation and mechanical properties of shale. Journal of Taiyuan University of Technology, 2015, 46(4): 414-418 [in Chinese].

[7] Yu B. Classification and characterization of gas shale pore system. Earth Science Frontiers, 2013, 20(4): 211-220 [in Chinese].

[8] Zhao P, Li X, Tian X, Su G, Zhang M, Guo M, Dong Z, Sun M, Wang F. Study on micropore structure characteristics of Longmaxi formation shale gas reservoirs in the southern Sichuan basin. Natural Gas Geoscience, 2014, 25(6): 947-956 [in Chinese].

[9] Li J. Prediction on lithology of sandstone reservoirs based on fractal theory. Sino-global Energy, 2011, 16(2): 61-65 [in Chinese].

[10] Hou P, Gao F, Yang Y, Zhang Z, Gao Y, Zhang X, Zhang J. Effect of bedding plane direction on acoustic emission characteristics of shale in Brazilian tests. Rock and Soil Mechanics, 2016, 37(6): 1603-1612 [in Chinese].
[11] Yu Y, Wang T. Study on relationship between splitting behaviour and elastic modulus of three gorges granite. Chinese Journal of Rock Mechanics and Engineering, 2004, 19: 3258-3261 [in Chinese].

Chapter 3: An improved relative permeability model for gas-water displacement in fractal porous media

3.1. Introduction

Many research results show that the interaction of gas-water-rock directly determines the evolution of relative permeability, which ultimately affects the fluid flow mechanism in complex porous media. However, how to effectively describe the evolution of relative permeability with fractal dimensions still lacks relevant research. A gas-water relative permeability model based on fractal theory is proposed in this chapter. It aims to explore the gas-water displacement mechanism in complex fractal porous media. This novel fractal model considers the complexity of pore structure, geometrical correction factor, water film and real gas effects, and can further study the evolution of gas-water relative permeability in complex porous media.

3.2 Classical relative permeability models

The gas-water relative permeability has been investigated through experiments, theoretical modeling, and numerical simulations. Fig. 3.1 summarizes some classical relative permeability models and provides a brief introduction to the development of relative permeability model in recent years. The Purcell model calculated the permeability through capillary pressure data and formulated a relatively primitive permeability model [1]. This model assumed that the sum of the gas and water relative permeability was equal to 1, which did not agree with the actual fluid flow in porous media. Subsequently, this model was further modified by many scholars. Gates and Leitz [2] integrated the relative permeability

from the capillary pressure. Burdine [3] thought that the assumption of capillary parallelism was not accurate and introduced the tortuosity factor into the Purcell model. Mualem [4] proposed an integration method based on the Purcell model. For simplicity, Romm [5] developed a relative permeability model which ignored the phase interference between the gas and water phases. This model was also called the X model. Brooks and Corey [6] introduced a pore-size distribution index to modify the capillary pressure function and proposed a more generalized gas-water relative permeability model. The Brooks–Corey model was widely used in modeling two-phase flow in complex porous media. Fourar and Lenormand [7] derived a viscous coupling model after integrating Stokes' equation and the effect of viscosity. Combined with momentum balance, viscosity, and cubic law, Chima and Geiger [8] developed a new relative permeability model. After ignoring the capillary pressure, Chima's model became a unique form of the viscous coupling model. Li et al. [9] improved Chima's model through the consideration of the influences of capillary tortuosity and irreducible water saturation on relative permeability. The above relative permeability models made significant contributions to the prediction of two-phase flow in porous media. They also found that the relative permeability of the gas phase was more susceptible to the geometry of flow channels. However, these relative permeability models did not thoroughly consider the effects of complex pore microstructures on fluid flow.

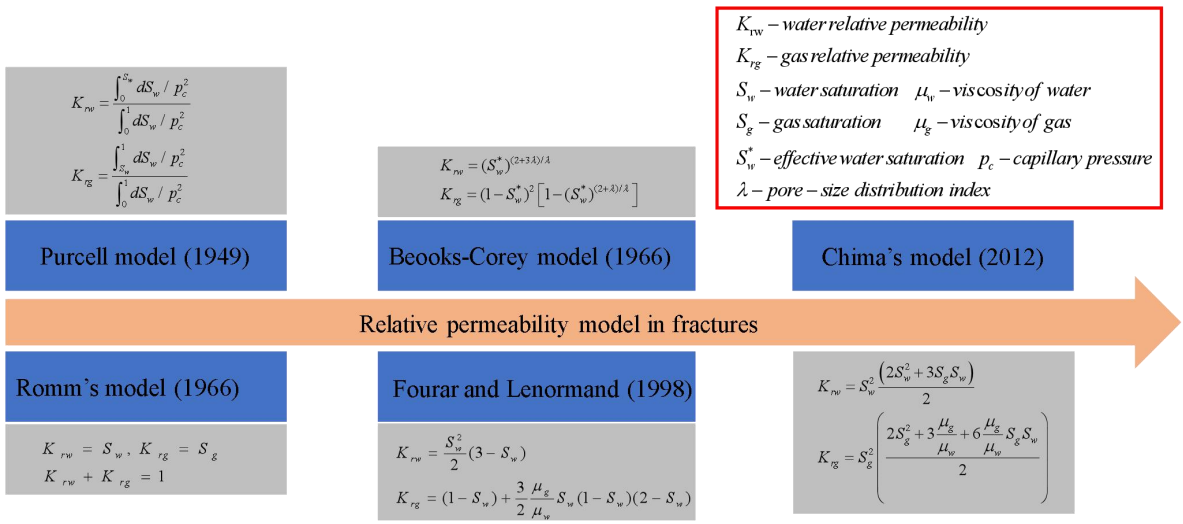

Fig. 3.1. The schematic diagram for the development of relative permeability model.

Complex nanoscale pore structures of shale gas reservoirs can be directly observed by the advanced image technology such as focused ion beam-scanning electron microscopes (FIB-SEM) and broad ion beam-scanning electron microscopes (BIB-SEM), but the inclusion of these complex microstructures into the relative permeability model has become a challenging problem. There are several mathematical and physical issues to be solved. The first issue is the description of complex microstructures. Mandelbrot [10] first developed the fractal theory for self-similarity in complex porous media. The fractal theory was regarded as a useful tool to describe nanoscale pore structures [11–13]. The second issue is the interaction between complex microstructures and fluid flow in porous media. Many scholars discussed the influence of the complex pore structure on the flow mechanism in the relative permeability model [14–16]. For example, Li et al. [17] considered some non-interconnected tortuous capillaries in fractal-like porous media and proposed a novel gas-water displacing model. Lei et al. [11] developed a relative permeability model in multiscale porous media, which takes lognormal distribution function and residual water saturation into consideration. Ghanbarian et al. [15] developed a relative permeability model to consider the tortuosity-connectivity factor and effective saturation. The influences of drawdown pressure

on the relative permeability of water and gas phase were experimentally investigated by Mo et al. [18]. Their experimental results indicated that gas relative permeability increases with drawdown pressure. Additionally, the increase in drawdown pressure reduced irreducible water saturation. Huo and Benson [19] experimentally investigated the dependence of relative permeability on stress. They found that both irreducible water saturation and endpoint gas phase relative permeability decreased with the increase of effective stress at the same flow rate. Lei et al. [20] proposed a fractal model for the prediction of gas-water relative permeability in fractures. They found that increasing the complexity of pore structure (fractal dimension) would result in a decrease of water relative permeability, while the gas relative permeability had a corresponding increase with the ratio of fluid viscosity. Geng et al. [12] deduced a fractal apparent permeability model for shale gas flow in the heterogeneous matrix (organic and inorganic matters). If the organic matter in the matrix was ignored, the apparent permeability was overestimated up to 24.1%. Therefore, pore shape, maximum pore size, and porosity were primary factors that had significant effects on apparent permeability [21]. Cai et al. [22] proposed an improved permeability model to consider viscous flow, molecular diffusion, and surface diffusion. However, this model used a uniform diffusion coefficient to deduce gas permeability, ignoring the effect of water on the transport mechanism. Wang et al. [23] considered surface effects (hydrogen bond, double layer repulsive force, Vander Waals force, and structure repulsive force) into the gas-water relative permeability model. They found that the effect of hydrogen bond significantly enhanced fluid flow in porous media. However, the interaction of microstructures and fluid flow regimes was not well-described in relative permeability models.

3.3. Proposed gas-water relative permeability model

In this section, the two-phase flow mechanism in complex pore structures is investigated. The threshold pressure gradient and the critical capillary radius are depicted in a conceptual model to emphasize the influence of capillary size on the gas-water displacing process. Then, the fractal dimensions are introduced to describe the complexity of porous media. Finally, an improved gas-water relative permeability model is derived from accounting for the influences of the complex pore structure, geometric correction factor, water film and the real gas effect.

3.3.1. Two classical relative permeability models

3.3.1.1. Brooks–Corey model

In the Corey model, relative permeability is a function of capillary pressure as

$$K_{rw} = \left(\frac{h}{p_c} \right)^m \qquad \text{* MERGEFORMAT (3.1)}$$

where h is a constant, p_c is the capillary pressure in porous media, m is a correction coefficient, and K_{rw} is the water relative permeability.

For complex pore structures, this equation cannot predict the relative permeability with sufficient accuracy. Researchers find that relative permeability is sensitive to pore-size distribution. The classical Brooks–Corey model introduces a macroscopic parameter of pore-size distribution index λ to describe the heterogeneity of the pore structure. Their relative permeability model is

$$K_{rw} = \left(S_w^* \right)^{(2+3\lambda)/\lambda} \qquad \text{* MERGEFORMAT (3.2)}$$

$$K_{rg} = \left(1 - S_w^* \right)^2 \left[1 - \left(S_w^* \right)^{(2+\lambda)/\lambda} \right] \qquad \text{* MERGEFORMAT (3.3)}$$

where S_w^* represents the effective water saturation and is a function of capillary pressure p_c.

3.3.1.2. Viscous coupling model

Considering the effect of viscosity on fluid flow, Fourar and Lenormand [7] developed a gas-water relative permeability model as

$$K_{rw} = \frac{S_w^2}{2}(3 - S_w) \qquad \text{* MERGEFORMAT (3.4)}$$

$$K_{rg} = (1 - S_w) + \frac{3}{2}\mu_r S_w (1 - S_w)(2 - S_w)$$

* MERGEFORMAT (3.5)

where S_w is the water saturation. μ_r is the viscosity ratio of gas to water and is $\mu_r = \mu_g / \mu_w$.

3.3.2. Gas-water displacement and the variation of capillary pressure with water saturation

Fig. 3.2 presents a simplified conceptual diagram to express the variation of capillary pressure with water saturation. The solid red line represents the process of gas displacing water. The initial state of the rock formation is fully water-saturated, and the pressure increases with gas injection. When the capillary entry pressure is overcome, the front of two-phase flow starts to move. The accumulated pressure causes the gas to break through the upper boundary of the rock formation. This pressure is called breakthrough pressure. Finally, the increase of pressure does not further reduce water saturation in the fracture. This minimum water saturation is irreducible water saturation (IRWS). The blue dotted line represents the process of water imbibition. As the capillary pressure decreases, a portion of the gas is trapped in tinny pores or fractures under the wetting phase pressure. This minimum

capillary pressure is often termed as snap-off pressure. The corresponding saturation is irreducible gas saturation (IRGS).

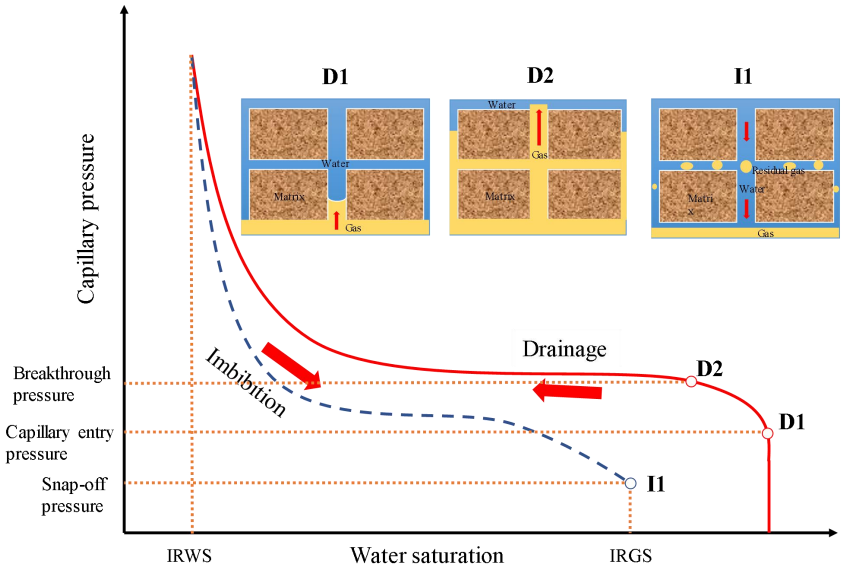

Fig. 3.2. Conceptual diagram of capillary processes

Both the pore-size distribution index and the capillary entry pressure are macroscopic parameters. They can express the complexity of the rock pore structure. Such a model can macroscopically match the experimental data of permeability but does not describe the interaction of gas and water from the microscopic mechanism. In fact, the effects of pore-size distribution and tortuosity on permeability should be discussed from the viewpoint of the fractal dimension. From a capillary theoretical model to the integration of capillaries in different radius sizes, fractal theory can better explore the effects of complex pore structure on permeability. Besides, the capillary entry pressure is usually regarded as a fixed value in the classical Brooks–Corey model. However, this value is difficult to determine using experimental tests. In this paper, we define the critical capillary radius, which corresponds to the capillary entry pressure. When the capillary tube size is smaller than the critical radius of the capillary, the gas cannot displace the water, and the water flow fills the entire capillary

flow channel. On this sense, this part of the water is the irreducible water and its saturation is called the irreducible water saturation in the two-phase flow.

3.3.3. Irreducible water saturation and threshold pressure gradient

This concept of irreducible water saturation is very similar to the threshold pressure gradient (TPG). From the macroscopic view, the residual water in the target reservoir blocks the pore-throat. Only when the capillary pressure is higher than the capillary entry pressure, the two-phase flow can be observed, as shown in Fig. 3.3. TPG is a vital parameter in describing the gas starting flow against viscous forces. This TPG makes the Darcy flow gradually transform into a low-velocity, non-Darcy flow when water saturation is gradually increasing. Many researchers indicate that permeability, water saturation, and pore pressure are controlling parameters for TPG in tight gas reservoirs [17, 19, 24]. On this sense, we propose the following formula for TPG:

$$\begin{aligned} TPG &= ae^{s_w} \cdot e^{b^* p_f + c^* p_f^2} \\ a &= e^{-(5.4491\times10^{15}\times k + 1.13293)} \\ b &= 8.81931\times10^{13}\times k - 0.06892 \\ c &= -5.83713\times10^{11}\times k + 0.0129 \end{aligned} \quad \text{* MERGEFORMAT (3.6)}$$

where k is the intrinsic permeability, p_f is the pore pressure, a is a correction coefficient for water saturation, and b and c are correction coefficients for pore pressure. These correction coefficients are also linked with shale permeability.

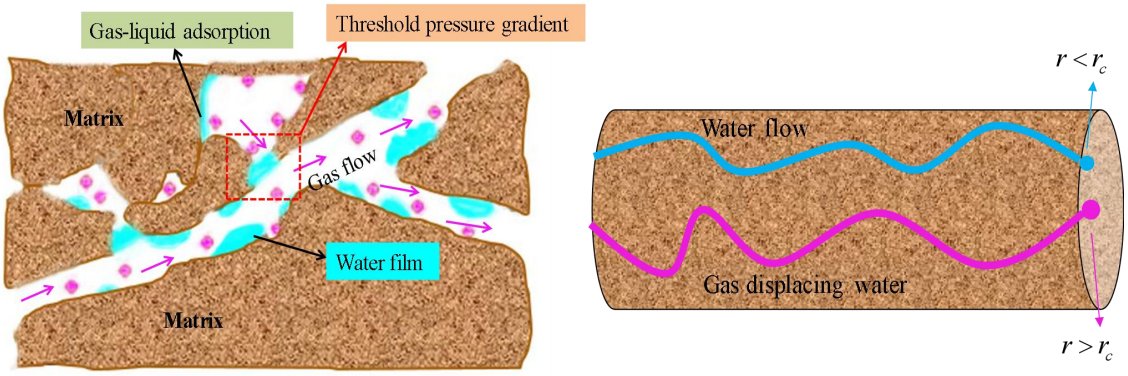

(a) Macroscopic threshold pressure gradient (b) Microscopic critical capillary radius

Fig. 3.3. A schematic diagram of water residual saturation at different scales

The accuracy of Eq. (3.6) is checked using the experimental data from Ding et al. [24]. Their comparison is shown in Fig. 4. Fig. 4(a) presents the rise of TPG with the increase of water saturation. Fig. 4(b) shows the effect of different permeabilities on TPG. Although TPG describes the gas-water displacement in capillary tubes, it does not consider the complex pore structure of porous media.

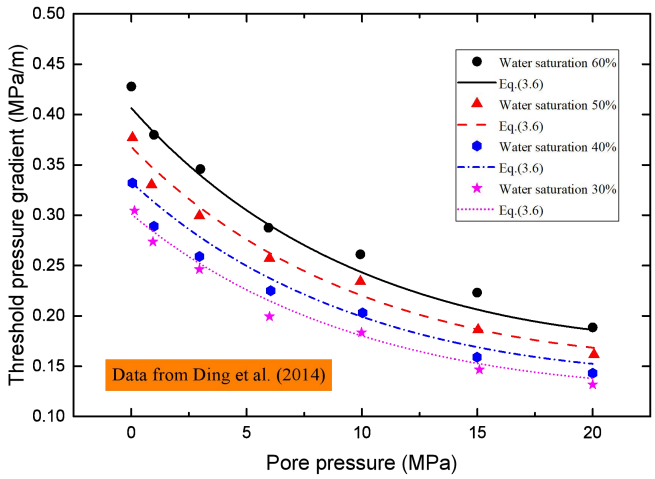

(a)

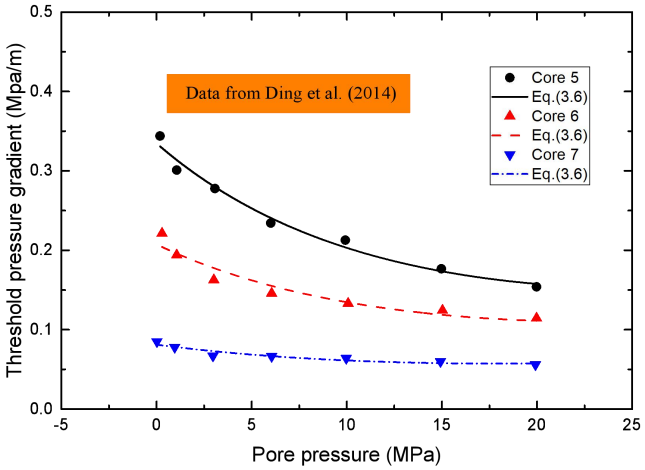

(b)

Fig. 3.4. Comparison of Eq. (3.6) with experimental data. (a) Variation with water saturation and (b) Variation with permeability

3.3.4. Calculation of water saturation and irreducible water saturation

Based on the Laplace formula, capillary pressure can be expressed as

$$p_c = \frac{2\sigma\cos\theta}{r_c} \qquad \text{* MERGEFORMAT (3.7)}$$

where p_c is the capillary pressure, σ represents the surface tension, and θ is the contact angle of the gas-water-rock interface.

If the surface tension and contact angle are constant, the capillary pressure has an inverse proportional relationship with the pore radius. There is a critical capillary radius r_c in the complex distribution of capillary pore size. When the pore size is larger than the critical capillary radius, the gas flow can occur in the capillary tube, and the water film is attached to the capillary wall. If the capillary tube size is smaller than the critical radius r_c, the capillary tube is fully saturated with water and gas flow does not occur. Therefore, from the

microscopic view, the gas can displace water only when the capillary tube radius is greater than the critical capillary tube radius.

The water sources come from two parts: One is a single water flow $(r < r_c)$, and the other is the gas-water two-phase flow $(r > r_c)$. According to the area ratio of pores, the water saturation can be calculated by pore-size distribution and water film as [14]

$$S_w = \frac{\int_{r_{\min}}^{r_c} \pi r^2 (-dN) + \int_{r_c}^{r_{\max}} \pi \left(r^2 - r_{wg}^2\right)(-dN)}{\int_{r_{\min}}^{r_{\max}} \pi r^2 (-dN)}$$

* MERGEFORMAT (3.8)

When the pore size is less than the critical capillary tube radius, there is not enough capillary pressure to further displace the water in pores. At this time, the water saturation is the irreducible water saturation and is calculated by

$$S_{wi} = \frac{\int_{r_{\min}}^{r_c} \pi r^2 (-dN)}{\int_{r_{\min}}^{r_{\max}} \pi r^2 (-dN)} = \frac{r_c^{2-D_f} - r_{\min}^{2-D_f}}{r_{\max}^{2-D_f} - r_{\min}^{2-D_f}} \quad \text{* MERGEFORMAT (3.9)}$$

Fig. 3.5 shows the variation of irreducible water saturation with critical capillary tube radius. No linear relationship is observed between the critical capillary radius and irreducible water saturation. When the critical capillary radius is large enough, the irreducible water saturation grows slowly and tends to be stable. In the case of the same capillary critical tube radius, the increase in the maximum capillary radius leads to a decrease in irreducible water saturation. The water flow is enhanced by the increase of capillary tube radius rather than being sealed in the capillary tube. When the critical capillary tube radius is small relative to the capillary tube size, the difference is not obvious. However, the irreducible water saturation changes from 0.2 to 0.4 when the critical capillary tube radius is 10 nm.

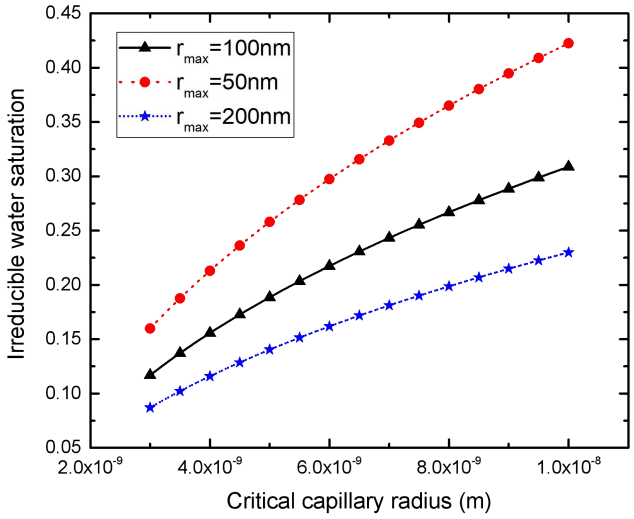

Fig. 3.5. Variation of irreducible water saturation with critical capillary radius

3.3.5. Fractal distribution of pores

Porous media have numerous capillary tubes with different pore sizes and tortuous lengths. These interpore structures are of self-similarity and can be described by fractal theory. The number of pore sizes greater than r can be expressed as

$$N(\delta \geq r) = \left(\frac{r_{\max}}{r} \right)^{D_f} \qquad \text{* MERGEFORMAT (3.10)}$$

where δ represents the scale of length, $r_{\max}$ and r are the maximum pore radius and pore radius, respectively, and D_f is the pore-size distribution (PSD) fractal dimension and in the range of $0 < D_f < 2$ in two dimensions. Yu and Li [25] found that this fractal dimension is related to the porosity ϕ and the radius ratio $r_{\min} / r_{\max}$.

$$D_f = d - \frac{\ln \phi}{\ln \left(r_{\min} / r_{\max} \right)} \qquad \text{* MERGEFORMAT (3.11)}$$

where d represents the Euclidean dimension.

Differentiating Eq. (3.10) with respect to r obtains the following expression:

$$-dN = D_f r_{\max}^{D_f} r^{-(D_f+1)} dr \qquad \text{* MERGEFORMAT (3.12)}$$

Thus, the probability density function of pore-size distribution is expressed as

$$f(r) = D_f r_{\max}^{D_f} r^{-(D_f+1)} \qquad \text{* MERGEFORMAT (3.13)}$$

Due to the tortuosity, the length of the capillary tube is higher than the straight capillary tube in complex porous media. Capillary length is related to the radius size with following fractal law [25]:

$$L(r) = (2r)^{1-D_t} L_0^{D_t} \qquad \text{* MERGEFORMAT (3.14)}$$

where L and L_0 represent the actual capillary length and representative capillary length, respectively. D_t is the fractal dimension of the tortuosity, and its range is between 1 and 2 in two-dimensional space. Therefore, the cross-sectional area of all pores could be written as [20]

$$A = \frac{(1-\phi)}{\phi} \frac{D_f \pi r_{\max}^2}{2 - D_f} \qquad \text{* MERGEFORMAT (3.15)}$$

Thus, the representative capillary length can be expressed as

$$L_0 = r_{\max} \sqrt{\frac{(1-\phi)}{\phi} \frac{D_f \pi}{2 - D_f}} \qquad \text{* MERGEFORMAT (3.16)}$$

3.3.6. Two-phase flow model in nanopores

3.3.6.1. Flow rate of gas

The flow channels in Fig. 3.6 were assumed to be capillary tubes with tortuosity. SEM images showed that the pore shape was not only circular, but also slit. Ignoring the influence of pore shape affected the understanding of the fluid flow mechanism in complex porous media. Mortensen et al. [26] stated that the capillary channel with a circular cross-section did not reflect the complexity of various cross-sectional shapes, such as elliptic, rectangular,

triangular, and harmonic-perturbed circles. A geometrical correction factor was introduced to describe different cross-sectional shapes in a unified form in this study.

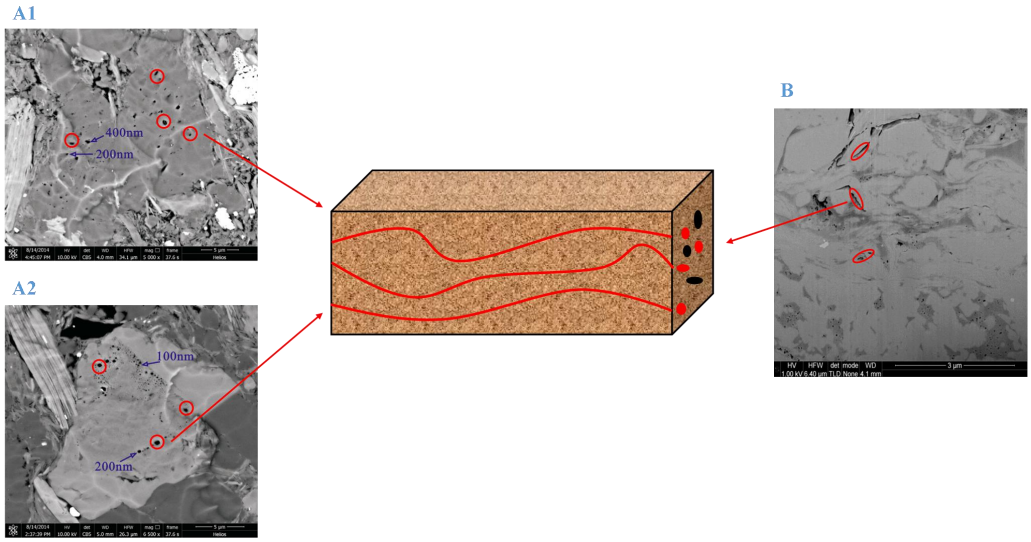

Fig. 3.6. Conceptual model of pore shape distribution. SEM images (A1 and A2) are from Ambrose et al. [27]. SEM image (B) is from Tang et al. [28]

When a steady-state laminar flow occurs within capillary tubes, Fig. 3.7 gives the flow distribution of the gas and water phases. This conceptual model has three different regions: The gas flow region, the typical viscosity water flow region, and a high-viscosity water film region. The fluid flow in these three regions has different flow mechanisms. They are mathematically described below.

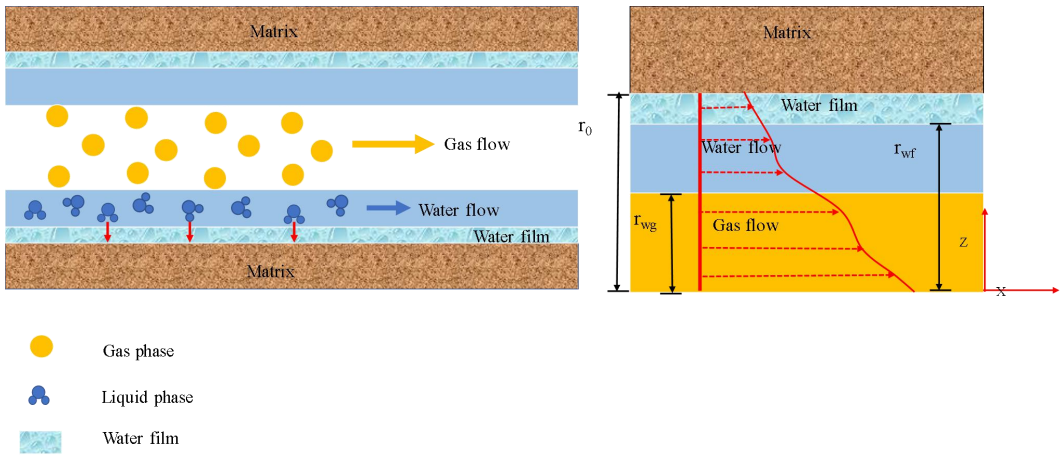

Fig. 3.7. Conceptual model of two-phase flow in nanopores

Based on the Hagen–Poiseuille equation, the gas flow rate in a capillary tube is obtained below if slip flow and free molecular flow are considered in the continuum flow regime.

$$q_g = \frac{\pi r^4}{128\mu_g}(1+\beta K_n^*)\left(1+\frac{4K_n^*}{1-\alpha K_n^*}\right)\frac{\Delta p}{L}$$

* MERGEFORMAT (3.17)

where r and L are the capillary tube radius and capillary tube length, respectively, Δp is the pressure difference applied to the external capillary tube, μ_g is the gas viscosity, and β represents a dimensionless rarefaction coefficient. When β changes from 0 to $\frac{64}{3\pi(1-4/\alpha)}$, a slip flow regime transforms into a free molecular flow regime. α represents the slip coefficient and can be obtained from the linearized Boltzmann solution or velocity distribution given by the Poiseuille flow in a cylindrical tube [29]. K_n^* is the modified Knudsen number, which is the ratio of the mean free path of gas flow to the characteristic size of gas flow channel. Details are provided in the next section.

3.3.6.2. Geometrical correction factor and real gas effect

Shale formation has various shapes of pores. This study introduces a geometric correction factor to express the deviation of pore shape from a circular pore channel [30, 31].

$$K_n^* = \frac{\eta}{2\gamma r}$$

* MERGEFORMAT (3.18)

where γ is the geometric correction factor. The γ is 1 for the circular pore, 1.094 for the square pore, and is 1.1186 for the equilateral triangle pore [18]. η is the gas mean free path.

$$\eta = \frac{\mu_g}{p_g}\sqrt{\frac{\pi ZRT}{2M}}$$

* MERGEFORMAT (3.19)

where p_g is the gas pressure, R is the universal gas constant, T is the reservoir temperature, M is the gas molecule mass, and Z is the gas compressible factor, which

expresses the real gas effect on gas density and viscosity. It is noted that previous models usually neglected this real gas effect (that is $Z = 1$), but this effect becomes more notable at high pressure and temperature. Z can be expressed as [30]:

$$Z = 1 + A_1 p_r + A_2 p_r^2 + \frac{A_3 p_r^{A_4}}{T_r^{A_5}} + \frac{A_6 p_r^{(A_4+1)}}{T_r^{A_7}} + \frac{A_8 p_r^{(A_4+2)}}{T_r^{(A_7+1)}}$$

$$p_r = p / p_{gc}, \quad T_r = T / T_{gc}$$

* MERGEFORMAT (3.20)

where p_{gc} and T_{gc} are the gas critical pressure and temperature, respectively, and A_1 - A_8 are tuned coefficients.

Jarrahian and Heidaryan [33] developed a generalized gas viscosity model with a range of pressures (0.1–137.8 MPa) and temperatures (241–473 K). This study described their expression of gas viscosity as

$$\mu_g = \mu_a \left[1 + \frac{A_{11}}{T_r^5} \left(\frac{p_r^4}{T_r^{20} + P_r^4} \right) + A_{12} \left(\frac{P_r}{T_r} \right)^2 + A_{13} \left(\frac{P_r}{T_r} \right) \right]$$

* MERGEFORMAT (3.21)

where μ_a is the gas viscosity under the standard condition, and A_{11}, A_{12}, and A_{13} are temperature, pressure, and molar weight independently tuned coefficients, respectively.

Beskok and Karniadakis [34] found that gas flow was in the slip flow regime when $\beta = 0, \alpha = -1$. Combining Eqs (3.17-3.21), we extended the gas flow rate to consider the geometric correction factor and real gas effect in a capillary tube and obtain the flow rate as

$$q_g = \frac{\pi r_{wg}^4}{8\mu_g} \left(1 + \frac{4K_n^*}{1 + K_n^*} \right) \frac{\Delta p}{L} \qquad \text{* MERGEFORMAT (3.22)}$$

Integrating Eq. (3.22), the total gas volumetric flow rate is expressed as

$$Q_g = D_f r_{\max}^{D_f} \int_{r_c}^{r_{\max}} \frac{\pi r_{wg}^4}{8\mu_g}\left(1+\frac{4K_n^*}{1+K_n^*}\right)\frac{\Delta p}{L}\cdot r^{-(D_f+1)}dr$$
$$= \varepsilon_g \int_{r_c}^{r_{\max}} r_{wg}^4 \cdot r^{D_t-D_f-2}(1+4K_n^*)dr$$

* MERGEFORMAT (3.23)

where r_{wg} is the distance from the center of the circular pore to the gas-water interface and r_c is the critical capillary tube radius. $\varepsilon_g = D_f r_{\max}^{D_f} \frac{\pi\Delta p}{2^{4-D_t}\mu_g L_o^{D_t}}$.

3.3.6.3. Water film effect

The water with normal viscosity occupies the most of capillary channels. Due to influences of the hydrophilicity of the matrix, the high-viscosity water forms a water film on the surface of capillary tubes. For the flow region of normal viscosity water, the governing equation can be obtained based on the Hagen–Poiseuille equation.

$$\mu_w \frac{1}{r}\frac{d}{dr}\left(r\frac{dv_w}{dr}\right) = \frac{\Delta p}{L} \quad r \in \left[r_{wg}, r_{wf}\right]$$

* MERGEFORMAT (3.24)

The governing equation of water film region is

$$\mu_{wf} \frac{1}{r}\frac{d}{dr}\left(r\frac{d\left(v_{wf}+\zeta v_v\right)}{dr}\right) = \frac{\Delta p}{L} \quad r \in \left[r_{wf}, r_0\right]$$

* MERGEFORMAT (3.25)

where μ_w and μ_{wf} are the water viscosity for the typical viscosity water region and water film region, respectively, ζ is the correction factor of the vapor flow rate, and v_v represents the vapor flow rate.

The ratio of these two viscosities is related to the contact angle θ [35]:

$$\frac{\mu_w}{\mu_{wf}} = -0.018\theta + 3.25 \qquad \text{* MERGEFORMAT (3.26)}$$

With the combined effects of temperature, pressure, and gas flow rate, the water film adhering to the surface of the channel will diffuse into the gas under evaporation reaction and be extracted with the gas. The influence of water vapor on the pressure of the gas is small and was thus ignored. However, the evaporation of the water film directly affects the flow rate of the water film. If the effect of water vapor flow rate on the water film flow rate is not considered, the water film flow rate will be overestimated. This vapor flow rate could be calculated as [36]

$$v_v = \frac{\pi M_v D_{va}}{RT} \frac{\Delta p_v}{L} \qquad \text{* MERGEFORMAT (3.27)}$$

where M_v is the molecule mass of vapor, D_{va} is the diffusion coefficient, and Δp_v is the pressure difference of vapor.

The boundary conditions for water flow and water film regions are as follows:

$$\begin{cases} v_w \big|_{r=r_{wf}} = v_{wf} \big|_{r=r_{wf}} \\ v_w \dfrac{\partial v_w}{\partial r}\Big|_{r=r_{wf}} = v_{wf} \dfrac{\partial v_{wf}}{\partial r}\Big|_{r=r_{wf}} \\ v_{wf} \big|_{r=r_0} = 0 \end{cases} \qquad \text{* MERGEFORMAT (3.28)}$$

By substituting Eqs (3.26-3.28) into Eqs (3.24) and (3.25), the final flow velocities are obtained as

$$v_w = \frac{\left(r_{wf}^2 - r^2\right)}{4\mu_w} \frac{\Delta p}{L} + \frac{\left(r_0^2 - r_{wf}{}^2\right)}{4\mu_{wf}} \frac{\Delta p}{L} \quad r \in \left[r_{wg}, r_{wf}\right]$$

* MERGEFORMAT (3.29)

$$v_{wf} = \frac{\left(r_0^2 - r^2\right)}{4\mu_{wf}} \frac{\Delta p}{L} \quad r \in \left[r_{wf}, r_0\right] \qquad \text{* MERGEFORMAT (3.30)}$$

By integrating Eqs (3.29) and (3.30) on the cross-section of the circular tube, the volumetric flow rate of the water is obtained as

$$q_w = \int_{r_{wg}}^{r_{wf}} v_w dA + \int_{r_{wf}}^{r_0} v_{wf} dA$$
$$= \frac{\pi}{8\mu_w}\frac{\Delta p}{L}\left(r_{wf}^2 - r_{wg}^2\right)^2 + \frac{\pi}{4\mu_{wf}}\frac{\Delta p}{L}\left(r_{wf}^2 - r_{wg}^2\right)\left(r_0^2 - r_{wf}^2\right) + \frac{\pi}{8\mu_{wf}}\frac{\Delta p}{L}\left(r_0^2 - r_{wf}^2\right)^2$$

* MERGEFORMAT (3.31)

When only water flows in the capillary tube ($r_{wg} = 0$), the volumetric flow rate of water can be simplified as

$$q_{w-single} = \frac{\pi\Delta p}{8\mu_w L} r_{wf}^4 + \frac{\pi\Delta p}{8\mu_{wf} L}\left(r_0^2 - r_{wf}^2\right)\left(r_0^2 + r_{wf}^2\right)$$

* MERGEFORMAT (3.32)

Similarly, combining with fractal theory obtains the volumetric flow rate of water as

$$Q_w = D_f r_{\max}^{D_f} \int_{r_{\min}}^{r_c} \left[\frac{\pi}{8\mu_w}\frac{\Delta p}{L}\left(r_{wf}^2 - r_{wg}^2\right)^2 + \frac{\pi}{4\mu_{wf}}\frac{\Delta p}{L}\left(r_{wf}^2 - r_{wg}^2\right)\left(r_0^2 - r_{wf}^2\right)\right]$$
$$+ D_f r_{\max}^{D_f} \int_{r_c}^{r_{\max}} \left[\frac{\pi}{8\mu_w}\frac{\Delta p}{L}\left(r_{wf}^2 - r_{wg}^2\right)^2 + \frac{\pi}{4\mu_{wf}}\frac{\Delta p}{L}\left(r_{wf}^2 - r_{wg}^2\right)\left(r_0^2 - r_{wf}^2\right) + \frac{\pi}{8\mu_{wf}}\frac{\Delta p}{L}\left(r_0^2 - r_{wf}^2\right)^2\right]$$
$$= \varepsilon_w \left[\int_{r_{\min}}^{r_{\max}} \left(r_{wf}^2 - r_{wg}^2\right)\left(r^2 - r_{wg}^2\right)\cdot r^{D_t - D_f - 2} dr + \int_{r_c}^{r_{\max}} \left(r^2 - r_{wg}^2\right)^2 \cdot r^{D_t - D_f - 2} dr\right]$$

* MERGEFORMAT (3.33)

where $\varepsilon_w = D_f r_{\max}^{D_f} \dfrac{\pi\Delta p}{2^{4-D_t}\mu_w L_0^{D_t}}$.

3.3.7. Intrinsic permeability

Intrinsic permeability is an inherent property of rock. It is only related to the rock microstructures and is thus independent of fluid type. For two-phase flow, the effective permeability of each phase depends on its saturation and intrinsic permeability. Experimental results have suggested that the effective permeability of the non-wetting phase tends to be higher than the effective permeability of the wetting phase [37]. Relevant literature summarized the following reasons [38]: (1) The rock is rich in swelling clay minerals. When

the effective permeability of the wetting phase is measured, the clay mineral in the matrix absorbs water and swells. This leads to the reduction of the flow channel of fractures; (2) The existence of a water film on the structure surface reduces the effective radius of the flow channel; (3) The high viscosity of the movable water film zone increases the viscous force of normal flowing water. Thus, higher shear stress is required to start the water flow. Fig. 3.8 compares several sets of experimental data on the relationship between water and gas permeability. These experimental data were obtained from Busch and Hildenbrand [37]. These data showed that the gas effective permeability was slightly higher than the water effective permeability. This was related to the complex micropore structure and the flow mechanism of two-phase flow.

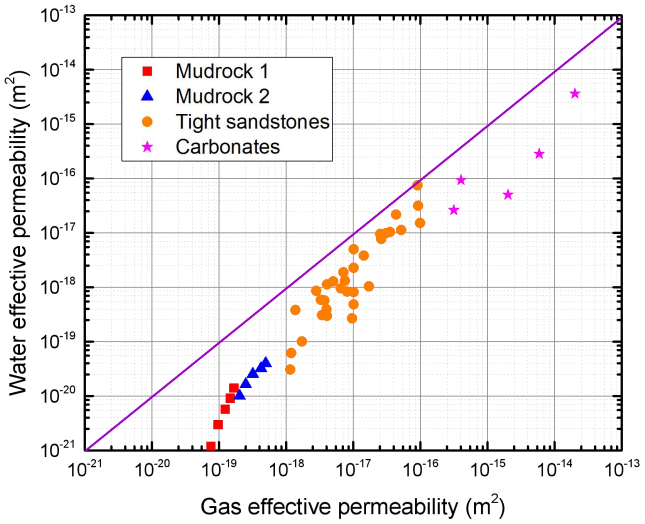

Fig. 3.8. The comparison of gas and water effective permeability in experimental measurements (modified from Busch and Hildenbrand [37])

Two mainstream methods are usually used to calculate the intrinsic permeability of the rock. The first is the Kozeny–Carman equation or its modified form. The intrinsic permeability of rocks, especially with high permeability, is expressed as

$$k = \frac{Br_{mean}^2}{K}\frac{\phi^3}{1-\phi^2} \qquad \text{* MERGEFORMAT (3.34)}$$

where B is a constant, r_{mean} is the average radius of grains. K represents the Kozeny–Carman constant and has

$$K = c_K \tau \qquad \text{* MERGEFORMAT (3.35)}$$

where c_K is the dimensionless Kozeny constant and τ is the tortuosity of rock.

Another method was proposed by Yang and Aplin. This method does not only consider the pore size and porosity but also includes the effect of mineral composition (clay content) in the intrinsic permeability:

$$k = 2.2446 \times 10^{-17} J_v^{1.18} r_{mean}^{1.074} \qquad \text{* MERGEFORMAT (3.36)}$$

where

$$\begin{aligned} J_v &= \frac{9}{8}\phi(\sin o)^2 \frac{J_1^3}{\left(1+J_1+J_1^2\right)^2} \\ J_1 &= 2.371 - 1.626\chi^2 + 153.8\phi^4 \\ o &= 45^\circ - 10.24^\circ\left(e_{100} - e\right) \\ e_{100} &= 0.3024 + 1.687\chi + 1.951\chi^2 \\ e &= \phi/(1-\phi) \end{aligned} \qquad \text{* MERGEFORMAT (3.37)}$$

e is the volume ratio of pores to the matrix and e_{100} is the volume ratio of pores to the matrix at the effective stress of 0.1 MPa, χ is the clay mineral content, and o represents the angle between the average pore alignment angle and bedding direction.

3.3.8. Gas-water relative permeability model

The water flow velocity is expressed in Darcy's law:

$$Q_w = \frac{k_w \phi}{\mu_w S_w}\frac{\Delta p}{L} \qquad \text{* MERGEFORMAT (3.38)}$$

By substituting Eq. (3.33) into Eq. (3.38), the effective permeability of water is obtained as

$$k_w = -\frac{\mu_w S_w L_0 \varepsilon_w}{A\Delta p}\left[\int_{r_{\min}}^{r_{\max}}\left(r_{wf}^2 - r_{wg}^2\right)\left(r^2 - r_{wg}^2\right)\cdot r^{D_t - D_f - 2}dr + \int_{r_c}^{r_{\max}}\left(r^2 - r_{wg}^2\right)^2 \cdot r^{D_t - D_f - 2}dr\right]$$

* MERGEFORMAT (3.39)

Similarly, the effective permeability of gas is

$$k_g = -\frac{\mu_g\left(1 - S_w\right)L_0}{A\Delta p}\varepsilon_g \int_{r_c}^{r_{\max}} r_{wg}^4 \cdot r^{D_t - D_f - 2}(1 + 4K_n^*)dr$$

* MERGEFORMAT (3.40)

Thus, the relative permeability for water is

$$k_{rw} = \frac{-\frac{\mu_w S_w L_0 \varepsilon_w}{A\Delta p}\left[\int_{r_{\min}}^{r_{\max}}\left(r_{wf}^2 - r_{wg}^2\right)\left(r^2 - r_{wg}^2\right)\cdot r^{D_t - D_f - 2}dr + \int_{r_c}^{r_{\max}}\left(r^2 - r_{wg}^2\right)^2 \cdot r^{D_t - D_f - 2}dr\right]}{k}$$

* MERGEFORMAT (3.41)

and the relative permeability for gas is

$$k_{rg} = \frac{-\frac{\mu_g\left(1 - S_w\right)L_0}{A\Delta p}\varepsilon_g \int_{r_c}^{r_{\max}} r_{wg}^4 \cdot r^{D_t - D_f - 2}(1 + 4K_n^*)dr}{k}$$

* MERGEFORMAT (3.42)

In this study, our intrinsic permeability was calculated by Yang and Aplin's method. The clay content was 0.1 and the porosity of rock was 0.2.

3.4. Model Validation

Our improved fractal relative permeability model for gas and water is compared with the classic Brooks–Corey model and viscous coupling model and further verified against experimental data. The parameters used in this validation are listed in Table 3.1.

Table 3.1. Parameters for model validation

Parameters	Unit	Value	Physical Meanings
$r_{\min}$	m	10^{-9}	Maximum pore radius
$r_{\max}$	m	10^{-7}	Minimum pore radius
R	J/(mol•K)	8.314	Universal gas constant
M	Kg/mol	0.016	Methane molecular weight
T	K	298.15	Temperature

μ_{wf}	Pa•s	2.6811×10^{-3}	Water film viscosity
μ_w	Pa•s	8.937×10^{-4}	Water viscosity
γ		1	Geometric correction factor
p_g	MPa	1	Gas pressure
ϕ		0.2	Porosity
A_1		0.007698	Tuned coefficient
A_2		0.003839	Tuned coefficient
A_3		−0.467212	Tuned coefficient
A_4		1.018801	Tuned coefficient
A_5		3.805723	Tuned coefficient
A_6		−0.087361	Tuned coefficient
A_7		7.138305	Tuned coefficient
A_8		0.08344	Tuned coefficient
A_{11}		7.9	Temperature tuned coefficient
A_{12}		9×10^{-6}	Pressure tuned coefficient
A_{13}		0.28	Molar weight tuned coefficient

The comparison of our fractal model with the classic Brooks–Corey model and the viscous coupling model is presented in Fig. 3.9. The residual water saturation of the Brooks–Corey model was 0.2, and the pore-size distribution index was infinite.

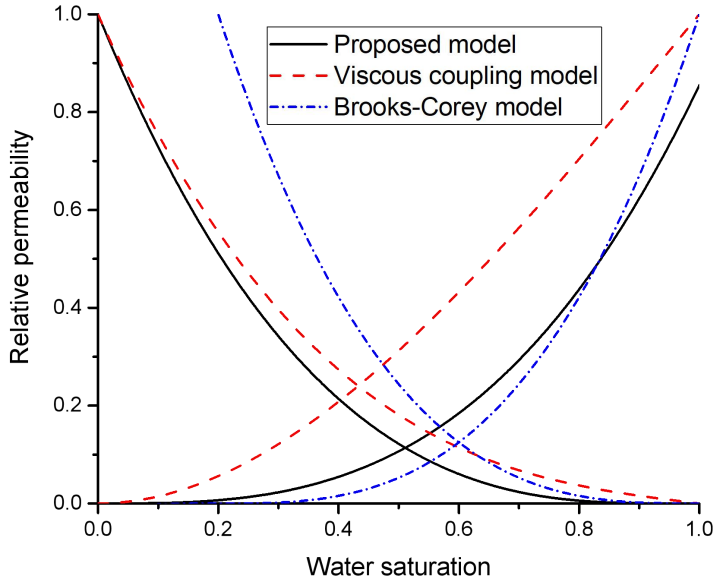

Fig. 3.9. Comparison with classical relative permeability models

The viscous coupling model takes the viscosity ratio of the gas and water phase into account. When the viscosity difference between the gas and liquid phase is significant, the viscous coupling model is similar to the Brooks–Corey model. Our fractal model has similar trends to the two classic models. However, our fractal model has some features that the classic models missed: (1) The pore-size distribution index in the classical model is constant and difficult to measure. However, the pore-size distribution fractal dimension and tortuosity fractal dimension is calculated by the capillary pore distribution and pore size. Through fractal dimensions, complex porous media is better expressed; and (2) The real gas effect and water film flow are not considered in the classical models. These factors are particularly important in high-temperature, pressure, and humidity formations. Further, our fractal model is compared with experimental data, and the results are presented in Fig. 3.10. These experimental data were measured by Mahiya [39] for the relative permeability of water and vapor at 120 °C. The permeability and porosity of Berea core samples used in this experiment were 1200 md and 0.24. Subsequently, the relative permeability of nitrogen and water were measured by Li and Horne [40]. Diomampo et al. [41] conducted drainage experiments for the rough-walled fractures, and relative permeability data of nitrogen and water were obtained. In their experiments, the fracture was initially saturated with water, and the non-wetting phase was injected with a constant flow rate. Wang et al. [42] measured the relative permeability of oil and water in carbonate core samples. The permeability and porosity of this sample were 33.9 md and 0.18. Our fractal relative permeability model is in good agreement with these experimental data. This indicates that this improved fractal model can describe the evolution of gas-water relative permeability in complex porous media.

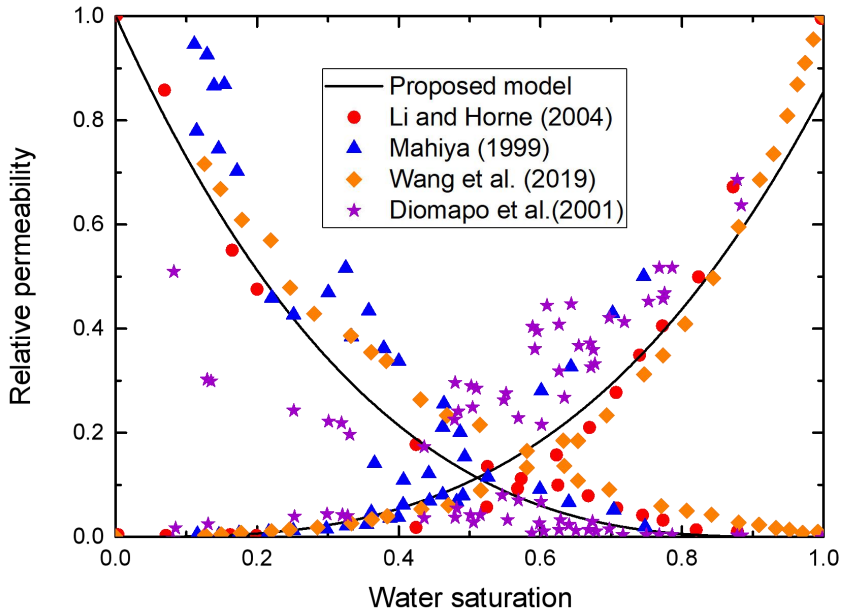

Fig. 3.10. Comparison with several experimental data

3.5. Discussions

3.5.1. Effects of pore-size distribution and tortuosity fractal dimension

The structural parameters, pore-size distribution (PSD) fractal dimension, and tortuosity fractal dimension are used to describe the structural complexity of porous media. Porous media have multiscale capillary structures from micron to nanoscale. The distribution and heterogeneity of the pore structure are described by the PSD fractal dimension. Fig. 3.11 shows that the effective permeability of gas and water decreased significantly as the PSD fractal dimension increased from 1.2 to 1.8. When the tortuosity fractal dimension was constant at 1.48, the increase of the PSD fractal dimension increased the complexity of the pore-size distribution and resulted in a decrease of effective permeability for both gas and water.

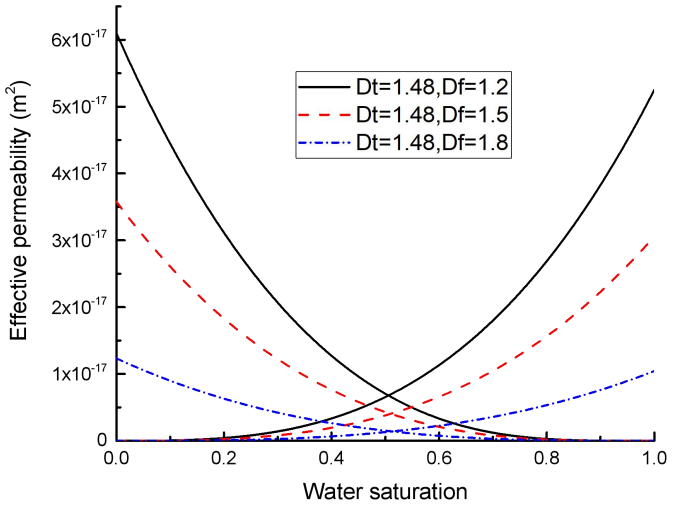

Fig. 3.11. Distribution of water-gas effective permeability under different pore-size distribution (PSD) fractal dimensions

The tortuosity fractal dimension was first introduced into this improved fractal model to reflect the variation of capillary tortuosity with pore size. Fig. 3.12 provides the variation of effective permeability of gas and water with the increase of PSD fractal dimension. This trend was similar to the variation of the PSD fractal dimension, but the degree of decline was not significant. This indicated that the influence of the PSD fractal dimension on both gas and water permeability was greater than the tortuosity fractal dimension.

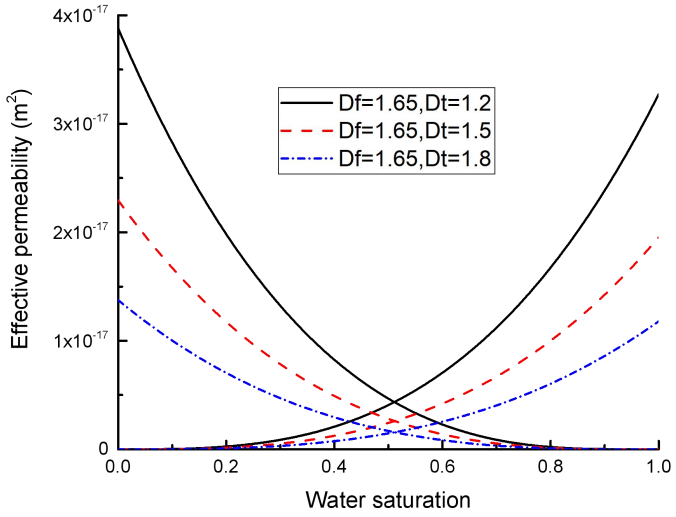

Fig. 3.12. Distribution of water-gas effective permeability under different tortuosity fractal dimensions

3.5.2. Effect of nanotube size

The size of nanotubes is directly related to the gas-water effective permeability. When the maximum radius of the nanotubes was changed from 100 nm to 50 nm, the gas-water effective permeability significantly declined, as shown in Fig. 3.13. Because the capillary tube radius was still very large relative to the size of critical capillary tube radius and water film thickness, residual water could not block the capillary tube and single-phase flow did not occur. The effective permeability of the gas and water decreased at almost the same speed.

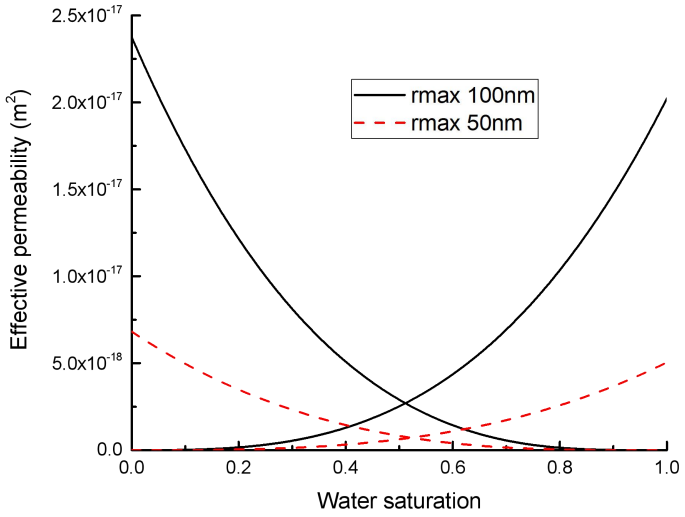

Fig. 3.13. Variation of water-gas effective permeability with nanotube size

3.5.3. Effect of water film thickness

Our fractal model has some parameters in the gas or water effective permeability. For example, the water film adhered to the surface of the capillary tube is an important parameter that affects the effective permeability of water. The viscosity of the water film is greater than that of water in the normal flowing zone. An increase in the water film thickness directly reduces the water flow flux. Moreover, the water film produces a drag force on the normally flowing water. This reduces the flow rate of the wetting phase. Some studies considered the water film as the non-flowable film, which absorbed on the surface of the matrix to form residual water in the porous medium. This assumption exaggerated the effect of water film on the relative permeability of the wetting phase. Eqs (3.29) and (3.30) provided the expressions of water flow rate and water film flow rate, respectively. If a capillary radius was 100 nm, water saturation was 0.5, and a pressure difference was 1 MPa, the effect of water film thickness on the water and water film flow rates are presented in Fig. 3.14, where the evolution of water flow rate is plotted under different water film thicknesses. When the water

film thickness increased from 0.7 nm to 7 nm, a significant decrease in water flow rate was observed. In addition, a slight decrease of the normal water flow zone was observed due to the increase of water film thickness.

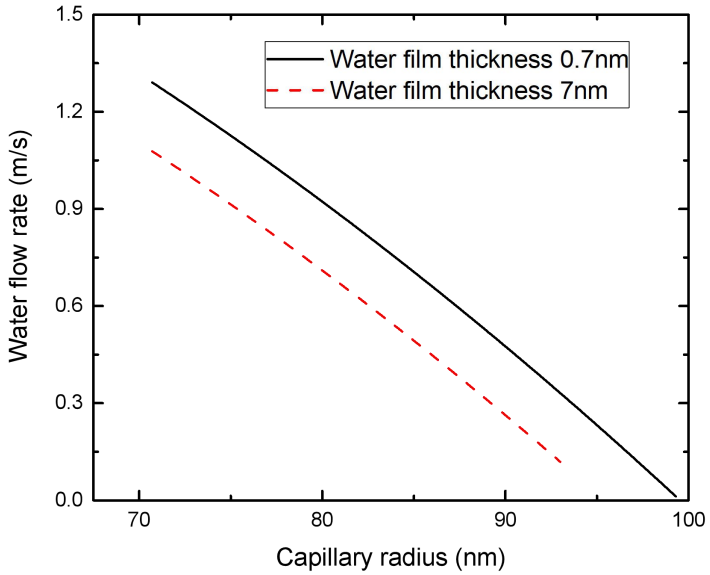

Fig. 3.14. Evolution of water flow rate under different water film thickness

Fig. 3.15 shows the effect of water film thickness on the water film flow rate. It is worth noting that the flow rate of the water film is not affected by the change in water film thickness. There are two reasons: (1) The thickness of the water film is much smaller than the radius of the capillary tube; and (2) The water film is a high-viscosity water flow zone, which mainly causes dragging force on the normally flowing water. However, the increase of the water film thickness significantly increases the zone where the water film flows, and the flow flux of the water film obtained by this integration increases correspondingly. Finally, Fig. 3.16 is the evolution of gas-water effective permeability with different water film thickness. The increase of water film thickness has little influence on the effective permeability of gas, but has a negative influence on the effective permeability of the wetting phase.

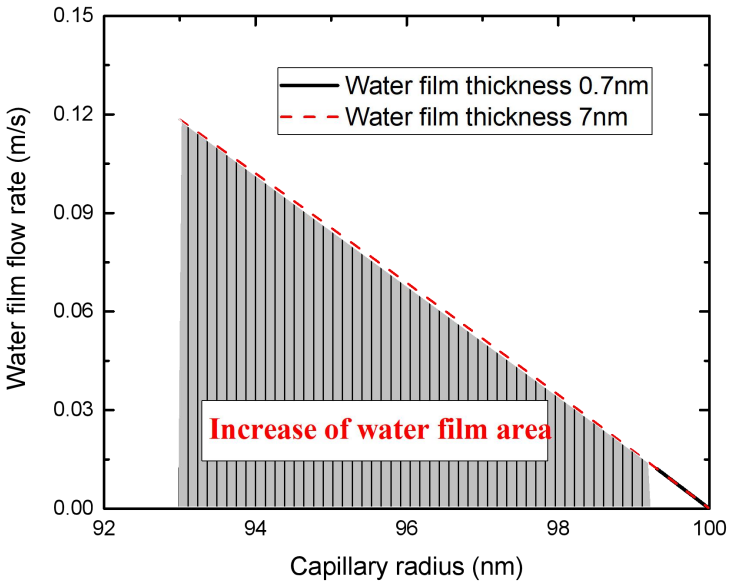

Fig. 3.15. Evolution of water film flow rate under different water film thickness

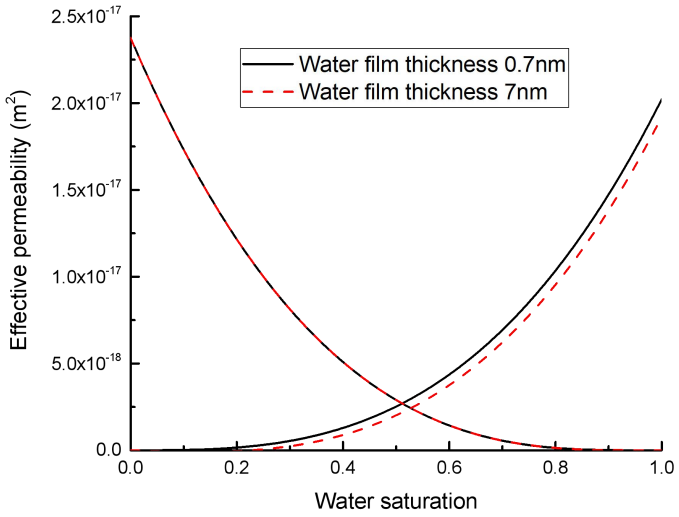

Fig. 3.16. Effect of water film thickness on water-gas effective permeability

3.5.4. Effect of the geometric correction factor

The pores in porous media have various shapes. In this chapter, the relative permeability was derived based on the circular tube, and the geometric correction factor was introduced to

redefine the Knudsen number (see Eq. (3.18)). The Knudsen number reflects the motion state of gas molecules. Therefore, the change of the Knudsen number directly affects the gas flow rate, resulting in a change of the gas effective permeability. Fig. 3.17 provides the variation of Knudsen number with a geometric correction factor. It states that the shape irregularity of pores reduced the Knudsen number. As the capillary radius increases, this effect gradually decreases. When the flow channel is large enough, the free path of gas molecules is much smaller than the characteristic length, and the shape irregularity of the pores is no longer significant.

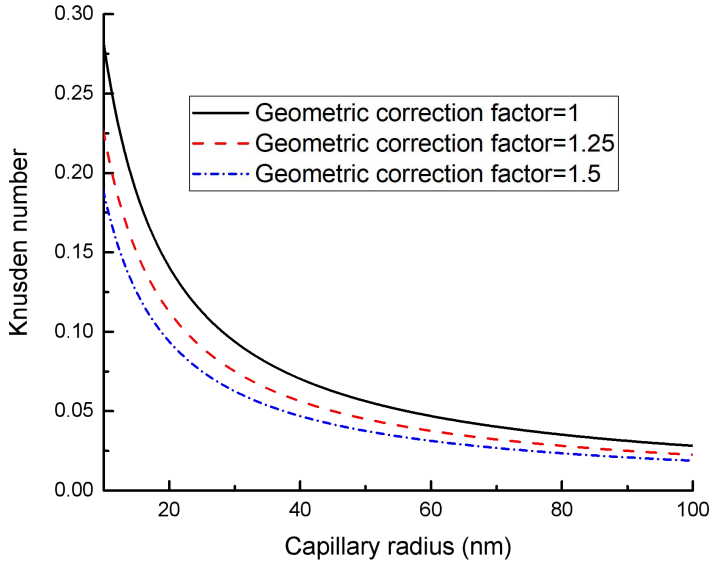

Fig. 3.17. Effect of geometric correction factor on Knudsen number

Fig. 3.18 shows the variation of gas-water effective permeability with the increase of geometric correction factor. The increase of the geometric correction factor directly reflects the increase of capillary irregularity. Therefore, the effective gas permeability decreases when the geometric correction factor increases. The effective permeability of the wetting phase is not affected by the shape correction factor. Furthermore, the effect of the geometric correction factor is less than the effect of structural parameters (PSD fractal dimension and

tortuosity fractal dimension). This is why the capillary is generally assumed to be a circular tube in many numerical simulations, regardless of its shape variation.

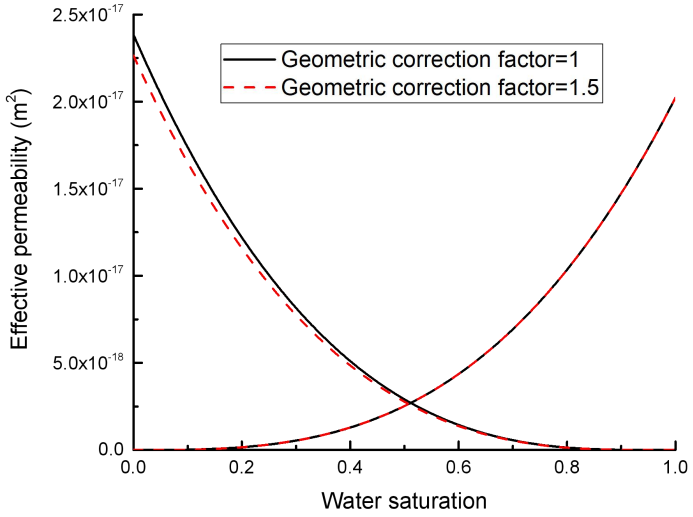

Fig. 3.18. Effect of geometric correction factor on water-gas effective permeability

3.5.5. Real gas effect

The real gas effect refers to the variation of gas compressibility and viscosity relative to an ideal gas. Both temperature and pressure affect the real gas effect and ultimately lead to a change of gas flow. Fig. 3.19 presents the importance of real gas effect on the effective permeability of water and gas. The effective permeability of gas is slightly higher after considering the real gas effect. Although the viscosity of the gas increases, the gas is more compressible when the real gas effect is considered. In addition, the increase of the Knudsen number means an enhancement of gas slip effect, which is beneficial to the effective gas permeability. These indicate that the real gas effect cannot be ignored in the evolution of gas effective permeability. This effect becomes more significant in high-pressure and temperature conditions.

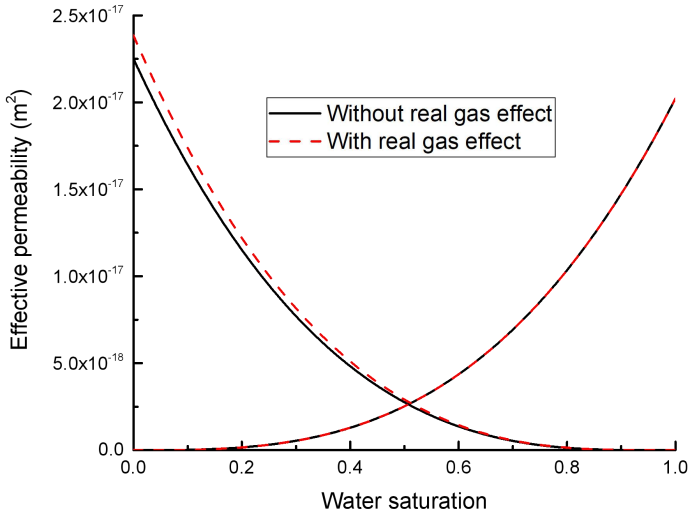

Fig. 3.19. Effect of real gas effect on water-gas effective permeability

3.6. Conclusions

In this chapter, an improved fractal model was developed for the gas-water relative permeability in porous media to incorporate the structural parameters (PSD fractal dimension and tortuosity fractal dimension), water film, geometric correction factor, and real gas effect. First, the threshold pressure gradient was introduced to describe the gas starting flow against viscous forces in two-phase flow. This threshold pressure gradient was expressed by some macroscopic parameters, such as water saturation, pore pressure, and permeability. Their linkage with complex pore structures (critical capillary radius) was explored through a microscopic theoretical model. Then, the gas-water relative permeability model was derived based on the circular cross-section flow channels and complex fractal pore structures. The improved fractal model was compared with two classical models and verified against available experimental data. Finally, the sensitivities of structural parameters, water film,

geometric correction factor, and real gas effect to gas-water effective permeability were investigated. Based on these investigations, the following conclusions can be drawn:

Pore-size distribution fractal dimension and tortuosity fractal dimension well-described the complexity of pore-size distribution and tortuosity distribution of porous media, respectively. Their higher dimensions caused a decrease of the water-gas effective permeability. It was found that the pore-size distribution determined the flow pattern: Single-phase flow or two-phase flow and the pore-size distribution fractal dimension had a more significant influence on gas-water effective permeability.

The water film thickness had a negative effect on the water effective permeability. It increased the water film zone and loses the space for normal water flows, thus causing a reduction in the water flow rate. Moreover, the high-viscosity water film also applied a viscous force to normal water, reducing its flow rate. If the water film thickness was much smaller than the pore size, the effect of water film thickness on the gas effective permeability was negligible.

The pore geometry directly affected the mechanism of gas flow. When the irregularity of the pore geometry increased, the Knudsen number decreased. The collision between gas molecules was intensified and the gas flow transitioned to the continuous medium flow. The geometric correction factor well-described the gas effective permeability for any shape of pores.

The gas effective permeability was slightly higher if the real gas effect was considered. Notably, this real gas effect on the gas effective permeability became obvious at high-temperature and pressure conditions and is thus not ignorable.

3.7. References

[1] Purcell W. Capillary pressures—their measurement using mercury and the calculation of permeability therefrom. Journal of Petroleum Technology. 1949, 1, 39-48.

[2] Gates J, Lietz W. Relative permeabilities of California cores by the capillary pressure method. In Drilling and Production Practice, 1950, API-50-285.

[3] Burdine N. Relative permeability calculations from pore-size distribution data. Journal of Petransam. Technology. 1953, 5: 71-79.

[4] Mualem, Y. A new model for predicting the hydraulic conductivity of unsaturated porous media. Water Resources Research. 1976, 12, 513-522.

[5] Romm, E. Fluid Flow in Fractured Rocks. Nedra Publishing House: Moscow, Russia, 1966, (In Russian).

[6] Brooks R, Corey A. Properties of porous media affecting fluid flow. Journal of the Irrigation and Drainage Division. 1966, 92: 61-90.

[7] Fourar M, Lenormand R. A viscous coupling model for relative permeabilities in fractures. In SPE Annual Technical Conference and Exhibition, 1998, SPE-49006-MS.

[8] Chima A, Geiger S. An analytical equation to predict gas/water relative permeability curves in fractures. In SPE Latin America and Caribbean Petroleum Engineering Conference, 2012, SPE-152252-MS.

[9] Li Y, Li X, Teng S, Xu D. Improved models to predict gas–water relative permeability in fractures and porous media. Journal of Natural Gas Science and Engineering, 2014, 19: 190-201.

[10] Mandelbrot B. The Fractal Geometry of Nature. American Journal of Physics, 1982, 51: 286–287.

[11] Lei G, Dong P, Wu Z, Gai S, Mo S, Li Z. Multi-scale structures of porous media and the flow prediction. Journal of Natural Gas Science and Engineering, 2014, 21: 986–992.

[12] Geng L, Li G, Zitha P, Tian S, Sheng M. A fractal permeability model for shale gas flow through heterogeneous matrix systems. Journal of Natural Gas Science and Engineering, 2016, 35: 593-604.

[13] Hu B, Wang J, Wu D, Wang H. Impacts of zone fractal properties on shale gas productivity of a multiple fractured horizontal well. Fractals, 2019, 27: 1950006.

[14] Xu P, Qiu S, Yu B, Jiang Z. Prediction of relative permeability in unsaturated porous media with a fractal approach. International Journal of Heat and Mass Transfer, 2013, 64: 829-837.

[15] Ghanbarian B, Ioannidis M, Hunt A. Theoretical insight into the empirical tortuosity-connectivity factor in the Burdine-Brooks-Corey water relative permeability model. Water Resources Research, 2017, 53: 10395-10410.

[16] Chen L, Li D, Ming F, Shi X, Chen X. A fractal model of hydraulic conductivity for saturated frozen soil. Water, 2019, 11: 369.

[17] Li X, Yi L, Yang Z, Chen Y. A new model for gas–water two-immiscible-phase transport in fractal-like porous media. Journal of Applied Physics, 2015, 118: 224306.

[18] Mo S, He S, Lei G, Gai S, Liu Z. Effect of the drawdown pressure on the relative permeability in tight gas: a theoretical and experimental study. Journal of Natural Gas Science and Engineering, 2015, 24: 264-271.

[19] Huo D, Benson S. Experimental investigation of stress-dependency of relative permeability in rock fractures. Transport in Porous Media, 2016, 113, 567–590.

[20] Lei G, Dong P, Mo S, Gai S, Wu Z. A novel fractal model for two-phase relative permeability in porous media. Fractals, 2015, 23: 1550017.
[21] Wu W, Zoback M, Kohli A. The impacts of effective stress and CO_2, sorption on the matrix permeability of shale reservoir rocks. Fuel, 2017, 203: 179-186.
[22] Cai J, Lin D, Singh H, Zhou S, Meng Q, Zhang Q. A simple permeability model for shale gas and key insights on relative importance of various transport mechanisms. Fuel, 2019, 252: 210-219.
[23] Wang J, Song H, Rasouli V, Kilough J. An integrated approach for gas-water relative permeability determination in nanoscale porous media. Journal of Petroleum Science and Engineering, 2019, 173: 237–245.
[24] Ding J, Yang S, Nie X, Wang Z. Dynamic threshold pressure gradient in tight gas reservoir. Journal of Natural Gas Science and Engineering, 2014, 20: 155-160.
[25] Yu B, Li J. Some fractal characters of porous media. Fractals, 2001, 9: 365-372.
[26] Mortensen N, Okkels F, Bruus H. Reexamination of Hagen-Poiseuille flow: shape dependence of the hydraulic resistance in microchannels. Physical Review E, 2005, 71: 057301.
[27] Ambrose R, Hartman R, Campos M, Akkutlu I, Sondergeld C. New Pore-Scale Consideration for Shale Gas in Place Calculations. Society of Petroleum Engineers: Pittsburgh, USA, 2010, SPE-131772-MS.
[28] Tang X, Jiang Z, Li Z, Gao Z, Bai Y, Zhao S, Feng J. The effect of the variation in material composition on the heterogeneous pore structure of high-maturity shale of the Silurian Longmaxi formation in the southeastern Sichuan Basin, China. Journal of Natural Gas Science and Engineering, 2015, 23: 464–473.
[29] Loyalka S, Hamoodi S. Poiseuille flow of a rarefied gas in a cylindrical tube: solution of linearized Boltzmann equation. Physics of Fluids A: Fluid Dynamics, 1990, 2: 2061–2065.
[30] Cai J, Perfect E, Cheng C, Hu X. Generalized modeling of spontaneous imbibition based on hagen-poiseuille flow in tortuous capillaries with variably shaped apertures. Langmuir, 2014, 30(18): 5142-5151.
[31] Ren W, Li G, Tian S, Sheng M, Fan X. An analytical model for real gas flow in shale nanopores with non-circular crosssection. Aiche Journal, 2016, 62(8): 2893-2901.
[32] Sanjari E, Lay E N. An accurate empirical correlation for predicting natural gas compressibility factors. Journal of Natural Gas Chemistry, 2012, 21(2): 184-188.
[33] Jarrahian A, Heidaryan E. A simple correlation to estimate natural gas viscosity. Journal of Natural Gas Science and Engineering, 2014, 20: 50-57.
[34] Beskok A, Karniadakis G. Report: a model for flows in channels, pipes, and ducts at micro and nano scales. Microscale Thermophysical Engineering, 1999, 3(1): 43-77
[35] Wu K, Chen Z, Li J, LI X, Xu J, Dong X. Wettability effect on nanoconfined water flow. Proceedings of the National Academy of Sciences, 2017, 114(13): 3358-3363.
[36] Moghaddam A, Prat M, Tsotsas E, Kharaghani A. Evaporation in capillary porous media at the perfect piston-like invasion limit: evidence of nonlocal equilibrium effects. Water Resources Research, 2017, 53(12): 10433-10449
[37] Busch A, Hildenbrand A. Predicting capillarity of mudrocks. Marine and Petroleum Geology, 2013, 45(4): 208-223.
[38] Wang C, Elsworth D, Fang Y. Influence of weakening minerals on ensemble strength and slip stability of faults. Journal of Geophysical Research: Solid Earth, 2017, 122: 7090-7110.

[39] Mahiya G. Experimental measurement of steam-water relative permeability. Stanford University, 1999.
[40] Li K, Horne R. Experimental study of gas slippage in two-phase flow. Society of Petroleum Engineers, 2004, 7(6): 409-415.
[41] Diomampo G. Relative permeability through fractures. In Proceedings of the 27th Workshop on Geothermal Reservoir Engineering, 2001, DOI: 896520-MS.
[42] Wang F, Jiao L, Lian P, Zeng J. Apparent gas permeability, intrinsic permeability and liquid permeability of fractal porous media: carbonate rock study with experiments and mathematical modelling. Journal of Petroleum Science and Engineering, 2019, 173: 1304-1315.

Chapter 4: A two-phase flowback model for multi-scale diffusion and flow in fractured shale gas reservoirs

4.1. Introduction

In shale gas reservoirs, the gas-enriched porous medium is tight rock. Its reservoir contains complex pore structures, ranging from micro-scale fractures to nano-scale pores. In Chapter 2, the pore-structure complexity of shale matrix is explored through sorption testing and fractal analysis. The complexity of the pore structure is a critical factor that determines the mechanism of gas multi-scale flow and diffusion. After the artificial stimulation measures of hydraulic fracturing are carried out, fracturing fluid flows in the channels in the range from macro-scale to meso-scale or even micro-scale. The difficulty for this research is that the fluid flow process in these three scale channels has not only free flow but also slow diffusion. It is a flow-diffusion coupling process. However, the current theory based on traditional fluid mechanics is not completely applicable. Due to the multi-scale and heterogeneity of the matrix, it is required to study the coupling process of free flow and diffusion and to explore the flow consistency at different scales in fractured shale gas reservoirs. Therefore, this chapter establishes a three-zone multi-scale flow-diffusion model based on two-phase flow, viscous flow, Knudsen diffusion, molecular diffusion, and surface diffusion. The nonlinear diffusion characteristics of the shale matrix are revealed.

4.2. A conceptual model

In order to enhance the permeability of the shale matrix, a big amount of water-based fracturing fluid is injected through the horizontal well, forming a fractured zone (called

stimulated reservoir volume or SRV). The water is retained in the fractures and increases the water saturation. With gas production, 10-40% of the water is recovered along with the hydraulic fractures [1]. In this period, the capillary pressure is directly linked with the process of two-phase flowback, which is necessary to be discussed. Hydraulic fractures are the main channels for the flow from the fractured zone to the well, whose properties are important to gas production. In the fractured zone, macro-scale water-gas two-phase flow in the fractures and micro-scale diffusion in the shale matrix occur simultaneously. With the process of flowback or continuous gas extraction, the gas pressure in the matrix began to decline and gas desorbs from the surface of the matrix. This free gas diffuses from the matrix to the fractured zone and further flows into the wellbore along with the hydraulic fractures. Therefore, the flow consistency in the matrix, fractured zone and hydraulic fractures should be the focus.

Based on different flow regimes, a given computational domain is roughly divided into three zones as shown in Fig. 4.1: shale matrix or naturally fractured zone (zone 1), (artificially and naturally) fractured zone (zone 2) and hydraulic fractures (zone 3). In zone 1, the shale matrix is usually regarded as a single-porosity model in the traditional models. However, experimental measurements (such as SEM and CT) observed a mass of micro-pores even micro-fractures in the shale [2]. The gas diffusion and flow in the micro-fractures of the shale matrix are considerably complicated [3, 4]. Thus, the traditional models neglecting the micro-diffusion in the matrix block are not applicable. In this study, a dual-porosity model is proposed to describe the gas diffusion and flow mechanisms in zone 1. A new apparent permeability model for the matrix is introduced into the dual-porosity model to consider three important physical processes: viscous flow, free molecular diffusion and surface diffusion. In zone 2, the fractured zone is also defined as a dual-porosity model, but they have different properties. The two-phase flow is considered in the fracture and relative

permeability varies with water saturation. The micro-fractures in this zone are different from those in zone 1, which are also induced by water fracturing. It is noted that the effective connectivity of different kinds of micro-fractures (in zones 1 and 2) is not described in this paper. In zone 3, the two-phase flow is still considered along with the hydraulic fractures. The capillary pressure and relative permeability models are the same as the fractured zone.

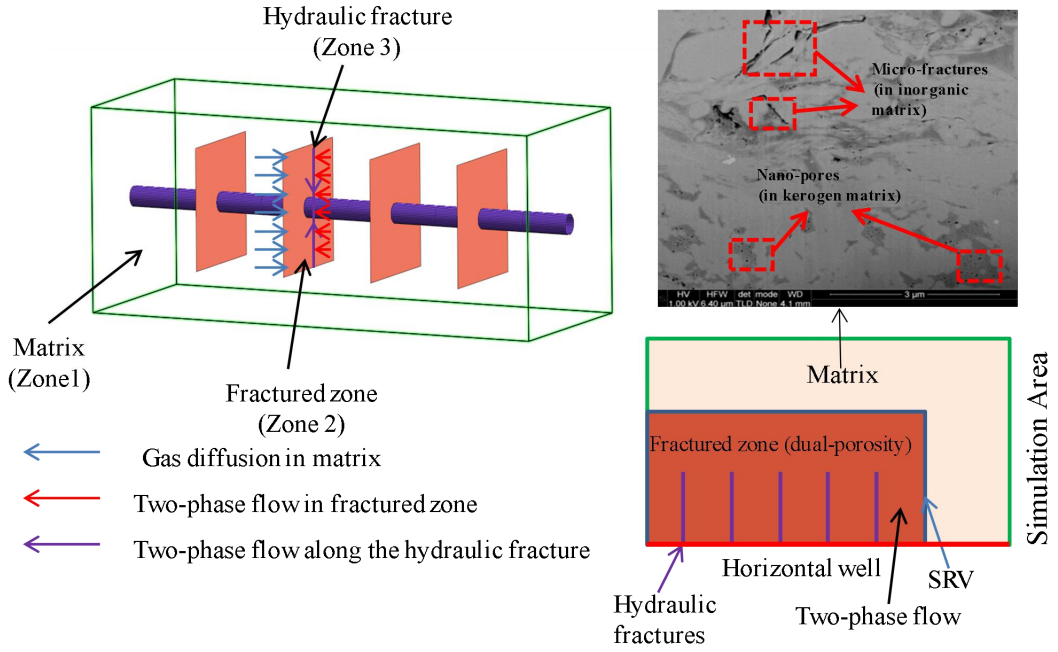

Fig. 4.1. Snapshot of shale gas recovery in typical three zones (SEM from Ambrose et al., 2010)

Overall, a series of interactions are included in the shale gas production within the reservoir. The three zones interact with each other and have a consistency impact of flow and pressure on short-term and long-term shale gas productions. In the following section, we will formulate this conceptual model by a set of governing equations in the three zones.

4.3. Governing equations for gas and water flows in multi-scale porous media

The three zones model is shown in Fig. 4.1. The flows in each zone have different diffusion and flow mechanisms. Fig. 4.2 presents the details of the diffusion and flow in each zone. Their governing equations are stated below.

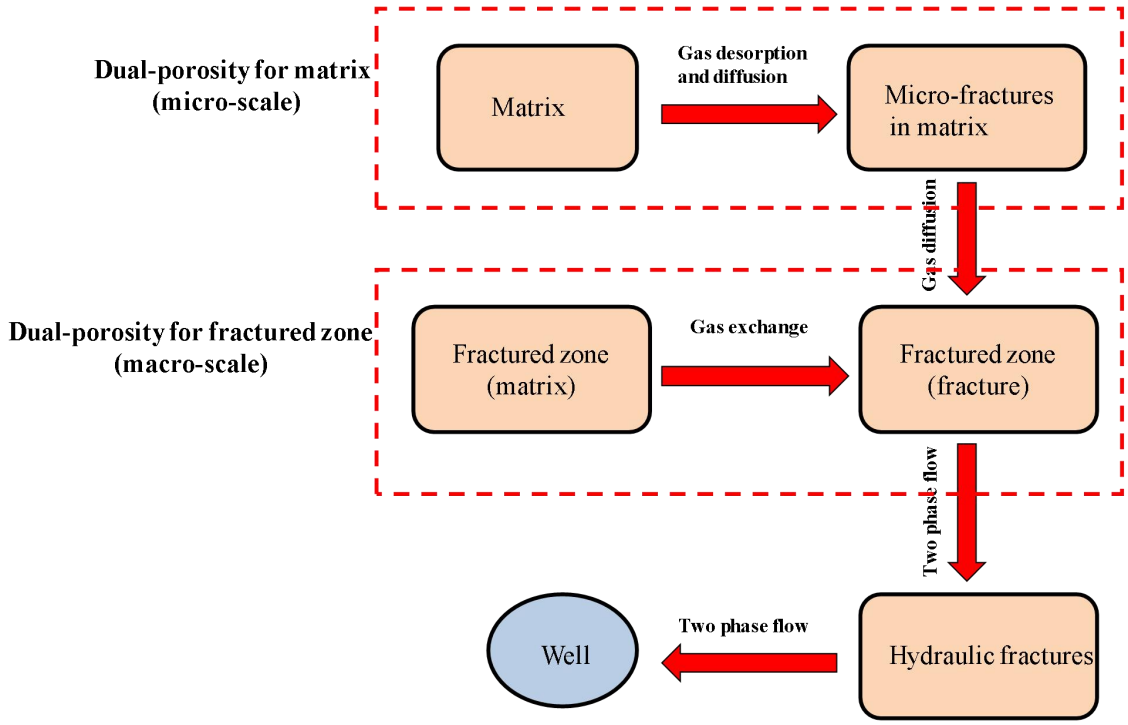

Fig. 4.2. Flow and diffusion processes in multi-scale zones

4.3.1. Shale gas flow in the micro-fractures of the matrix (zone 1)

The mass conservation law for the gas flow in the micro-fractures of the matrix (zone 1) is governed by

$$\frac{\partial(\rho_{gf}\phi_f)}{\partial t} - \nabla\cdot(\frac{k_{mapp}}{\mu_{nw}}\rho_{gf}\nabla p_f) = Q_{mf} \quad \text{* MERGEFORMAT (4.1)}$$

where ρ_{gf} is the gas density in the micro-fractures, ϕ_f is the porosity of micro-fractures. It is noted that only free gas is taken into consideration in micro-fractures of this matrix (zone

1). μ_{nw} and p_f represent the gas viscosity and pressure, respectively. k_{mapp} is the apparent permeability for micro-fractures in the matrix (zone 1). This apparent permeability is directly expressed as [5]

$$k_{mapp} = \frac{\phi_f d_f^{\,2}}{32\tau_h}\left(1+\frac{b}{p_f}\right) \qquad \text{* MERGEFORMAT (4.2)}$$

where d_f is the aperture of micro-fractures in this zone and can be measured by many experiments such as SEM, AFM and CT tests. τ_h reflects the degree of tortuosity in a porous medium. b is a Klinkenberg factor determined by the pore structure of the matrix and the reservoir temperature.

$$b = \frac{64\mu_{nw}}{3\pi d_f M}\sqrt{2\pi MRT} \qquad \text{* MERGEFORMAT (4.3)}$$

where M is the gas molecular weight. R represents the universal gas constant. T is the reservoir temperature. The right-hand term of Eq. (4.1), the Q_{mf} , is the source of gas. It expresses the gas exchange between micro-pores and micro-fractures in the matrix.

$$Q_{mf} = \frac{\rho_{gm} k_k a}{\mu_{nw}}(p_m - p_f) \qquad \text{* MERGEFORMAT (4.4)}$$

where p_m is the gas pressure in the matrix. k_k is the apparent permeability of the matrix which will be described in the next section. ρ_{gm} is the gas density in the shale matrix. *a* is a shape factor of matrix block. For the isotropic matrix, the shape factor is [6]

$$a = \pi^2\left(\frac{1}{L_x^2}+\frac{1}{L_y^2}\right) \qquad \text{* MERGEFORMAT (4.5)}$$

where L_x and L_y are the fracture spacing in the *x*-direction and the *y*-direction, respectively.

4.3.2. Gas diffusion in shale matrix

In molecular dynamics of gas, the probability of gas collisions or diffusion is directly related to an important index, the molecular mean free path. This free path is the mean path for a molecular free motion in an interval of two consecutive collisions [7]:

$$\lambda = \frac{\mu_{nw}}{p_m}\sqrt{\frac{\pi RT}{2M}} \qquad \text{* MERGEFORMAT (4.6)}$$

The gas molecular flow usually obeys different mechanisms, depending on the scale of the flow channel. Knudsen number is defined as the ratio of the mean free path of gas flow to the characteristic size of the gas flow channel:

$$K_n = \frac{\lambda}{d_f} \qquad \text{* MERGEFORMAT (4.7)}$$

4.3.4. Diffusion in the matrix

The mass conservation law for the gas diffusion in the matrix can be given as

$$\frac{\partial(m_m)}{\partial t} - \nabla\cdot(\frac{k_k}{\mu_{nw}}\rho_{gk}\nabla p_k) = -Q_{mf} \qquad \text{* MERGEFORMAT (4.8)}$$

$$m_m = \rho_{gk}\phi_m + \rho_{ga}\rho_s\frac{V_L p_m}{p_m + V_L} \qquad \text{* MERGEFORMAT (4.9)}$$

The gas mass (m_m) in the matrix consists of both free phase and absorbed phase gases. ρ_{gk} is the gas density in the matrix. $-Q_{mf}$ means the gas exchange between the matrix and micro-fractures of the matrix. k_k is the permeability of matrix which is obtained by

$$k_k = \frac{D\mu_{nw}}{p_m} \qquad \text{* MERGEFORMAT (4.10)}$$

where D is the effective diffusion coefficient of the matrix and has three components:

$$D = D_c + D_e + D_{es} \qquad \text{* MERGEFORMAT (4.11)}$$

The diffusion coefficients D_c, D_e, D_{es} are determined as follows.

For a given temperature, the gas mass in matrix transports mainly in three forms: 1. viscous flow; 2. molecular and Knudsen diffusion; 3. surface diffusion in the absorbing layer.

The viscous flow induced diffusion coefficient is [4]:

$$D_{\mathrm{c}} = \frac{\phi_m}{\tau_h}(1+8K_n)\frac{{d_m}^2 p_m}{32\mu_{nw}} \qquad \text{* MERGEFORMAT (4.12)}$$

where ϕ_m is the porosity of the matrix. d_m is the diameter of pores in the matrix.

Further, the effective diffusion coefficient varies from the limit of molecular diffusion ($K_n \to 0$) to fully developed Knudsen diffusion ($K_n \to \infty$) [8]. Therefore, the effective molecular - Knudsen diffusion coefficient is

$$D_e = \frac{\phi_m}{\tau_h} D_k (\zeta^{-(D_f-2)} + K_n^{-1})^{-1} \qquad \text{* MERGEFORMAT (4.13)}$$

where ζ is the ratio of molecular size to average pore diameter. D_f means the fractal dimension of the surface of the pores and is assumed to be 2.5 in this study. D_k represents the Knudsen diffusion coefficient which is obtained as

$$D_k = \frac{1}{3} d_m \sqrt{\frac{8RT}{\pi M}} \qquad \text{* MERGEFORMAT (4.14)}$$

In addition to the gas desorption from the surface of matrix pores, gas can migrate within the absorbed layer [9, 10], forming a surface diffusion. This diffusion is usually significant when the temperature is high relative to the normal boiling point of the adsorbed gas [11]. Its effective surface diffusion coefficient is given as

$$D_{es} = \frac{1+\phi_m}{\phi_m} \rho_s \rho_{ga} \frac{V_L P_L}{(P_L + p_m)^2} D_s \qquad \text{* MERGEFORMAT (4.15)}$$

where ρ_s and ρ_{ga} are the matrix density and the gas density under standard conditions, respectively. V_L is the Langmuir volume constant and P_L is the Langmuir pressure. D_s is the surface diffusion coefficient which is expressed as [12]

$$D_s = 8.29\times10^{-7}\times T^{0.5}\exp(-20/(RT))$$

* MERGEFORMAT (4.16)

Combining Eqs. , and , the final effective diffusion coefficient for the whole matrix is given as

$$D=\frac{\phi_m}{\tau_h}(1+8K_n)\frac{{d_m}^2 p_m}{32\mu_{nw}}+\frac{\phi_m}{\tau_h}D_k(\zeta^{-(D_f-2)}+K_n^{-1})^{-1}+\frac{1+\phi_m}{\phi_m}\rho_s\rho_{ga}\frac{V_L P_L}{(P_L+p_m)^2}D_s$$

* MERGEFORMAT (4.17)

4.3.5. Two-phase flow in the fractured zone

The two-phase flow of gas and water occurs in the micro-fractures of the fractured zone, where the wetting phase is water and the non-wetting phase is gas. Their governing equations are obtained from the mass conservation laws of water and gas, respectively.

For the water phase:

$$\frac{\partial(\phi\rho_w s_w)}{\partial t}+\nabla\left(-\frac{kk_{rw}}{\mu_w}\rho_w\nabla p_w\right)=f_w$$

* MERGEFORMAT (4.18)

For the gas phase:

$$\frac{\partial(\phi\rho_{nw} s_{nw})}{\partial t}+\nabla\left(-\frac{kk_{rnw}}{\mu_{nw}}\rho_{nw}\nabla p_{nw}\right)=f_{nw}$$

* MERGEFORMAT (4.19)

where k is the absolute permeability of the fractured zone. ϕ is the porosity of the fractured zone. μ_w and μ_{nw} are the viscosities of water and gas under in-situ conditions, respectively. p_w is the pore pressure of water in the fractures and p_{nw} is the pore pressure of the gas in the fractures. s_w denotes the saturation of water and s_{nw} denotes the saturation of gas. k_{rw} and k_{rnw} are the relative permeabilities of water and gas, respectively. Saturation, capillary pressure and relative permeability satisfy capillary pressure model and relative permeability

model as given in the Appendix. At the right term, f_w and f_{nw} are the sources of water and gas, respectively. f_{nw} has two sources: one is the gas exchange between fractures and matrix in the fractured zone (zone 2), the other is the generated gas source at the site. The gas from zone 1 is input into zone 2 as a boundary source.

4.3.6. Two-phase flow in hydraulic fractures

In the two-dimensional computational model of this study, the hydraulic fractures are expressed by one-dimensional lines. The two-phase flow in hydraulic fractures still follows the Darcy law. The porosity of hydraulic fractures is usually enhanced or limited by the effects of pressure, swelling and geochemical reaction. Xu et al. [13] indicated that 30% of the effective fracture volume is lost due to pressure depletion during early-time water flowback. In this study, these effects are not considered for hydraulic fractures and thus the porosity of each hydraulic fracture is constant. Therefore, the mass conservation equations along a hydraulic fracture are:

For water

$$d_{hf}\frac{\partial}{\partial t}(\rho_w\phi_{hf}S_w)+\nabla_T(-d_{hf}\rho_w\frac{k_{hf}k_{rw}}{\mu_w})=d_{hf}Q_w$$

* MERGEFORMAT (4.20)

For gas

$$d_{hf}\frac{\partial}{\partial t}(\rho_{nw}\phi_{hf}S_{nw})+\nabla_T(-d_{hf}\rho_{nw}\frac{k_{hf}k_{rnw}}{\mu_{nw}})=d_{hf}Q_{nw}$$

* MERGEFORMAT (4.21)

where d_{hf} is the average width of a hydraulic fracture. ϕ_{hf} and k_{hf} are the porosity and permeability of the hydraulic fracture, respectively. Q_w represents the source or sink of water and Q_{nw} represents the source or sink of gas.

4.4. Model validations

The above fully coupled model describes the multi-physical processes and interactions in different scales, including two-phase flow, capillary pressure, relative permeability, multi-scale diffusion and flow. This formulates a fully coupled flowback model for the two-phase flow simulations of the shale gas production in a fractured shale reservoir. COMSOL Multiphysics, a commercial partial differential equation solver, is used for its implementation. This fully coupled model is validated through the following two examples.

4.4.1. Example 1 - Comparison of single-phase and two-phase flows

The gas production is predicted and compared with single-phase flow and two-phase flow models. Yu and Sepehrnoori [14] performed the history matching with two sets of field gas production data from the Barnett shale and the Marcellus shale. They analyzed the contribution of gas desorption and geomechanics on gas production through single-phase flow. The immediate two-phase flow was also observed in the Barnett shale [15]. Therefore, our fully coupled model was applied to the Barnett shale. A typical computational model was set up in Fig. 4.3. This model was 550 m long and 145 m high, and the initial reservoir pressure was 20.34 MPa. This horizontal well was located at the bottom boundary with a fixed pressure (3.45 MPa), and no-flow was assumed at its left and right boundaries.

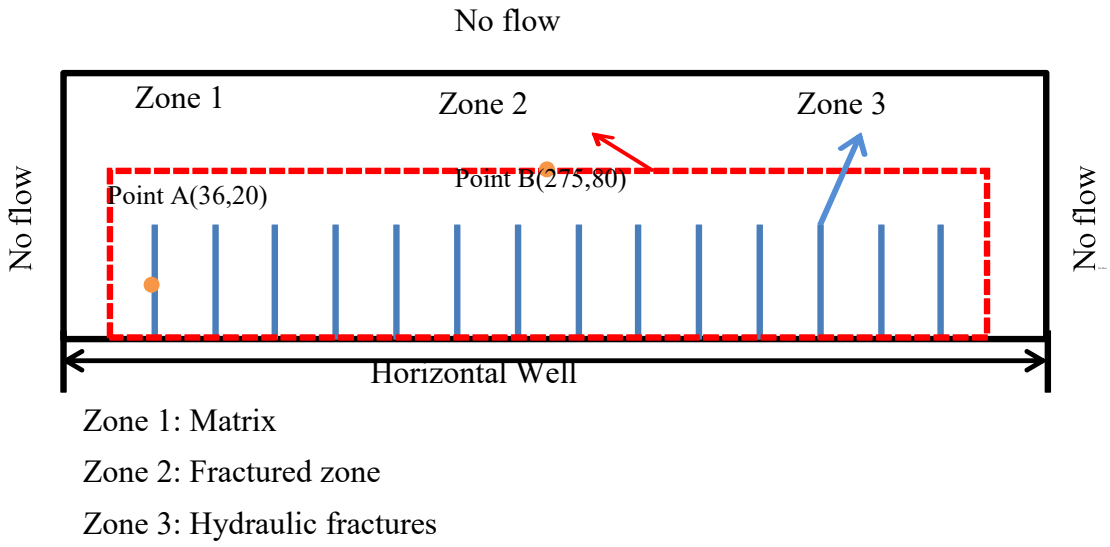

Fig. 4.3. A computational model for fractured shale reservoirs

The simulation parameters and hydraulic fractures for the Barnett shale are listed in Table 4.1. The parameters used in this simulation are taken from the paper of Yu and Sepehrnoori [14]. Most of the parameters are the same as those used in the literature. This example has no water flowback data available, thus we take longer gas production time than two-phase flowback period for comparison.

Table 4.1. Model parameters for Barnett shales

Parameter	Unit	Value	Physical Meanings
S_{rnw}		0.15	Residual saturation of gas
S_{rw}		0.6	Residual saturation of water
μ_{w}	Pa•s	3.6×10^{-4}	Water viscosity
λ_{w}		2	Pore size distribution index
N_{w}		2	Corey parameter for water
N_{nw}		2	Corey parameter for gas
P_i	MPa	20.34	Initial reservoir pressure
h_f	m	47.2	Fracture half-length
P_b	MPa	3.45	Well pressure
k_0	mD	0.7	Initial permeability in fractured zone
ϕ_0		0.2	Initial porosity in fractured zone
k_{hf}	mD	50	Permeability in hydraulic fracture

ϕ_{hf}		0.25	Porosity in hydraulic fracture
ϕ_f		0.03	Initial porosity in micro-fracture of matrix
ϕ_m		0.01	Initial porosity in matrix
N_f		14	Number of hydraulic fractures
p_e	MPa	2	Entry capillary pressure
ν		0.3	Poisson's ratio of shale
ρ_c	kg/m^3	2300	Shale density
P_L	MPa	6	Langmuir pressure of gas in shale
V_L	m^3/kg	0.03	Langmuir sorption capacity of shale for gas
$k_{rw}^{\max}$		0.9	End-point relative permeability for water phase
$k_{rnw}^{\max}$		1	End-point relative permeability for gas phase
T	K	352	Reservoir temperature
d_f	m	1×10^{-7}	Aperture of micro-fracture in matrix
d_m	m	1×10^{-9}	Diameter of pore in matrix
d_{hf}	m	0.003	Hydraulic fracture width

The numerical results are used to validate the prediction accuracy of long-term gas production with two-phase flowback model. The comparison of the simulation results and field data is presented in Fig. 4.4. This figure observes that the two-phase flowback model better matches with actual gas production data than a single gas flow model. After 200 days, the gas production rate declines by 80%, reaching the value of 5×10^4 m^3 / d. The flow rate of simulation is a little lower than that from the field data during the later production. This is because the permeability in the actual condition would be higher than the uniform hydraulic fracture in the simulation model. The hydraulic fractures are usually multi-scale, and contact with natural fractures to form a complicated fracture network. Thus, uniform fractures are not sufficient to describe this problem. The effects of fracture properties should be further discussed in four aspects: fracture spacing, fracture width, fracture uniformity, and fracture geometry.

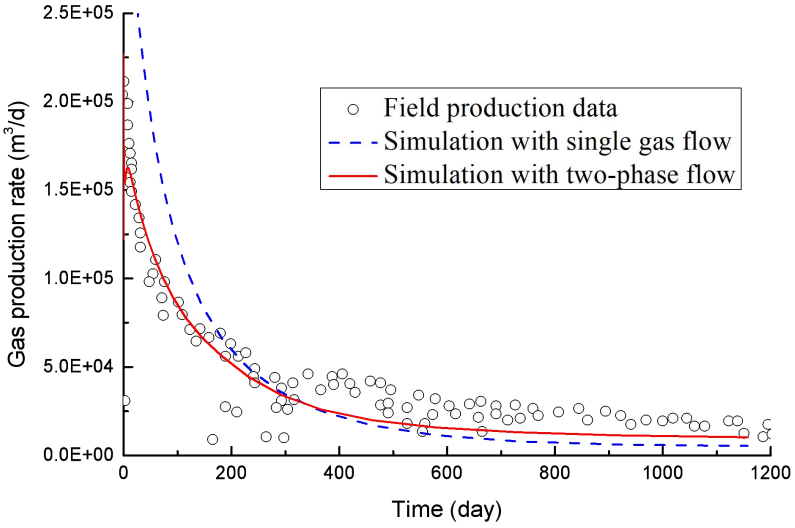

Fig. 4.4. Comparison of numerical simulation and site production in Barnett shale reservoir

4.4.2. Example 2 - Two-phase flowback data of a China shale gas well

Further, both gas and water productions from an actual shale gas well [16] are used to verify this model. This computational model is 1380 m long and 250 m high and has 11 hydraulic fractures. The initial reservoir pressure is 27.4 MPa and the bottom hole pressure is 19.67 MPa. Its left and right boundaries are assumed to be no-flow. The parameters in simulations are taken from Yang et al. [16] and listed in Table 4.2.

Table 4.2. Simulation parameters for field data

Parameter	Unit	Value	Physical Meanings
S_{rmw}		0.15	Residual saturation of gas
S_{rw}		0.2	Residual saturation of water
λ_{w}		2	Pore size distribution index
N_{w}		2	Corey parameter for water
N_{mw}		2	Corey parameter for gas
P_i	MPa	27.4	Initial reservoir pressure
h_f	m	143	Fracture half-length
P_b	MPa	19.67	Well pressure

k_0	mD	0.0008	Initial permeability in fractured zone
ϕ_0		0.08	Initial porosity in fractured zone
k_{hf}	mD	0.1	Permeability in hydraulic fracture
ϕ_{hf}		0.25	Porosity in hydraulic fracture
ϕ_f		0.03	Initial porosity in micro-fracture of matrix
ϕ_m		0.01	Initial porosity in matrix
N_f		11	Number of hydraulic fractures
p_e	MPa	2	Entry capillary pressure
ν		0.3	Poisson's ratio of shale
ρ_c	kg/m^3	2630	Shale density
P_L	MPa	6	Langmuir pressure of gas in shale
V_L	m^3/kg	0.03	Langmuir sorption capacity of shale for gas
T	K	327.6	Reservoir temperature

The gas production rate is presented in Fig. 4.5 (a) and the water flow rate is compared in Fig. 4.5 (b). It is noted that gas flow rate rapidly increases and reaches the maximum of 2×10^5 m$^3/d$ at the 10th day, then follows a slight decline. The water flowback rate has a rapid decrease from 22 m^3/d to 2.8 m^3/d after the first 50 days and then keeps stable during the flowback period up to 200 days. Our simulations are in a good match with both production rates of gas and water.

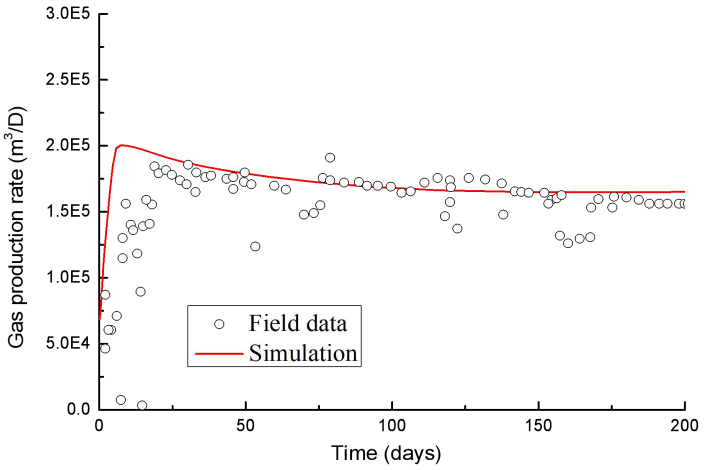

(a) Gas production data

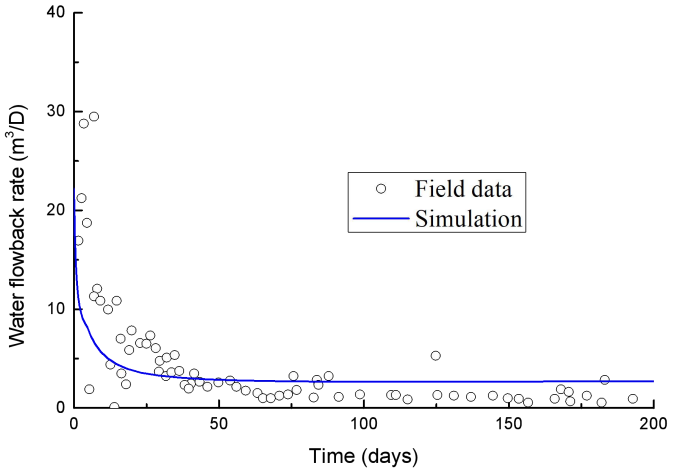

(b) Water flowback rate

Fig. 4.5. Comparison of numerical simulation with field production data at some China shale gas well

These two examples verify the applicability of this fully coupled model to different periods. Example 1 focuses on the prediction accuracy of long-term gas production when the two-phase flowback is considered. Example 2 compares the production data of both water and gas in the early production period. These two examples suggest that this fully coupled model is feasible to evaluate the gas production in the short-term and long-term period.

4.5. Parametric study and discussions

4.5.1. Impact of two-phase flowback on gas production in the early period

The impact of two-phase flowback on gas production in the early period is investigated here. The two-phase flowback usually occurs in zones 2 and 3, because the water-based fracturing fluid can only penetrate such a range [17]. Fig. 4.6 compares the cumulative gas productions with and without the consideration of two-phase flowback. Generally, the cumulative gas production increases rapidly in the early 100 days. This increase then starts to

slow down until 230 days. At this time, the cumulative gas production reaches $1.3\times10^7 m^3$ for the case of two-phase flowback and is $2.07\times10^7 m^3$ for the case of single-phase gas flow. Obviously, the cumulative gas production is much lower if the two-phase flowback is considered. On the other hand, the two-phase flowback would affect gas production in the early period. This is the reason why the previous models based on single-phase gas flow usually have a higher production rate than actual field data.

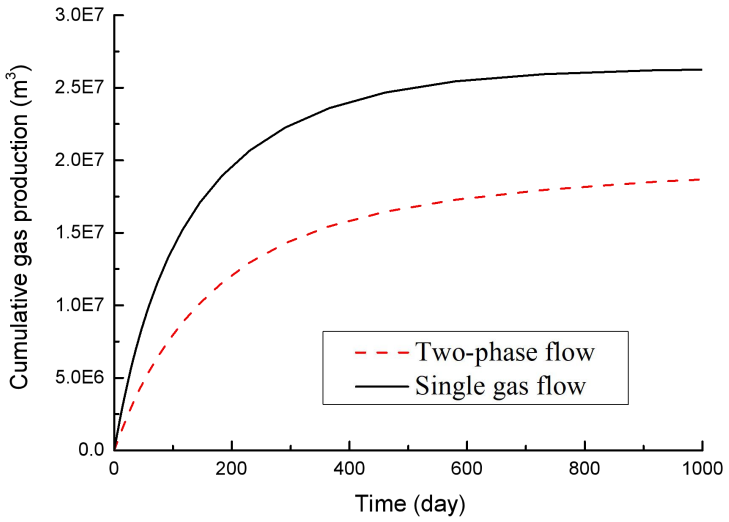

Fig. 4.6. Comparisons of cumulative gas production for single-phase gas flow and two-phase flow

4.5.2 Impacts of fracture properties on gas production

As a fine-tune, the impacts of fracture properties on long-term gas production are investigated. Following four parameters are chosen: the fracture spacing, the fracture width, the fracture uniformity, and the fracture geometry. They describe the fracture properties in the two-phase flow process. This parametric study is to explore the favorable fracture properties for the enhancement of long-term gas production.

4.5.2.1. Effect of fracture spacing

The fracture spacing is an index to express the density of fractures generated in a fixed domain which has a definite volume. In this computation, each fracture has the same properties, but 14 hydraulic fractures are distributed in the hydraulic fractured zone with different spacings. Two fracture spacings of 36.2 m and 25 m are assumed. Fig. 4.7 compares the gas production rate under these two spacings. In the same region, a more sparse distribution of hydraulic fractures means larger stimulated reservoir volume (zone 2) and less matrix volume (zone 1). Thus, the pressure nearby hydraulic fracturing zone decreases quickly and the gas in the fractured zone flows into the well easily. With the process of gas production, the difference of gas production rate under different fracture spacings gradually vanishes due to the completion of pressure. The gas production rate with fracture spacing of 25 m is higher than that of the original model at later production time because the gas in zone 1 begins to flow into the well.

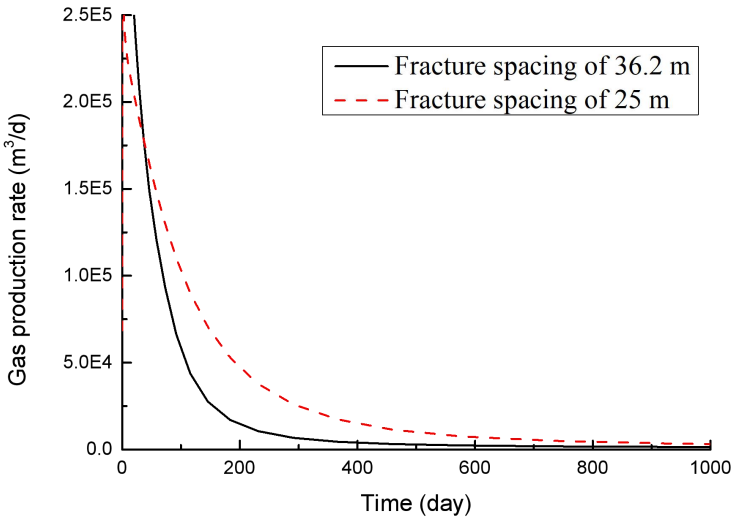

Fig. 4.7. Effect of fracture density on gas production rate

4.5.2.2. Effect of fracture width

The fracture properties such as fracture conductivity heavily change with fracture width. In this sub-section, the effect of fracture width on gas production is examined. The fracture width is taken as 0.03, 0.003, and 0.0003 m, respectively. As shown in Fig. 4.8, the gas production rate declines rapidly. However, the history curves are almost identical regardless of fracture width. This implies that the gas production rate is not controlled by the conductivity of fracture. This is reasonable because fracture only provides a channel for gas flow. When its capacity is larger than the demand for gas flow, the fracture does not affect the gas flow any more.

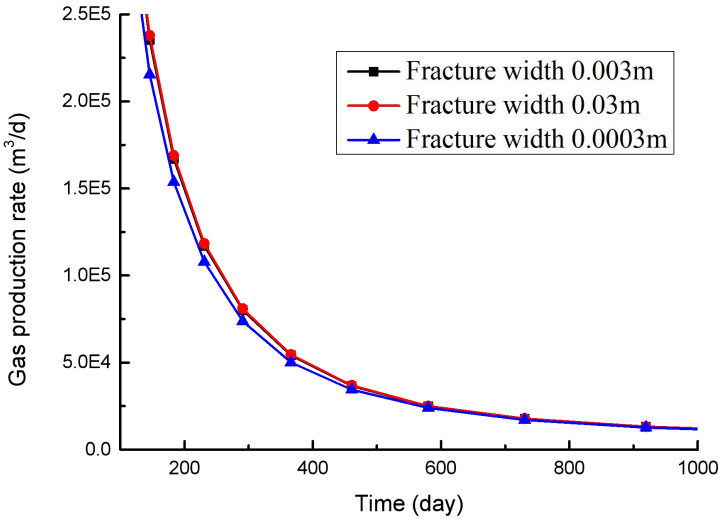

Fig. 4.8. Effect of fracture width on gas production rate

4.5.2.3. Effect of fracture uneven length

After the treatment of hydraulic fracturing in shale gas reservoirs, a complex fracture network is generated in the fractured zone. In the previous discussion, the hydraulic fractures are assumed to have equal length, called uniform fracture length. The fracture length may vary in the actual field. In order to evaluate the impact of fracture length on gas production

rate, the total length of fractures is kept constant but each fracture has different length. This case is called uneven fracture length. The gas production rates of these two cases are compared in Fig. 4.9. The gas production rate with the uniform fracture length decreases quickly and soon falls to a low point. After the production of 230 days, the gas production rate decreases to approximate $1.06\times10^{4} m^{3}/d$. The gas production rate with the uneven fracture length only declines to about $7\times10^{3} m^{3}/d$ at 230 days. This is a good explanation of why the simulated gas production rate with uniform fracture length is lower than the actual filed data.

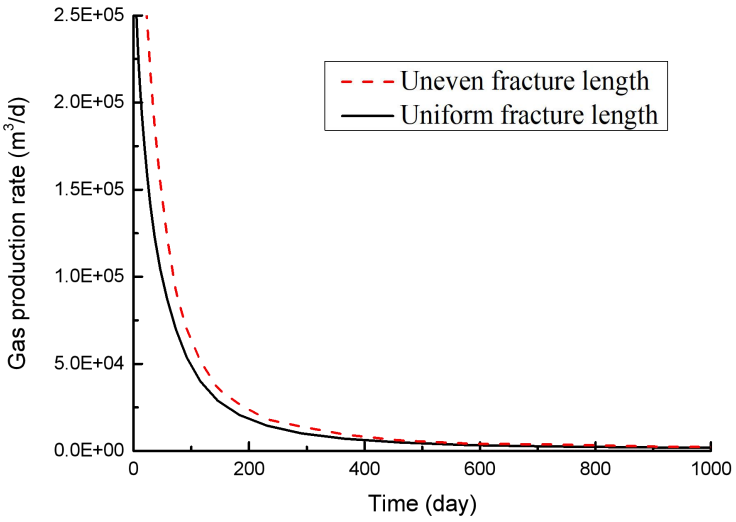

Fig. 4.9. Effect of fracture uniformity on gas production rate

4.5.2.4. Effect of fracture geometry

In the simulation model, the hydraulic fracture is usually assumed to be a straight line. This deviates from the real case where the complicated fracture network is formed. The assumption of the straight line affects the distributions of gas and water pressure, further changes the gas production rate. In order to reveal the effect of fracture geometry on gas and water production, the gas drainage maps are presented in Fig. 4.10. After the 36.5 days, the

fractures in both geometry 1 and 2 have their own drainage area. The hydraulic fractures would have interference with neighbouring fracture network to form an integrated drainage area. The drainage area varies with the geometric shape of fractures. If the height of the fracture is the same, the length of fracture in geometry 2 is longer because of tortuosity. This means that the hydraulic fracture has a larger contact area with the surrounding fractured zone.

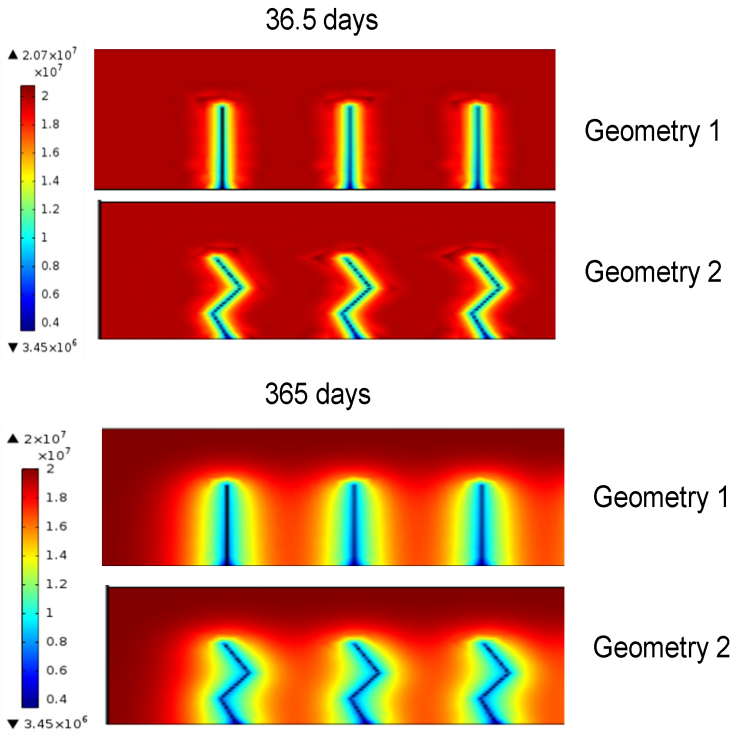

Fig. 4.10. Effect of fracture geometry on gas pressure at the early and late production periods

Fig. 4.11 compares the gas production rates in geometry 1 and 2. Because geometry 2 adds the contact area, its gas production rate is always higher. This effect is similar to that of fracture uniformity.

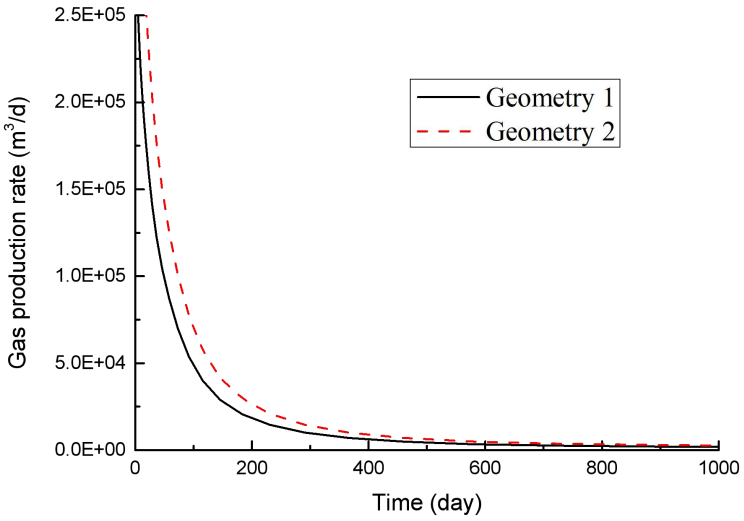

Fig. 4.11. Effect of fracture geometry on gas production rate

As a summary, both fracture uniformity and geometry shape add the complexity of the fracture network. Their effects on the gas production rate are similar. Denser distribution of hydraulic fractures means a higher level of hydraulic fracturing and can enhance gas production. However, the increase of hydraulic fracture width has less influence on gas production, if the hydraulic fracture width is larger than some value.

4.5.3. Evolution of capillary pressure

Capillary pressure ($p_c = p_{nw} - p_w$) is the difference between water pressure p_w (the wetting phase) and gas pressure p_{nw} (the non-wetting phase). It is an important parameter in two-phase flow and is affected by many factors like wettability, contact angle, pore size distribution and permeability. When the capillary pressure is higher, the gas production rate is greater at the beginning of flowback but declines later. The water saturation is a function of capillary pressure as:

$$s_w = \left(\frac{p_e}{p_c} \right)^{\lambda_w} (1 - s_{rnw} - s_{rw}) + s_{rw} \quad \text{* MERGEFORMAT (4.22)}$$

This equation shows that the capillary pressure is directly related to water saturation. Point A (36, 20) near the hydraulic fracture is selected for observation. The evolution of water saturation with capillary pressure is plotted in Fig. 4.12(a). The changes in water saturation and capillary pressure with time at this point A are plotted in Fig. 4.12(b). During the gas production, water originally in the fracture is extracted with the two-phase flowback. The capillary pressure changes from 2.4 MPa to 5 MPa. This reflects the process of gas-water displacement. As a sequence, the water saturation declines from 0.78 to 0.66 after almost 100 days. In computation, irreducible water saturation is specified as 0.6. The free water in the fractured zone is too little to form water flow when the water saturation at point A decreases to 0.66. The remaining water adsorbs on the surface of the matrix and may form a thin film of water. As the gas production continues, the water would be extracted with the gas flow.

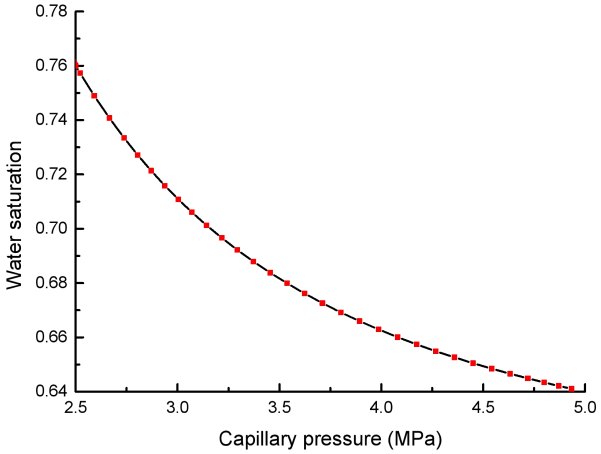

(a) Relationship between water saturation and capillary pressure

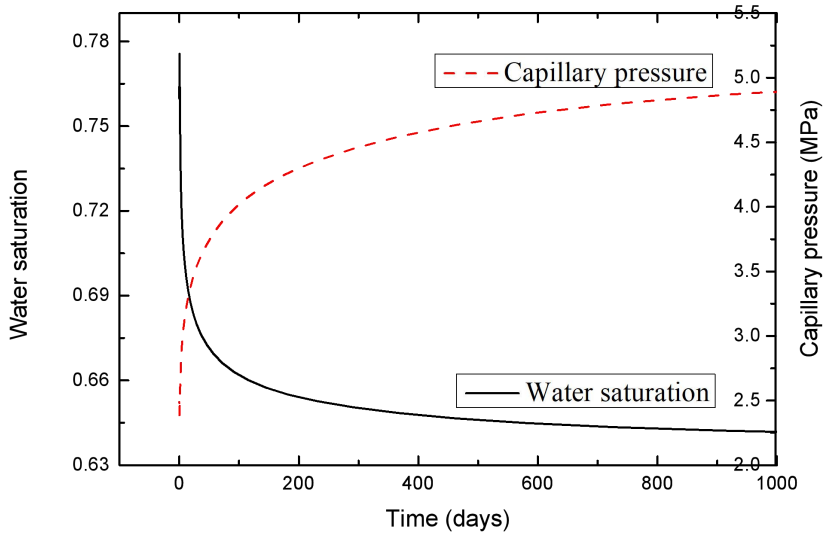

(b) Variation of water saturation and a capillary with time

Fig. 4.12. Chang of water saturation and a capillary with time at point A (36, 20) near the hydraulic fracture

4.5.4. Impact of entry capillary pressure

Entry capillary pressure describes the occurrence of gas-water displacement and directly depends on the aperture of fracture. This entry capillary pressure varies with rock type and a typical range of 0.1 - 48.3 MPa were observed. In this study, the effect of entry capillary pressure on gas production is investigated when entry capillary pressure is taken as 2, 4, and 6 MPa, respectively. The effect is presented in Fig. 4.13(a) on gas production rate and in Fig. 4.13(b) on water production rate. Both gas and water production rates decrease with the increase of entry capillary pressure. At the production of 100 days, the water flowback rate declines to almost 98.8 m^3/d for $P_e = 2MPa$, which is higher 35.5% than that at $P_e = 6MPa$. This difference of gas production rate due to entry capillary pressure is larger at

100 days. These results show that the increase of entry capillary pressure has much more increasing impacts on gas production rate than on water flowback rate.

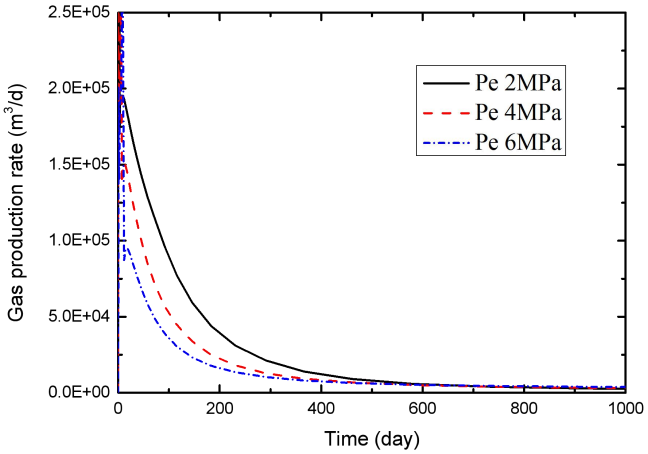

(a) Gas production rate

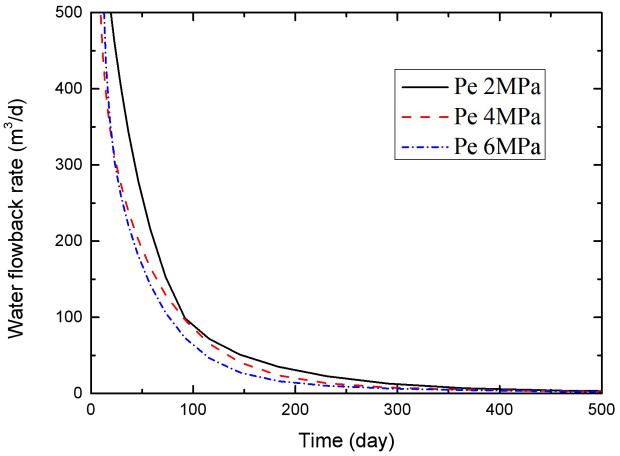

(b) Water flowback rate

Fig. 4.13. Impact of entry capillary pressure on gas and water flowback rates

4.5.5. Contribution of multi-scale diffusion mechanism to gas production

The shale gas production rate has been investigated by single-scale models, in which the fractured zone has hydraulic fractures with high permeability and matrix with low

permeability. Such models ignore the micro-fractures in the matrix. This loses the prediction accuracy of the gas production rate. If the matrix is only treated as a porous medium with extremely low permeability, the micro-scale gas diffusion cannot be described. This produces lower gas production than the actual field data. This section will use our fully coupled model (called the multi-scale model) to discuss the evolutions of permeability in the fractured zone and the apparent permeability in micro-fractures of the matrix. The gas pressure in the matrix and the gas exchange rate as the gas source between micro-fractures and matrix are also discussed in long-term gas production.

4.5.5.1. Fracture permeability

When a large amount of water-based fracturing fluid is extracted with the two-phase flow, the gas pressure in the fractured zone is lower than its initial value. At this time, the gas absorbed on the surface of the matrix begins to flow into the fractured zone through the micro-scale diffusion and flow mechanism. Fig. 4.14(a) gives the comparison of gas production rates in single-scale and multi-scale models. The gas production rate with multi-scale diffusion is always higher than that with single-scale diffusion. Because of micro-scale diffusion, the gas in micro-fractures would offer a stable source of gas production. The cumulative gas production is shown in Fig. 4.14(b). Before the production of 100 days, the cumulative gas productions in single-scale and multi-scale models are almost the same. The gap between the single-scale model and multi-scale model is 21.9% after 580 days. These results indicate that gas flows in zones 2 and 3 dominate the early gas production. During this period, the contribution of micro-scale gas diffusion in the matrix can be ignored. As the gas production continues, most of the gas in the fractures is extracted and the gas pressure begins to decline. Due to the pressure difference, the gas in matrix flows into the fractured zone. This process becomes significant in gas production and the effect of

micro-scale diffusion and flow on gas production is presented. Therefore, the micro-scale diffusion and flow mechanism in the matrix should be carefully considered, especially for the gas production in the later period.

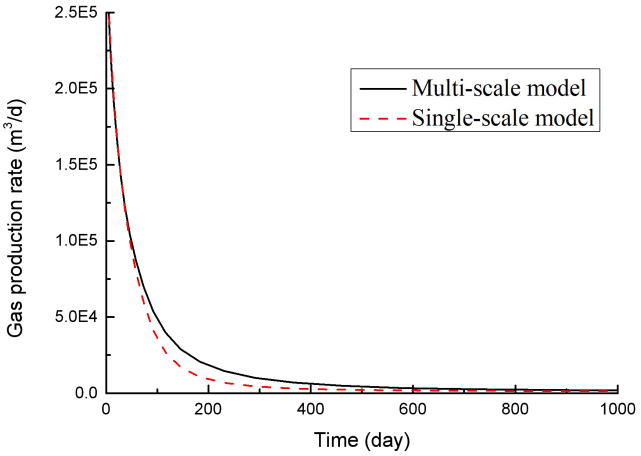

(a) Gas production rate

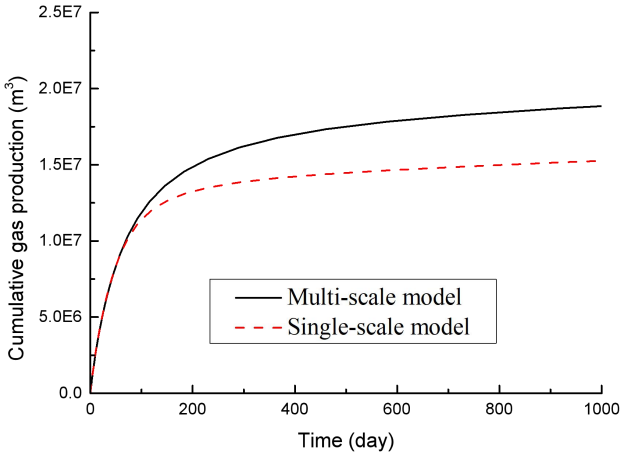

(b) Cumulative gas production

Fig. 4.14. Comparison of gas production prediction by multi-scale and single-scale models

The permeabilities of micro-fractures in the matrix and fractured zone are in different orders of magnitude. The evolution of permeabilities in the matrix and fractured zone at point B (275, 80) are presented in Fig. 4.15. Due to the decline of pore pressure induced by gas

extraction, the pore volume in the fractured zone would decrease accordingly. Therefore, this permeability declines with production time. Such a decline is consistent with the curve of the gas production rate. Finally, a 0.7% decrease in permeability in the fractured zone is observed. However, the apparent permeability of micro-fractures in the matrix has the opposite variation. Because of the gas desorption, the matrix shrinks and the permeability of micro-fractures in the matrix gradually increases, approaching to the permeability in the fractured zone. Though the permeability of micro-fractures in the matrix is a few orders of magnitude lower than that in the fractured zone, it increases by 10.4% compared to its initial value. If the micro-fracture size is bigger, the contribution of micro-scale diffusion and flow to gas production is greater.

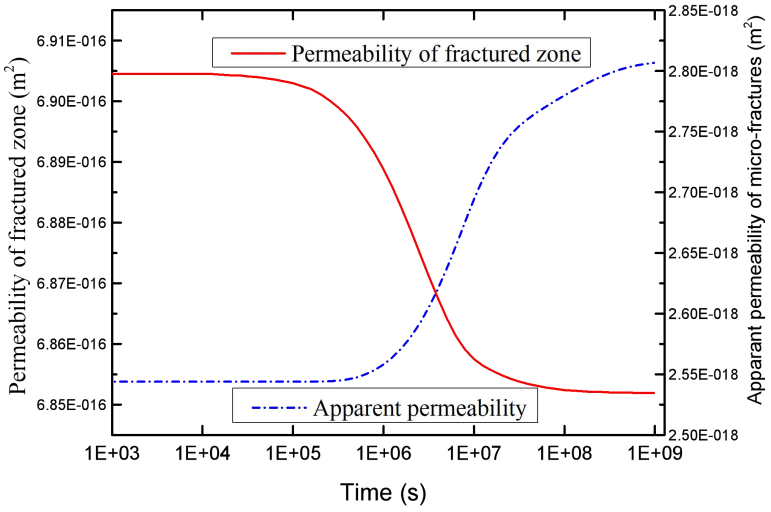

Fig. 4.15. Evolutions of permeabilities in the fractured zone and micro-fractures of matrix

4.5.5.2. Apparent permeability

The above results indicate that the aperture of micro-fractures in the matrix becomes a critical parameter to the gas exchange between the fractured zone (zone 2) and matrix (zone 1). The aperture is observed to vary from 10 nm to 50 μm [18]. The value of the aperture is

used to divide the matrix system into micro-fractures and micro-pores in this paper. Here, the apertures of micro-fractures are assumed to be 100 nm and 900 nm, respectively. Fig. 4.16 presents the variation of apparent permeability with the aperture at point B. The black line represents the base case that is presented in Fig. 4.15. The red dotted line represents the apparent permeability when the micro-fracture aperture is 900 nm. This figure shows that the aperture of micro-fracture has important impacts on apparent permeability. When the aperture is 900 nm, the apparent permeability is nearly two orders of magnitude higher than the base case. This value would get closer to the permeability of fractures (zone 2) as the aperture increases. The previous study shows that with the pressure decline in the fractured zone, the gas in matrix flows into the fractured zone and dominates the gas production. The aperture of micro-fractures has a salient influence on the apparent permeability. Therefore, the gas in the matrix through the micro-scale diffusion and flow is the key contribution to gas production, especially in the later production period.

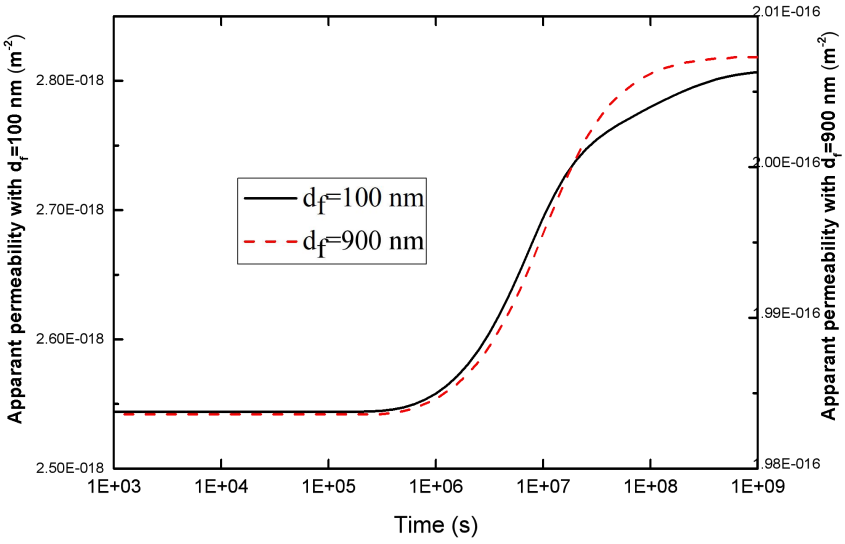

Fig. 4.16. Evolution of apparent permeability with time under different apertures

4.5.5.3. Gas exchange between micro-fractures and matrix

Pore size is an important parameter to gas production because it is the channel of gas diffusion from the matrix into the micro-fractures. When the diameters of pores in the matrix are assumed to be 1, 3 and 9 nm, respectively, Fig. 4.17 presents the variation of gas pressure with diameter. It is found that the pore size is greater, the pressure drops faster. More gas desorbs from the surface of the matrix when the diameter of the pore in the matrix is 9 nm.

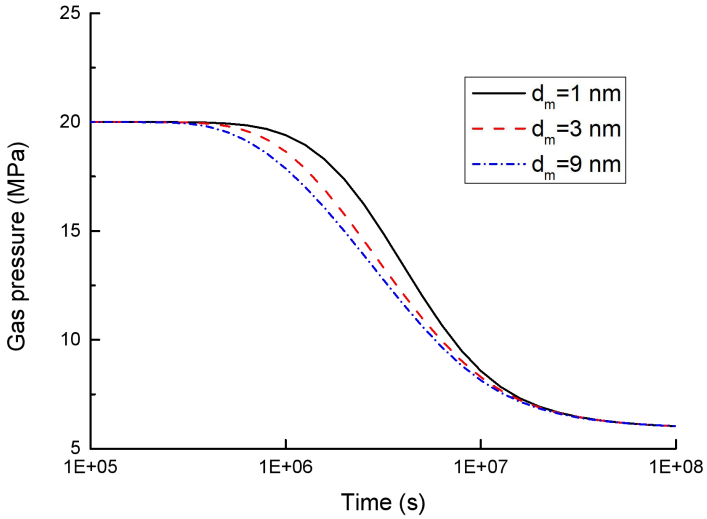

Fig. 4.17. Gas pressures in the matrix at different pore sizes

The impact of pore diameter on the gas exchange rate between the matrix and micro-fractures is presented. These variation curves all present the shapes of the mountain in Fig. 4.18. Due to the faster gas pressure drop, the gas exchange rate firstly increases when the diameter of pore is 9 nm. With the decrease of pore diameter, this increase in gas exchange rate would delay correspondingly. Further, the diameter of pore is bigger, the diffusion coefficient is bigger and the gas exchange rate reaches a higher peak. That is because the bigger diameter of pore is directly linked to higher matrix permeability. Finally, the gas exchange rate becomes zero. It means that the pressure in the matrix and the pressure in

micro-fractures reach a balance. More gas desorbs from the surface of the matrix when the diameter of pore is bigger. This is the gas supply to gas production after the gas in the fractured zone is extracted.

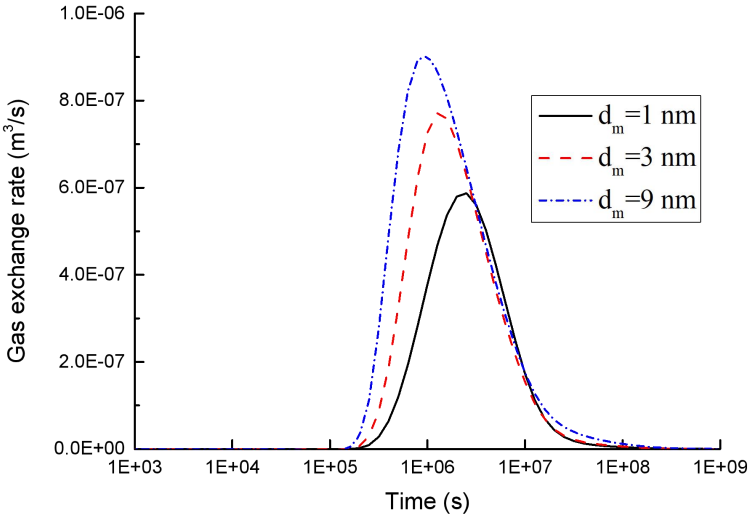

Fig. 4.18. Variation of the gas exchange rate with time at different pore sizes

4.6. Conclusions

This chapter numerically investigated the impact of water flowback in the water-based fracturing fluid on the short-term and long-term shale gas production. A fully coupled multi-scale two-phase flowback model was proposed for the three zones model and the multi-scale diffusion and flow mechanisms were incorporated. Both water and gas production rates in the early period and the gas production rate in the later production period were studied under different fracture properties like fracture spacing, fracture width, fracture uniformity and fracture geometry. The evolution curves of capillary pressure and water saturation, the contribution of multi-scale diffusion and flow to gas production, and the gas

exchange between micro-fractures and matrix in different zones were explored. From these studies, the following conclusions can be made.

First, this fully coupled multi-scale two-phase flowback model can not only describe the process of two-phase flowback in the early production period but also well describe the impacts of fracture properties, multi-scale gas flow and diffusion in the later production period. It thus provides a useful tool for the assessment of gas production in the water-based fracturing process. The two-phase flow affects the gas production in the early and long-term periods. Our example shows that the cumulative gas production at the 230 days has a 58.2% decline after considering the effect of two-phase flowback. Thus, the two-phase flowback should be carefully included when the gas production in fractured shale reservoirs is evaluated.

Second, the hydraulic fracture properties of fracture spacing, fracture width, fracture uniformity and fracture geometry have variable influences on gas production rate. The increase of fracture density has an obvious positive enhancement on the gas production rate. The uniformity and geometry of fractures have similar effects on the gas production rate, particularly at the early production period. The fracture width have no effect when it is larger than some value. The hydraulic fracture network in the actual field is interconnected and not uniform. Their impacts on the gas production rate should be further studied.

Finally, the gas production rate with multi-scale two-phase flow model is always higher than that with the single-scale model. In micro-scale diffusion and flow mechanism, the gas in micro-fractures of the matrix is a stable source of gas production. With gas extraction, the permeability of micro-fractures in matrix gradually increases and approaches to the permeability in the fractured zone. This phenomenon reflects the flow consistency in the

macro-scale flow and the micro-scale diffusion. The contribution from micro-fractures is obvious when the aperture of micro-fractures increases, thus being not ignorable.

4.7. References

[1] Wattenbarger R, Alkouh A. New advances in shale reservoir analysis using flowback data. SPE Eastern Regional Meeting, 2013, DOI: 10.2118/165721-MS.

[2] Ambrose R J, Hartman R C, Diaz-Campos M, Akkutlu I, Sondergeld C. Shale gas-in-place calculations part i: new pore-scale considerations. SPE Journal, 2012, 17(1): 219-229.

[3] Gao F, Liu J, Wang J G, Ju Y, Leung C. Impact of micro-scale heterogeneity on gas diffusivity of organic-rich shale matrix. Journal of Natural Gas Science and Engineering, 2017, 45: 75-87.

[4] Singh H, Javadpour F. A new non-empirical approach to model transport of fluids in shale gas reservoirs. Unconventional Resources Technology Conference, 2013, 13: 1258-1273.

[5] Liu J, Wang J G, Gao F, Zhang X, Zhang L. Flow consistency between non-darcy flow in fracture network and nonlinear diffusion in matrix to gas production rate in fractured shale gas reservoirs. Transport in Porous Media, 2016, 111(1): 97-121.

[6] Lim K, Aziz K. Matrix-fracture transfer shape factors for dual-porosity simulators. Journal of Petroleum Science & Engineering, 1995, 13(3-4): 169-178.

[7] Civan F. Effective correlation of apparent gas permeability in tight porous media. Transport in Porous Media, 2010, 82(2): 375-384.

[8] Lunati I, Lee S H. A dual-tube model for gas dynamics in fractured nanoporous shale formations. Journal of Fluid Mechanics, 2014, 757: 943-971.

[9] Akkutlu I Y, Fathi E. Multiscale gas transport in shales with local kerogen heterogeneities. SPE Journal, 2012, 17(4): 1002-1011.

[10] Xiong X, Devegowda D, Millazon, G. A fully-coupled free and adsorptive phase transport model for shale gas reservoirs including non-darcy flow effects. Presented at the SPE Annual Technical Conference and Exhibition, San Antonio, Texas, USA, 8-10 October, 2012, DOI: 10.2118/159758-MS.

[11] Hashemifard S A, Ismail A F, Matsuura T. To what extent the conventional gas permeation testing method is reliable for membrane systems? Separation and Purification Technology, 2013, 114: 90-98.

[12] Wu K, Li X, Wang C. Model for surface diffusion of adsorbed gas in nanopores of shale gas reservoirs. Industrial & Engineering Chemistry Research, 2015, 54(12): 3225-3236.

[13] Xu Y, Dehghanpour H, Ezulike O, Virues C. Effectiveness and time variation of induced fracture volume: lessons from water flowback analysis. Fuel, 2017, 210: 844-858.

[14] Yu W, Sepehrnoori K. Simulation of gas desorption and geomechanics effects for unconventional gas reservoirs. Fuel, 2014, 116: 455-464.

[15] Zhang Y, Ehlig C. Accounting for remaining injected fracturing fluid in shale gas wells. Unconventional Resources Technology Conference, 2014, DOI: 10.15530/urtec-2014-1892994.

[16] Yang R, Huang Z, Li G. An innovative approach to model two-phase flowback of shale gas wells with complex fracture networks. SPE Technical Conference and Exhibition, 2016, DOI: 10.2118/181766-PA.
[17] Zhang X, Wang J G, Gao F, Ju Y, Liu J. Impact of water and nitrogen fracturing fluids on fracturing initiation pressure and flow pattern in anisotropic shale reservoirs. Computers and Geotechnics, 2017, 81: 59-76.
[18] Javadpour F, Fisher D, Unsworth M. Nanoscale gas flow in shale gas sediments. Journal of Canadian Petroleum Technology, 2007, 46(10): 55-61.

Chapter 5: Interaction of shale gas recovery and moisture transport in post two-phase flowback stage

5.1. Introduction

After the two-phase flowback stage of shale gas production, the residual water in the fractures is no longer enough to form a stable continuous flow but migrates by the moisture. However, the mechanism that residual water affects gas migration is still not clear. This chapter investigates the migration of residual water during shale gas production from the following three aspects: First, the residual water forms a water film on the surface of the fractures, making Darcy flow no longer applicable in the fractures. An empirical formula for threshold pressure gradient that comprehensively considers permeability, residual water saturation and pore pressure is proposed. Second, moisture is transported in three forms: diffusion, convection and evaporation reactions. Especially, the evaporation of the water film depends on the surrounding humidity, water activity and gas flow rate. The evolution of water film is a dynamic equilibrium process, which will directly affect the fracture permeability. Third, the residual water in the matrix interacts with clay minerals to form bound water. This part of residual water changes the adsorption capacity of shale gas in the matrix, which is expressed by the modified Langmuir isotherm adsorption. This chapter will discuss its mechanism through the above three aspects and explore how moisture transport affects the shale gas production.

5.2. A conceptual model for residual water effects

In chapter 4, a two-phase flowback model was established for the multi-scale diffusion in fractured shale gas reservoirs. This model only considered the behaviors of two-phase flow and thus ignored the moisture transport as residual water in long-term gas production. Actual production data indicate that the two-phase flow model is only applicable within the first approximate 100 days of production [1, 2].

A conceptual model is presented in Fig. 5.1 for the gas and moisture transports within a fractured shale reservoir. The fractured shale reservoir is a composite of the fracture network and matrix. The fracture network is the main channel for gas flow and moisture transport. Residual water forms a water film adhering on the surface of fractures [3, 4] and drys through a dynamic evaporation process. The matrix has a much lower permeability and porosity compared to the fracture system. When the gas pressure in fractures decreases to a lower value, the adsorption gas flows into the fractures through a slow diffusion process.

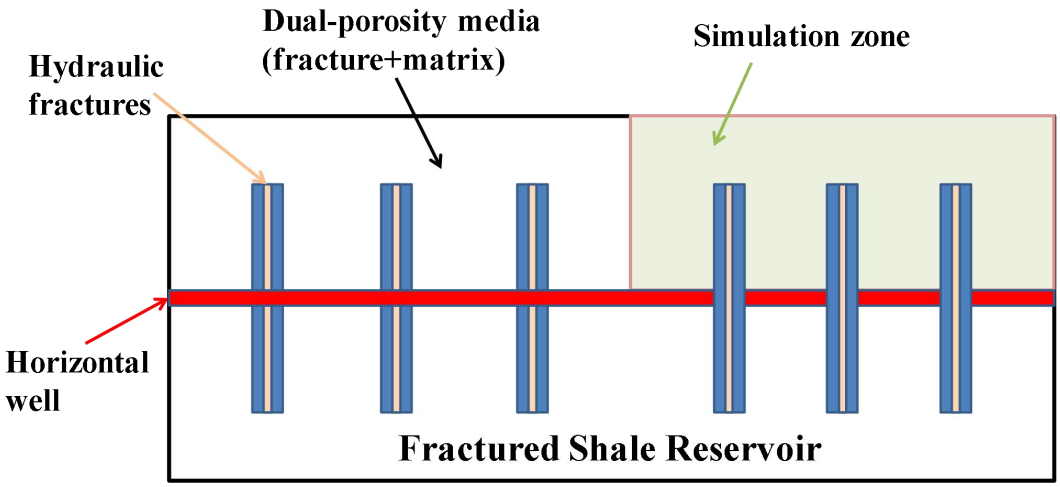

Fig. 5.1. A conceptual model for fractured shale reservoir

A series of interactions occur in shale gas production. For these processes, a mechanical-hydro-moisture coupled model is formulated to include additional two

mechanisms: First, a new non-Darcy model with a threshold pressure gradient is established. This gradient is directly related to residual water saturation. Second, the residual water affects the adsorption mechanism of gas and thus Langmuir adsorption isotherm is modified by water saturation.

5.3. Formulation of this conceptual model

5.3.1. Threshold pressure gradient under residual water saturation

Shale gas reservoirs usually have the characteristics of low porosity and low permeability. After hydraulic fracturing, a shale gas reservoir becomes highly water-saturated. In the early stage of shale gas flowback, gas and water form a bubble water flow or a two-phase flow in the fractured zone. With the continuous decrease of water saturation, water is not sufficient to form a continuous flow. Fig. 5.2 shows that this residual water remains in pore channels and forms a layer of the water film.

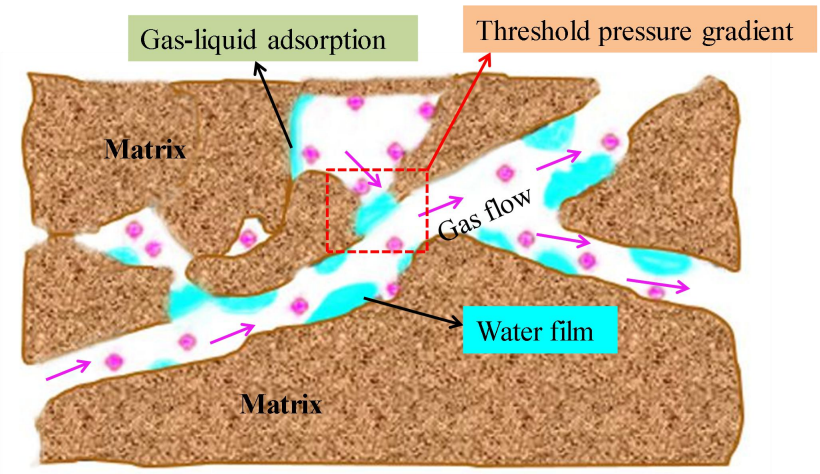

Fig. 5.2. This process of gas flow under residual water saturation

This water film has very important effects on the flow channels of gas. For example, the pressure difference between the two sides of water film reaches a certain value which is a

necessary condition for the initiation of gas flow. The pressure gradient should also maintain this pressure gradient during the gas flow. Otherwise, the water film at the pore throat will be formed again, and the gas flow will stop. This pressure gradient is defined as a threshold pressure gradient (TPG). This TPG expresses the gas starting flow against viscous forces between solid and gas. As an important parameter to describe the nonlinear flow of low-velocity gas, TPG has been discussed in many experimental and theoretical studies [5-7]. Dou et al. [8] stated that the low-velocity non-Darcy flow gradually transitions to Darcy-flow with the increase of permeability and the decrease of residual water saturation. In moist shale reservoirs, the gas flow in the fractures follows the non-Darcy flow with a threshold pressure gradient [9, 10]:

$$\vec{v}_g = \begin{cases} -\dfrac{k_f k_{rg}}{\mu_g}\left(\nabla p - G\right) & \left|\nabla p\right| \geq G \\ 0 & \left|\nabla p\right| < G \end{cases} \quad \text{* MERGEFORMAT (5.1)}$$

where μ_g is the gas viscosity. k_f represents the permeability of fractures and is determined by several factors such as pore pressure, gas adsorption swelling, and water film evaporation. k_{rg} is the gas relative permeability.

This TPG is a function of permeability, water saturation and pore pressure and expressed as a semi-empirical formula:

$$G = ae^{s_w} \cdot e^{b^* p_f + c^* p_f^2} \quad \text{* MERGEFORMAT (5.2)}$$

where s_w is the water saturation in fractures. p_f is the pore pressure. Parameter a is the water saturation correction factor. Parameters b and c represent the pore pressure correction and are also linked with shale permeability. These three parameters are fitted as

$$\begin{aligned} a &= e^{-(5.4491\times10^{15}\times k + 1.13293)} \\ b &= 8.81931\times10^{13}\times k - 0.06892 \\ c &= -5.83713\times10^{11}\times k + 0.0129 \end{aligned} \quad \text{* MERGEFORMAT (5.3)}$$

where k is the permeability of shale.

Obviously, the effect of water saturation on TPG decreases with the increase of permeability. When the permeability is larger, the residual water cannot effectively block the gas flow. Fig. 5.3(a) shows the comparison of threshold pressure gradient considering water saturation and experimental data. It is observed that the threshold pressure gradient increases with the increase in water saturation and decreases with the increases of pore pressure. Fig. 5.3(b) presents the variations of threshold pressure gradient with permeability. Bigger permeability means a larger gas flow channel. The threshold pressure gradient significantly decreases with the increases of permeability. However, the complexity of the pore size distribution is not considered in this study. Cai and Yu [5] indicated that the threshold pressure gradient and permeability analytically exhibit the scaling behavior $G \sim k^{-D_T/(1+D_T)}$. D_T represents the fractal dimension for tortuous capillaries. How to use fractal theory to reasonably describe the impact of residual water saturation on gas production is still an interesting topic for further study.

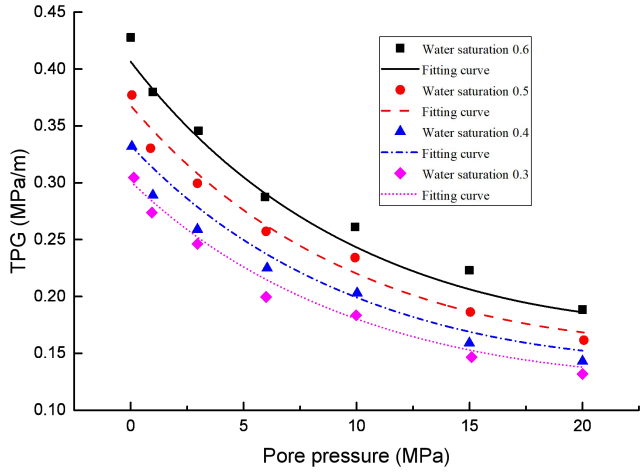

(a) Different water saturations

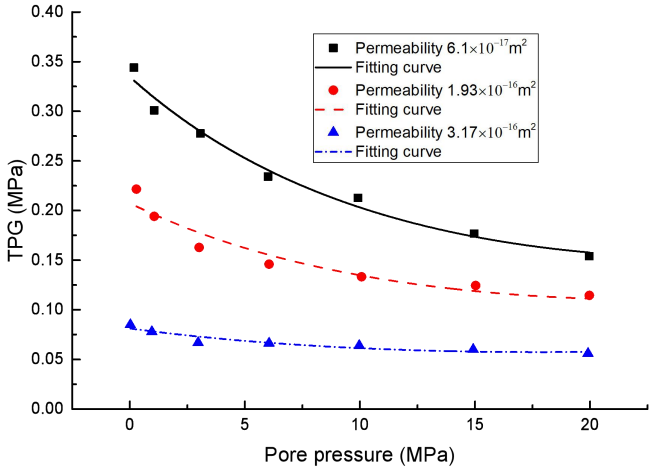

(b) Different permeabilities

Fig. 5.3. Verification of threshold pressure gradient under different water saturation and permeabilities

5.3.2. Gas non-Darcy flow in fractures

The mass conservation law for the gas flow in fractures is

$$\frac{\partial\left(\rho_g\phi_f\right)}{\partial t}+\nabla\cdot\left(\rho_g\vec{v}_g\right)=Q_s+Q_m \qquad \text{* MERGEFORMAT (5.4)}$$

where ρ_g is the gas density under the in-situ condition. At the right term of Eq. (5.4), Q_s is the gas source caused by extraction or injection; Q_m is the dynamic gas exchange between fractures and matrix.

The gas flow in the moist shale reservoir is a mixture of shale gas and volatile matter such as water vapor. Since the content of water vapor is extremely small relative to the content of shale gas, the partial pressure of water vaporization in the mixed gas is negligible. Therefore, the gas density is

$$\rho_g=\rho_v+\frac{p_fT_a}{p_aT}\rho_{ga}\approx\frac{p_fT_a}{p_aT}\rho_{ga} \qquad \text{* MERGEFORMAT (5.5)}$$

where p_f and p_a represent the gas pressures in fractures and the gas pressure under the standard condition, respectively. T and T_a are the gas temperatures in the shale reservoir and the gas temperature under the standard condition, respectively. ρ_{ga} is the gas density under the standard condition and ρ_v is the density of water vapor.

Substituting Eqs. (5.1), (5.2), and (5.5) into the mass conservation law of Eq. (5.4) obtains the final governing equation for non-Darcy gas flow in the fractures as

$$\phi_f \frac{\rho_{ga} T_a}{p_a T} \frac{\partial p_f}{\partial t} + \nabla \cdot \left(-\rho_g \frac{k_f k_{rg}}{\mu_g} (\nabla p - a e^{s_w} \cdot e^{b^* p_f + c^* p_f^2}) \right) = Q_s + Q_m - \frac{\partial \phi_f}{\partial t}$$

when $|\nabla p| \geq G$

* MERGEFORMAT (5.6)

Since the fracture network mainly provides flow channels, the gas mass content m only refers to free gas. The adsorbed gas mainly exists in the matrix. This paper will further consider different adsorption mechanisms of moist shale matrix below.

5.3.3. Moisture transport in fractures

5.3.3.1. Governing equations for moisture transport in fractures

The residual water in the fractured shale is recovered in the form of two-phase flow during the initial stage of flowback. As water saturation continues to decrease, discontinuous residual water in fractures replaces the two-phase flow. According to the mass conservation law, moisture transport can be expressed as

$$\frac{\partial c_w}{\partial t} + \nabla \cdot \left(-D_w \nabla c_w + \vec{u} c_w \right) = -R_w \qquad \text{* MERGEFORMAT (5.7)}$$

where $\vec{u}$ is the moisture convection velocity. c_w is the concentration of discontinuous water in the fractures, D_w is the diffusion coefficient driven by water concentration gradient:

$$D_w = 1\times10^{-8}\exp(-2.8+2\theta) \qquad \text{* MERGEFORMAT (5.8)}$$

where θ is the volume content of water film on the surface of fractures, which can be obtained by concentration of discontinuous water:

$$\theta = \frac{c_w M_w}{\rho_c} \qquad \text{* MERGEFORMAT (5.9)}$$

For the Eq. (5.7), the first term at the left-hand side represents the change rate of the moisture content in fractures, and the second term on the left-hand side represents the diffusion and convection during the moisture transport process. The term at the right-hand side is the change of moisture through the evaporation process. This evaporation distributed spatially and over time is a complex function of water concentration, vapor concentration and water activity.

$$R_w = K\cdot\left(a_w c_{sat} - c_v\right) \qquad \text{* MERGEFORMAT (5.10)}$$

where K (1/s) is the evaporation rate, c_{sat} is the saturated vapor concentration, and c_v is the current vapor concentration. a_w is the water activity, which describes the content of water evaporated into the gas. Generally, this parameter depends on the water content in the surrounding gas and temperature. Because the water content changes slowly in porous media, a_w is approximately taken as 0.9 in this paper.

5.3.3.2. Gas and liquid relative permeability

Although the residual moisture no longer forms a continuous flow, the basic definition of saturation is still similar to the two-phase flow in porous media.

$$s_g + s_w = 1 \qquad \text{* MERGEFORMAT (5.11)}$$

where s_g is the gas saturation in the fractures. s_w represents the saturation of water in the fractures, which can be expressed by the concentration of discontinuous water:

$$s_w = \frac{c_w M_w}{\rho_w \phi_f} \qquad \text{* MERGEFORMAT (5.12)}$$

where ρ_w and M_w are the density of water and the molecular weight of water, respectively. ϕ_f is the porosity of fracture, which is modified by shale volumetric strain, pore pressure and water film evaporation.

For a moist shale reservoir, gas or liquid phase permeability is further broken down into intrinsic permeability and relative permeability, given by the following expressions:

$$k_{fw} = k_f \times k_{rw} \qquad \text{* MERGEFORMAT (5.13)}$$

$$k_{fg} = k_f \times k_{rg} \qquad \text{* MERGEFORMAT (5.14)}$$

Due to different rock samples, various relative permeability models have been proposed [11]. In this study, relative permeability is directly linked with saturation [12]:

$$k_{rw} = \begin{cases} \left(\dfrac{s_w - s_{iw}}{1 - s_{iw}} \right)^3 & s_w > s_{iw} \\ 0 & s_w \le s_{iw} \end{cases} \qquad \text{* MERGEFORMAT (5.15)}$$

$$k_{rg} = \begin{cases} 1 - 1.1 s_w & s_w \le 1/1.1 \\ 0 & s_w > 1/1.1 \end{cases} \qquad \text{* MERGEFORMAT (5.16)}$$

Substituting Eqs. (5.8), (5.10), (5.13), (5.15) into the moisture transport equation (5.7), the final expression can be deduced as

$$\frac{\partial c_w}{\partial t} + \nabla \cdot \left(-D_w \nabla c_w - \frac{k_f k_{rw}}{\mu_w} \nabla p_f c_w \right) = -K \cdot \left(a_w c_{sat} - c_v \right)$$

* MERGEFORMAT (5.17)

5.3.3.3. Water film evaporation

Similar to the derivation of the moisture transport described in the previous section, the vapor transport equation can be also obtained from the mass conservation law as

$$\frac{\partial c_v}{\partial t} + \nabla \cdot \left(-D_e \nabla c_v + \vec{v} c_w \right) = K \cdot \left(a_w c_{sat} - c_v \right)$$

* MERGEFORMAT (5.18)

In this equation, its right-hand term represents the dynamic process of water film vaporization, providing source terms. Its left-hand side presents two migration mechanisms: one is the flow of water vapor with shale gas extraction, and the other is the flux generated by the binary diffusion of water vapor and dry shale gas. The effective diffusion coefficient D_e between these two components can be usually described by the Millington & Quirk equation.

$$D_e = D_{va} \phi_f^{4/3} s_g^{10/3} \qquad \text{* MERGEFORMAT (5.19)}$$

where the vapor-air diffusivity is $D_{va} = 2.6 \times 10^{-5} m^2 / s$.

5.3.4. Gas adsorption on the surface of the moist matrix

Fractures are the main flow channels of shale gas, but most of the shale gas is stored in the shale matrix with the adsorbed state. The adsorption of a gas on the surface of the dry matrix is a gas-solid interface effect, which belongs to physical adsorption. The absorbed content m_{dry} is related to the gas pressure in the matrix p_m through traditional Langmuir isotherm adsorption:

$$m_{dry} = \frac{V_L p_m}{p_L + p_m} \qquad \text{* MERGEFORMAT (5.20)}$$

where p_L is the Langmuir pressure and V_L is the Langmuir volume constant.

In this study, the traditional Langmuir isotherm adsorption cannot properly explain the adsorption mechanism because the residual water would diffuse into the shale matrix through infiltration. Many experimental observations indicate that the shale matrix is rich in clay minerals [13, 14]. Water molecules firstly adsorb on the surface of clay pores, as the clay minerals are hydrophilic. Thus, gas molecules do no longer directly contact with the solid interface and are replaced by gas-liquid interface adsorption on the surface of the water

molecule layer. This sorption mechanism of gas-liquid-solid is shown in Fig. 5.4. Based on Gibbs adsorption for the gas-liquid interface, the adsorbed content m_{wet} can be expressed as [15, 16]

$$V^* = -A(\frac{\partial \sigma}{\partial p_m})_T \frac{p_m}{RT} \qquad \text{* MERGEFORMAT (5.21)}$$

$$m_{wet} = \frac{V^* p_m}{p_m + P_L} \qquad \text{* MERGEFORMAT (5.22)}$$

where σ is the gas-water surface tension, V^* is the maximum adsorption capacity per unit volume, A is the pore specific surface area.

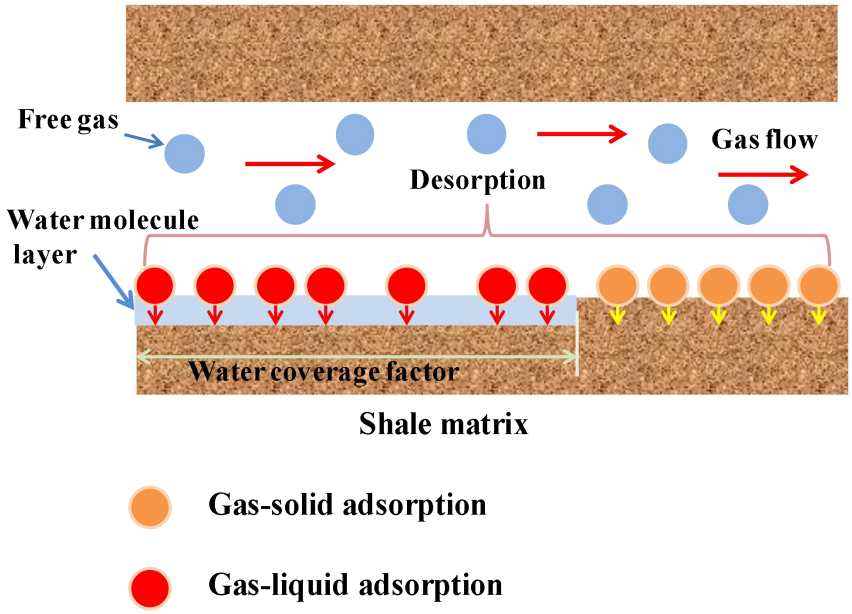

Fig. 5.4. Gas adsorption on the moist shale matrix

It is found that this adsorption expression also conforms to the Langmuir isotherm. To correct the effect of the residual water on the gas adsorption capacity in the matrix, following unified expression for gas-liquid-solid adsorption is proposed as

$$m_{ad}=\begin{cases}\dfrac{V_L p_m}{p_L+p_m} & s_w=0\\ (1-\chi)\dfrac{V_L p_m}{p_L+p_m}+\chi\dfrac{V_L p_m}{p_L+p_m}\exp\left(-\lambda\theta\right) & 0<s_w<s_{sat}\end{cases}$$

* MERGEFORMAT (5.23)

where χ is the water coverage factor, $\chi=n_{H_2O}/n_{total}$. λ is the gas adsorption reduction factor for moist shale matrix.

5.3.5. Gas diffusion in matrix

For the gas flow in the shale matrix, the mass conservation equation is

$$\frac{\partial m_m}{\partial t}+\nabla\cdot\left(-\rho_{gm}\frac{k_m}{\mu_g}\nabla p_m\right)=-Q_m \quad \text{* MERGEFORMAT (5.24)}$$

where ρ_{gm} is the density of gas in the matrix. m_m is the total gas content in the matrix which consists of free gas in pores and adsorbed gas on the pore surface of the moist shale matrix:

$$m_m=\rho_{gm}\phi_m+\rho_{ga}\rho_s(1-\chi)\frac{V_L p_m}{p_L+p_m}+\rho_{ga}\rho_s\chi\frac{V_L p_m}{p_L+p_m}\exp\left(-\lambda\theta\right)$$

* MERGEFORMAT (5.25)

The right term of Eq. (5.24) represents the dynamic gas exchange between fractures and matrix.

$$Q_m=\frac{\rho_{gm}k_m\delta}{\mu_g}\left(p_m-p_f\right) \quad \text{* MERGEFORMAT (5.26)}$$

where δ is the shape factor for the shale matrix, which reflects the effect of matrix geometry on the gas source term. It can be deduced as

$$\delta=\pi^2\left(\frac{1}{L_x^2}+\frac{1}{L_y^2}\right) \quad \text{* MERGEFORMAT (5.27)}$$

where L_x and L_y are the shale matrix spacing in the *x*-direction and the *y*-direction, respectively. k_m is the apparent permeability of the matrix, which expresses the gas diffusion from the matrix pores into the fractures. This apparent permeability is directly expressed as [17]

$$k_m = \frac{\phi_f d_f^{\,2}}{32\tau_h}\left(1+\frac{\omega}{p_f}\right) \qquad \text{* MERGEFORMAT (5.28)}$$

where d_f is the diameter of pores in the matrix and can be measured by many experiments such as SEM, AFM and CT tests. τ_h reflects the degree of tortuosity in a porous medium. ω is a Klinkenberg factor which is determined by the pore structure of the matrix and the reservoir temperature as

$$\omega = \frac{64\mu_g}{3\pi d_f M}\sqrt{2\pi MRT} \qquad \text{* MERGEFORMAT (5.29)}$$

where M is the gas molecular weight. R represents the universal gas constant and T is the reservoir temperature.

Therefore, the final gas flow equation in a moist matrix can be deduced as

$$\left(\phi_m \frac{\rho_{ga}T_a}{p_a T}+\rho_{ga}\rho_s(1-\chi)\frac{p_a}{p_m}\frac{V_L P_L}{(P_L+p_m)^2}+\rho_{ga}\rho_s\chi\frac{V_L P_L}{(P_L+p_m)^2}\exp(-\lambda\theta)\right)\frac{\partial p_m}{\partial t}$$
$$+\nabla\cdot\left(-\frac{k_m}{\mu_g}\nabla p_m\right)=-\rho_{gm}\frac{\partial\phi_m}{\partial t}+\lambda M_w\rho_{ga}\chi\frac{V_L p_m}{P_L+p_m}\exp(-\lambda\theta)\frac{\partial c_w}{\partial t}-\frac{k_m a}{\mu_g}\left(p_m-p_f\right)$$

* MERGEFORMAT (5.30)

5.3.6. Computational procedure of this coupled multi-physical model

This coupled multi-physical model includes the complex interactions among the deformation of fractured shale, non-Darcy gas flow and moisture transport in fracture network, gas absorption/adsorption in the moist matrix. Fig. 5.5 describes their interactions. As the bottom hole pressure in the horizontal well decreases, gas and water begin to be

extracted as two-phase flow. When the water can no longer form a stable flow, residual water migrates in the form of moisture. At this time, the evaporation of the water film adhering to the surface of the fracture network has to be considered. It does affect the dynamic evolution of permeability and thus has influences on gas production. If the gas pressure in the fractures continues to decrease, the adsorbed gas in the matrix diffuses into the fractures through a slow process. The above physical processes indicate three differences in this current study: Firstly, threshold pressure gradient evolves in the effect of pore pressure and water saturation. Secondly, moisture transports in fractures and water film evaporation modify fracture permeability. Thirdly, the gas-liquid-solid adsorption mechanism exists in the moist shale matrix, further providing a gas source for the fracture network.

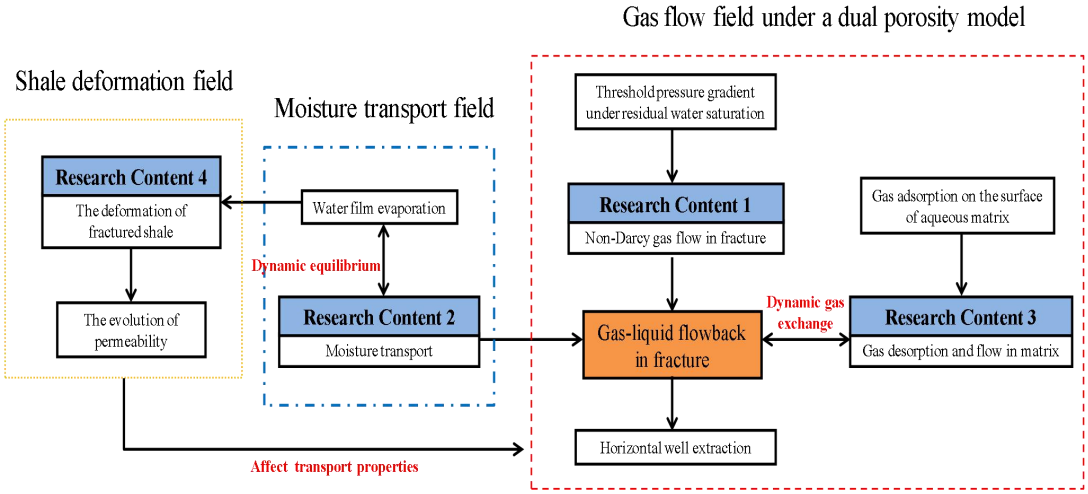

Fig. 5.5. Interactions among this mechanical-hydro-moisture coupled model

5.4. Validation of this model by gas production data

This coupled model is firstly validated by gas production data. Fig. 5.6 shows a typical computation model. Its dimensions are 550 meters long and 145 meters high. A total of 14 hydraulic fractures (the length of each fracture is 47.5 meters) are evenly distributed in the

model. The initial gas pressure in both fractures and matrix is 19.9 MPa. This horizontal well is located at the bottom boundary with a fixed pressure of 3.45 MPa, and no-flow is assumed at its left and right boundaries. The parameters used in the computational model are obtained from the Barnett shale [18] and listed in Table 5.1.

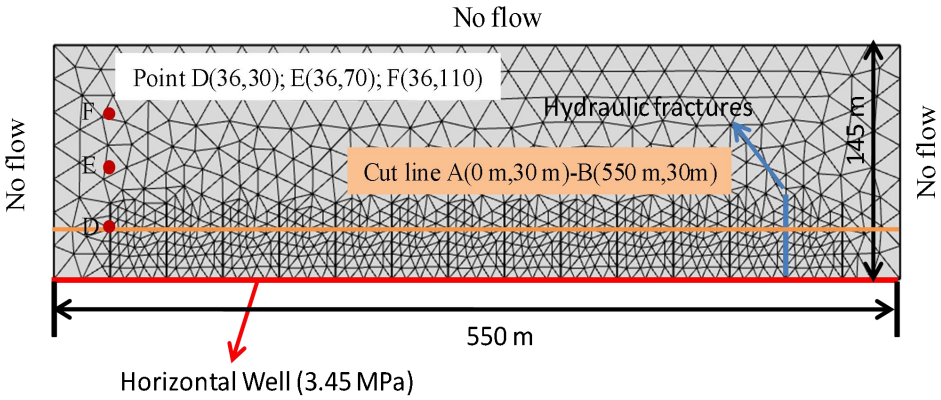

Fig. 5.6. A computational model for a fractured shale gas reservoir

Table 5.1. Parameters for the computational model

Parameter	Value	Physical Meanings	References
S_{iw}	0.2	irreducible water saturation	Given
s_{w0}	0.6	Initial water saturation	Given
c_{v0}	0 mol/m^3	Initial vapor concentration	---
c_{sat}	10 mol/m^3	Saturated water vapor concentration	Given
μ_w	$3.6\times10^{-4} Pa*s$	Water viscosity	Given
μ_{nw}	$2\times10^{-5} Pa*s$	Gas viscosity	Yu and Sepehrnoori [18]
P_{fi}	19.9 MPa	Initial gas pressure in fracture	Yu and Sepehrnoori [18]
P_{mi}	19.9 MPa	Initial gas pressure in matrix	Yu and Sepehrnoori [18]
h_f	47.2 m	Fracture half-length	Yu and Sepehrnoori [18]
P_b	3.45 MPa	Well pressure	Yu and Sepehrnoori [18]
k_0	0.7 mD	Initial permeability in fractured zone	Yu and Sepehrnoori [18]
ϕ_0	0.2	Initial porosity in fractured zone	Yu and Sepehrnoori [18]
k_{hf}	50 mD	Permeability in hydraulic fracture	Yu and Sepehrnoori [18]
ϕ_{hf}	0.25	Porosity in hydraulic fracture	Yu and Sepehrnoori [18]
ϕ_m	0.06	Initial porosity in matrix	Yu and Sepehrnoori [18]
k_m	1.5×10^{-19}m^2	Initial porosity in matrix	Yu and Sepehrnoori [18]
N_f	14	Number of hydraulic fractures	Yu and Sepehrnoori [18]
ν	0.33	Poisson's ratio of shale	Given
ρ_c	2300 kg/m^3	Shale density	Wang and Peng [19]

P_L	6 MPa	Langmuir pressure of gas in shale	Wang and Peng [19]
V_L	0.03 m^3/kg	Langmuir sorption capacity for gas	Wang and Peng [19]
T	352 K	Reservoir temperature	Given
a_w	0.9	Water activity	Given
z	0.1	Water coverage factor	Given
λ	20	Gas adsorption decay coefficient	Teng et al. [20]
M	16 g/mol	Gas molecular weight	---
M_w	18 g/mol	Water molecular weight	---
d_f	$1\times10^{-9}m$	Diameter of pore in matrix	Given

Our previous study used a two-phase flowback model to fit the gas production curve. It is found that the two-phase flow model can describe the gas production rate well in the early stage of shale gas flowback (about 100 days), but the gas production rate is lower than the actual production data in a longer production period. This implies that the shale gas production is divided into different stages and each stage has its own mechanism. Fig. 5.7 shows the entire process of gas production. In stage 1, the two-phase flow is observed in the fractures and a large amount of fracturing fluid is extracted with the gas flow. Usually, this period lasts within 100 days. In stage 2, the water saturation decreases continuously, and the residual water saturation is insufficient to form a continuous flow. At this time, the mechanism of two-phase flow is no longer applicable, and moisture transport becomes the main form of water flow.

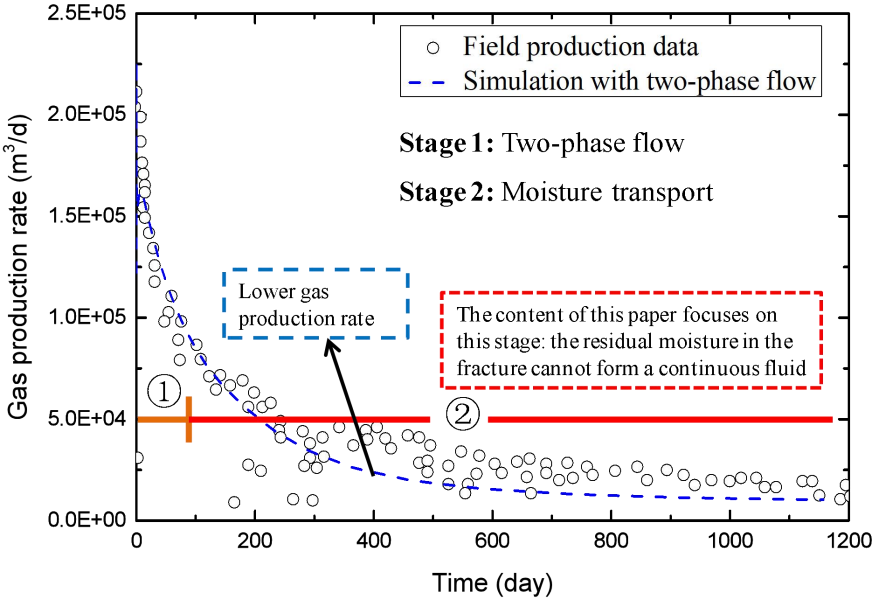

Fig. 5.7. Two stages of water saturation changes in shale gas production

This coupled model of moisture transport is verified by the gas production rate in the post-two-phase flowback period. Fig. 5.8 shows that the gas production rate of the two-phase flow model drops to about 2.4 m^3/d on the 400th day. While, the gas production rate of the moisture transport model is approximate 3.9 m^3/d on the 400th day, which is more consistent with the actual production data. The reason for this difference is that the water in the shale gas reservoir is not sufficient to form a stable water flow after the two-phase flowback stage. If the two-phase flow is still used to predict the gas production, the water production rate is overestimated and the gas production rate is underestimated. Another reason is that the water film vaporization from the surface of fractures is considered in the coupled model of this paper. With the exploitation of gas, the water film adsorbed on the surface of the fractures gradually disappears, increasing the permeability of the fractures and thus enhancing the gas production rate.

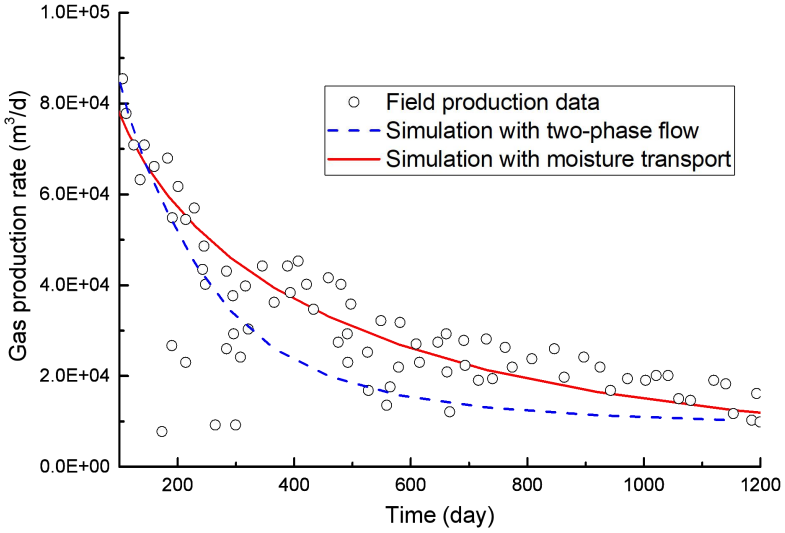

Fig. 5.8. Comparison of numerical simulation with production data in Barnett shale reservoir

5.5. Discussions

5.5.1. Evolution of gas pressure and water saturation in fractures

As shale gas production continues, the gas pressure and water saturation in the fractures begin to fall. Fig. 5.9(a) and 5.9(b) show the distribution of gas pressure and water saturation in fractures at the 100th-day gas production, respectively. A fractured zone is formed around the hydraulic fractures. In this zone, gas pressure and water saturation first begin to decrease. The process of shale gas recovery can be reflected in this figure: the bottom hole pressure decreases, the gas pressure close to the hydraulic fracture begins to decrease and more free gas flows to the hydraulic fracture due to the gas pressure gradient. The water remaining in fractures is also carried out by diffusion and convection under the gas flow.

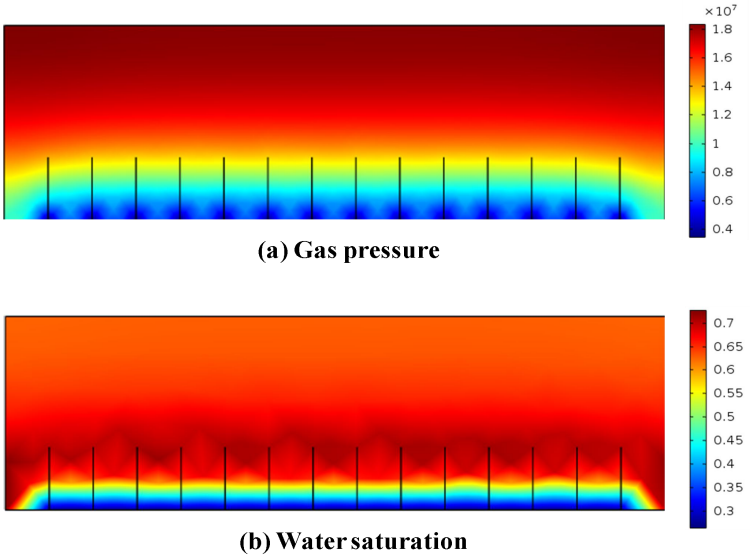

Fig. 5.9. Distribution of (a) gas pressure and (b) water saturation in fracture at the 100th day of gas production

To further describe the evolution of gas pressure and water saturation in fractures, a straight line AB crossing the model is selected. Fig. 5.10(a) gives the distribution of gas pressure in the fractures at the 10th, 100th and 1000th day along the cut line AB. Gas pressures at these times have similar declines. However, the gas pressure at the 1000th day drops little, indicating that the gas extraction in this area is nearly completed. Fig. 5.10(b) shows the distribution of water saturation in the fractures at the 10th, 100th and 1000th day along the cut line AB. Overall, this evolution is similar to gas pressure. However, on the 1000th day, there is still a significant drop in water saturation. It is seen that the transport of moisture depends on the gas flow and lags behind the gas flow.

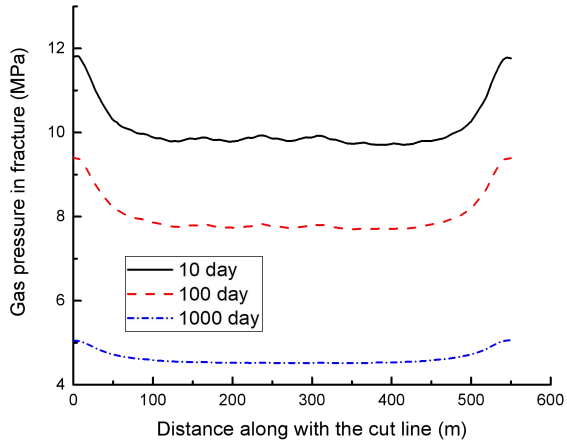

(a) Gas pressure

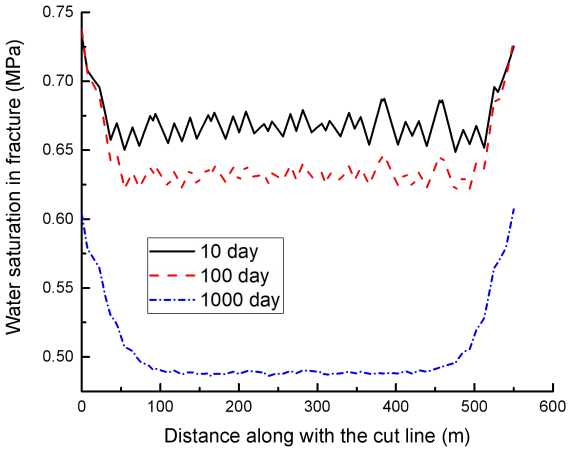

(b) Water saturation

Fig. 5.10. Gas pressure and water saturation in fractures along the cut line AB

5.5.2. Effect of water film on the evolution of fracture porosity

After the initial stage of flowback, the residual water can no longer form a stable flow but is adsorbed on the surface of the fracture as a water film. Evaporation of this layer of water film is directly linked to the flow channel of fractures and affects the shale gas production efficiency. Fig. 5.11 shows the comparison of fracture porosity with and without

water film. If the effect of water film is not considered, the fracture porosity is mainly affected by the volumetric strain and pore pressure. Therefore, the fracture porosity decreases with gas extraction until the gas pressure approaches to the bottom hole pressure. However, the evolution of fracture porosity considering water film experiences two different stages: In the first stage, the water film evaporation strengthens the flow capacity of the fracture channel, the pore pressure of gas drops rapidly, thus the pores are still compacted. In the second stage, the pore pressure drop tends to be slow, and the evaporation of the water film is further taken out by the gas flow. Thus, the fracture porosity presents a self-enhancement. This evolution is consistent with the behavior that moisture transport lags behind gas flow as shown in Fig. 5.10.

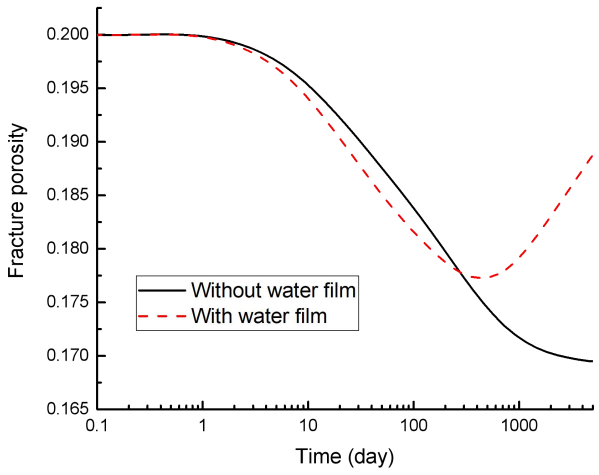

Fig. 5.11. Effect of water film on evolution of fracture porosity

The vertical distance from the well affects the efficiency of water film evaporation, which is important to the evolution of fracture permeability. Three points (D, E, F) with different distances from the well are taken along the vertical direction. Fig. 5.12(a) shows the fracture porosity of these three points on the 200th day. In this stage, the gas pore pressure drops rapidly, the pores are still compacted. Thus, the fracture porosity decreases faster when

it is closer to the well. The evolution of fracture porosity in stage 2 is opposite. The closer to the well, the effect of water film evaporation is more obvious. Thus, point D has the maximum of fracture porosity on the 2000th day (see Fig. 5.12(b)). It is found that the variation of fracture porosity with distance from the well is larger than that in stage 1. This means that the efficiency of water film evaporation greatly varies with the distance from the well.

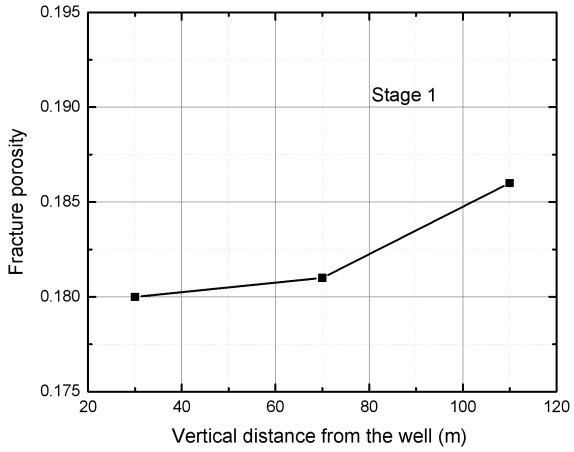

(a) at stage 1

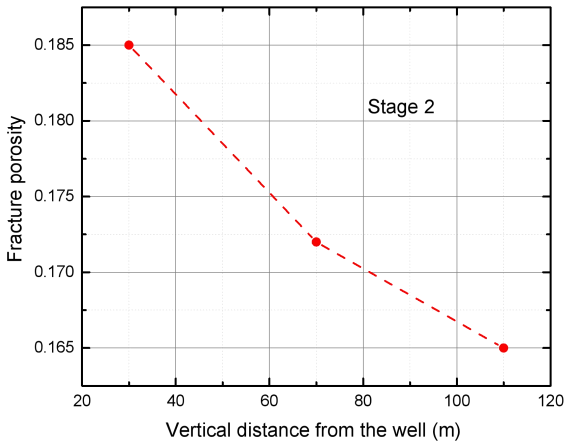

(b) at stage 2

Fig. 5.12. Evolution of fracture porosity with vertical distance from the well at different stages

5.5.3. Effect of non-Darcy flow on gas production rate

5.5.3.1. Comparison of non-Darcy flow and Darcy flow

The effect of the threshold pressure gradient on shale gas production rate is studied. Two contrasting cases have been designed in this section: non-Darcy flow with TPG and Darcy flow. Fig. 5.13 shows the evolution of the gas production rate with production time in these two cases. It is found that the gas production rate considering TPG effect is lower than that of Darcy flow at the initial production period. When the gas production rate begins to decline rapidly, the influence of TPG is no longer important, and these two gas production rate curves basically coincide. In the later stage of gas production, the gas pressure gradient decreases to a relatively low value, the TPG effect will restart and obstruct the flow channel.

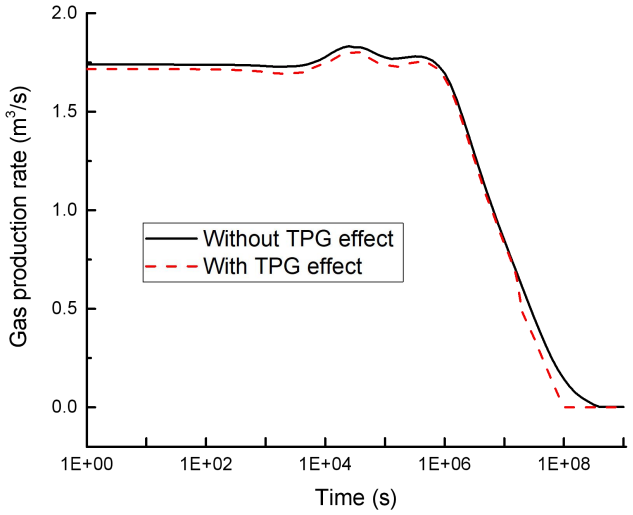

Fig. 5.13. Effect of TPG on gas production rate

5.5.3.2. Evolution of threshold pressure gradient

In order to investigate the evolution of the threshold pressure gradient under the residual water saturation, the three points of D, E, and F shown in Fig. 5.6 will be studied. Since their distances from the well are different, the evolution of the threshold pressure gradient at the three points is not the same. Fig. 5.14 shows that the threshold pressure gradient at point D (the closest point to the well) is the first to change, and the trend is to increase first and then decrease. The evolutions of the threshold pressure gradient at these three points are similar. However, the point far from the well shows a hysteresis and the maximum value is greater.

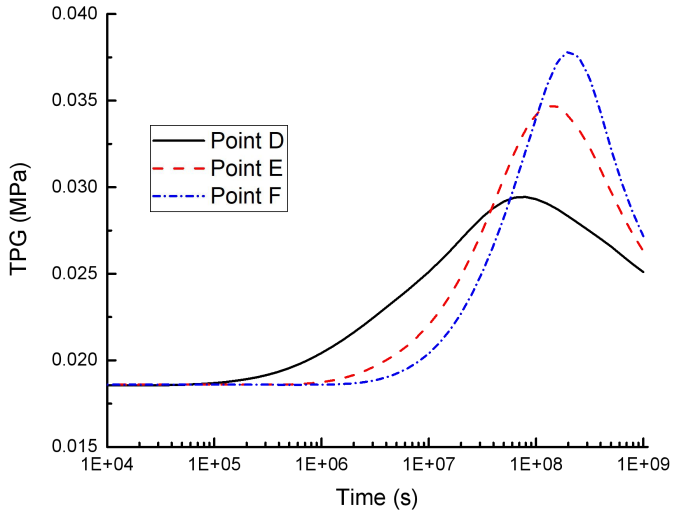

Fig. 5.14. Evolution of TPG at different distances from well

The changes in gas pressure and water saturation in fractures are presented in Fig. 5.15(a) and 5.15(b), respectively. The distance from the well is farther, the gas pressure in fractures also shows a hysteresis. This is the reason why the threshold pressure gradient varies with the distance from the well. Eq. (5.2) shows that two important factors affect the threshold pressure gradient. Except for the pore pressure, the other is water saturation. Fig. 5.15(b) compares the water saturations at these three points. When the distance from the well is

farther, the water film remaining on the surface of fractures cannot be rapidly taken out due to the slower gas flow rate. Therefore, there is a transient increase in water saturation and then decreases. This change leads to a corresponding increase in the threshold pressure gradient away from the well.

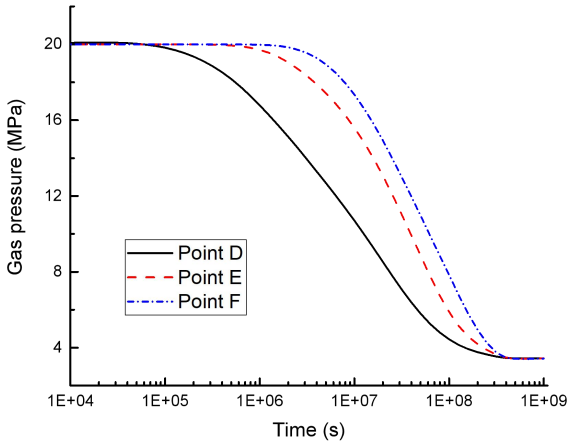

(a) Gas pressure

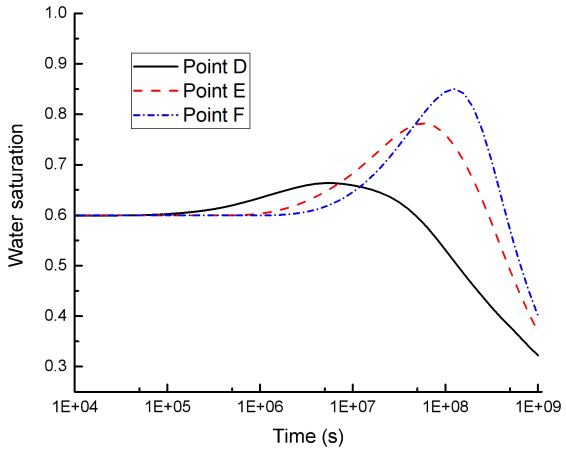

(b) Water saturation

Fig. 5.15. Evolutions of gas pressure and water saturation at three points of D, E and F

5.5.4. Gas exchange between fractures and matrix

Dynamic gas exchange occurs between the fractures and the matrix. As the gas pressure in the fractures continues to decrease, gas adsorbed on the surface of the matrix desorbs and then flow into the fracture through a slow diffusion process. This gas is an important source during the later stage of production and has important implications for the accurate assessment of shale gas production. This slow diffusion process is affected by many factors such as pore size, swelling of clay minerals, and moisture content.

5.5.4.1. Effect of gas adsorption decay coefficient on gas exchange

λ is the gas adsorption decay coefficient to reflect the gas adsorption capacity in the moist shale matrix. In this study, λ is 20 which was obtained from the literature [20]. In order to investigate the effect of gas adsorption decay coefficient on gas exchange, two cases are presented in Fig. 5.16. In a short-term gas production, the gas extracted is mainly from the free gas in fractures. The cumulative gas exchange content increases slowly. When the gas pressure in fractures drops to a lower value, the gas exchange content rises rapidly and the effect of gas adsorption decay coefficient becomes obvious. The reduction of the gas adsorption decay coefficient means that more gas is absorbed on the matrix. Thus, the gas exchange content is greater. When the gas adsorption decay coefficient is 20, 7.15% decline of cumulative gas exchange content is observed in Fig. 5.16.

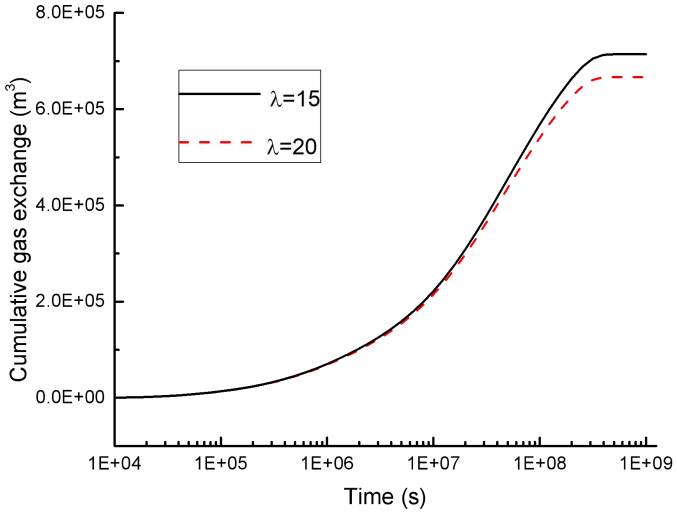

Fig. 5.16. Effect of gas adsorption decay coefficient on cumulative gas exchange

5.5.4.2. Effect of water coverage factor on gas exchange

The water coverage factor χ describes the proportion of gas-solid adsorption and gas-liquid adsorption, which is depicted in Fig. 5.4. In this study, the Langmuir adsorption formula is modified by the residual water saturation. When the water saturation is higher, more gas adsorbed in the shale matrix is reduced accordingly due to the competitive adsorption of water molecules and gas molecules. When the clay minerals in the matrix are relatively higher, this phenomenon is more obvious. Fig. 5.17 shows the cumulative gas exchange under different water coverage factors. When the water coverage factor is 0.1, the cumulative gas exchange content can reach $7.5\times10^{5}\,m^{3}$. Compared with the case of water coverage factor is 0.1, a 13.3% reduction is measured.

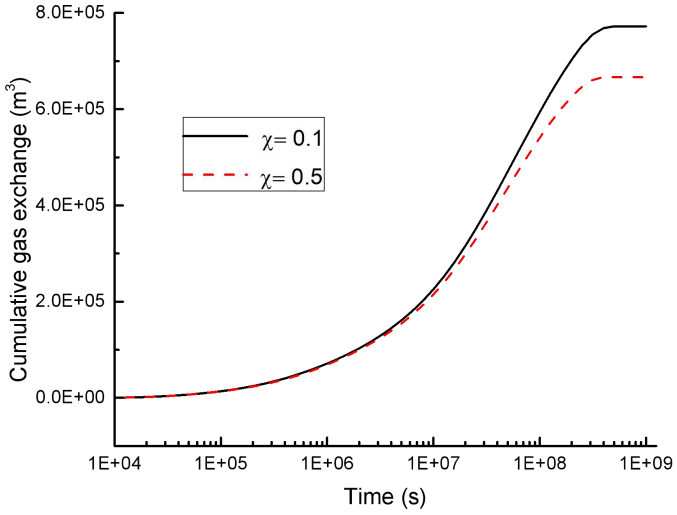

Fig. 5.17. Effect of water coverage factor on cumulative gas exchange

5.6. Conclusions

This chapter introduced moisture transport into our previous fully-coupled model for shale gas production and explored the threshold pressure gradient under residual water saturation, the water film evaporation on the surface of fractures, and the gas-liquid-solid adsorption mechanism in the matrix. These interactions were incorporated into the mechanical-hydro-moisture coupled model. Based on these studies, the following conclusions can be obtained.

First, the overestimation of water production data by the two-phase flowback model led to an excessive decrease in the predicted gas production rate. This coupled model of moisture transport was more suitable for long-term gas production. Further, the water saturation was affected by gas flow but lags behind the gas flow. Similarly, the fracture porosity increased due to water film evaporation, but this evaporation process also lagged behind the effect of pore pressure.

Second, the non-Darcy flow due to overcoming the threshold pressure gradient had an obvious influence on gas production rate at the beginning of production and near the end of production. This threshold pressure gradient varied with the distance from the well. It was found that the closer to the well, the threshold pressure gradient changed faster, but the smaller maximum was obtained.

Finally, the residual water saturation modified the gas-liquid-solid sorption capacity. Two parameters of gas adsorption decay coefficient and water coverage factor were used to describe this effect. The former reflected the influence of residual water on gas adsorption capacity. The latter described the proportion of water molecules on the surface of the matrix. They changed gas exchange content and thus affected gas production rate.

5.7. References

[1] Ezulike O D, Dehghanpour H. Modelling flowback as a transient two-phase depletion process. Journal of Natural Gas Science and Engineering, 2014, 19: 258-278.

[2] Xue Y, Zhang X, Ding G. Mathematical model study on gas and water two-phase of early-time flowback in shale gas wells. Science Technology and Engineering, 2017, 24: 218-222.

[3] Feng D, Li X, Wang X, Li J, Sun F, Sun Z, Zhang T, Li P, Chen Y, Zhang X. Water adsorption and its impact on the pore structure characteristics of shale clay. Applied Clay Science, 2018, 155: 126-138.

[4] Zhong Y, Zhang H, Shao Z, Li K. Gas transport mechanisms in micro- and nano-scale matrix pores in shale gas reservoirs. Chemistry and Technology of Fuels and Oils, 2016, 52(2): 238-238.

[5] Cai J, Yu B. A discussion of the effect of tortuosity on the capillary imbibition in porous media. Transport in Porous Media, 2011, 89(2): 251-263.

[6] Hao F, Cheng L S, Hassan O, Hou J, Liu C, Feng J. Threshold pressure gradient in ultra-low permeability reservoirs.Liquid Fuels Technology, 2008, 26(9): 1024-1035.

[7] Wang X, James J S. Discussion of liquid threshold pressure gradient. Petroleum, 2017, 3(2): 232-236.

[8] Dou H, Ma S, Zou C, Yao S. Threshold pressure gradient of fluid flow through multi-porous media in low and extra-low permeability reservoirs. Science China(Earth Sciences), 2014, 57(11): 2808-2818.

[9] Prada A, Civan F. Modification of Darcy's law for the threshold pressure gradient. Journal of Petroleum Science & Engineering, 1999, 22(4): 237-240.

[10] Zhang Z, Jiang H, Yu C. Influence factors of shale gas productivity considering the start-up pressure gradient and stress sensitivity. Complex Hydrocarbon Reservoirs, 2014, 2: 47-50.
[11] Bachu S, Bennion B. Effects of in-situ conditions on relative permeability characteristics of CO_2-brine systems. Environmental Geology, 2008, 54(8): 1707-1722.
[12] Datta A K. Porous media approaches to studying simultaneous heat and mass transfer in food processes. I: problem formulations. Journal of Food Engineering, 2007, 80(1): 80-95.
[13] Deriszadeh M, Wong R C. One-dimensional swelling behavior of clay and shale under electrical potential gradient. Transport in Porous Media, 2014, 101(1): 35-52.
[14] Lyu Q, Ranjith P G, Long X, Kang Y, Huang M. A review of shale swelling by water adsorption. Journal of Natural Gas Science and Engineering, 2015, 27: 1421-1431.
[15] Belton G R. Langmuir adsorption, the gibbs adsorption isotherm, and interracial kinetics in liquid metal systems. Metallurgical Transactions B, 1976, 7(1): 35-42.
[16] Li J, Li X, Wang X. Water distribution characteristic and effect on methane adsorption capacity in shale clay. Petroleum Exploration & Development, 2016, 35(5): 606-612.
[17] Liu J, Chen J, Rui F, Xue N, Wang J. Numerical simulation for effect of discrete fracture network on shale gas productivity of horizontal well. Coal Geology and Exploration, 2017, 45(6): 66-71.
[18] Yu W, Sepehrnoori K. Simulation of gas desorption and geomechanics effects for unconventional gas reservoirs. Fuel, 2014, 116: 455-464.
[19] Wang J G, Peng Y. Numerical modeling for the combined effects of two-phase flow, deformation, gas diffusion and CO_2 sorption on caprock sealing efficiency. Journal of Geochemical Exploration, 2014, 144: 154-167.
[20] Teng T, Wang J G, Gao F, Ju Y, Xia T. Impact of water film evaporation on gas transport property in fractured wet coal seams. Transport in Porous Media, 2016, 113(2): 357-382.

Chapter 6: Sealing efficiency analysis for shallow-layer caprocks in CO_2 geological storage

6.1. Introduction

When CO_2 migrates from deep reservoirs to shallow caprocks, it experiences a transition from a supercritical phase to a subcritical phase (gas or liquid phase, called the phase transition) depending on the burial depth of the caprock. This phase transition causes a sharp change in the viscosity and density of CO_2, further penetrating the caprock. This is a key scientific issue for the safety of geological storage of CO_2-the phase transition in the critical depth caprock. However, there is still a lack of fully coupled multi-physical model considering this phase transition when the sealing efficiency of the caprock is evaluated. Therefore, this chapter continues to expand the two-phase flow model to consider the phase transition effect in the shallow caprock. The drastic changes of CO_2 viscosity and density are coupled into the model through data interpolation. Then, based on the shallow caprock at a depth of 800 m, the effects of temperature and pressure on the sealing efficiency of the caprock are numerically investigated.

6.2. Compressibility and viscosity of real gas

In most instances, CO_2 is injected into deep reservoirs in a supercritical state. A small amount of CO_2 leaked into shallow layers would transform into a gas or liquid phase. Both the density and viscosity of this CO_2 have a rapid change around the critical state. The evolutions of viscosity and density with temperature or pressure are presented in Fig. 6.1. These figures are based on the CO_2 parameters and calculated from the NIST (www.nist.gov).

When the temperature is at the critical value, both viscosity and density of CO_2 increase with gas partial pressure (see Fig. 6.1(a)). The physical properties of CO_2 dramatically change when the gas partial pressure is close to the critical pressure. Both viscosity and density can increase by 150% in the critical region. Further, this behavior may modify the CO_2 penetration process. When the gas partial pressure is at the critical value, the evolutions of viscosity and density with temperature are shown in Fig. 6.1(b). With the increase of temperature, both viscosity and density of CO_2 begin to decline and about 65% reduction is observed in the critical region. Thus, a brief conclusion can be drawn from the above results: When the CO_2 is in the critical region, its physical properties change dramatically because of its phase transition and this phase transition affects the CO_2 transport. Therefore, the phase transition of CO_2 should be carefully considered for the assessment of CO_2 leakage at the critical depth.

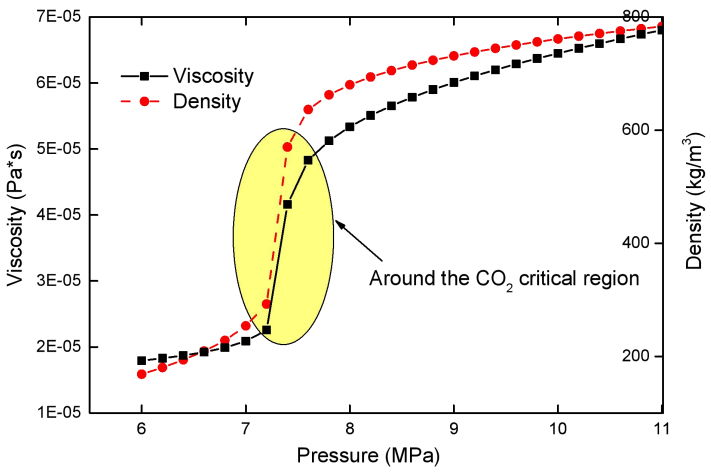

(a) Evolution of viscosity and density with pressure

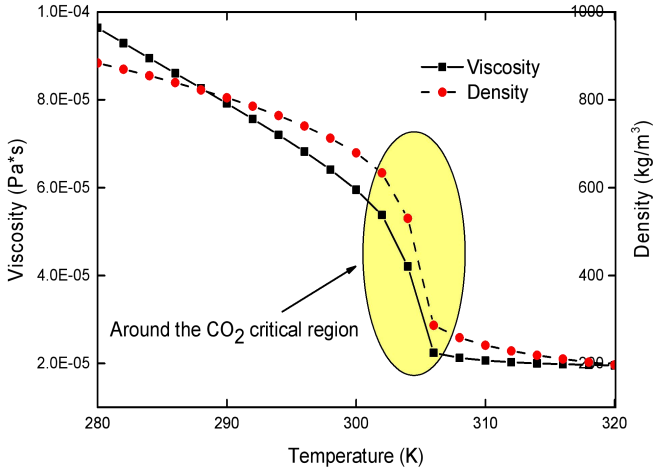

(b) Evolution of viscosity and density with temperature

Fig. 6.1. Evolution of viscosity and density in the critical state region

In the process of CO_2 displacing brine water within the caprock, the water density ρ_w remains unchanged, but the CO_2 density ρ_{nw} varies with temperature and gas partial pressure. Based on the equation of state, the CO_2 density is expressed as

$$\rho_{nw} = \frac{M_{CO_2}}{ZRT} p_{nw} \qquad \text{* MERGEFORMAT (6.1)}$$

The changes of CO_2 density with respect to pressure and temperature are expressed in terms of their compressibility:

For pressure:
$$c_p = \frac{\partial \rho}{\partial p_{nw}} = \frac{M_{CO_2}}{ZRT} - \frac{M_{CO_2}}{Z^2 RT} \frac{\partial Z}{\partial p_{nw}}$$

* MERGEFORMAT (6.2)

For temperature:
$$c_T = \frac{\partial \rho}{\partial T} = -\frac{M_{CO_2} p_{nw}}{ZRT^2} - \frac{M_{CO_2} p_{nw}}{Z^2 RT} \frac{\partial Z}{\partial T}$$

* MERGEFORMAT (6.3)

where p_{nw} represents the partial pressure of CO_2. M_{CO_2} is the molecular weight of CO_2, R is the universal gas constant, and T is the gas temperature. Z is the compressibility factor of real gas which represents the degree of gas compression. Because the CO_2 physical properties

change sharply near the critical point, it is difficult to find a fitting curve to accurately describe the compressibility factor in this critical region. Because the critical depth of caprock layer is considered, temperature and pressure are focused in a small range (6-10 MPa, 290-320 K) around the critical point. In this small range, the compressibility factor of Z can be obtained by a CO_2 physical calculator from NIST (www.nist.gov). It can be generally expressed as

$$Z = f(P,T) = f(P_1 : \Delta P : P_2; \quad T_1 : \Delta T : T_2)$$
$$= f(6 : 0.2 : 10MPa; \quad 290 : 2 : 320K)$$

* MERGEFORMAT (6.4)

This relationship of Z with pressure and temperature is presented in Fig. 6.2. For a given pair of temperature and pressure, Z and its partial derivatives can be obtained through the interpolation in the neighbourhood of the pair. This is done by a MATLAB script. The computational algorithm has been incorporated into our fully coupled multi-physical model within the framework of COMSOL with MATLAB.

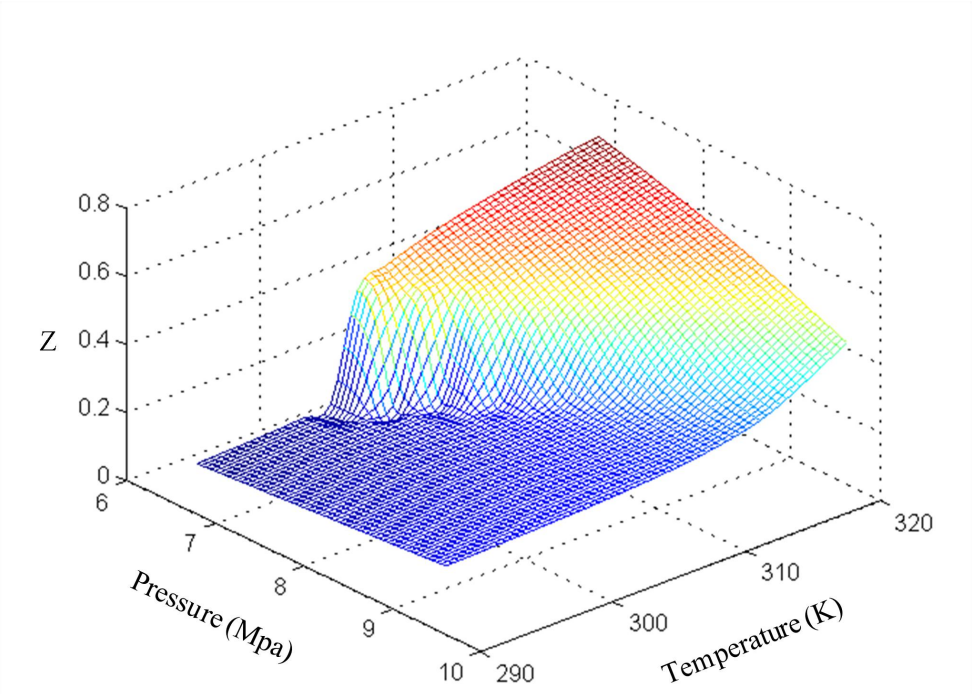

Fig. 6.2. Meshgrid of CO_2 compressibility factor around the critical state

The viscosity of CO_2 is a function of reduced temperature and reduced pressure. Jarrahian and Heidaryan [1] proposed a generalized correlation in wide ranges of pressures (0.1 - 137.8 MPa) and temperatures (241 - 473 K). Thus, the viscosity of CO_2 can be expressed as

$$\mu = \mu_a \left[1 + \frac{A_{11}}{T_r^5} \left(\frac{p_r^4}{T_r^{20} + P_r^4} \right) + A_{12} \left(\frac{P_r}{T_r} \right)^2 + A_{13} \left(\frac{P_r}{T_r} \right) \right]$$

* MERGEFORMAT (6.5)

where reduced pressure is $p_r = p_{nw} / p_c$ and the reduced temperature is $T_r = T / T_c$. T_c and p_c are the critical temperature and pressure of the real gas, respectively. μ_a is the viscosity under the standard condition. A_{11}, A_{12} and A_{13} are independently tuned coefficients.

6.3. Fully coupled multi-physical model for real gas transports in caprock

6.3.1. Governing equation for caprock deformation

For linear elastic caprocks, the Navier equation is expressed as [2]

$$G u_{i,jj} + \frac{G}{1-2\nu} u_{k,kj} = K(\varepsilon_{s1,i} + \varepsilon_{s2,i}) - \alpha p_{,i} - f_i$$

* MERGEFORMAT (6.6)

where u_i is the displacement in the i th direction. G and ν are the shear modulus and the Poisson ratio, respectively. $\alpha = 1 - \frac{K_c}{K_s}$ is defined as the Biot coefficient. ε_{s1} and ε_{s2} present the sorption volumetric strain and the thermal expansion strain, respectively. This

governing equation has four components of body forces: gravity force (f_i), pore pressure induced drag force ($\alpha p_{,i}$), and body forces caused by thermal expansion and gas sorption.

6.3.2. Governing equations for heat transfer

If the inter-thermal convertibility is neglected, the governing equation of thermal equilibrium can be obtained by [3-5]

$$\frac{\partial[(\rho c)_M \cdot T]}{\partial t} = -TK_{nw}\alpha_{nw}\nabla\left(\frac{-kk_{rnw}}{\mu_{nw}}\nabla p_{nw}\right) - TK\alpha_T\frac{\partial\varepsilon_v}{\partial t} - \nabla q_T$$

* MERGEFORMAT (6.7)

where α_T is the thermal expansion coefficient, K is the bulk modulus of the porous medium. ε_v is the volumetric strain. k is the absolute permeability and k_{rnw} is the relative permeability for gas. u_{nw} is the viscosity of the gas. K_{nw} is the bulk modulus of the gas and α_{nw} is the thermal expansion coefficient of the gas [4]. $(\rho c)_M$ is the specific heat capacity of the porous medium. T is the current temperature.

The total heat flux q_T has two parts: the transmitted heat flux and the convective heat flux. They are written as

$$q_T = -\lambda_M\nabla T + \rho_{nw}c_{nw}\frac{-kk_{rnw}}{\mu_{nw}}\nabla p_{nw}\left(T - T_a\right)$$

* MERGEFORMAT (6.8)

$$\lambda_M = (1-\phi)\lambda_s + \phi\lambda_{nw} \qquad \text{* MERGEFORMAT (6.9)}$$

where ρ_{nw} is the mass density of the gas, and c_{nw} is the gas specific heat constant. λ_M , λ_s and λ_{nw} are the thermal conductivities of caprock, matrix, and gas, respectively. T_a is the storage temperature.

The governing equation of heat transport is finally simplified as

$$(\rho c)_M \frac{\partial T}{\partial t} + TK_{nw}\alpha_{nw}\nabla\left(\frac{-kk_{rnw}}{\mu_{nw}}\nabla p_{nw}\right) + TK\alpha_T \frac{\partial \varepsilon_v}{\partial t} = \lambda_M \nabla^2 T - \rho_{nw} c_{nw} \frac{-kk_{rnw}}{\mu_{nw}} \nabla p_{nw} \nabla T$$

* MERGEFORMAT (6.10)

6.3.3. Governing equations for two-phase flow

6.3.3.1. Porosity and permeability models

The porosity model proposed by Wang et al. [6] is here extended to consider the thermal expansion, too. The porosity is then expressed as

$$\phi = \phi_0 + \alpha(\varepsilon_v + \frac{p}{K_s} - \varepsilon_{s1} - \varepsilon_{s2})$$

* MERGEFORMAT (6.11)

where ϕ_0 is the initial porosity and ϕ is the current porosity. At the right-hand side of the above equation, the second term presents the volumetric strain (ε_v), the strain induced by pore pressure (p/K_s) and the sorption strain (ε_{s1}), respectively. ε_{s2} represents the contribution of thermal expansion ($\alpha_T \Delta T$) to the change of porosity. $\Delta T = T - T_0$ is the temperature increment where T_0 is the reference temperature. K_s is the bulk modulus of grains. The pore pressure is the weighted average of water pressure and gas pressure.

Therefore, the differentiation of ϕ with time is

$$\frac{\partial \phi}{\partial t} = \alpha(\frac{\partial \varepsilon_v}{\partial t} + \frac{1}{K_s}\frac{\partial p}{\partial t} - \frac{\partial \varepsilon_{s1}}{\partial t} - \alpha_T \frac{\partial T}{\partial t})$$

* MERGEFORMAT (6.12)

The relationship between porosity and permeability can be expressed through the Kozeny-Carman type model [7]

$$\frac{k}{k_0}=\left(\frac{\phi}{\phi_0}\right)^3\left(\frac{1-\phi_0}{1-\phi}\right)^2 \qquad \text{* MERGEFORMAT (6.13)}$$

where k is the current permeability and k_0 is the initial permeability at the porosity of ϕ_0. Thus, the following cubic relationship is obtained if the porosity is less than 10%:

$$\frac{k}{k_0}=\left(\frac{\phi}{\phi_0}\right)^3$$

* MERGEFORMAT (6.14)

6.3.3.2 Relative permeability model

Oostrom et al. [8] checked six different models by their test data of sandstone. Their test results showed that the saturation distribution in the process of two-phase flow largely depended on relative permeability model. Li et al. [9] conducted the CO_2 effective permeability experiment of caprock. They found that CO_2 leakage by volumetric flow was disastrous once it occurred. Bachu and Bennion [10] measured the relationship of relative permeability and saturation in sandstone, carbonate, and several shale formations. Fig. 6.3 presents the fittings with the following equations for the nonlinear relationship between relative permeability and CO_2 / water saturation during the drainage process.

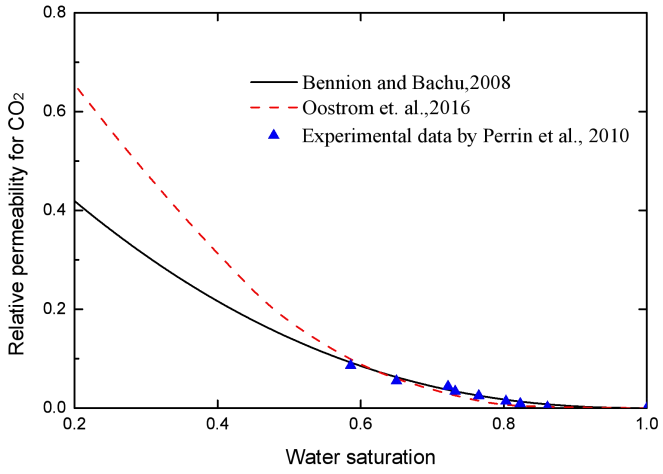

(a) Relationship of gas relative permeability and water saturation

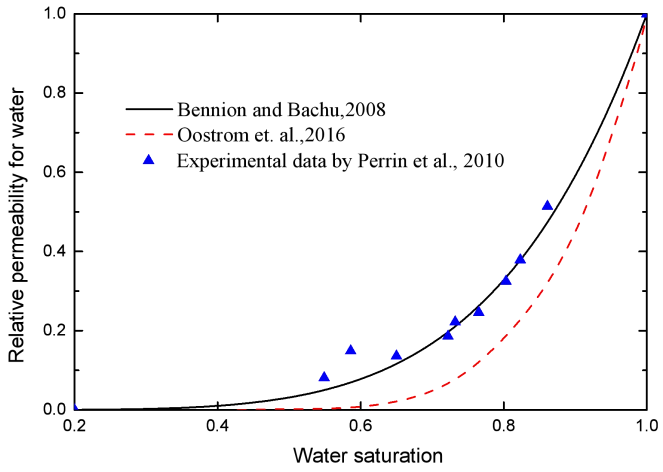

(b) Relationship of water relative permeability and water saturation

Fig. 6.3. Relative permeability-water saturation relations during the drainage process

It shows that the following relative permeabilities are applicable to many rocks, but their model coefficients vary with rocks [10].

$$k_{rw} = k_{rw}^{\max}(s_w^*)^{N_w} \qquad \text{* MERGEFORMAT (6.15)}$$

$$k_{rnw} = k_{rnw}^{\max}(s_{nw}^*)^{N_{nw}} \qquad \text{* MERGEFORMAT (6.16)}$$

$$s_w^* = 1 - s_{nw}^* \qquad \text{* MERGEFORMAT (6.17)}$$

$$s_{nw}^* = \frac{s_{nw} - s_{nwi}}{1 - s_{wi} - s_{nwi}} \qquad \text{* MERGEFORMAT (6.18)}$$

where k_{rw} and k_{rnw} are the relative permeabilities of water and CO_2, respectively. $k_{rw}^{\max}$ and $k_{rnw}^{\max}$ represent the endpoint relative permeabilities for water and CO_2, respectively. N_w and N_{nw} are the reference parameters. s_{nw} is the saturation of CO_2. s_{wi} is the water irreducible saturation, and s_{nwi} is the CO_2 irreducible saturation.

6.3.3.3. Governing equations for CO_2-water flow

The two-phase flow of CO_2 and water occurs in the fracture, where the wetting phase is water and the non-wetting phase is CO_2. Their governing equations are obtained from the mass conservation laws of water and CO_2, respectively.

For the water phase, the mass conservation law is

$$\frac{\partial(\phi\rho_w s_w)}{\partial t}+\nabla\left[-\frac{kk_{rw}}{\mu_w}\rho_w(\nabla p_w+\rho_w g\nabla H)\right]=f_w$$

* MERGEFORMAT (6.19)

For the CO_2 phase, it is

$$\frac{\partial m}{\partial t}+\nabla\left[-\frac{kk_{rnw}}{\mu_{nw}}\rho_{nw}(\nabla p_{nw}+\rho_{nw}g\nabla H)\right]=f_{nw}$$

* MERGEFORMAT (6.20)

The CO_2 mass in the fracture exists in both free phase and absorbed phase. This CO_2 mass can be given by

$$m=\phi\rho_{nw}s_{nw}+\rho_{ga}\rho_c\frac{V_L p^*}{p_L+p^*}+\rho_{ga}\rho_c m_b$$

* MERGEFORMAT (6.21)

where μ_w and μ_{nw} are the viscosities of water and CO_2 under in-situ conditions, respectively. p_w and p_{nw} are the pore pressures of water and CO_2 in the fracture, respectively. $p^*=s_{nw}p_{nw}$ is the partial gas pressure. s_w and s_{nw} present the saturations of water and CO_2, respectively. V_L is the Langmuir volume constant and p_L is the Langmuir pressure. H denotes the coordinate for vertical elevation. ρ_c is the density of the shale caprock, and ρ_{ga} is the gas density under the standard conditions. g is the gravitational acceleration. At the right term, f_w and f_{nw} are the sources of water and CO_2, respectively.

m_b is the CO_2 content in the matrix. Its change depends on the gas exchange between fractures and matrix.

Eqs. (6.1-6.3), (6.11), (6.21) are substituted into Eqs. (6.19) and (6.20) after some simplifications, the final governing equations of two-phase flow can be obtained as follows.

For water:

$$\phi c_s \frac{\partial p_{nw}}{\partial t} - \phi c_s \frac{\partial p_w}{\partial t} + s_w \frac{\partial \phi}{\partial t} - \nabla\left[-\frac{kk_{rw}}{\mu_w}(\nabla p_w + \rho_w g \nabla H)\right] = f_w$$

* MERGEFORMAT (6.22)

For CO_2:

$$\begin{aligned}
&\left[\phi s_{nw} c_p - \phi c_s + \frac{ZT}{Z_a T_a}\frac{p_a}{p_{nw}}\rho_c \frac{V_L p^*}{(p_L + p^*)^2}(s_{nw} - p_{nw} c_s)\right]\frac{\partial p_{nw}}{\partial t} \\
&+\left[\phi c_s + p_{nw} c_s \beta \rho_c \frac{V_L p^*}{(p_L + p^*)^2}\right]\frac{\partial p_w}{\partial t} \\
&+\phi s_{nw} c_T \frac{\partial T}{\partial t} + \beta \rho_c \frac{dm_b}{dt} + s_{nw}\frac{\partial \phi}{\partial t} \\
&+\nabla\left[-\frac{kk_{rnw}}{\mu_{nw}}\rho_{nw}(\nabla p_{nw} + \rho_{nw} g \nabla H)\right] = f_{nw}
\end{aligned}$$

* MERGEFORMAT (6.23)

where Z_a, T_a and p_a are the compressibility factor, temperature and pressure at the standard condition, respectively. s_w is the saturation of water and c_s is the compressibility of water saturation with respect to capillary pressure.

6.3.4. Computational procedure of this fully coupled multi-physical model

This fully coupled multi-physical model includes the complex interactions among the deformation of caprock, two-phase flow in fracture, CO_2 absorption/adsorption in the matrix and the heat transport in the caprock. Fig. 6.4 describes these interactions among multi-physical processes. With the process of CO_2 displacing water, a new profile of water

and CO_2 pressures is formed. This pressure profile can give rise to the deformation of caprock. For the fracture, caprock deformation changes both porosity and permeability and directly modifies the transport capacity of the fluid. On the other hand, the two-phase flow applies a drag force to the shale skeleton. For the matrix, any change of pressure would affect the gas adsorption/desorption from the surface of the matrix, thus the gas storage capacity of shale caprock is altered by the deformation of caprock and the two-phase flow in the fracture. This paper added the heat transfer to this fully coupled multi-physical model. This meant that the current study had the following two differences: Firstly, the physical properties of CO_2 are not only affected by pressure, but also by temperature. The phase transition in the shallow layer is heavily affected by both pressure and temperature. Secondly, thermal expansion has impacts on both porosity and permeability.

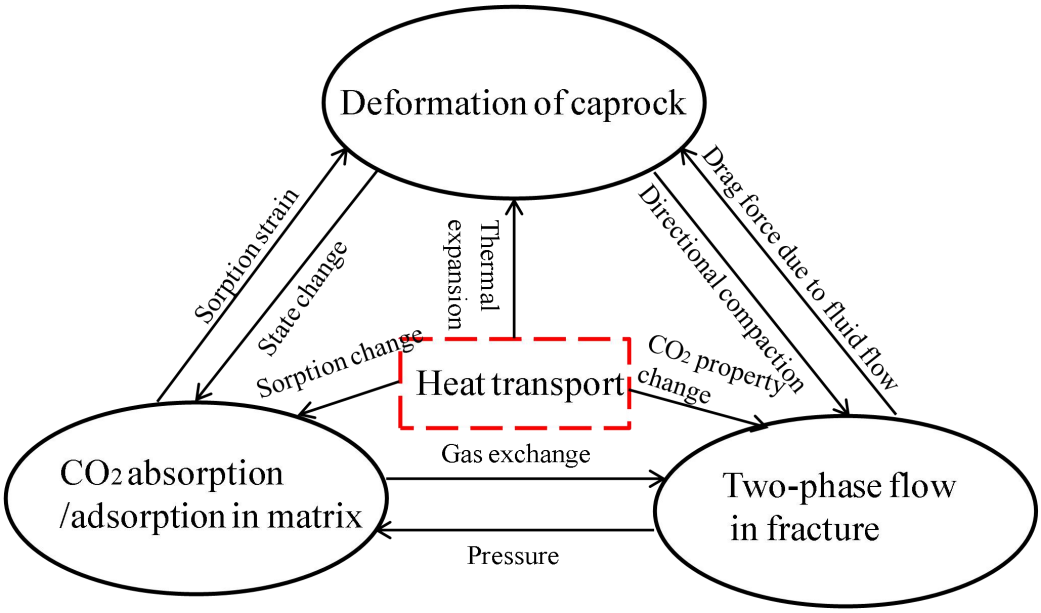

Fig. 6.4. Interactions of multi-physical processes in shale caprock

6.4. Numerical analysis for CO_2 penetration depth in the phase transition zone

The above fully coupled multi-physical model is used to assess the caprock sealing efficiency of a caprock layer at the burial depth of approximately 800 m, where CO_2 may be in the critical state and its physical properties may change dramatically. In this critical region, CO_2 may exist in three states: supercritical phase, superheated gas, and supercooled liquid. During the CO_2 phase transition from supercritical state to gas state, the viscosity decreases rapidly to help CO_2 easily penetrate into the caprock. With the decrease of temperature, the CO_2 may change from supercritical state to liquid or gas. In this phase transition process, the decrease of viscosity is in favor of CO_2 penetration, but the thermal expansion of the shale matrix reduces the permeability of caprock and hence hinders the penetration. Both the physical properties of CO_2 and the permeability play important roles in caprock sealing efficiency. Further, the CO_2 penetration depth is an effective and convenient measure for the caprock sealing efficiency and is determined by the flow mobility, pressure, temperature, and their interactions with rocks.

6.4.1. Model parameters in simulations

The computational model is a domain of 10 m×10 m as shown in Fig. 6.5. This is a two-dimensional problem located at the depth of 800 m.

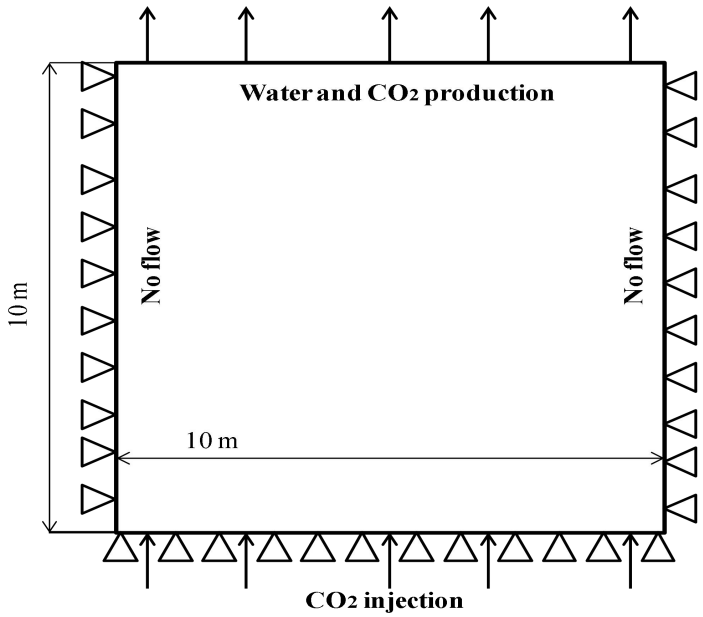

Fig. 6.5. A computational model for CO_2-water displacement

The reservoir pressure is 7.15 MPa. CO_2 injection pressure is applied at the bottom boundary and the CO_2 injection pressure increases from the reservoir pressure to 9 MPa with an exponential function. At the top boundary, the reservoir pressure is given. Water and CO_2 can flow out with fractional flow rates according to their flow mobility. The CO_2 in the deeper layer has a higher temperature. It flows from the bottom to the top through the two-phase flow. Table 6.1 lists all parameters used in simulations.

Table 6.1. Model parameters in a computation

Parameter	Unit	Value	Physical Meanings
S_{rnw}		0.15	Residual saturation of CO_2
S_{rw}		0.6	Residual saturation of water
μ_{w}	Pa•s	3.6×10^{-4}	Water viscosity
λ_{w}		6.5	Corey parameter for water
λ_{nw}		2.6	Corey parameter for CO_2
P_{w0}	MPa	7.15	Initial water pressure in caprock
P_{nw0}	MPa	7.3	Initial CO_2 pressure in caprock
E_c	GPa	8	Young's modulus of shale
E_s	GPa	20	Young's modulus of shale grains

P_{wf}	MPa	7	Pressure at the top boundary
T_c	K	304	Critical temperature of CO_2
k_0	m^2	1.5×10^{-19}	Initial absolute permeability
ϕ_0		0.08	Initial porosity
ν		0.3	Poisson's ratio of shale
ρ_c	kg/m^3	2300	Shale density
P_L	MPa	6	Langmuir pressure of CO_2 in shale
V_L	m^3/kg	0.03	Langmuir sorption capacity of shale for CO_2
ε_L		0.027	Langmuir swelling strain
k_{rw}^{max}		1	End-point relative permeability for water phase
k_{rnw}^{max}		0.015	End-point relative permeability for CO_2 phase
m_{b0}	m^3/kg	5.916×10^{-3}	Initial gas content in the matrix
p_c	MPa	7.38	Critical pressure of CO2
μ_a	Pa•s	1.37×10^{-5}	Viscosity of CO_2 at standard condition
A_{11}		7.9	temperature tuned coefficient
A_{12}		9×10^{-6}	pressure tuned coefficient
A_{13}		0.28	molar weight tuned coefficient
α_T	1/K	2.4×10^{-5}	Coefficient of thermal expansion
c_{nw}	J/(kg•K)	800	Specific heat of fluid
c_s	J/(kg•K)	900	Specific heat of solid
λ_s	W/(m•K)	3	Thermal conductivity of shale

6.4.2. Factors affecting CO_2 penetration depth

The factors which affect the CO_2 penetration depth are analyzed here. Fig. 6.6 presents the distribution of water saturation along the Y-axis (height) at 31.7 years. The definition of CO_2 penetration depth is also plotted in terms of this saturation profile. The front of the two-phase flow is determined by the reflection point of water saturation. Therefore, the penetration depth is the distance of the two-phase flow front away from the bottom boundary. This figure shows that water saturation increases with the CO_2 displacing water. Because both viscosity and density of CO_2 are the functions of temperature and pressure, the factors affecting the caprock sealing efficiency can be analyzed from real gas properties, pressures and variable temperatures.

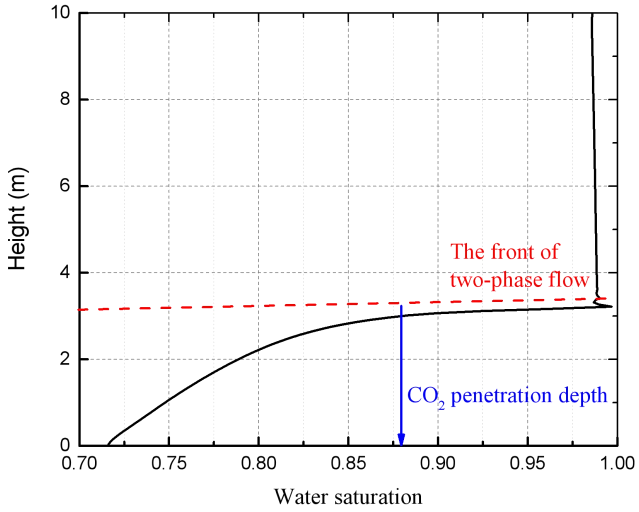

Fig. 6.6. Spatial distribution of water saturation and definition of penetration depth at 31.7 years

6.4.2.1. Effect of real gas properties in two-phase flow

The physical properties of CO_2 experience a dramatic change due to the phase transition in the shallow layer at the depth of around 800 m. Fig. 6.7 compares the penetration depths with time when the real gas effect is considered or not. In Fig. 6.7 (a), the shape of penetration depth with time is similar in the early time of 3.17 years. The penetration depth of real gas increases more rapidly. The penetration depth has a 5.9% growth for the real gas compared to an ideal gas. It is further found that square root law is still observed in the relationship of penetration depth and time. Fig. 6.7 (b) presents this relationship in the domain of time square root. Both real gas and ideal gas almost follow a straight line but with different slopes. This difference of slopes is determined by the change of CO_2 physical properties. The linearity of this relationship is modified by the phase transition. In the deep layer, this change has little contribution to CO_2 penetration and is not considered in most

cases. However, Fig. 6.7 shows that the phase transition becomes important to the assessment of CO_2 leakage risk in the shallow layer near the depth of 800 m.

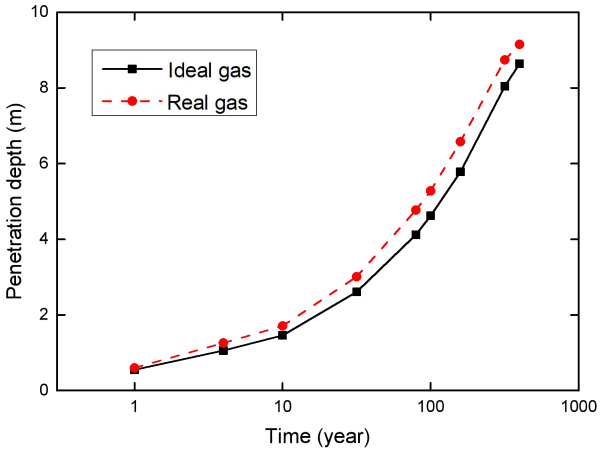

(a) Penetration depth with time

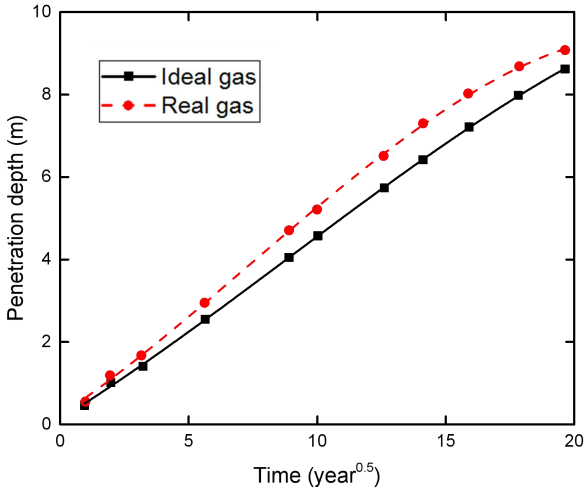

(b) Penetration depth with time square root

Fig. 6.7. Comparisons of penetration depth for ideal gas and real gas model

6.4.2.2. Effect of pressure on CO_2 penetration depth

The time square root law has also been observed in many penetration experiments on concrete or mortar [11-13]. Further, Wang et al. [14] modified this relationship to consider

the pressure effect when CO_2 penetration depth into a caprock layer is estimated. Their penetration depth is expressed as

$$H=\sqrt{\frac{2kt}{\mu}(p_1-p_2)}\sqrt{(1+\frac{p_1}{p_2})/2} \quad \text{* MERGEFORMAT (6.24)}$$

where p_1 is a CO_2 injection pressure at the bottom boundary and p_2 is the reservoir pressure in the caprock. The pressure difference (p_1-p_2) is used as a driving force for CO_2 penetration into caprock. Fig. 6.8 presents our numerical results of penetration depth with time under the same reservoir pressure. The effect of pressure difference on penetration depth is observed. The CO_2 penetration depth increases faster for higher injection pressure. At the early stage, the CO_2 partial pressure starts to decrease with the process of two-phase flow. This pressure does not fall below the critical pressure. Under this circumstance, the pressure difference plays a vital role in the caprock sealing efficiency. With the continuous decrease of gas partial pressure, the CO_2 almost exists in a gas state when the injection pressure is 9 MPa. The penetration depth increases more slowly when injection pressures are 10 and 11 MPa.

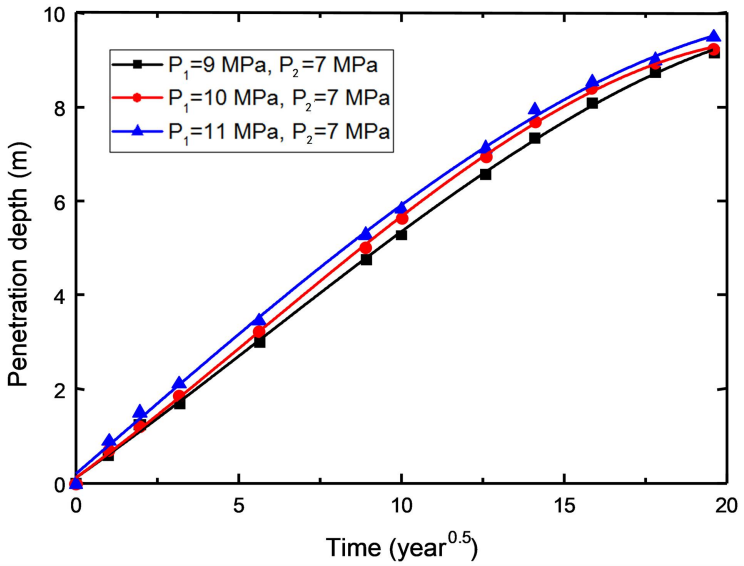

Fig. 6.8. Effect of pressure difference on CO_2 penetration depth

Another case is the constant pressure difference. The pressure varies with burial depth. Fig. 6.9 shows the effect of burial depth on penetration depth under the same pressure difference. In order to identify this difference clearly, this figure does not start from the origin and is enlarged at the scaled time interval of [6, 15]. It is found that the change of burial depth has a weaker influence on penetration depth than pressure difference. Further, a larger pressure difference has a bigger CO_2 penetration depth. When the burial depth is shallower, the penetration depth is higher. The injected CO_2 flows more easily near the critical state ($p_1 = 8\ MPa, p_2 = 6\ MPa$) because of the phase transition. This case indicates that the injected CO_2 near the critical state can easily migrate and increase the risk of CO_2 leakage.

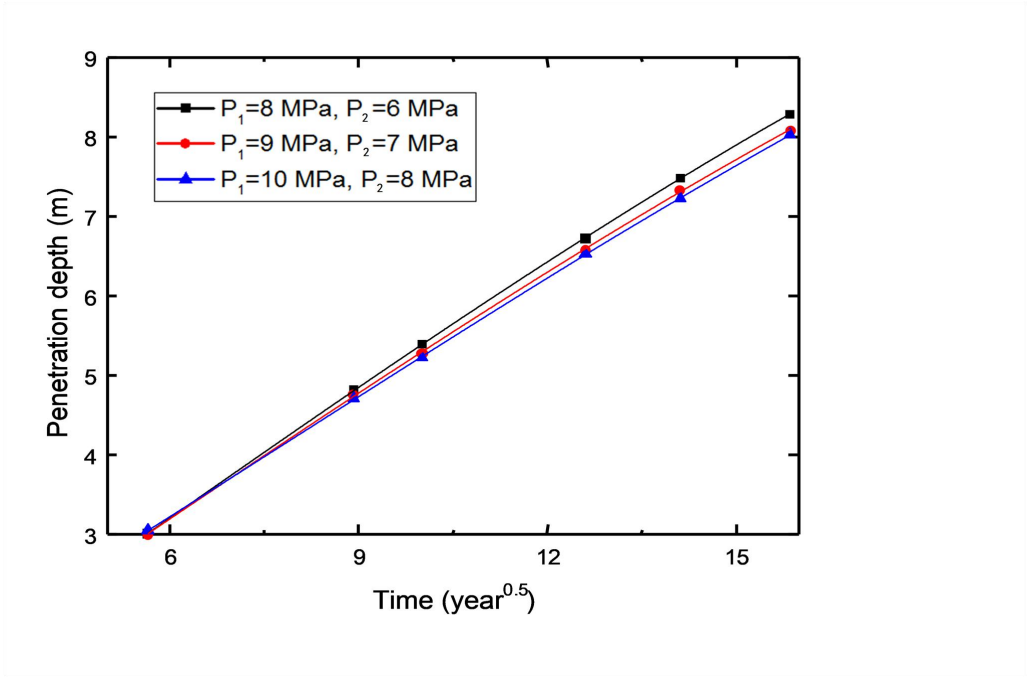

Fig. 6.9. Effect of burial depth on CO_2 penetration depth

6.4.2.3. CO_2 penetration depth under variable temperatures

Temperature is an important parameter to affect caprock sealing efficiency. Temperature can change the physical properties of CO_2 and also modify the permeability of caprock. The initial reservoir temperature is assumed to be 294 K, and three injection temperatures of 298,

302, and 304 K are respectively applied at the bottom of the caprock as the injection entry. CO_2 will reach temperature equilibrium during long-term migration, where different injection temperatures represent the temperatures brought about by the CO_2 leakage from the deeper layers under different geological conditions (such as different temperature gradients or faults appearing). Generally, higher injection temperature makes the CO_2 penetrate easier. Fig. 6.10 presents the square root law at different injection temperatures. This figure shows that temperature is a key parameter to caprock sealing efficiency, especially in a shallow caprock (the pressure is also nearby the critical value). When the injection temperature is 298 and 302 K, which is lower than the critical temperature, the CO_2 exists in the gas state. In these two cases, the CO_2 penetration depth almost observes a linear relationship with time square root. However, when the injection temperature is 306 K, the penetration depth of CO_2 has an obvious increase compared to other cases and the linear relationship of penetration depth with time square root is no longer observed. Thus, this phase transition modifies the linearity.

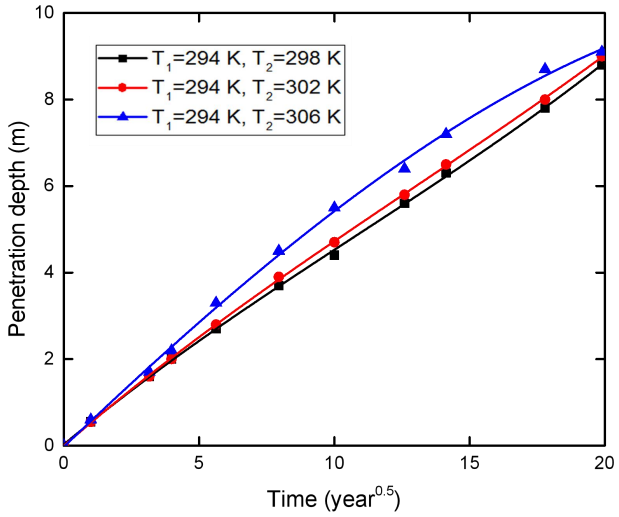

Fig. 6.10. Effect of variable temperatures on CO_2 penetration depth

Fig. 6.11 presents two cases of CO_2 in the gas and supercritical conditions to discuss the effect of variable temperature on caprock sealing efficiency. The temperature difference between the two cases is kept the same. This figure presents the spatial distribution of water saturation at 31.7 years. The distribution of water saturation changes a little in the front zone. The penetration front of two-phase flow is far away for higher temperature. This result is reasonable because the viscosity of CO_2 would decrease with the increase of temperature. This lower viscosity provides faster flow mobility of CO_2 in the caprock, thus having a bigger penetration depth. As for the CO_2-displaced region, the water saturation is slightly higher at the same penetration depth because the CO_2 penetrates further with higher temperature. The lower CO_2 partial pressure induces the more water reflux in the swept zone.

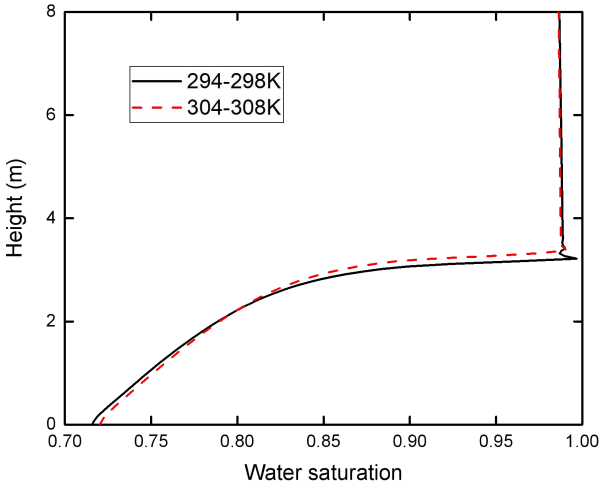

Fig. 6.11. Distribution of water saturation under variable temperatures at 31.7 years

The viscosity of CO_2 is affected by both temperature and pressure. Fig. 6.12 presents the profile of CO_2 partial pressure at the same time. This figure shows that temperature does not only affect the CO_2 partial pressure behind the front but also affects the CO_2 pressure in the front zone. The pressure is lower at the front of two-phase flow under higher temperature.

This decrease of CO_2 partial pressure causes lower CO_2 viscosity. This phenomenon is consistent with the result in Fig. 6.11.

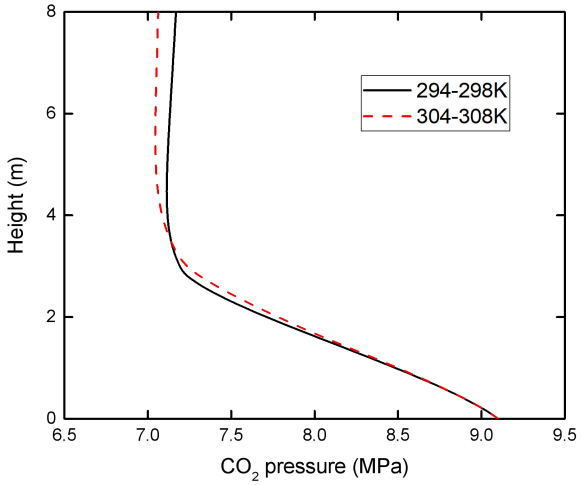

Fig.6.12. Distribution of CO_2 partial pressure at 31.7 years

6.4.3. Evolution of CO_2 flow mobility

The CO_2 flow mobility expresses the transport capacity of CO_2 in a porous medium. Eq. shows that the flow mobility (k/μ) significantly affects the CO_2 penetration depth in caprock. When buoyancy remains the same, this flow mobility makes the part of CO_2 more easily migrate to the shallow layer, increasing the risk of leakage. The flow mobility depends on both permeability and viscosity, thus these two factors should be carefully studied.

6.4.3.1. Effect of permeability on caprock sealing efficiency

In our model, the initial permeability is taken as a value between $1.5\times10^{-17}m^2$ and $1.5\times10^{-21}m^2$. Fig. 6.13 shows the change of the CO_2 penetration depth at 3.17 years with permeability. The penetration depths of real gas and ideal gas are compared. The CO_2 penetration depth changes slowly when the permeability is smaller than $1.5\times10^{-19}m^2$. The effect of a real gas is very small and ignorable. This result indicates that CO_2 is hard to break

through the caprock under this condition. The CO_2 penetration depth begins to have a rapid increase when the permeability is in the range of $1.5\times10^{-18}m^2$ to $1.5\times10^{-17}m^2$. Similarly, the effect of real gas also begins to be in effects with the increase of permeability. The penetration depth of real gas increases by 7% compared with an ideal gas. Thus, this range (the permeability is in the range of $1.5\times10^{-18}m^2$ to $1.5\times10^{-17}m^2$) is called as the dangerous region for CO_2 storage. Avoiding this permeability range can improve the caprock sealing efficiency.

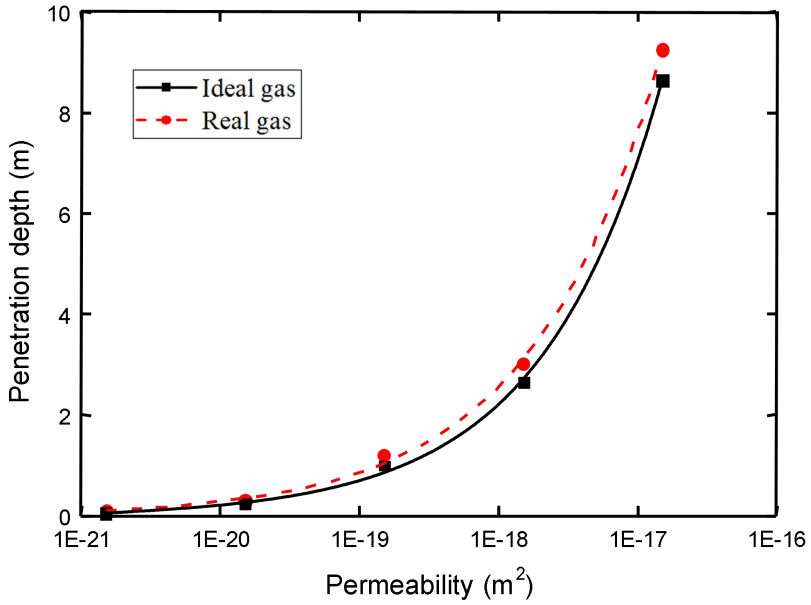

Fig. 6.13. Comparison of CO_2 penetration depth with permeability for ideal and real gas

6.4.3.2. Effect of entry capillary pressure on caprock sealing efficiency

The entry capillary pressure decides the occurrence of CO_2 displacing brine water and reflects the difficulty of this displacement process. The entry capillary pressure usually varies in a large range of 0.1 - 48.3 MPa [15]. In this study, the capillary entry pressure is taken as 0.1 MPa due to the shallow layer. Fig. 6.14 shows that the CO_2 penetration depth obviously decreases with the increase of entry capillary pressure. When the entry capillary pressure

increases from 0.1 MPa to 1.5 MPa, the CO_2 penetration depth has a linear drop. When the capillary pressure continues to increase, the CO_2 penetration depth becomes a slower drop. This indicates that the CO_2 does not easily penetrate into the caprock when the entry capillary pressure excesses some value.

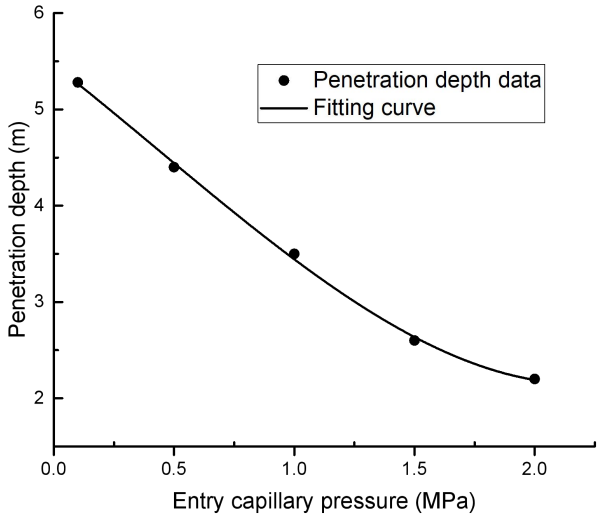

Fig. 6.14. Effect of entry capillary pressure on caprock sealing efficiency

6.4.3.3. Evolution of CO_2 physical property

The flow mobility is affected by the CO_2 viscosity, particularly during phase transition. Fig. 6.15 presents the snapshots of three-phase coexistence at 100 years.

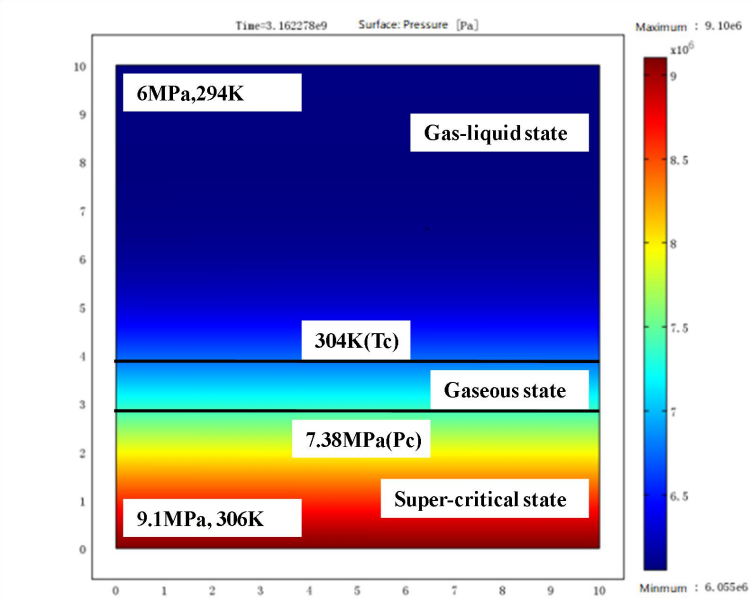

Fig. 6.15. Snapshots of three-phase coexistence at 100 years

In order to further analyze the physical properties of CO_2 at this moment, Fig. 6.16 gives the spatial distributions of both viscosity and density with height. Both viscosity and density firstly decrease and then increase rapidly. For the whole process, the decrease of viscosity makes CO_2 more easily penetrate into the caprock. The decrease in density means lower gas pressure in caprock.

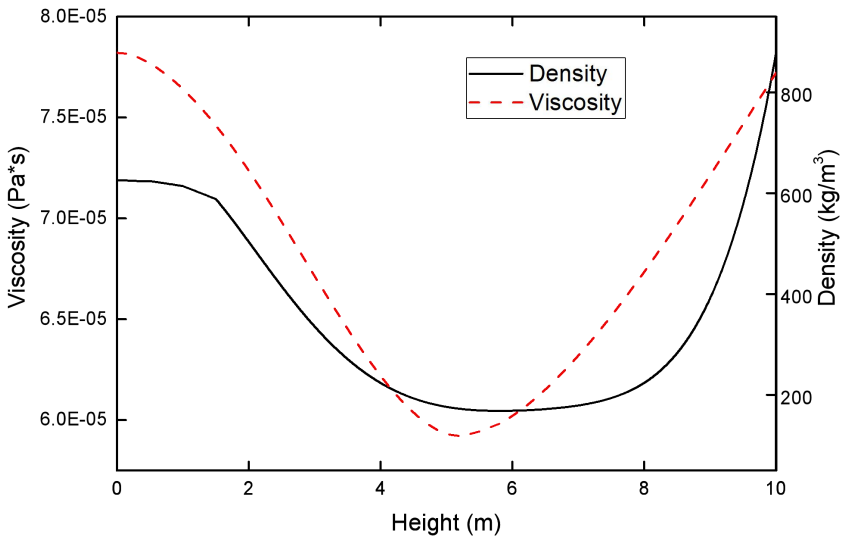

Fig. 6.16. Vertical distribution of viscosity and density at 100 years

Fig. 6.17 shows the spatial distribution of CO_2 partial pressure and temperature with height. With the process of two-phase flow, the CO_2 partial pressure decreases continually. The pressure is stable beyond the front of two-phase flow. The temperature linearly decreases in the whole process. In contrast to the density distribution in Fig. 6.16, both CO_2 partial pressure and temperature decreases along with the height. These changes of temperature and pressure make the CO_2 in different phase states. Thus, the density of CO_2 depends on both temperature and pressure but is mainly determined by CO_2 partial pressure. The viscosity of CO_2 is declining until reaching the front of two-phase flow. The decline of CO_2 partial pressure is the cause of the decrease of CO_2 viscosity. This decrease of viscosity makes CO_2 penetrate into caprock more easily. The decrease of temperature would take an opposite influence on the viscosity of CO_2. At this stage, the viscosity has a similar change with CO_2 partial pressure, which implies that the CO_2 partial pressure plays a more important role in this process than temperature. Finally, CO_2 partial pressure does not change any more and the decrease of temperature makes viscosity roughly rise to its original value. This result highlights that pressure is important to the change in physical property. The decrease of pressure would make CO_2 more easily break through the caprock. This case again indicates that burial depth needs to be considered for caprock sealing efficiency. The caprock sealing efficiency is reduced when CO_2 leakages near the critical state.

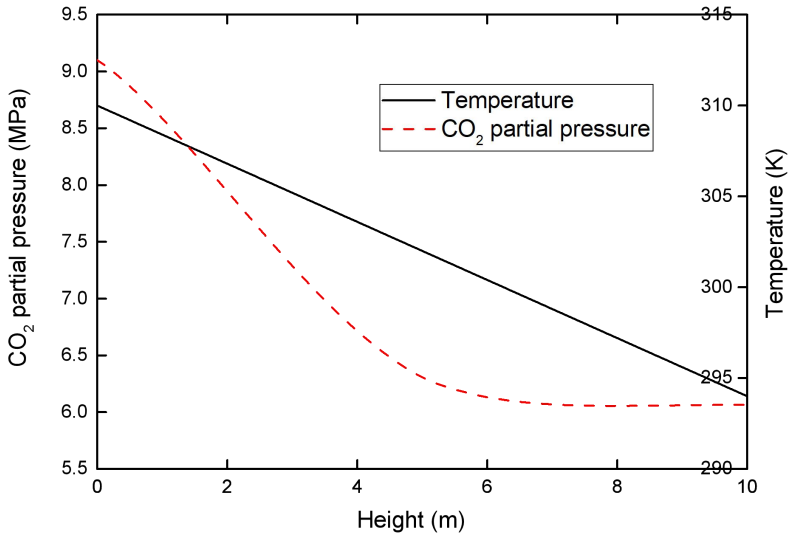

Fig. 6.17. Vertical distribution of CO_2 partial pressure and temperature at 100 years

6.5. Conclusions

This chapter extends our previous fully coupled multi-physical model to include the phase transition effect at the critical depth. The effects of temperature, pressure, caprock deformation on the caprock sealing efficiency are numerically analyzed. From these initial studies, the following conclusions can be made.

First, the extended fully coupled multi-physical model can well describe the process of two-phase flow, caprock deformation, CO_2 sorption, and heat transport in the caprock layer. The real gas effect in the phase transition zone should be carefully considered in a shallow caprock layer near the critical depth. At about 400 years, the penetration depth has a 5.9% growth after considering the real gas effect.

Second, both pressure and temperature have important but different impacts on caprock sealing efficiency. The injection pressure takes an obviously positive effect on CO_2 penetration depth. When CO_2 is in the gas state, the penetration depth complies with a linear

relationship of time square root. However, the phase transition due to temperature change modifies this linearity.

Third, caprock sealing efficiency varies with reservoir permeability and entry capillary pressure. The CO_2 penetration depth has a rapid increase when the permeability is in the range of $1.5\times10^{-18}m^2$ to $1.5\times10^{-17}m^2$. When the entry capillary pressure increases from 0.1 MPa to 1.5 MPa, the CO_2 penetration depth has a linear drop. This drop becomes slower for larger entry capillary pressure.

6.6. References

[1] Jarrahian A, Heidaryan E. A simple correlation to estimate natural gas viscosity. Journal of Natural Gas Science and Engineering, 2014, 20: 50-57.

[2] Wang J G, Liu J, Kabir A. Combined effects of directional compaction, non-darcy flow and anisotropic swelling on coal seam gas extraction. International Journal of Coal Geology, 2013, 109: 1-14.

[3] Zhu W, Wei C, Liu J, Qu H, Elsworth D. A model of coal-gas interaction under variable temperatures. International Journal of Coal Geology, 2011, 86(2-3): 213-221.

[4] Tong F, Jing L, Zimmerman R W. A fully coupled thermo-hydro-mechanical model for simulating multiphase flow, deformation and heat transfer in buffer material and rock masses. International Journal of Rock Mechanics and Mining Sciences, 2010, 47(2): 205-217.

[5] Zhou Y, Rajapakse R, Graham J. A coupled thermoporoelastic model with thermo-osmosis and thermal-filtration. International Journal of Solids and structures, 1998, 35: 4659-4683.

[6] Wang J G, Kabir A, Liu J, Chen Z. Effects of non-Darcy flow on the performance of coal seam gas wells. International Journal of Coal Geology, 2012, 93: 62-74.

[7] Mavko G, Nur A. The effect of a percolation threshold in the kozeny-carman relation. Geophysics, 1997, 62(5): 1480-1482.

[8] Oostrom M, White M D, Porse S L, Krevor S, Mathias S. Comparison of relative permeability-saturation-capillary pressure models for simulation of reservoir CO_2 injection. International Journal of Greenhouse Gas Control, 2016, 45: 70-85.

[9] Li Z, Dong M, Li S, Huang S. CO_2 sequestration in depleted oil and gas reservoirs - caprock characterization and storage capacity. Energy Conversion and Management, 2006, 47(11-12): 1372-1382.

[10] Li Y, Fang Q, Ke Y, Dong J, Ma X. Effect of high salinity on CO_2 geological storage: A case study of Qianjiang depression in Jianghan Basin. Earth Science-Journal of China University of Geosciences, 2012, 37(2): 283-288.

[11] Matteo E N, Scherer G W. Experimental study of the diffusion-controlled acid degradation of class h portland cement. International Journal of Greenhouse Gas Control, 2012, 7: 181-191.

[12] Yoo J, Lee H, Ismail M A. An analytical study on the water penetration and diffusion into concrete under water pressure. Construction and Building Materials, 2011, 25(1): 99-108.
[13] Murata J, Ogihara Y, Koshikawa S. Study on watertightness of concrete. Materials Journal, 2004, 101(2): 107-116.
[14] Wang J G, Ju Y, Gao F, Liu J. A simple approach for the estimation of CO_2 penetration depth into a caprock layer. Journal of Rock Mechanics and Geotechnical Engineering, 2016, 8(1): 75-86.
[15] Tonnet N, Mouronval G, Chiquet P, Beoseta D. Petrophysical assessment of a carbonate-rich caprock for CO_2 geological storage purposes. Energy Procedia, 2011, 4: 5422-5429.

Chapter 7: Coupled hydro-thermal-mechanical analysis for cold CO_2 injection into deep saline aquifers

7.1 Introduction

Injected CO_2 is usually colder than the reservoir. This causes thermal contraction and thermal stress. When high-pressure CO_2 is injected into the low-pressure reservoir, the CO_2 expands, causing further temperature drop due to Joule-Thomson cooling. However, there is no analysis of the thermal-hydro-mechanical coupling mechanism for the influence of thermal effects on CO_2 migration in deep saline aquifers. This chapter will extend our two-phase flow model to include thermal stress and Joule-Thomson effects. Thermal stress is included in a new porosity model to investigate the matrix shrinkage caused by cold CO_2 injection. The Joule-Thomson effect is considered in the changes in CO_2 physical properties. Further, the effect of capillary entry pressure on CO_2 plume is numerically explored. The influence of injection boundary conditions on the accumulation of CO_2 pressure at the bottom of the caprock is investigated, which provides guidance for the initial value of gas pressure in the caprock model.

7.2. Governing equations for non-isothermal two-phase flow

CO_2 plume is formed in the deep saline aquifer under the effect of gravity after a large amount of CO_2 is injected. During the gas displacing water process, the gas-water front is a moving boundary. This front is affected by the relationship between relative permeability and saturation. When the injection rate is high, the CO_2 cannot be kept in thermal equilibrium with the reservoir. An assumption of constant temperature is not reasonable. Thus, a

non-isothermal process is necessarily considered in the hydro-thermal-mechanical coupled model here.

7.2.1. Mass conservation equation for two-phase flow

The mass conservation law for the flow of each phase fluid in a porous medium can be expressed below [1].

For the water phase:

$$\frac{\partial(\phi\rho_w s_w)}{\partial t}+\nabla\left[-\frac{kk_{rw}}{\mu_w}\rho_w(\nabla p_w+\rho_{\mathrm{w}}g\nabla H)\right]=Q_w$$

* MERGEFORMAT (7.1)

For the CO_2 phase:

$$\frac{\partial m}{\partial t}+\nabla\left[-\frac{kk_{rg}}{\mu_g}\rho_g(\nabla p_g+\rho_g g\nabla H)\right]=Q_g$$

* MERGEFORMAT (7.2)

where ϕ is the porosity and s_w is the saturation of water. p_w and p_g are the water pressure and gas pressure, respectively. Water saturation varies with capillary pressure. ρ_w and ρ_g represent the density of water and CO_2, respectively. k is the intrinsic permeability. k_{rw} and k_{rg} are the relative permeability of water and gas, respectively. The constitutive relationship of relative permeability varying with water saturation can refer to our previous work [2]. μ_w and μ_g are the viscosities of water and gas, respectively. g is the gravitational acceleration. H is the elevation in the vertical direction. Q_w and Q_g represent the sources of water and CO_2, respectively.

The water exists only in the free-flowing state. However, the mass of gas term includes not only the free-flowing gas but also the adsorbed gas. This CO_2 mass can be given by

$$m = \phi \rho_g s_g + \rho_{ga} \rho_c \frac{V_L p_g}{p_L + p_g} \exp\left(-\frac{c_1 \Delta T}{1 + c_2 p_g} \right)$$

* MERGEFORMAT (7.3)

where s_g represents the saturation of CO_2, $s_g = 1 - s_w$. ρ_c is the density of rock, and ρ_{ga} is the CO_2 density under the standard conditions. V_L is the Langmuir volume constant and p_L is the Langmuir pressure. The mass of adsorbed CO_2 is still calculated by the classical Langmuir formula. Because of non-isothermal flow, the effect of temperature variation on CO_2 adsorption is considered. This is done by the introduction of an index correction term into the Langmuir adsorption formula. c_1 is the temperature correction coefficient of gas adsorption (K^{-1}), and c_2 is the pressure correction coefficient of gas adsorption (MPa^{-1}).

Compared to gas, water is often treated as an incompressible fluid. Its density does not change in the CO_2 geological storage. The density of CO_2 is affected by ambient conditions (temperature and pressure) and can be calculated by Peng and Robinson equation of state:

$$\rho_g = \frac{M_{CO_2}}{ZRT} p_g \qquad \text{* MERGEFORMAT (7.4)}$$

where M_{CO_2} is the molecular weight of CO_2, R is the universal gas constant, and T is the gas temperature. Z is the compressibility factor of real gas which represents the degree of gas compression.

Since the pressure and the temperature of CO_2 in this study vary in a certain range (14MPa-26MPa; 310K-324K). The compressibility factor Z is given in Table 7.1. It is defined as an interpolation factor for the computation in Comsol Multiphysics. The compressibility with respect to temperature and pressure can be derived as

$$c_T = \frac{1}{\rho_g} \frac{\partial \rho_g}{\partial T} = -\left(\frac{1}{T} + \frac{1}{Z} \frac{\partial Z}{\partial T} \right) \qquad \text{* MERGEFORMAT (7.5)}$$

$$c_p = \frac{1}{\rho_g}\frac{\partial \rho_g}{\partial p_g} = \left(\frac{1}{p_g} - \frac{1}{Z}\frac{\partial Z}{p_g}\right) \qquad \text{* MERGEFORMAT (7.6)}$$

In addition to the change of CO_2 density, CO_2 viscosity varies with temperature and pressure. The viscosity is related to the flow mobility of CO_2 in the reservoir and further affects the pressure accumulation at the bottom of the caprock. Heidaryan et al. [3] developed a formula to calculate the CO_2 viscosity in ranges of pressures (7.5-101.4 MPa) and temperatures (310-900 K):

$$\mu_g = \frac{A_1 + A_2 + A_3 p_g^2 + A_4 \ln(T) + A_5(\ln(T))^2 + A_6(\ln(T))^3}{1 + A_7 p_g + A_8 \ln(T) + A_9(\ln(T))^2}$$

* MERGEFORMAT (7.7)

It is worth noting that the pressure and temperature here are expressed in bar and K, respectively. The viscosity unit is centipoise (cp). Unit conversion is required before calculation. A_1 - A_9 are the tuned coefficients [3]. Substituting Eqs. (7.3-7.6) into Eqs. (7.1) and (7.2) obtains the final governing equations of two-phase flow as follows.

For water:

$$\phi c_s \frac{\partial p_g}{\partial t} - \phi c_s \frac{\partial p_w}{\partial t} + \nabla\left[-\frac{kk_{rw}}{\mu_w}(\nabla p_w + \rho_w g \nabla H)\right] = Q'_w - s_w \frac{\partial \phi}{\partial t}$$

* MERGEFORMAT (7.8)

For CO_2:

$$\left[-\phi c_s + \phi s_g c_p + \frac{\rho_{ga}\rho_c}{\rho_g}\exp\left(-\frac{c_1\Delta T}{1+c_2 p_g}\right)\left(\frac{V_L P_L}{(P_L+p_g)^2} - \frac{V_L p_g}{P_L+p_g}\frac{c_1 c_2 \Delta T}{(1+c_2 p_g)^2}\right)\right]\frac{\partial p_g}{\partial t}$$
$$+\phi c_s \frac{\partial p_w}{\partial t} + \nabla\left[-\frac{kk_{rg}}{\mu_g}(\nabla p_g + \rho_g g \nabla H)\right]$$
$$= -\left[\phi s_g c_T \frac{\rho_{ga}\rho_c}{\rho_g}\frac{V_L p_g}{P_L+p_g}\exp\left(-\frac{c_1\Delta T}{1+c_2 p_g}\right)\frac{-c_1}{1+c_2 p_g}\right]\frac{\partial T}{\partial t} - s_g \frac{\partial \phi}{\partial t} + Q'_g$$

* MERGEFORMAT (7.9)

7.2.2. Thermoelastic strain of porous media

The porous medium is assumed to be linear elastic, uniform, and isotropic. The deformation of the porous medium is affected by the effects of pore pressure, sorption strain and thermal expansion/shrinkage:

$$\varepsilon_{ij} = \frac{1}{2G}\sigma_{ij} - \left(\frac{1}{6G} - \frac{1}{9K}\right)\sigma_{kk}\delta_{ij} + \frac{\alpha}{3K}p\delta_{ij} + \frac{\varepsilon_s}{3}\delta_{ij} + \frac{\varepsilon_T}{3}\delta_{ij}$$

* MERGEFORMAT (7.10)

where α is the Biot coefficient, $\alpha = 1 - \frac{K}{K_s}$. K is the bulk modulus of rock and K_s is the bulk modulus of rock grain. G is the shear modulus, ν is the Poisson ratio and p represents the gas pressure in the pores.

Therefore, the porosity model considering the above physical processes is proposed as

$$\phi = \phi_0 + \alpha(\varepsilon_v + \frac{p}{K_s} - \varepsilon_{s1} - \varepsilon_{s2}) \quad \text{* MERGEFORMAT (7.11)}$$

where ϕ_0 is the initial porosity and ϕ is the current porosity. At the right-hand side of the above formula, the second term presents the volumetric strain (ε_v), the strain induced by pore pressure (p/K_s) and the sorption strain (ε_{s1}), respectively. ε_{s2} represents the contribution of thermal expansion ($\alpha_T \Delta T$) to the change of porosity.

The evolution of porosity in the two-phase flow is further expressed as

$$\frac{\partial \phi}{\partial t} = \alpha(\frac{\partial \varepsilon_v}{\partial t} + \frac{1}{K_s}\frac{\partial p}{\partial t} - \frac{\partial \varepsilon_{s1}}{\partial t} - \alpha_T \frac{\partial T}{\partial t})$$

* MERGEFORMAT (7.12)

7.2.3 Energy conservation for heat transfer

During the injection of CO_2 into the geological reservoir, the heat transfer satisfies the energy conservation [4].

$$\frac{\partial (C_{eq}T)}{\partial t} - \phi\left(\rho_g c_g \mu_{JT} + 1\right)\frac{\partial p_g}{\partial t} + K\alpha_T T\frac{\partial \varepsilon_v}{\partial t} + \nabla \cdot \nu_T = 0$$

* MERGEFORMAT (7.13)

where K is the bulk modulus of porous media. α_T is the thermal expansion coefficient. ε_v is the volumetric strain. ν_T represents the average heat transfer rate and can be divided into heat conduction and heat convection. μ_{JT} is the Joule-Thomson coefficient to express the change of temperature with pressure, K/MPa.

$$\nu_T = -K_{eq}\nabla T + \rho_g c_g \frac{kk_{rg}}{\mu_g}\nabla p_g \left(T - \mu_{JT} p_g\right)$$

* MERGEFORMAT (7.14)

C_{eq} is the specific heat capacity of the porous medium, which consists of the specific capacity of rock and gas:

$$C_{eq} = \phi\rho_g c_g + (1-\phi)\rho_c c_s \qquad \text{* MERGEFORMAT (7.15)}$$

Substituting Eqs. (7.14) and (7.15) into Eq. (7.13) gets the final governing equation of heat transfer as

$$\left(\phi\rho_g c_g + (1-\phi)\rho_c c_s\right)\frac{\partial T}{\partial t} - \phi\left(\rho_g c_g \mu_{JT} + 1\right)\frac{\partial p_g}{\partial t} + K\alpha_T T\frac{\partial \varepsilon_v}{\partial t}$$
$$= K_{eq}\nabla^2 T + \rho_g c_g \frac{kk_{rg}}{\mu_g}\nabla p_g \left(\nabla T - \mu_{JT}\nabla p_g\right)$$

* MERGEFORMAT (7.16)

7.3. Setup of the numerical model

This coupled hydro-thermal-mechanical model includes the two-phase flow (see Eqs. (7.8) and (7.9)), the deformation of the porous medium (see Eq.(7.10)), and the heat transfer (see Eq.(7.16)). They are coupling through these governing equations and corresponding constitutive models. This model will be numerically solved by the finite element method for the simulation of cold CO_2 injection into a deep saline aquifer.

7.3.1 Computational model

The same geological formation used by Vilarrasa et al. [5] is used. In the numerical model, a 100 m thick homogeneous horizontal aquifer is overlaid by a caprock layer. We have studied the penetration of CO_2 into the caprock in our previous study, thus this study only focuses on the non-isothermal flow of CO_2 in the storage reservoir. The computation model is shown in Fig. 7.1.

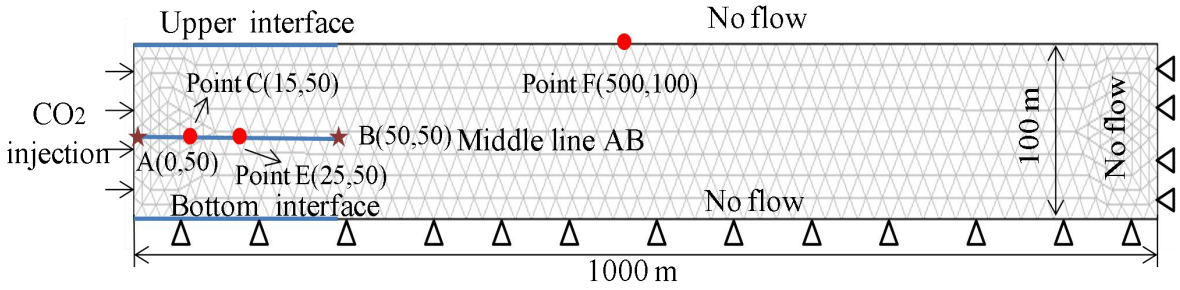

Fig. 7.1. A two-dimensional computational model

This computational model is composed of a two-dimensional domain and is located at the depth of 1500 m. The domain is 1000 m long and 100 m high. Its top and bottom boundaries are no-flow. The hydrostatic pressure is initially distributed in the computational domain as initial reservoir pressure. The reservoir temperature is 322.5 K. The cold CO_2 (310

K, still in the supercritical state) is injected from the left boundary with a prescribed CO_2 mass flow rate (1.0 Mt/yr). The model parameters are listed in Table 7.1.

Table 7.1. Model parameters used in the computation

Parameter	Unit	Value	Physical Meanings
μ_w	Pa s	5.5×10^{-4}	Water viscosity
p_{w0}	MPa	10.1+0.0102×(500-y)	Initial water pressure in the reservoir
p_{g0}	MPa	$p_{w0} + p_e$	Initial CO_2 pressure in the reservoir
E_c	GPa	5	Young's modulus of shale
E_s	GPa	15	Young's modulus of shale grains
p_e	MPa	0.1	Capillary entry pressure
T_0	K	323	Temperature
k_0	m^2	1×10^{-13}	Initial absolute permeability
ϕ_0		0.15	Initial porosity
ν		0.25	Poisson's ratio of shale
ρ_c	kg/m^3	1250	Shale density
P_L	MPa	6	Langmuir pressure of CO_2 in shale
V_L	m^3/kg	0.03	Langmuir sorption capacity of shale for CO_2
ε_L		0.015	Langmuir swelling strain
M	kg/mol	0.044	Molecular weight of CO_2
ρ_w	kg/m^3	1020	Water density
C_g	J/(kg·K)	800	Specific heat of CO_2
C_s	J/(kg·K)	900	Specific heat of rock
α_T	1/K	1×10^{-5}	Coefficient of thermal expansion
μ_{JT}	K/MPa	0.7	Joule-Thomson coefficient
A_1		1.146067×10^{-1}	Tuned coefficient 1 for viscosity
A_2		6.97838×10^{-7}	Tuned coefficient 2 for viscosity
A_3		3.976765×10^{-10}	Tuned coefficient 3 for viscosity
A_4		6.33612×10^{-2}	Tuned coefficient 4 for viscosity
A_5		-1.166119×10^{-2}	Tuned coefficient 5 for viscosity
A_6		7.142596×10^{-4}	Tuned coefficient 6 for viscosity
A_7		6.519333×10^{-6}	Tuned coefficient 7 for viscosity
A_8		-3.567559×10^{-1}	Tuned coefficient 8 for viscosity
A_9		3.180473×10^{-2}	Tuned coefficient 9 for viscosity

7.3.2. Verification of this hydro-thermal-mechanical coupled model

Vilarrasa et al. [5] studied the migration of CO_2 in the reservoir and discussed the effects of physical properties of liquid CO_2 and supercritical CO_2 on the distribution of CO_2 plume. Fig. 7.2(b) presents the CO_2 plume after one-year injection which is computed by our

hydro-thermal-mechanical coupled model. The CO_2 plume in the Vilarrasa's simulation is also presented in Fig. 7.2(a) for comparison. Both CO_2 plumes are similar in spatial distribution. The migration distance of the CO_2 plume at the upper boundary in our model is slightly smaller than Vilarrasa's one. Our model considers the gas adsorption. The gas adsorption causes the expansion of the matrix and reduces the porosity. All of these produce slower front migration and smaller CO_2 migration distance. Both the spatial distribution and the migration distance of CO_2 in the reservoir show that the computational model in this study is reliable for solving CO_2 migration problems.

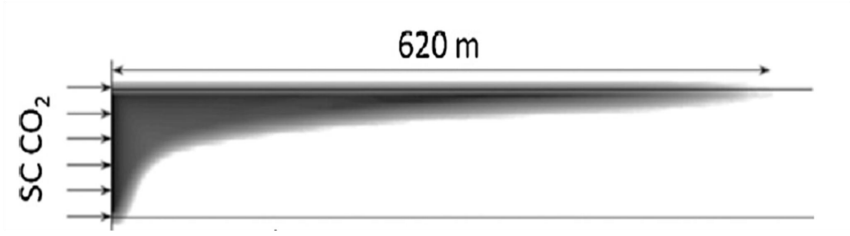

(a**)** Calculated by Vilarrasa et al. (2013)

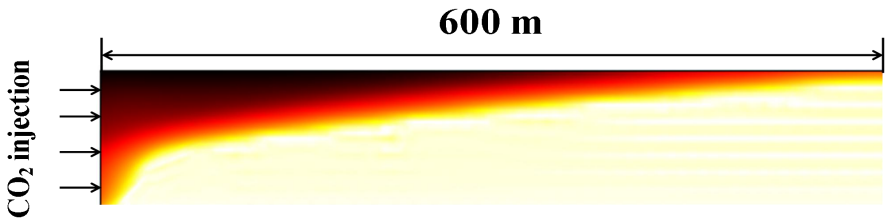

(b**)** Calculated by this model

Fig. 7.2. Comparison of CO_2 plume after one-year injection

7.4. Results and Discussions

7.4.1 Temperature evolution near the injection well

When a large amount of cold CO_2 is injected into the reservoir, the profile of temperature will change with heat transfer, especially near the injection well. This change of

temperature can induce the increase of thermal stress and the modification of permeability. AB line from point (0, 50) to point (50, 50) is taken to observe the evolution of temperature profile with injection time. Fig. 7.3 is the temperature distribution after 1 month, 6 months and 1 year of CO_2 injection along this AB line. After 1 month of CO_2 injection, the temperature influence range is less than 10 m. After one year, the range is expanded to 50 m away from the injection well. These results indicate that the cold CO_2 injection only affects the temperature in the zone near the injection well. The CO_2 will be in equilibrium with reservoir temperature in a short range of injection well.

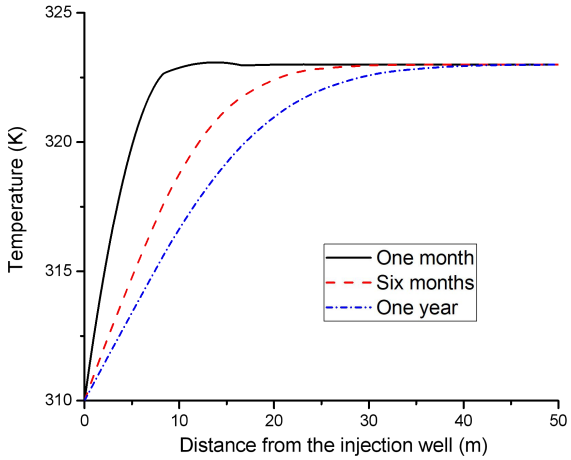

Fig. 7.3. Distribution of CO_2 temperature near the injection well

Since CO_2 migrates upward under buoyancy, the temperature transfer also shows the coincidence with the gas flow. The upper, middle and bottom lines are displayed in the computational model. Fig. 7.4 shows the distribution of temperature along these three lines after one year of CO_2 injection. Temperature changes are almost the same along the middle and bottom boundaries. However, the temperature distribution at the upper boundary is significantly lower than the other two lines. This also indicates that the upward migration of CO_2 causes the temperature decrease in the upper area of the reservoir.

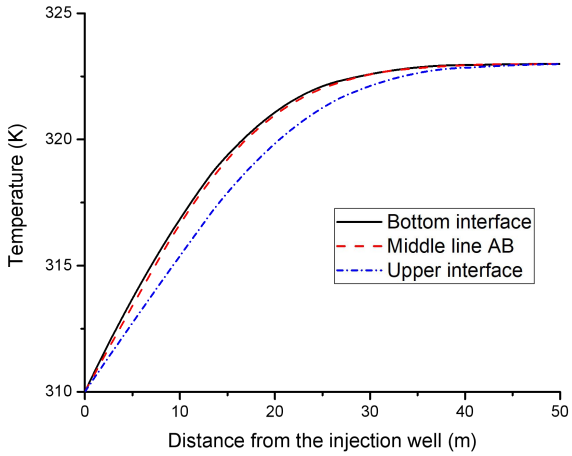

Fig. 7.4. Temperature distribution along three horizontal lines at one-year CO_2 injection

Thermal stress causes the change of permeability in this hydro-thermal-mechanical coupled model. The flow of cold CO_2 brings a cooling effect to the reservoir, so the matrix shrinks and the permeability increases. Fig. 7.5 shows the comparison of permeability ratio at a typical point C (15, 50) with and without thermal stress. Since the injection of CO_2 causes an increase in pore pressure, more pore space is opened. The permeability increases whether the flow is isothermal or non-isothermal. However, the permeability increases more at the non-isothermal flow due to thermal stress. This increase in permeability makes CO_2 migration more easily.

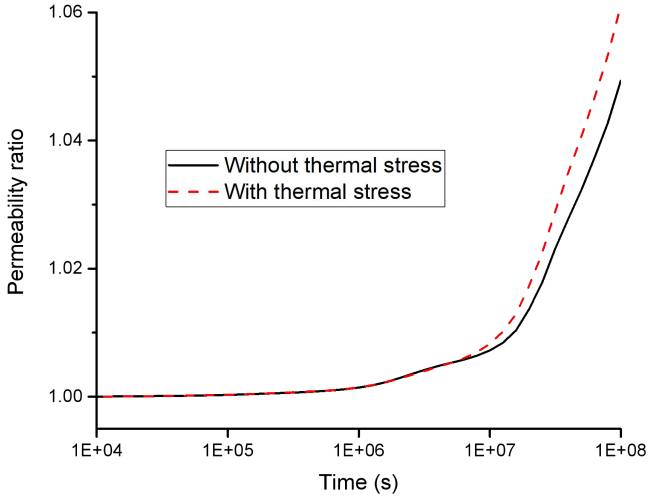

Fig. 7.5. Comparison of permeability ratio at point C (15, 50) with /without thermal stress

7.4.2. Effect of Joule-Thomson cooling on CO_2 physical properties

A great pressure drop occurs near the well when CO_2 is injected into the reservoir. Due to the Joule-Thomson effect, this pressure drop can give rise to a temperature drop. The physical properties of CO_2 (density and viscosity) experience a significant change near the injection well due to the combined action of temperature and pressure drops. The density directly affects the storage efficiency of CO_2 in the reservoir. The viscosity is related to the CO_2 migration in the reservoir and the pressure buildup at the bottom of the caprock. Fig. 7.6 shows the distributions of CO_2 saturation with or without Joule-Thomson effect after one-year injection. Because the constitutive relationship between saturation and capillary pressure is the same, the front of CO_2 displacing water is almost identical. However, with considering the Joule-Thomson effect, the injected high-pressure CO_2 expands freely and the density decreases. More CO_2 migrates upward under the action of buoyancy. Thus, this CO_2 saturation is higher.

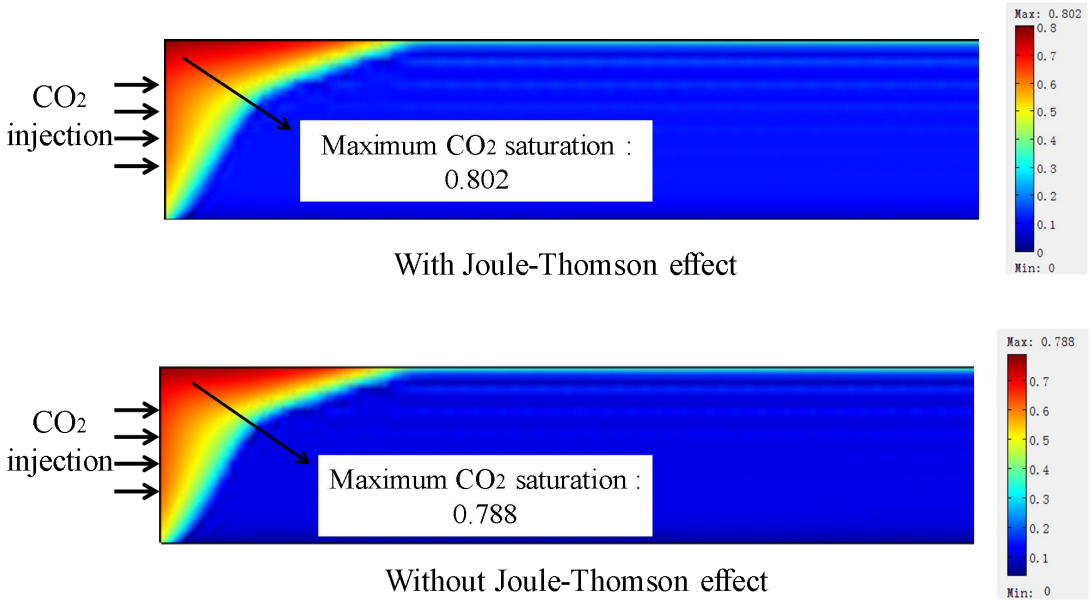

Fig. 7.6. Distributions of CO_2 saturation after one-year injection

In order to evaluate this injection efficiency, we define the effective density of CO_2 ($\rho_e = s_g \rho_g$). Fig. 7.7 gives the comparison of effective density. The CO_2 saturation is higher after considering the Joule-Thomson effect in Fig. 7.6, but the effective density is lower. This implies that the Joule-Thomson effect reduces the injection efficiency of CO_2. Fig. 7.8 further compares the temperature variation at point G with and without Joule-Thomson effect. It is found that the pressure drop of CO_2 causes a more obvious temperature drop due to the Joule-Thomson effect. This is because the volume expansion releases more energy and causes Joule-Thomson cooling when the high-pressure CO_2 is injected into the low-pressure reservoir.

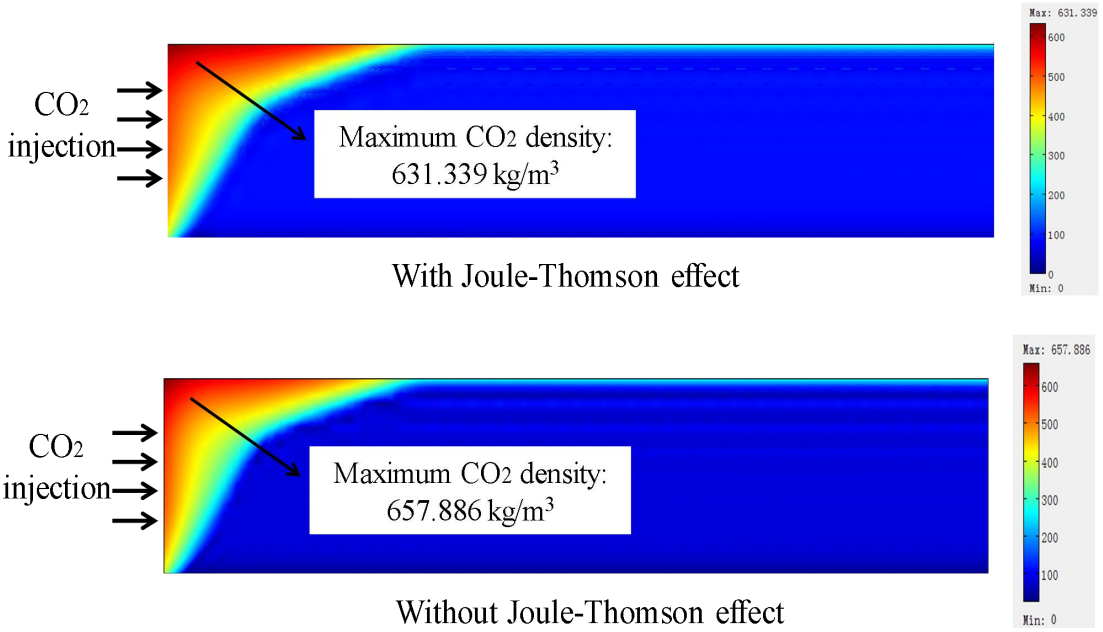

Fig. 7.7. Comparisons of the CO_2 effective density after one-year injection

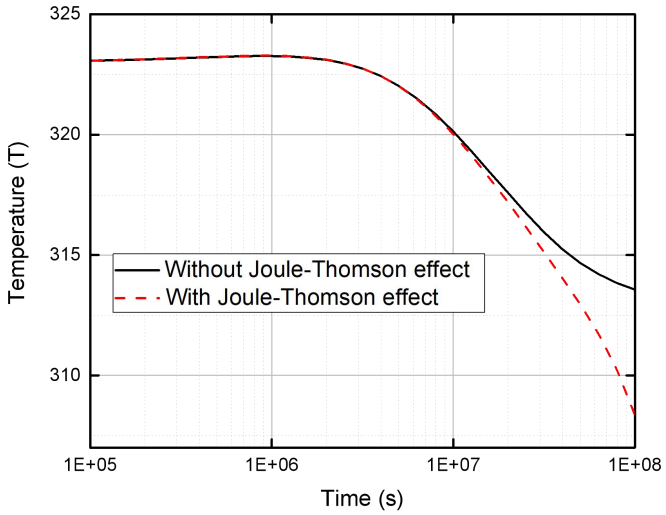

Fig. 7.8. Effect of Joule-Thomson cooling on temperature variation at point E (25, 50)

The CO_2 density with the Joule-Thomson effect in Fig. 7.9 is also slightly lower. Therefore, this CO_2 expansion reduces the injection efficiency and has been a negative factor for CCS projects.

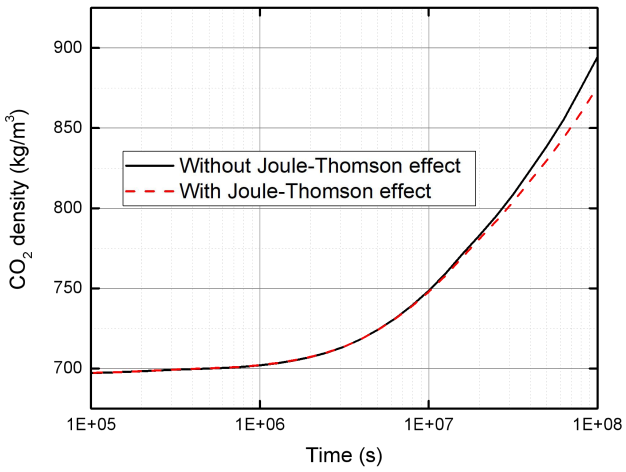

Fig. 7.9. Effect of Joule-Thomson cooling on CO_2 density at point E (25, 50)

The viscosity of CO_2 is an important parameter related to flow mobility. The viscosity increases with the accumulation of pressure when high-pressure CO_2 is injected into the reservoir. When the CO_2 injection pressure remains the same, the variations of injection temperatures become more important to the CO_2 viscosity. Fig. 7.10 shows the evolutions of CO_2 viscosity with an injection temperature of 310, 314 and 318 K. The injected CO_2 is colder, the viscosity is higher. This increase in viscosity makes CO_2 migrate slower in the reservoir.

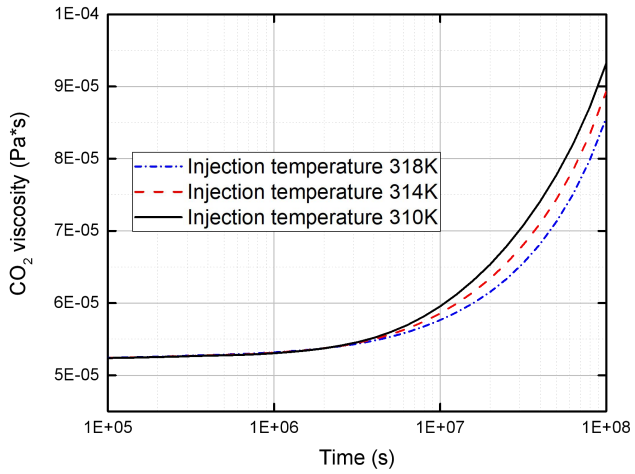

Fig. 7.10. Variation of CO_2 viscosity at point E (25, 50) under different injection temperatures

7.4.3 Effect of capillary entry pressure on CO_2 plume

Capillary entry pressure does not only determine the efficiency of CO_2 capillary capture but also affects the degree of CO_2 displacing water in the caprock. Tonnet et al. [6] found that the capillary entry pressure had a wide variation from 0.1 MPa to 48.3 MPa. This value depended on different geological reservoir or caprock. In this study, the capillary entry pressure was assumed to be 0.1, 0.2 and 0.3 MPa, respectively.

Fig. 7.11 shows the spatial distribution of CO_2 plume after 3 years of CO_2 injection. When the capillary entry pressure is 0.1 MPa, the injected CO_2 firstly migrates upward under the action of buoyancy, and quickly accumulates at the bottom of the caprock and migrates laterally. As the capillary pressure increases, the lateral migration distance of the CO_2 plume is significantly reduced. This implies that capillary entry pressure prevents the spatial migration of CO_2. In addition, the increase of capillary entry pressure causes an increase of CO_2 capillary storage efficiency. It is found that more CO_2 is sealed in the zone near the injection well instead of migrating upwards.

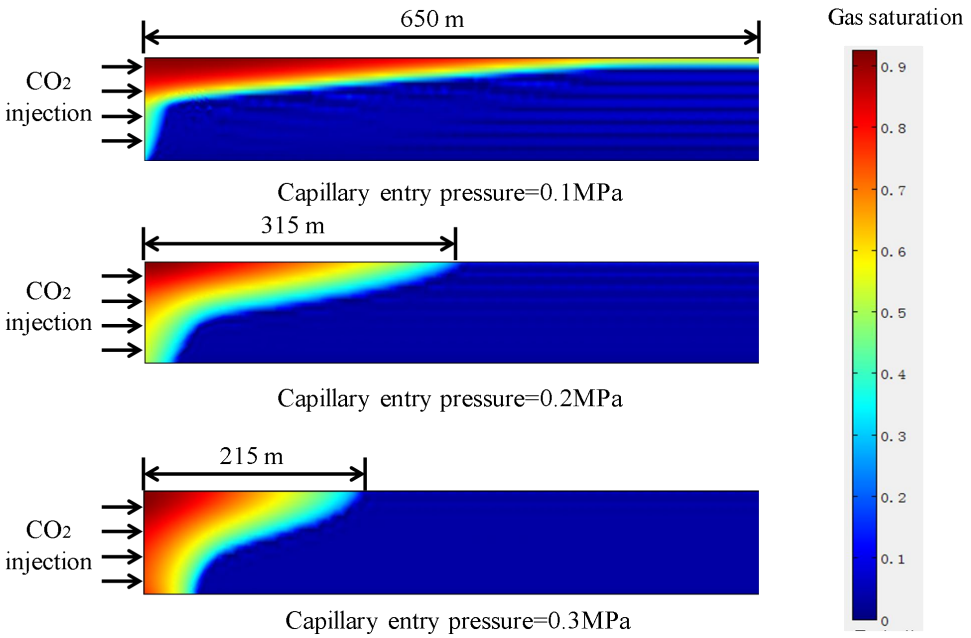

Fig. 7.11. Effect of capillary entry pressure on the shape of CO_2 plume after 3-year injection

The migration distance of CO_2 in the lateral direction is related to the accumulation of gas pressure under the caprock. This is important to the CO_2 storage efficiency in the reservoir, and will further affect the stability of the caprock in a longer time. Thus, the lateral migration distance of CO_2 is calculated after a three-year injection when the capillary entry pressure is 0.1, 0.15, 0.2, 0.25, and 0.3 MPa, respectively. The results are presented in Fig. 7.12. With the increase of capillary entry pressure, the lateral migration distance of CO_2 decreases significantly. Especially when the capillary entry pressure is below 0.2 MPa, the lateral migration distance changes dramatically. As the capillary entry pressure increases, a linear relationship with the lateral migration distance is approximately observed. This indicates that capillary entry pressure is an important parameter for CO_2 storage efficiency.

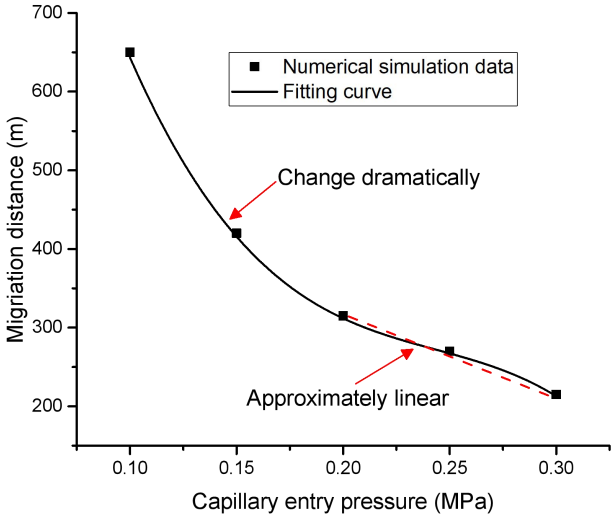

Fig. 7.12. CO_2 migration distance varies with a capillary entry pressure

7.4.4. Variation of CO_2 pressure accumulation at the bottom of caprock with injection methods

The CO_2 migration in the reservoir is accumulated at the bottom of the caprock, forming a higher accumulative pressure. This pressure is directly related to the sealing safety of caprock. Existing research shows that the CO_2 injection method significantly affects the accumulation of gas pressure in the reservoir. Flow flux boundary is commonly used during the actual CO_2 injection into the storage. Hence, three CO_2 injection cases for this coupled model are designed to investigate the accumulative gas pressure: Flow flux boundary is specified for Case A and Case B, but the CO_2 injection rate per one year is 1 MT for Case A and 0.5 MT for Case B. Case C specifies the pressure boundary of 25 MPa. These three cases have the same computational parameters. Fig. 7.13 shows the evolutions of their gas pressures at the point F (500,100). Under the pressure boundary, the initial pressure difference is the largest and the CO_2 injection rate is also the highest. This makes the pressure at the bottom of the caprock increase earliest. The flow flux boundary has a constant CO_2

injection rate. Only when the injected CO_2 reaches a certain amount, the cumulative gas pressure begins to rise. Cases A and B are similar at the initial stage. With the going-on injection, their difference becomes more obvious. Compared with the constant pressure boundary, these constant injection rates have slower accumulation pressure. Furthermore, injecting more CO_2 in a short time will also cause the Joule-Thomson effect and reduce the injection efficiency. Thus, a reasonable injection rate is critical to CO_2 storage efficiency. This will be further studied in the future.

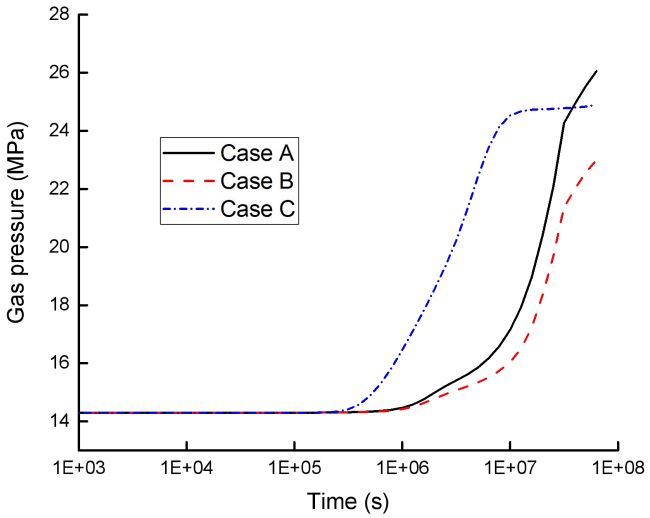

Fig. 7.13. Cumulative gas pressure under three injection cases at point F (500, 100)

7.5. Conclusions

This chapter extends our previous two-phase flow model to include the thermal effects (thermal stress and Joule-Thomson cooling). The variations of CO_2 physical properties (density and viscosity) with pressure and temperature are included. Pore pressure buildup, adsorption expansion and thermal contraction are incorporated through the modified porosity model. The effects of the two thermal effects, capillary entry pressure, injection boundary and

injection rate are numerically investigated. From these studies, the following conclusions can be drawn.

First, the hydro-thermal-mechanical coupled model can well describe the process of CO_2 displacing water, the deformation of the porous medium, the CO_2 sorption, and the heat transfer in deep saline aquifers. The temperature effect of cold CO_2 mainly occurs near the injection well, and the temperature of the upper interface is lower due to the CO_2 upward migration. The permeability ratio of non-isothermal flow is 1.5% higher than that of isothermal flow due to thermal stress.

Second, the density of CO_2 decreases slightly with considering the Joule-Thomson effect. The injected CO_2 temperature is lower, and the viscosity is greater. The shape of the CO_2 plume is affected by capillary entry pressure. When capillary entry pressure is lower, more CO_2 migrates upward under buoyancy, and the CO_2 lateral migration distance is greater.

Finally, the CO_2 cumulative pressure at the bottom of caprock varies with injection boundary and injection rate. Under the pressure injection boundary, the cumulative pressure rises earlier. The more CO_2 is injected under flow flux boundary, the greater difference of CO_2 accumulative pressure is in the later stage.

7.6. References

[1] Wang J G, Peng Y. Numerical modeling for the combined effects of two-phase flow, deformation, gas diffusion and CO_2 sorption on caprock sealing efficiency. Journal of Geochemical Exploration, 2014, 144: 154-167.

[2] Wang J G, Ju Y, Gao F, Peng Y, Gao Y. Effect of CO_2 sorption-induced anisotropic swelling on caprock sealing efficiency. Journal of Cleaner Production, 2015, 103: 685-695.

[3] Heidaryan E, Hatami T, Rahimi M, Moghadasi J. Viscosity of pure carbon dioxide at supercritical region: measurement and correlation approach. Journal of Supercritical Fluids, 2011, 56(2): 144-151.

[4] Teng T, Wang J G, Gao F, Ju Y, Xia T. Impact of water film evaporation on gas transport property in fractured wet coal seams. Transport in Porous Media, 2016, 113(2): 357-382.

[5] Vilarrasa V, Silva O, Carrera J, Olivella S. Liquid CO_2 injection for geological storage in deep saline aquifers. International Journal of Greenhouse Gas Control, 2013, 14: 84-96.
[6] Tonnet N, Mouronval G, Chiquet P, Broseta D. Petrophysical assessment of a carbonate-rich caprock for CO_2 geological storage purposes. 10th International Conference on Greenhouse Gas Control Technologies, 2011, 2011: 5422-5429.

Chapter 8: Conclusions and future research

8.1. Conclusions

This thesis aims to investigate the two-phase flow and multi-physical coupling problem in the process of shale gas flowback and CO_2 geological storage. This research comprehensively used experimental testing, theoretical derivation, numerical simulation to investigate the effect of water-based fracturing fluid remaining in the reservoir on the short-term and long-term of shale gas production, as well as the migration mechanism of gas-water two-phase flow in deep saline aquifers. The following conclusions were drawn.

The water-rock geochemical reactions of shale in different geological conditions irreversibly change the mineral composition, micro-pore structure and mechanical properties, which further affects the shale gas production or the storage efficiency of CO_2. From the analysis of mineral components before and after immersion, the dissolution effects of three solutions on shale are: alkaline solution>acid solution>distilled water. It is worth noting that the reaction of clay minerals in acidic solutions is the most obvious. Furthermore, the water-rock reaction has a slight effect on the surface morphology of shale, but it is mainly focused on micro-fracture and inter-particle pores. The intergranular pore structure has no obvious changes after 30 days of immersion. It is found that the specific surface area, pore volume, and average pore diameter of the shale samples soaked in the solution has significantly increased. The increase of specific surface area and pore volume is caused by the dissolution of micro-pores in organic matter after soaking in the solution, while the increase of average pore diameter is caused by the conversion of micro-pores into meso-pores or macro-pores under the effect of dissolution. Therefore, the average pore diameter after soaking in acidic solution and the alkaline solution is much larger than that of the rock

sample soaking in distilled water. The average tensile strength of shale dropped significantly after being soaked in distilled water, reaching 27.4%. This proves that the swelling of shale after absorbing water has the most significant impact on the mechanical characteristics of the shale sample.

Pore-size distribution fractal dimension and tortuosity fractal dimension can well-describe the complexity of pore-size distribution and tortuosity distribution of porous media, respectively. It is found that the pore-size distribution determines the flow pattern: Single-phase flow or two-phase flow and the pore-size distribution fractal dimension has a more significant influence on gas-water effective permeability. The water film thickness has a negative effect on the water effective permeability. It increases the water film zone and loses the space for normal water flows, thus causing a reduction in the water flow rate. If the water film thickness is much smaller than the pore size, the effect of water film thickness on the gas effective permeability is negligible. The pore geometry directly affects the mechanism of gas flow. When the irregularity of the pore geometry increases, the Knudsen number decreases. The collision between gas molecules is intensified and the gas flow transitions to the continuous medium flow. The geometric correction factor can well-describe the gas effective permeability for any shape of pores. The gas effective permeability can be slightly higher if the real gas effect is considered. Notably, this real gas effect on the gas effective permeability becomes obvious at high-temperature and pressure conditions, and is thus not ignorable.

This fully coupled multi-scale two-phase flowback model can not only describe the process of two-phase flowback in the early production period, but also well describe the impacts of fracture properties, multi-scale gas flow and diffusion in the later production period. It thus provides a useful tool for the assessment of gas production in the water-based

fracturing process. The two-phase flow affects the gas production in the early and long-term periods. Our example shows that the cumulative gas production at the 230 days has a 58.2% decline after considering the effect of two-phase flowback. Thus, the two-phase flowback should be carefully included when the gas production in fractured shale reservoirs is evaluated. Second, the hydraulic fracture properties of fracture spacing, fracture width, fracture uniformity and fracture geometry have variable influences on gas production rate. The increase of fracture density has an obvious positive enhancement on the gas production rate. The uniformity and geometry of fractures have similar effects on the gas production rate, particularly at the early production period. The fracture width may have no effect when it is larger than some value. The hydraulic fracture network in the actual field is interconnected and not uniform. Their impacts on the gas production rate should be further studied. Finally, the gas production rate with multi-scale two-phase flow model is always higher than that with the single-scale model. In micro-scale diffusion and flow mechanism, the gas in micro-fractures of the matrix is a stable source of gas production. With gas extraction, the permeability of micro-fractures in matrix gradually increases and approaches to the permeability in the fractured zone. This phenomenon reflects the flow consistency in the macro-scale flow and the micro-scale diffusion. The contribution from micro-fractures is obvious when the aperture of micro-fractures increases, thus being not ignorable.

The overestimation of water production data by the two-phase flowback model leads to an excessive decrease in the predicted gas production rate. This coupled model of moisture transport is more suitable for long-term gas production. Further, the water saturation is affected by gas flow but lags behind the gas flow. Similarly, the fracture porosity increases due to water film evaporation, but this evaporation process also lags behind the effect of pore pressure. Second, the non-Darcy flow due to overcoming the threshold pressure gradient has

an obvious influence on gas production rate at the beginning of production and near the end of production. This threshold pressure gradient varies with the distance from the well. It is found that the closer to the well, the threshold pressure gradient changes faster, but the smaller maximum can be obtained. Finally, the residual water saturation modifies the gas-liquid-solid sorption capacity. Two parameters of gas adsorption decay coefficient and water coverage factor can be used to describe this effect. The former reflects the influence of residual water on gas adsorption capacity. The latter describes the proportion of water molecules on the surface of the matrix. They change gas exchange content and thus affects the gas production rate.

The extended fully coupled multi-physical model can well describe the process of two-phase flow, caprock deformation, CO_2 sorption, and heat transport in the caprock layer. The real gas effect in the phase transition zone should be carefully considered in a shallow caprock layer near the critical depth. At about 400 years, the penetration depth has a 5.9% growth after considering the real gas effect. Second, both pressure and temperature have important but different impacts on caprock sealing efficiency. The injection pressure takes an obviously positive effect on CO_2 penetration depth. When CO_2 is in the gas state, the penetration depth complies with a linear relationship of time square root. However, the phase transition due to temperature change modifies this linearity. Third, caprock sealing efficiency varies with reservoir permeability and entry capillary pressure. The CO_2 penetration depth has a rapid increase when the permeability is in the range of $1.5\times10^{-18}m^2$ to $1.5\times10^{-17}m^2$. When the entry capillary pressure increases from 0.1 MPa to 1.5 MPa, the CO_2 penetration depth has a linear drop. This drop becomes slower for larger entry capillary pressure.

The hydro-thermal-mechanical coupled model can well describe the process of CO_2 displacing water, the deformation of the porous medium, the CO_2 sorption, and the heat

transfer in deep saline aquifers. The temperature effect of cold CO_2 mainly occurs near the injection well, and the temperature of the upper interface is lower due to the CO_2 upward migration. The permeability ratio of non-isothermal flow is 1.5% higher than that of isothermal flow due to thermal stress. Second, the density of CO_2 decreases slightly with considering the Joule-Thomson effect. The injected CO_2 temperature is lower, and the viscosity is greater. The shape of the CO_2 plume is affected by capillary entry pressure. When capillary entry pressure is lower, more CO_2 migrates upward under buoyancy, and the CO_2 lateral migration distance is greater. Finally, the CO_2 cumulative pressure at the bottom of caprock varies with injection boundary and injection rate. Under the pressure injection boundary, the cumulative pressure rises earlier. The more CO_2 is injected under flow flux boundary, the greater difference of CO_2 accumulative pressure is in the later stage.

8.2. Future research

In this thesis, the coupling mechanism among the two-phase flow, moisture field, temperature field and solid deformation field for the shale gas production and CO_2 geological storage were investigated. Based on experimental testing, theoretical derivation and numerical simulation, the theory of multi-field coupling two-phase flow in fractured shale were developed. Then, this theory was applied to the study of shale gas flowback mechanism and the evaluation of CO_2 geological storage efficiency. Furthermore, the following subjects are suggested for the future study.

(1) The immersion reaction of shale samples with supercritical CO_2 in a high-pressure vessel and the permeability tests have not been carried out. Although the experiment in this thesis qualitatively describes the changes of pore-structure and mechanical properties after

soaking in different pH solutions, the evolution of permeability and flow mechanism of fractured shale after geochemical reactions are worthy of further study.

(2) The phenomenon of self-heal or self-elevate is observed in fractures after the water-rock reaction. This thesis has conducted experimental research on shale under acid-base degradation in Chapter 2, the chemical-hydro-mechanical multi-physical coupling mechanism in shale caprock needs to be further investigated.

(3) This thesis theoretically derived a gas-water relative permeability model based on fractal theory. Applying the fractal relative permeability relationship to the shale gas production model would be the next step.

(4) The three-zone model in this thesis mainly focuses on three scales: matrix, natural fractures and hydraulic fractures. Homogenization assumption was used to explore the characteristics of shale gas multi-scale migration. When focusing on hydraulic fracturing stimulation, a discrete hydraulic-natural fracture network is generated, which can further investigate the optimization of shale gas production by fracture complexity.

(5) The research in this thesis is based on the two-dimensional model. However, the three-dimensional modelling is essential for accurately solving the engineering problems. Researchers have to face the challenge of high computing cost of model validation and simulations. Furthermore, the CO_2 geological storage involves two physical processes: the migration of CO_2 in the reservoir and the CO_2 penetration in the caprock. How to combine these two processes in a fully coupled model is the focus of future improvement.